Detection of temporarily flooded vegetation using time series of dual polarised C-band synthetic aperture radar data

Dissertation zur Erlangung des
Doktorgrades an der Fakultät für Geowissenschaften der
Ludwig-Maximilians-Universität München

Vorgelegt von
Viktoriya Tsyganskaya

München, 23. September 2019

Acknowledgments

First of all, I would like to thank **Prof. Dr. Ralf Ludwig** and **Dr. Philip Marzahn** from the Department of Geography of the Ludwig-Maximilians-University Munich for giving me the opportunity to start this PhD project and been my supervisors during the whole period. Their passion for science inspired and motivated me constantly and their great and endless support helped me to find my own path and continue even in the most discouraging phases of PhD. Furthermore, I would like to especially thank Dr. Philip Marzahn for taking his time and for constructive very inspiring discussions about required methods and data analysis. I benefited a lot from his experience and his deep understanding of microwave remote sensing and geostatistics.

I want to sincerely thank **Prof. Dr. Günter Strunz**, Head of Department "Geo Risks and Civil Security" at the Earth Observation Centre of the German Aerospace Center (DLR), who agreed to become my second referee and encouraged me to write this work cumulatively from the beginning.

Special thanks to my supervisor at DLR, **Dr. Sandro Martinis**, Head of Research Group Natural Hazards at the Earth Observation Centre of the DLR, for the introduction to flood detection and the fruitful comments and suggestions for several aspects of my work.

I would also like to thank my colleagues (**Prof. Dr. Andreas Schmitt, Dr. Simon Plank, Andre Twele, Wenxi Coa, Dr. Marianne Jilge**) at DLR for providing data sets, valuable exchange and mental support.

I am also very grateful to all the colleagues and friends from Deparment of Geography at the LMU for having a great time together and their helpful expertise and advices. I would like to thank Vera Erfurt for the organisational support of all doctoral students and for her open ear. My special thanks go to Dr. Janja Vrzel and Thomas Weiß for their unwavering faith, for the special moments and the unforgettable time. I would also like to thank my new colleagues at Cubert GmbH for their patience and understanding.

Many thanks to all my important people, my family and friends. Thank you very much for your patience, the unconditional support during thesis-related crises and the cheering all the time. Special thanks go to Lukas for his support in implementing the methodology, but especially for his unlimited emotional support and always being there for me.

Summary

The intense research of the last decades in the field of flood monitoring has shown that microwave sensors provide valuable information about the spatial and temporal flood extent. The new generation of satellites, such as the Sentinel-1 (S-1) constellation, provide a unique, temporally high-resolution detection of the earth's surface and its environmental changes. This opens up new possibilities for accurate and rapid flood monitoring that can support operational applications. Due to the observation of the earth's surface from space, large-scale flood events and their spatio-temporal changes can be monitored. This requires the adaptation of existing or the development of new algorithms, which on the one hand enable precise and computationally efficient flood detection and on the other hand can process a large amounts of data.

In order to capture the entire extent of the flood area, it is essential to detect temporary flooded vegetation (TFV) areas in addition to the open water areas. The disregard of temporary flooded vegetation areas can lead to severe underestimation of the extent and volume of the flood. Under certain system and environmental conditions, Synthetic Aperture Radar (SAR) can be utilized to extract information from under the vegetation cover. Due to multiple backscattering of the SAR signal between the water surface and the vegetation, the flooded vegetation areas are mostly characterized by increased backscatter values. Using this information in combination with a continuous monitoring of the earth's surface by the S-1 satellites, characteristic time series-based patterns for temporary flooded vegetation can be identified. This combination of information provides the foundation for the time series approach presented here.

This work provides a comprehensive overview of the relevant sensor and environmental parameters and their impact on the SAR signal regarding temporary open water (TOW) and TFV areas. In addition, existing methods for the derivation of flooded vegetation are reviewed and their benefits, limitations, methodological trends and potential research needs for this area are identified and assessed. The focus of the work lies in the development of a SAR and time series-based approach for the improved extraction of flooded areas by the supplementation of TFV and on the provision of a precise and rapid method for the detection of the entire flood extent.

The approach developed in this thesis allows for the precise extraction of large-scale flood areas using dual-polarized C-band time series data and additional information such as topography and urban areas. The time series features include the characteristic variations (decrease and/or increase of backscatter values) on the flood date for the flood-related classes compared to the whole time series. These features are generated individually for each available polarization (VV, VH) and their ratios (VV/VH, VV-VH, VV+VV). The generation of the time series features was performed by Z-transform for each image element, taking into account the backscatter values on the flood date and the mean value and standard deviation of the backscatter values from the non-flood dates. This allowed the comparison of backscatter intensity changes between the image elements. The time series features constitute the foundation for the hierarchical threshold method for deriving flood-related classes. Using the Random Forest algorithm, the importance of the time series data for the individual flood-related classes was analyzed and evaluated. The results showed that the dual-polarized time series features are particularly relevant for the derivation of TFV. However, this may differ depending on the vegetation type and other environmental conditions.

The analyses based on S-1 data in Namibia, Greece/Turkey and China during large-scale floods show the effectiveness of the method presented here in terms of classification accuracy. The

supplementary integration of temporary flooded vegetation areas and the use of additional information resulted in a significant improvement in the detection of the entire flood extent. It could be shown that a comparably high classification accuracy ($\sim 80\%$) was achieved for the flood extent in each of study areas. The transferability of the approach due to the application of a single time series feature regarding the derivation of open water areas could be confirmed for all study areas. Considering the seasonal component by using time series data, the seasonal variability of the backscatter signal for vegetation can be detected. This allows for an improved differentiation between flooded and non-flooded vegetation areas. Simultaneously, changes in the backscatter signal can be assigned to changes in the environmental conditions, since on the one hand a time series of the same image element is considered and on the other hand the sensor parameters do not change due to the same acquisition geometry. Overall, the proposed time series approach allows for a considerable improvement in the derivation of the entire flood extent by supplementing the TOW areas with the TFV areas.

Zusammenfassung

Die intensive Forschung der letzten Jahrzehnte in dem Bereich Hochwassermonitoring hat gezeigt, dass mit Hilfe von Mikrowellensensoren wertvolle Informationen über die Hochwasserausdehnung abgeleitet werden können. Die neuen Satelliten-Generationen, wie die S-1 Konstellation, ermöglichen heutzutage eine in dieser Form neue, zeitlich hoch aufgelöste Erfassung der Erdoberfläche und deren Umweltveränderungen. Dadurch eröffnen sich neue Möglichkeiten für eine genaue und schnelle Hochwasserüberwachung, die den operationellen Einsatz unterstützen können. Durch die Erfassung der Erdoberfläche aus dem Weltall können unter anderem großflächige Hochwasserereignisse und ihre räumlich-zeitliche Veränderung beobachtet werden. Dies erfordert die Anpassung bestehender oder die Entwicklung neuer Algorithmen, welche zum einen eine präzise und rechnerisch effiziente Hochwassererkennung ermöglichen und zum anderen große Datenmenge verarbeiten können.

Um die Gesamtausdehnung der Hochwasserfläche vollständig zu erfassen ist neben den offenen Wasserflächen die Detektion von temporär unterfluteten Vegetation (TUV) erforderlich. Die Nichtberücksichtigung der unterfluteten Vegetationsflächen kann zu gravierenden Unterschätzungen des Hochwasserausmaßes und -volumens führen. Unter bestimmten System- und Umweltbedingungen kann das Synthetic Aperture Radar (SAR) eingesetzt werden, um Informationen unter der Vegetationsdecke zu extrahieren. Aufgrund von Mehrfachrückstreuungen des SAR-Signals zwischen der Wasserfläche und der Vegetation sind die unterfluteten Vegetationsflächen meist durch erhöhte Rückstreuwerte charakterisiert. Mit Hilfe dieser Information in Kombination mit einer zeitlich hochaufgelösten Erfassung der Erdoberfläche durch die S-1 Satelliten können charakteristische, zeitserienbasierte Muster für TUV identifiziert werden. Diese Verknüpfung von Information dient als Grundlage für den hier vorgestellten Zeitserienansatz.

Arbeit gibt einen umfangreichen Überblick über die relevanten Sensor- und Umweltparameter sowie ihre Auswirkung auf das SAR-Signal in Bezug auf offene Wasserflächen und unterflutete Vegetationsflächen. Zusätzlich werden bereits bestehenden Methoden für die Ableitung von unterfluteter Vegetation untersucht und deren Nutzen, Limitierungen, methodische Trends und der potenzielle Forschungsbedarfs für diesen Bereich aufgezeigt und bewertet. Der Schwerpunkt der Arbeit liegt auf der Entwicklung eines zeitserienbasierten SAR Ansatzes zur verbesserten Ableitung von Überschwemmungsflächen durch die Ergänzung von TUV und auf der zur Verfügung stellen einer präzisen und schnellen Methode für Detektion des gesamten Überflutungsausmaßes.

Der in der vorliegenden Arbeit entwickelte Ansatz ermöglicht die präzise Ableitung von großflächigen Überschwemmungsgebieten auf der Grundlage von dual-polarisierten C-Band Zeitseriendaten und Zusatzinformationen, wie der Topographie und urbanen Flächen. Zu diesem Zweck wurden mehrere Zeitserienfeatures entwickelt. Die Zeitreihenmerkmale beinhalten die charakteristischen Variationen (Abfall und/oder Anstieg der Rückstreuwerte) für die hochwasserrelevanten Klassen zum Hochwasserzeitpunkt im Vergleich zu der gesamten Zeitreihe. Die Zeitserienmerkmale werden für jede verfügbare Polarisation (VV, VH) und deren Verhältnisse (VV/VH, VV-VH, VV-VH, VV+VV) individuell generiert. Die Generierung der Zeitreihenmerkmale erfolgte mittels Z-Transformation für jedes Bildelement unter Berücksichtigung der Rückstreuungswerte zum Hochwasserzeitpunkt und des Mittelwerts und der Standardabweichung der Rückstreuungswerte von Nicht-Hochwasserzeitpunkten. Dies ermöglichte die Vergleichbarkeit von Rückstreuintensitätsänderungen zwischen den Bildelementen. Die Zeitserienfeatures

fungieren als Grundlage für die hierarchische Schwellenwertmethode, durch die die flutbedingten Klassen abgeleitet werden. Mit Hilfe des Random Forest Algorithmus wurde die Relevanz der Zeitseriendaten für die individuellen flutbedingten Klassen untersucht und bewertet. Die Ergebnisse zeigten, dass vor allem die dualpolarisierte Zeitserienfeatures für die Ableitung von TUV relevant sind. Dies kann sich aber in Abhängigkeit von des Vegetationstyps und weiterer Umweltbedingungen unterscheiden.

Die Untersuchungen auf der Grundlage von S-1 Daten in Namibia, Griechenland/Türkei und China während großräumiger Überschwemmungen zeigen die Wirksamkeit der präsentierten Methode in Bezug auf Klassifikationsgenauigkeit. Die ergänzende Integration von TUV und der Einsatz von zusätzlichen Informationen, führten zu einer deutlichen Verbesserung in der Detektion der gesamten Hochwasserausdehnung. Es konnte gezeigt werden, dass in allen Untersuchungsgebieten eine vergleichsweise hohe Klassifikationsgenauigkeit (ca. 80 %) für die Hochwasserflächen erreicht wurde. Die Übertragbarkeit des Ansatzes durch die Verwendung eines einzigen Zeitserienfeatures bezüglich der Ableitung von offenen Wasserflächen konnte aber für alle Untersuchungsgebiete bestätigt werden. Unter Berücksichtigung der saisonalen Komponente durch den Einsatz von Zeitseriendaten kann die saisonale Variabilität des Rückstreusignals für Vegetation erfasst werden. Dies ermöglicht eine verbesserte Unterscheidung zwischen gefluteten und nicht gefluteten Vegetationsbereichen. Gleichzeitig können Veränderungen des Rückstreusignals Veränderungen in den Umweltbedingungen zugeordnet werden, da zum einen eine Zeitreihe desselben Bildelements betrachtet wird und zum anderen die Sensorparameter aufgrund der gleichen Aufnahmegeometrie sich nicht verändern. Insgesamt ermöglicht der in dieser Arbeit vorgestellte Zeitserienansatz eine erhebliche Verbesserung in der Ableitung der gesamten Hochwasserausdehnung durch die Ergänzung der temporären offenen Wasserflächen mit TUV.

Contents

List of figures

List of tables

List of acronyms

EM	Electromagnetic
ESA	European Space Agency
EW	Extra Wide Swath Mode
GMES	Global Monitoring for Environment and Security
GRD	Ground Range Detected
H	Horizontal
IW	Interferometric Wide Swath Mode
NCS	Normalized Radar Cross Section
NDWI	Normalized Difference Water Index
PRF	Pulse Repetition Frequency
RAR	Real Aperture Radar
S-1	Sentinel-1
S-2	Sentinel-2
SAR	Synthetic Aperture Radar
SLAR	Side Looking Airborn Radar
SLC	Single Look Complex
SM	Stripmap Mode
TFV	Temporary Flooded Vegetation
TOW	Temporary Open Water
V	Vertical

1 **Introduction**

The growing demand for information regarding the characteristics of flood events is a fundamental motivation for ongoing research in various fields. The frequent and widespread occurrence of floods worldwide causes high economic costs and also significant social and environmental impact. Especially for various institutions such as aid organisations, first rescuers, crisis management authorities, insurance companies or environmental agencies, precise and timely information on the extent of the floods is essential for providing a foundation for their decisions and actions. Besides, temporary open water, temporary flooded vegetation (TFV) is an important component for the detection of the entire inundation area. TFV can be described as areas in which water bodies occur temporary beneath vegetation. Thereby, an important characteristic of TFV is that the vegetation is not completely covered by water.

In this thesis, temporary flooded vegetation areas are considered as an essential part of flood detection. Floods are natural events that regularly occur at certain times of the year, depending on the discharge regime. The causes of flooding are mostly continuous, extensive, large-scale precipitation, often in combination with snowmelt (Vormoor et al. 2015). In addition, high waves in coastal zones can be a natural cause of flood events. However, human intervention (e.g. straightening of the river banks, large-area sealing and compaction of the soil, intensified land use and forestry) in the water system is also a strong driver for the occurrence of flood events (Bronstert 2003, Kundzewicz et al. 2018). Whether natural or anthropogenic, flood events are highly variable in space and time. A snapshot is mostly insufficient to obtain a comprehensive understanding of the hydrological process. The integration of the spatio-temporal component along with TFV is essential for gaining an understanding of the dynamics of flood events and for improving flood detection.

1.1 **Relevance of TFV**

In the context of flood detection, the relevance of TFVs can be particularly well demonstrated by the diversity of the affected fields and the intensity with which they are affected. The disregard of these areas has immense consequences from a hydrological, ecological and economic point of view. The duration, frequency, intensity and magnitude of flood events influence the intensity of the impacts.

According to CRED and UNISDR (2019), flood events in 2018 affected significantly more people than in any other year of the 21st century (UNISDR 2019). Floods are not only one of the most widespread natural disasters, which regularly involve human and economic losses, but also the most frequent disaster type in comparison to other natural hazards (Figure 1). In 2018, ~38.6% of all natural disasters worldwide were caused by flood events (EMDAT 2019). In the agricultural sector, the impacts can be particularly disastrous, as crop failures can not only cause economic damage to the farmers, but can also result in famine (FAO 2011). Figure 2 shows how devastating the impact of a flood event can be on agricultural areas.

Figure 1: Global reported natural disasters including Floods (Ritchie and Roser 2019).

Additionally, the inundation of agricultural areas leads to the contamination of the water catchment area with nutrients, heavy metal pollutants and pesticides (Ciszewski and Grygar 2016, Hafeez et al. 2019). The consequences are changes in water quality and species diversity. The worst case scenario is eutrophication of water bodies (Ansari and Gill 2014, OECD 2017). Flooding near the coast can lead to degradation of soils and may result in plant species changes due to saltwater or brackish water (Tully et al. 2019). In addition to agricultural areas, forested areas can also be flooded. A special form of forests, which are located on river banks and are regularly/seasonally flooded, are floodplain forests (Figure 3).

Figure 2: Flood August 2002 of the Elbe river with a dyke breach, Germany
© André Künzelmann/UFZ (Arnhold 2008).

1 Introduction

Floodplain forests have a high biodiversity and species diversity and represent an essential component for flood protection. The water flowing over the riverbank can spread into floodplain forests and be stored in the soil and vegetation (Junk 1997, Klimo and Hager 2001, Machar et al. 2019). Other man-made flood protection structures, such as dykes, can increase flood protection in combination with floodplain forests (Damm 2013, Gergel et al. 2002, Kryspin-Watson et al. 2017). This can reduce the probability of a dyke failure (Figure 2).

In the future it is expected that the magnitude and frequency of flood hazards will increase due to climate change (IPPC 2013, Rao et al. 2014, Schädler et al. 2012, Thistlethwaite et al. 2018). Flood hazard will probably increase due to the rising number of heavy and extreme precipitation events arising in many regions (Kundzewicz et al. 2018). A significant part of the increase in flood hazards can be attributed to non-climatic anthropogenic impacts. These include land-use changes such as urbanization, deforestation, removal of floodplains and wetlands, and river regulation (Stefanidis and Stathis 2013). This results in a reduction in infiltration capacity and water storage and an increase in runoff. Reasons for the intensification of flood events are, on the one hand, natural causes, such as snow melting in connection with heavy rainfall. On the other hand, humans and their interventions into the water system increase the probability of flood events (Zischg et al. 2018).

The increased occurrence of flood events will also have a greater impact on vegetation areas. The changes will take place mainly in shoreline areas (Garssen et al. 2017). The changes will mainly take place in riparian areas and will affect bio- and species diversity due to the possible degradation of soils or the formation of new habitats. In addition, an increased frequency of crop failures and thus higher economic damage is to be expected (IPPC 2012). Flood protection measures will have to be reevaluated and adapted for the future. Therefore, it will be important and necessary in the future to assess and detect the frequency, magnitude, duration and extent of flood events as precisely and quickly as possible. This work contributes to an improved flood detection by the implementation of a spatio-temporal component and the inclusion of TFV areas.
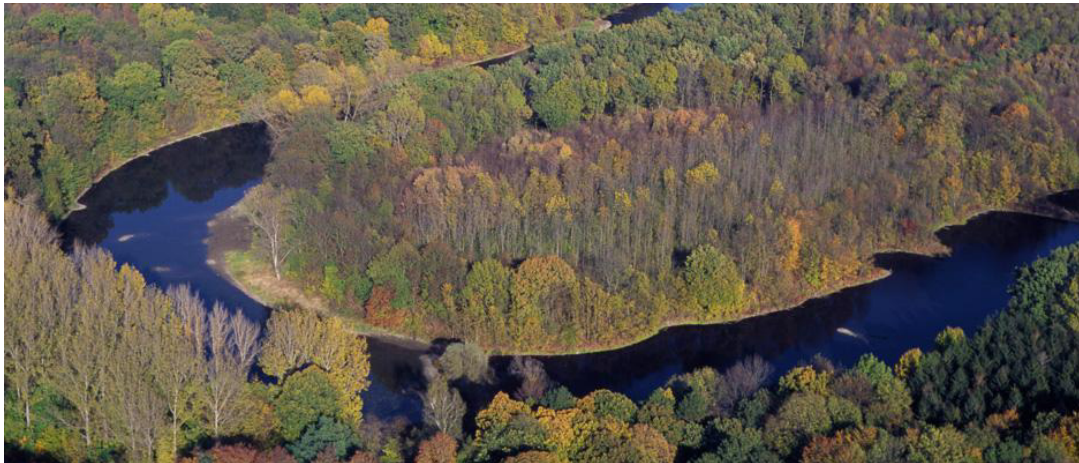

Figure 3: Floodplain forest in Germany © Stefan Ellermann (LAU) (Natura 2000, 2019).

1.2   Potential of SAR and time series data for detection and extraction of the TFV

Spaceborne remote sensing is a potential instrument for the acquisition of the entire flood extent, which allows for the monitoring of large areas of the earth's surface. Since the use of optical sensors during flood situations is often severely restricted by cloud cover, images taken with microwave satellites are mostly used as a basis for operational flood detection due to their independency towards weather and daylight. Therefore, this work focuses on microwave remote sensing. Due to the characteristics of microwave radiation to penetrate into a medium in dependence of the wavelength, microwave-based systems (radar, synthetic aperture radar (SAR)) are suitable for the detection of standing water surfaces beneath the vegetation. This is achieved by the capability of the radar signal to penetrate the vegetation canopy and the interaction between the water surface and the lower areas of the vegetation. The latter can lead to a strong backscatter signal, which is higher than under normal hydrological conditions (e.g. (Richards et al. 1987, Townsend 2001). Despite the advantage regarding the detection of TFV by SAR data, the interpretation of the backscatter signal from TFV is not always straightforward because the interaction between system parameters and environmental conditions strongly influences the backscatter signal. Therefore, essential statistical and on-site knowledge is required in order to obtain accurate results.

Studies about the derivation of flood extent have grown steadily over the last decades (Brown et al. 2016, Clement et al. 2017, Dellepiane et al. 2000, Schlaffer et al. 2015, Smith 1994). However, there are only a small number of studies including the TFV area for flood monitoring purposes (Long et al. 2014, Martinis et al. 2015, Pierdicca et al. 2008, Pulvirenti et al. 2010, Pulvirenti et al. 2016, Zhao et al. 2014). This is primarily due to the limited availability of appropriate SAR data. Despite the numerous operating microwave sensors, the availability of the regularly acquired spaceborne microwave data is restricted. Therefore, the majority of the analyzed studies used a single image or two images with flooded and non-flooded conditions. However, the lack of information about the normal conditions of the environment and the requirement of manual intervention can limit the reliability of results of the flood extent. With the launched C-band S-1 satellite missiona new age of flood monitoring was initiated due to the availability of high temporal resolution data with a revisit frequency of up to six days. The regularity of the data acquisition over a longer period provides information about different seasonal conditions of the vegetation and the corresponding backscatter signal.

The opportunity to include seasonal or annual fluctuations of backscatter using the free of charge short revisit SAR time series data provide an opportunity to extract TFV and to improve flood detection. However, the focus on the multi-temporal changes regarding TFV adds a new level of complexity. Therefore, an in-depth analysis is required to exhibit the effects and changes on the backscatter signal over time and during a flood event. To understand the effects regarding TFV, the analysis of the multi-temporal characteristics and pattern of S-1 data is crucial. Besides the SAR data, the integration of other data can be useful for obtaining an accurate extent of the flood. Topographical data, optical data or specific layers obtained from this data can be combined for a comprehensive analysis of inundation events and the extraction of special areas, such as TFV.

Depending on the different tasks, the availability of SAR data, the polarization modes, the phase information and the spatial or temporal resolution, various algorithms were applied to the

different applications and thus inconsistency exists in the methods for the derivation of TFV (Tsyganskaya et al. 2018b). Furthermore, there are a small number of papers in the literature dealing with the automatic and rapid flood extraction from SAR data for operational use (e.g. Martinis et al. 2009, Martinis and Twele 2010, Matgen et al. 2011, Pulvirenti et al. 2011, Pulvirenti et al. 2012, Schumann et al. 2009). Due to its complexity, TFV is barely included in flood detection approaches, as its transferability to different study areas is limited. Whenever TFV was incorporated into a method, single image and change detection approaches were mainly applied (Long et al. 2014, Martinis et al. 2015, Pierdicca et al. 2008, Pulvirenti et al. 2010, Pulvirenti et al. 2016, Zhao et al. 2014). Very few studies have attempted to detect the hydrological dynamics of flood events using time series data (Martinez and Le Toan 2007, Pulvirenti et al. 2011a, Pulvirenti et al. 2012). Schlaffer et al. (2016) showed that based on a multi-temporal image stack and using a harmonic model, the classification of wetland classes can be achieved. This method shows the potential for the detection of TFV integrating temporal and spatial variability. The use of frequently multi-temporal acquired S-1 data provide a potential foundation for the development of a SAR based time series approach for the extraction of TFV and improved flood detection. By incorporating seasonal or annual variations in vegetation, the complexity of the TFV can be considered. However, the processing and analysis of SAR time series data constitutes a challenge due to the large amounts of data. This requires the development of an adapted algorithm allowing for the processing of dual-polarized SAR time series data.

1.3   Scientific objectives

As shown in the previous Section 1.1, the detection of temporary flooded vegetation (TFV) is a key component in many applications. However, at the current stage, the causes, states, impact and implications of TFV are not sufficiently well characterized or understood. Furthermore, TFV is not adequately considered in the current flood mapping products, as the focus mostly lies on the extraction of temporary open water (TOW). Due to the lack of an appropriate data foundation in the past, an adequate extraction of TFV areas is still underrepresented and widely neglected. As the occurrence of TFV is a dynamic process, characterized by a spatio-temporal variability, it is important to take into account and fully understand the drivers of this dynamic. The use of SAR time series data has great potential for the detection and interpretation of TFV, since the spatial and temporal variability can be considered (Section 1.2). Based on these considerations, this thesis defines the following scientific objectives:

- Evaluation of the state of the art methods by providing an overview and comparison of the data sets and classification algorithms with their advantages, limitations and possible trends regarding the extraction of TFV.
- Analysis and evaluation of multitemporal characteristics and patterns regarding the backscatter signal for flood related classes, such as TOW and TFV.
- Establishing the comparability between the TFV backscatter values of the image elements and simplifying the complexity of multitemporal characteristics and patterns of flood-relevant classes by developing polarization-dependent time series features.
- Development, assessment and validation of a new SAR time series-based method for comprehensive and rapid mapping of entire flood extents using developed time series

features with a focus on the increased quality of maps for flood detection by including TFV.

- Demonstration of the transferability and the robustness of the methodology by analyzing the impact of time series data and different polarization for various TFV types in different study areas.

Based on the aforementioned scientific objectives, the following research questions have been formulated:

- *Research question 1: Does the comparison of the state of the art of the method provide an identification of trends regarding the SAR based classification algorithms for the extraction of TFV?*
- *Research question 2: Are the multitemporal characteristics and patterns of the SAR time series data suitable for identifying flood-related classes (TOW and TFV)?*
- *Research question 3: Do the operational dual-polarized SAR systems have the potential to provide time series features for the derivation of flood related classes (TOW and TVF)?*
- *Research question 4: Are dual-polarized Sentinel-1 time series data suitable for the development of a robust classification approach for TFV extraction and improved flood detection?*
- *Research question 5: Can the SAR time series approach be transferred to different study areas and vegetation types using a single time series feature for the extraction of TFV and thus be applied operationally?*

1.4 Structure of the thesis

In Chapter 2 the basic principles of microwave remote sensing are presented. The focus lies on the characteristics of SAR data. Furthermore, an overview of the S-1 sensors is provided, the data of which is predominantly applied in this thesis.

Interactions of microwave signal with open water surfaces and water bodies covered by vegetation are described in Chapter 3. Besides an explanation about the backscatter behavior of radar waves in general, the particular characteristics of radar reflectance from open water surfaces and flooded vegetation are also discussed.

In Chapter 4 an overview about the state of the art regarding SAR-based derivation of flooded vegetation and the developed time series approach for the extraction of TFV with the corresponding results are presented by three scientific peer-reviewed publications.

Section 4.1 presents the first paper reviewing the characteristics and approaches of SAR-based detection of flooded vegetation. In addition, a comprehensive review of sensor- and object parameters and their effects on the SAR signal regarding the detection of flooded vegetation is provided. Furthermore, an overview of the data sets used and the state of the art for the applied algorithms for the extraction of flooded vegetation is provided in the same publication, revealing their benefits, limitations, methodological trends, and pointing out the potential research needs for this field.

In Section 4.2 a SAR time series approach based on S-1 C-band data is proposed. For the detection of the entire flood extent with the focus on TFV, the developed method combines dual-polarized time series data with ancillary information. Based on the findings about

multitemporal characteristics and patterns (decrease and/or increase of the backscatter values on the flood date), which indicate flood-related classes, time series features are derived. The time series features were generated for each polarization and polarization combination by performing a Z-transform over the time series for each image element. Thereby, a comparison of the backscatter intensity change for the SAR signal between the pixels could be achieved. The capabilities of the method are demonstrated for a flood event in Namibia that occurred in 2017. Analyses regarding the impact of time series characteristics on the identification of flood related classes and the transferability of the SAR time series approach are described in Section 4.3. An analysis was carried out based on two independent study areas in Greece/Turkey and China containing different vegetation types, such as high grassland and forested areas. In order to demonstrate the transferability and the potential of the SAR time series approach for operational use, time series features are compared simultaneously with respect to their suitability for the extraction of TFV for all study areas.

The thesis concludes in Chapter 5 with an evaluation of the developed approach and discusses improvement opportunities as well as an outlook for future analysis and synergetic use of SAR data.

2   Theoretical basics

2.1   Physical fundamentals

The visualisation of the earth's surface in aerial and satellite images is defined by the properties of the sensor in capturing the electromagnetic radiation that reaches the sensor during the acquisition. The electromagnetic radiation serves as an information medium between the observed object and the remote sensing sensor, which propagates as a harmonic wave with the speed of light. The wave is detected as reflected or emitted radiation from the observed object and contains information about its properties.

The electromagnetic radiation is represented in the electromagnetic spectrum. The entire spectrum is divided into different areas, according to the origin and the effect of the radiations, which fuse into each other without sharp boundaries. The different wavelength ranges, their names, their transmissivity through the atmosphere and the most relevant recording methods are shown in Figure 4. The electromagnetic radiation is characterized by the wavelength λ and the frequency f (Lillesand et al. 2008). In comparison to the visible light (about 0.4 to 0.7 µm), which can be detected by optical sensors, the microwave radiation range is about between 1 mm and 1 m, which can be detected by radar methods. The detection of natural electromagnetic radiation (solar radiation reflected from the earth's surface as well as heat radiation emitted from the earth's surface itself) is called passive remote sensing, whereby artificially generated radiation, e.g. by radar, is referred to as active remote sensing (Ulaby and Long 2015).
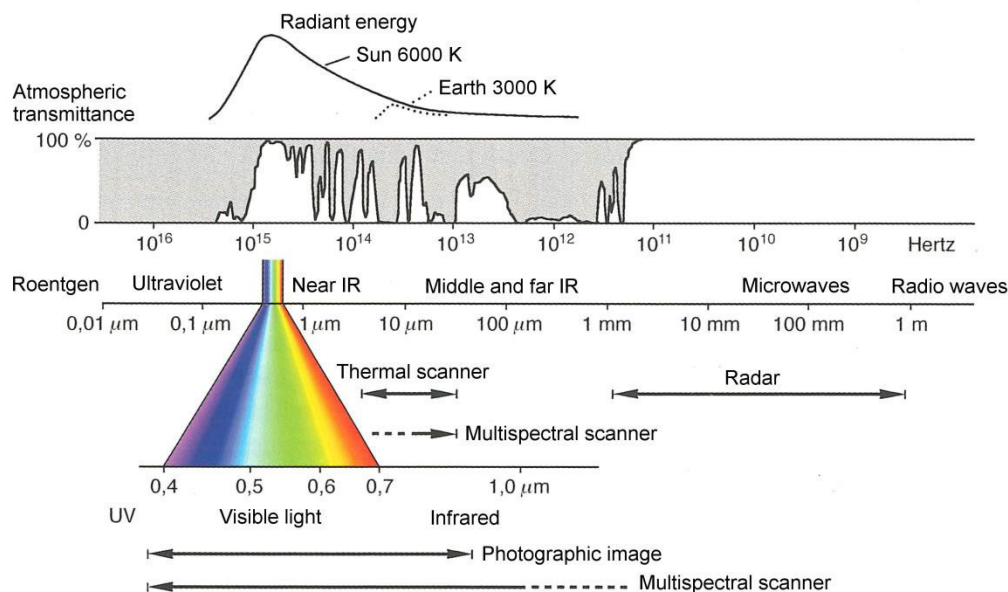
Figure 4: The electromagnetic spectrum and the acquisition ranges of different sensors based on Albertz 2007.

2.2   Basic principles of imaging radar systems

In this work, data and methods of radar remote sensing were applied. Radar (radio detection and ranging) is an active remote sensing method which uses the spectral range of microwaves. Data acquisition using a radar sensor is largely daylight- and weather-independent, providing a continuous temporal resolution in dependence on the orbit of the sensor. In addition, the complex calibration and correction procedures for the reduction of atmospheric influences are no longer necessary(Richards 2009).

Radar detection of the earth's surface is achieved by emitting microwave pulses at the pulse repetition frequency (PRF) and by measuring the amount of energy or transit time reflected back to the sensor by an antenna(Lillesand et al. 2008, Woodhouse 2006).The backscattering properties are influenced by sensor-specific system parameters and the object properties.

Operational principle and properties of Synthetic Aperture Radar (SAR)

Radar remote sensing systems can be categorized into non-imaging and imaging systems. Non-imaging systems include, for example, radar altimeters for determining heights on the land surface. Imaging systems are e.g. the Side Looking Airborne Radar (SLAR) or the Synthetic Aperture Radar (SAR) (Woodhouse 2006). Imaging radar systems provide a two-dimensional image of the Earth's surface after digital processing (Hein 2004).

For the remote sensing of the earth's surface from space, sensors are generally applied, which use the Synthetic Aperture Radar (SAR) acquisition technique. The scanning process of the earth's surface is carried out in a side-looking manner and perpendicular to the flight direction (Figure 5), since the radar is a distance measuring method that uses the double travel time of the microwave to spatially separate the received signals. Under optimal conditions, the sensor moves in a straight line over a landscape and sends an impulse at fixed intervals, which irradiates the area. Due to the relationship between antenna length and radiation characteristics, i.e. primarily the antenna beam width, the geometric resolution of e.g. the SLAR

with real aperture is limited (Lillesand et al. 2008).In comparison, SAR systems have a short antenna, but simulate a long antenna using the appropriate acquisition and processing technology (Woodhouse 2006).This method is based on the Doppler effect, which is used to generate a virtual antenna length that is a multiple larger than the physical antenna (Lillesand et al. 2008). During the overflight, the same object is repeatedly illuminated by the successive radar pulses. Thereby, the radar signal contributes several times to the received signals, which are correlated in a complex way. During signal processing, however, the data is treated as if it came from individual parts of a very long antenna. This reduces the effective radar beam width and achieves a higher resolution in flight direction (azimuth direction) in the radar image compared to a real beam width of the antenna.
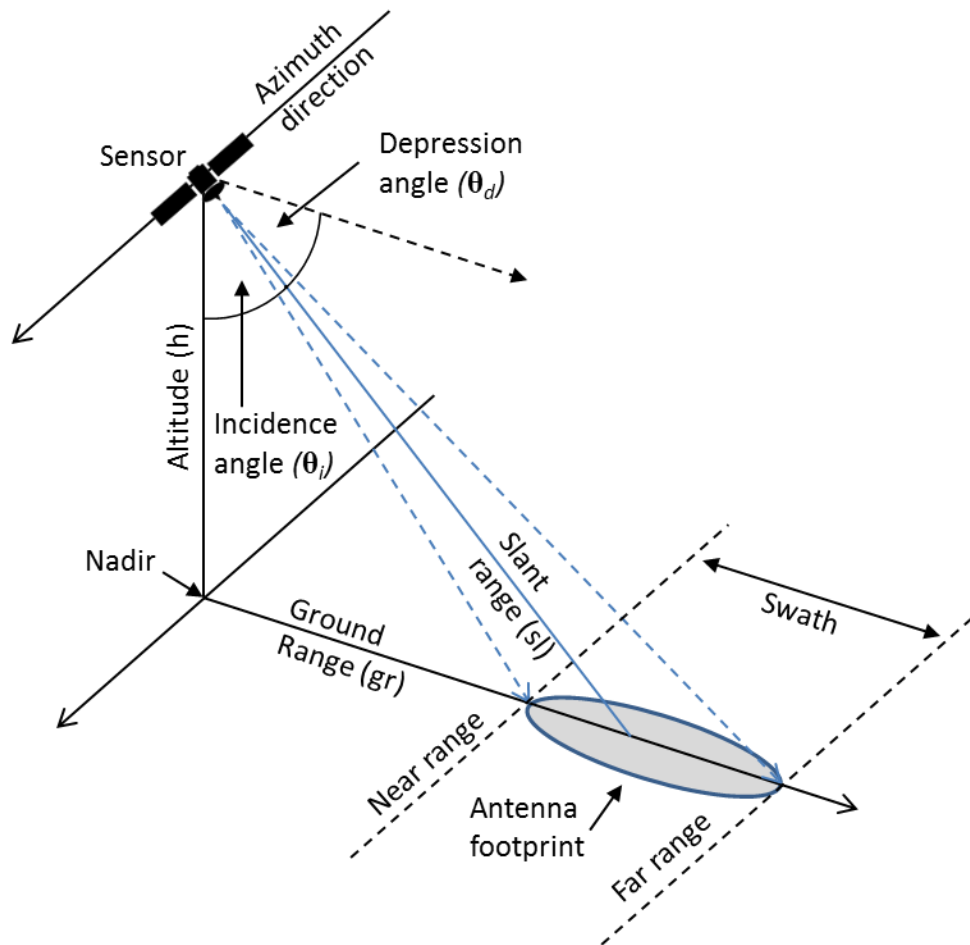
Figure 5: Imaging geometry of a space-based SAR sensor.

Resolution in range and in azimuth

A SAR system is characterized by its resolution in range (across-track) and azimuth (along-track). The range resolution can be described by the slant range or by the ground range resolution. In order to distinguish two object points in the slant range, their signals must be spatially separable from each other. For this purpose, their transit times (t_1 and t_2) must differ from each other by at least the length of the pulse length t($|t_2- t_1| \geq \tau$). Thus, the resolution (Figure 6) at slant range for Real Aperture Radar (RAR) and SAR is calculated with c for the speed of light and pulse duration τ (Woodhouse 2006):

$$r_{sl} = \frac{c * \tau}{2} \tag{1}$$

By projecting the slant range resolution with the angle of incidence θ_i on the ground, the resolution in ground range resolution can be obtained (Wooshouse 2006):

$$r_{gr} = \frac{c * \tau}{2 sin\theta i} \tag{2}$$

The slant range resolution remains constant, independent of the range. However, in ground range coordinates, the ground resolution depends on the angle of incidence. The crucial parameter for ground range resolution is not the height of the sensor above the ground, but the length of the pulse duration τ.

Therefore, reducing the pulse duration increases the resolution in the range direction. The pulse duration τ cannot be reduced arbitrarily in practice, since the energy to be sent increases with a shortening. The amount of energy is limited by the hardware. Technically, this is achieved by sending a much more extended, linear frequency-modulated signal instead of a short pulse. This signal is called chirp. After receiving this signal, it is converted into an equivalent short signal by the matched filter approach (Woodhouse 2006).
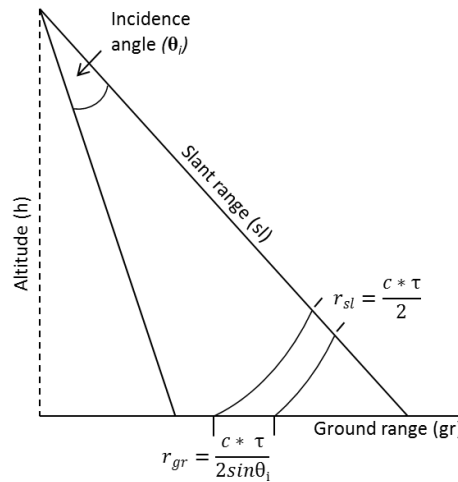
Figure 6: Resolution in slant range and ground range.

The azimuth resolution (r_a) along the flight direction (along-track) corresponds with traditional RAR approximately to the width of the footprint in flight direction. Using the RAR system, a ground point is only acquired once. Therefore, two objects can only be distinguished if they are not in the same footprint. The azimuth resolution depends on the beam width of the antenna footprint φ (Figure 7), which is defined by the ratio between the wavelength λ of the transmitted pulses and the physical antenna length L:

$$\varphi = \frac{\lambda}{L} \tag{3}$$

With this beam width, the geometric resolution of RAR results for a defined distance R on the ground to:

$$r_{a,RAR} = R * \varphi \approx \frac{R * \lambda}{L} \tag{4}$$

Using a RAR system on a satellite would require a very large antenna for adequate beam width resolution. However, the antenna size is limited by the sensor carrier. The SAR principle significantly improves the azimuth resolution by artificially extending the antenna. Thereby the PRF is increased so that an object is illuminated almost continuously (Figure 7). The SAR system emits the waves with a large antenna beam width, which means that individual objects are detected several times during the flight. For SAR, the maximum resolution in azimuth r_a defined by:

$$r_{a,SAR} = \frac{L}{2} \tag{5}$$

Since the azimuth resolution of SAR is determined by the length L of the half antenna, it is independent of the distance and wavelength. There are several approaches for the synthesis of the synthetic aperture and the merging of the individual images (Klausing and Holpp 2010). One approach is based on the Doppler effect. The Doppler effect takes advantage of the fact that every object on the Earth's surface is detected several times during a flight with a wide beam. Coherent characteristics of the signals as well as the known temporal pulse send and receiving sequences allow a subsequent phase-corrected processing, since the different single echoes of a ground objects can be separated by the Doppler frequencies of the backscattered signals (Raney 1998). The effective antenna length increases with increasing range, as targets on the ground are viewed more often in the far range than in the rear range. In Figure 7 point A is sampled less frequently compared to points B and C. Point C is most frequently scanned by the antenna beam width. Therefore, the ground range resolution increases with increasing distance from the sensor in range direction (Lillesand et al. 2015).

Figure 7: Acquisition principle of a SAR sensor.

Radar equation and backscatter coefficient

The received and recorded power (P_r) at the antenna of a SAR system can be transformed into a two-dimensional image (Bamler and Schättler 199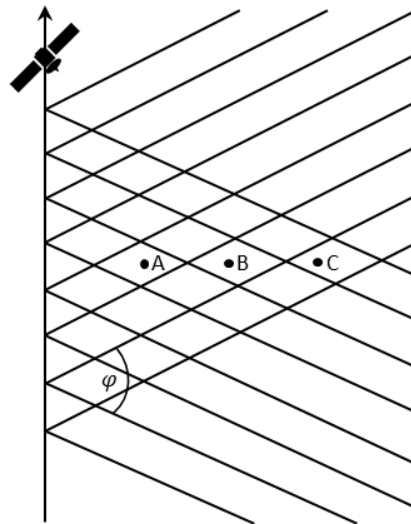3, Curlander and MacDonough 1991, Moreira et al. 2013). The power depends on the sensor and scattering properties of the illuminated object. Both variables influence the backscatter signal and can be described mathematically by the radar equation (Ulaby and Long 2015):

$$P_r = \frac{P_t G^2 \lambda^2 \sigma}{(4\pi)^3 R^4} \tag{6}$$

where P_t is s the emitted power, G is the antenna gain, λ the wavelength, R the distance to the target and σ represents the radar backscatter cross section.

The radar cross-section $\sigma[m^2]$ is the backscattering of a discrete objects. This is a function of the scattering properties or the reflection behavior of the target object on the earth's surface. For the characterization of distributed targets in the context of Earth observation, the radar backscatter coefficient σ^0 (normalized radar cross-section (NCS) or sigma naught) is used (Woodhouse 2006):

$$\sigma^0 = \frac{\sigma}{A} \left[\frac{m^2}{m^2} \right] \tag{7}$$

where A is the area over which the measurement is made. σ^0 is usually expressed logarithmically in decibel [dB]. For the description of imaging radar products, this parameter is best suited to accurately estimate the normalized cross-sectional values for a given pixel. The radar backscattering coefficient describes the scattering characteristics of an object (Hein 2004).

Speckle effect

A characteristic of radar images are the granular image structures, which also occur in homogeneous surfaces - the so-called speckle effect (Lillesand et al. 2015, Woodhouse 2006). The occurrence of speckle is physically caused by a monochromatic imaging system, due to the fact that the emitted coherent radiation is scattered differently at the objects within the image pixel and reflected in different phases. Due to the backscatter at countless particles (distributed target) on the ground, the individual waves overlap coherently and thus interfere with each other. The recorded signal is thus a combination of different individual signals with different phases (Raney 1998). Due to the speckle effect, the backscatter intensity of a pixel is only slightly correlated with the physical conditions on the ground. As a result, homogeneous surfaces are not homogeneously imaged, but appear rather granular in the image.
Speckle can be reduced by various digital image processing techniques, e.g. speckle filtering, which is crucial for adequate estimation of the backscattering coefficient σ^0. Mostly, efforts are made to reduce the influence of speckle by averaging the intensity and phase information pixel by pixel. This can be achieved by so-called multi-look procedures during SAR acquisition and processing. Thereby, the subdivision of the synthetic aperture into

several independent apertures (single looks) allows the detection of a terrain object by multiple acquisitions, which are averaged to produce multi-looked image.This method reduces the geometric resolution of the individual looks (Bähr and Vögtle 1998). For the reduction of the speckle effect different filter methods are used (e.g. Frost et al. 1982, Lee 1981, Lee and Pottier 2009).

Geometric effects (Layover, Shadowing and foreshortening)

Using the SAR system, objects can only be distinguished if the reflected pulses arrive at the sensor with a time delay. A resolution depending on the angle of incidence, as it is usual with optical sensors, is not possible without a side looking antenna. Therefore, the SAR sensor can never look down vertically (nadir), but has to look at the area diagonally from the side (side-looking). This results in some effects that complicate the interpretation of a radar image. Figure 8 shows schematically the predominantly occurring geometric effects in a SAR system. Slopes that face the sensor cause a shift from elevated terrain to the sensor. The side facing sensor shrinks to a fragment of its actual length. This effect is called foreshortening. Thereby, the energy of many scatters is compressed within few image pixels and the surface, which is directed towards the sensor, appears bright in the SAR image. Layover is an extreme form of the foreshortening effect, where the signal from the top of an object (mountain, building) reaches the sensor before that of the base. Areas facing away from the sensor or located behind steep walls or human buildings are not illuminated. Consequently, the objects hidden behind cannot be displayed because no backscatter return is therefore received from that shadow region (Ulaby and Long 2015).
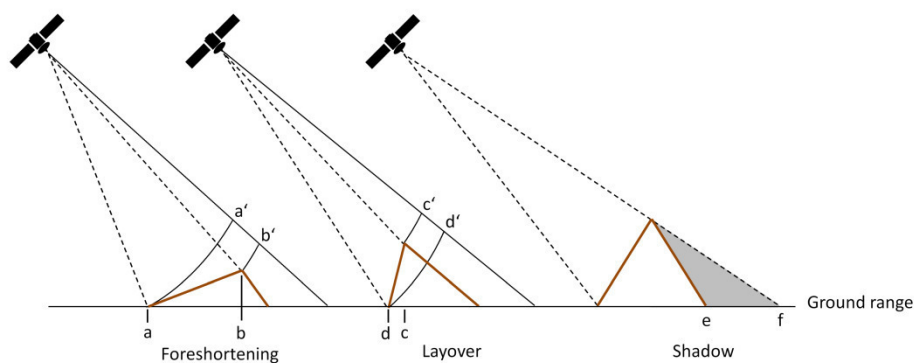
Figure 8: Geometric and radiometric relief distortions.

As long as the landscape is quite flat, the distortions are hardly noticeable. However, if the landscape has a strong relief, whether natural or man-made, the distortions occur (Woodhouse 2006).

The Foreshortening effect can be compensated with the help of an elevation model (Bayanudin and Jatmiko 2016). The finer the resolution of the elevation model used, the more detailed the geometric effects can be modeled. Layover can only be decomposed in exceptional cases if the signatures of the overlapping objects are known. However, a shadow cannot be removed mathematically due to a lack of information. In order to fill these gaps with image material, further acquisitions from other angles are required.

System specific imaging parameters (wavelength, polarization, incidence angle)

The representation of the earth's surface in radar images depends on the interaction of various individual factors. These are on the one hand the parameters of the acquisition system and on the other hand parameters of the terrain surface. The system parameters (sensor parameters) include the wavelength and frequency of the transmitted radiation, the polarization and the incidence angle (Ulaby and Long 2015).

In radar remote sensing, the wavelength [cm] or frequency range [GHz] between 0.75 cm and 100.0 cm or 40.0 GHz and 0.3 GHz is used. Above a wavelength of approx. 2 cm, microwave radiation can penetrate the atmosphere almost unaffected, even in cloudy conditions. Only strong rain events can affect the transmissivity of the radar signal up to a wavelength of approx. 4 cm. The wavelength determines the percentage of different types of scattering on certain object surfaces as well as the penetration depth of the waves and the signal attenuation in media such as vegetation or soil (Ulaby and Long 2015). In general, radar signals of lower frequencies are characterized by a higher capacity to penetrate media. Therefore, C-band and X-band SAR are preferred for the analysis of surface structures, while L-band SAR is preferred for the detection of structures below the surface (Lillesand et al. 2015).

The polarization of an electromagnetic wave is defined by the direction of the electric field (Bhatta 2011). Radar systems have the ability to transmit and receive electromagnetic waves in vertical (V) and horizontal (H) polarization planes. Like-polarised systems transmit and receive in the same polarization (VV and HH). The cross-polarised systems transmit in horizontal or vertical planes and receive the signals in the other plane (VH and HV) (Bhatta 2011, Lillesand et al. 2015). Radar systems can be equipped with single, multiple or fully polarized systems. A single polarized system captures information only in one transmitted and received polarization combination, while a multiple system allows to combine different channels. A fully polarized system is defined as a system in which the polarimetric phase information is stored in addition to the backscatter intensity. It allows the complete description of the scattering behavior of a terrain object by measuring a complex scattering matrix containing the scattering mechanisms and the scattering heterogeneity. The basics of polarimetry and its possible applications are discussed in Ulaby et al. (2015) and in Lee and Pottier (2009). Depending on the object properties, such as characteristic geometrical shape, different polarized radar beams are scattered differently and thus show different backscattering behavior.

The incidence angle θ_i is another relevant sensor parameter which is located between the nadir and the incident radar beam (Figure 5). This is supplemented by the depression angle θ_d at 90°. While the incidence angle is defined for a plane earth, the local incidence angle θ_{loc} takes the local terrain slope into account (Figure 9). This is defined as the angle between the radar beam and the surface normal. Since θ_{loc} depends on the orientation and slope of the terrain surface as well as on the incidence angle, it can be regarded as a system parameter as well as an object parameter. In addition, the interaction between the target and the electromagnetic (EM) wave depends on the incidence angle. The sensitivity of the signal to surface roughness or the contribution of the vegetation crown to the radar signal increases with the angle of incidence (Townsend 2001).
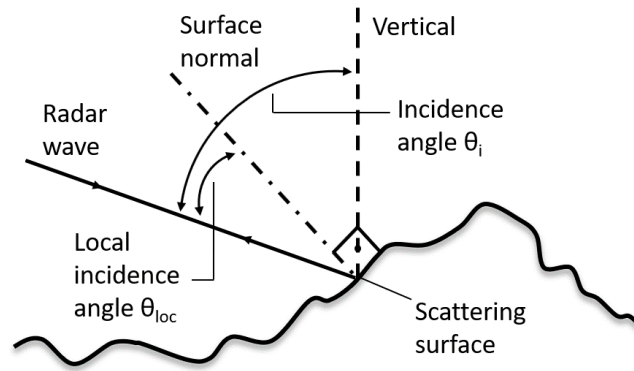
Figure 9: Local imaging geometry.

Object-specific parameters

Due to the interaction of radar radiation with objects on the earth's surface, various object-specific parameters influence the backscatter coefficient. The backscatter information can then be used to draw conclusions about certain properties of the surfaces analyzed. Besides the system parameters, the **roughness characteristic** and the **dielectric properties** of the object are significant.

Roughness characteristics is one of the dominant factors influencing the visual representation of a feature on radar images. In this context, roughness means the smoothness of the target in terms of wavelength and incidence angle (Lewis et al. 1998, Woodhouse 2006). At different frequencies and at different incidence angles the same surface shows different roughness.

When a smooth surface is hit by radiation, it is reflected away from the sensor by Snell's law (Figure 10). As a result, it tends to appear very dark in radar images. With increasing roughness, the proportion of diffuse scattering is greater. The incident energy is scattered in all directions and a significant part is returned to the sensor. With increasing roughness of a surface, the scattered element increases, while the reflected element of the signal decreases (Figure 10). With a very rough (Lambertian) surface, the energy is evenly scattered in all directions (Ulaby and Long 2015). In addition to the roughness itself, the wavelength (λ) and the incidence angle (θ_i) or the local incidence angle (θ_{loc}) determine the intensity of backscattering to the sensor.
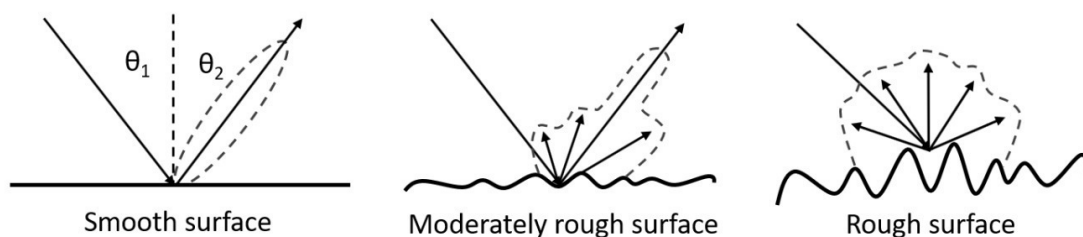
Figure 10: Radar reflection at a) smooth, b) moderately roughened and c) strongly roughened surfaces modified after Lillesand et al. (2015).

The Rayleigh criterion describes the relationship between these parameters and also allows to verify whether a surface is rough at a given wavelength and incidence angle. The Rayleigh criterion is expressed as follows:

$$s > \frac{\lambda}{8cos\theta_{loc}} \tag{8}$$

where s is the mean square height of the surface variations.

For natural surfaces, the Rayleigh criterion is often not strict enough, since the surfaces have a roughness spectrum similar to the wavelength, which leads to more frequent scattering. A stricter criterion, such as the Fraunhofer criterion proposed by Ulaby and Long (2015), is required:

$$s > \frac{\lambda}{32cos\theta_{loc}} \tag{9}$$

According to Rayleigh and the Fraunhofer criteria, a surface is rough once the phase difference $\Delta\Phi$ between two reflected waves is greater than $\pi/2$ radiant or $\pi/8$ radiant (Woodhouse 2006).

The scattering and absorption of radar radiation through a medium is strongly dependent on its dielectric properties. These are described by a complex dielectric constant ε, which is a measure for the interaction of electromagnetic radiation with a material and for the polarizability of the media, respectively (Raney 1998). It is mathematically described by a real component ε'' and an imaginary or image component ε''. The real component defines the degree of reflection at the transition of the radiation beams from one medium to another. The imaginary component represents the loss factor and describes the attenuation of the signal in the respective medium. The greater the contrast between the dielectric constants ε of two media, the stronger is the interaction of electromagnetic waves at the boundary between the two media and thus the radar backscattering (Bayer and Winter 1990). For the microwave range, most natural dry materials have a low value of ε′ between 3 and 8, while the dielectric constant of e.g. water is very high (ε′ = 80). Therefore materials with increased water content, but also metals, have a much higher dielectric constant (Lillesand et al. 2015, Ulaby and Long 2015). The dielectric properties of natural media are essentially determined by their water content (Dobson et al. 1995). This means that variations in soil moisture and plant water content have an effect on the dielectric properties and backscattering properties of these area. The dielectric constant of the soil depends not only on the soil moisture but also on the soil type and the frequency of the radar radiation (Ulaby and Long 2015). In general, the greater the roughness and the dielectric constant of the detected object, the stronger the radar backscatter signal (Kiage et al. 2005).

2.3 Sentinel-1

For this work spaceborne C-band (5.405 GHz) SAR data of the S-1 sensor were primarily used, which belongs to the Sentinel satellite series. These are Earth observation satellites of the Copernicus Program (formerly Global Monitoring for Environment and Security (GMES)) of European Space Agency (ESA)(Copernicus 2018). The S-1 mission is designed as a two-satellite constellation (Sentinel-1A and Sentinel-1B). The two satellites were launched on 3 April 2014 and 25 April 2016 respectively (ESA 2018b). Thereby, the two identical satellites operate in a near-polar, sun-synchronous orbit plane with 180° orbital phasing difference and at an altitude of almost 700 km. A single S-1 satellite is potentially able to map the global landmasses in the

Interferometric Wide Swath Mode (IW) once every 12 days, in a single pass (ascending or descending). The configuration of two satellites optimizes coverage and provides a global revision time of only six days. The Sentinel constellation is a dual polarised SAR system that also preserves the phase information. The acquisition can be performed in single polarization (HH or VV) mode as well as dual polarization (HH+HV or VV+VH) modes. The S-1 data is available free of charge and can be downloaded via the Sentinel Data Hub (ESA 2018a). S-1 data products acquired in Stripmap Mode (SM), IW mode, Extra Wide Swath Mode (EW), and Wave Mode (WV) (Table 1). SM mode is only used for extraordinary situations such as emergency management or for the detection of small islands. The monitoring of large-scale coastal areas, including shipping, oil spills and sea ice, is primarily carried out in EW mode. The IW and the WV modes allow conflict-free global coverage of the earth's surface via land with VV+VH and via open ocean with VV polarization respectively. Doppler centroid estimated, single look complex focused S-1 data are used in this work, additionally including image post-processing step for generation of the products Single Look Complex (SLC) and Ground Range Detected (GRD). While the SLC products (Table 2**Fehler! Verweisquelle konnte nicht gefunden werden.**) preserve the phase information and maintain the natural pixel spacing, the GRD products (Table 3) contain only the detected amplitude and are multi-looked to reduce the effects of speckle (ESA 2018b).

Table 1: Characteristics of SM, IW and EW modes.

	SM	IW	EW
Scene width	80 km	250 km	410 km
Incidence angle range (full performance)	18.3° - 46.8°	29.1° - 46.0°	21.6° - 25.1° 34.8° - 38.0°
Polarization	Dual HH+HV, VV+VH Single HH, VV	Dual HH+HV, VV+VH Single HH, VV	Single HH, VV

Table 2: Acquisition resolution Level-1 SLC.

Mode	Resolution (rg x az)	Pixel spacing (rg x az)
SM	1.7 x 4.3 m to 3.6 x 4.9 m	1.5 x 3.6 m to 3.1 x 4.1 m
IW	2.7 x 22.0 m to 3.5 x 22.0 m	2.3 x 14.1 m
EW	7.9 x 43.0 m to 15.0 x 43.0 m	5.9 x 19.9 m

Table 3: High resolution Level-1 GRD.

Mode	Resolution (rg x az)	Pixel spacing (rg x az)
SM	23x23 m	10x10 m
IW	20x22 m	10x10 m
EW	50x50 m	25x25 m

3   Interactions between SAR signal and open and vegetation covered water bodies

3.1 Backscatter behavior of radar waves

The total radiation captured by the sensor is the sum of the various complex scattering processes, which are dependent on the system and object parameters (Section 2.2) These

contribute differently to the backscatter coefficient (Figure 11). Two scattering mechanisms are distinguished in the interaction of radiation at the surface. The first is surface scattering, which takes place at the boundary layer of two media with different homogeneous dielectric properties (Ulaby and Long 2015). Thereby, the microwaves are partly absorbed and reflected (**specular reflection**) or diffusely scattered (**diffuse surface scattering**) depending on the properties of the lower medium. The second main scattering mechanism is volume scattering, which occurs in dielectrically inhomogeneous media, into which microwave radiation can penetrate. This is particularly the case for vegetation (**diffuse volume scattering**). A special case of surface scattering is corner reflection (**double bounce**), which occurs when a wave hits two flat surfaces at a 90° angle to each other. Thereby, the emitted radiation is reflected back to the radar sensor, which leads to a high backscatter value (Woodhouse 2006). These double or multiple specular reflections occur, for example, between the ground/water surface and tree trunks/vegetation stems or between streets and houses.
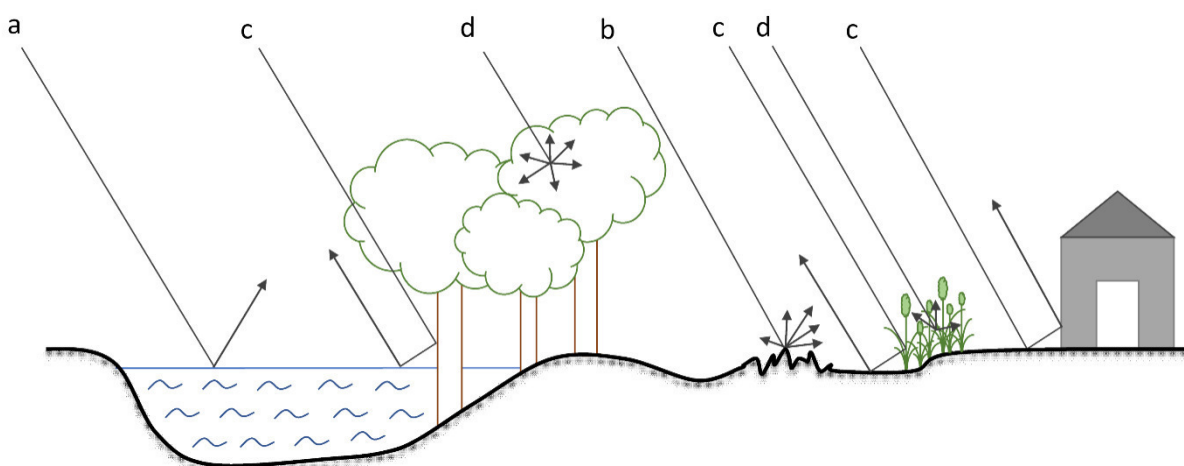
Figure 11: Scattering mechanisms between microwaves and the land surface: a). specular reflection, b) diffuse surface scattering, c) corner reflection (double bounce), d). diffuse volume scattering.

3.2 Open water

The ideal condition for detecting open inland water surfaces is when the water surface is smoother than the surrounding land surface in terms of wavelength and incidence angle. The smooth open water surface (Figure 10) with a high dielectric constant can easily be detected by the radar data, as it acts like a specular reflector reflecting the radar energy away from the sensor (Ulaby and Long 2015). As a result, only a very small portion of the signal returns, resulting in relatively dark pixels in the radar image. These provide a strong contrast to the rougher land surfaces/non-water surfaces, which are dominated by diffuse scattering and have higher backscattering values. With increasing incidence angle, the contrast between land and water increases, as steep angles imply low backscatter values (Mouginis 2017). With longer wavelengths, the sensitivity to diffuse scattering decreases and objects on land can appear smoother, increasing the probability of confusion between land and water surfaces. Furthermore, increased surface roughness of the water due to waves or precipitation reduces the ability to distinguish between water and land surfaces. An increasing roughness causes a higher backscatter signal and thus an increased backscatter intensity.

3.3   **Temporary flooded vegetation**

The signal backscatter from the TFV is very complex and depends strongly on the wavelength, polarizations, incidence angle, roughness, dielectric constant of the vegetation and the ground surface. The main advantage of SAR technology is the ability to detect TFV due to its capability to penetrate the vegetation canopy depending on the wavelength and its sensitivity to smooth water underneath the vegetation. The presence of water underneath vegetated areas can induce a significant increase of backscatter values due to the double- or multi-bounce interaction between the specularly reflecting water surface and vertical structures of the vegetation, such as trunks and stems (Figure 12) (Moser et al. 2016, Pulvirenti et al. 2011a, Pulvirenti et al. 2012). The interaction of the sensor and environmental parameters can be described by theoretical scattering models. According to Bourgeau-Chavez et al. (1997) and Ulaby et al. (2015) the total radar backscattering coefficient ($\sigma_{0,h}$) of wetlands, dominated by herbaceous vegetation, can be simplified by a two-layer model (canopy and surface layer):

$$\sigma_{0,h} = \sigma_{0,c} + \tau^2{}_c(\sigma_{0,s} + \sigma_{0,m}) \tag{10}$$

where

> $\sigma_{0,c}$ is the canopy backscatter coefficient (volume scattering);
> τ_c is the transmission coefficient of the vegetation canopy;
> $\sigma_{0,s}$ is the ground surface backscatter coefficient (surface scattering);
> $\sigma_{0,m}$ is the multi-path backscatter coefficient between the ground and the vegetation (multi-bounce scattering).

For a forest or woody dominated landscape, a three-layer model (canopy, trunk and surface layer) can be used. The total backscatter coefficient from woody vegetation is expressed as (Kasischke and Bourgeau-Chavez 1997, Townsend 2002, Wang et al. 1995):

$$\sigma_{0,w} = \sigma_{0,c} + \tau^2{}_c\tau^2{}_t(\sigma_{0,s} + \sigma_{0,m} + \sigma_{0,t} + \sigma_{0,d}) \tag{11}$$

where
> $\sigma_{0,c}$ is the canopy backscatter coefficient (volume scattering);
> τ_c is the transmission coefficient of the vegetation canopy;
> τ_t is the transmission coefficient of the vegetation canopy;
> $\sigma_{0,s}$ is the ground surface backscatter coefficient (surface scattering);
> $\sigma_{0,m}$ is the multi-path backscatter coefficient between the ground and the vegetation (multi-bounce scattering);
> $\sigma_{0,t}$ is the backscatter coefficient from the trunk layer (surface scattering);
> $\sigma_{0,d}$ is the double-bounce backscatter coefficient between surface and tree trunk (double-bounce scattering).

The elements of the two-layer and three-layer model are shown in Figure 12. Overall, the backscatter from vegetation include the scattering from the canopy as well as the soil surface. The backscatter of the vegetation canopy is dominated by volume scattering, as it contains many individual scatterers in the form of leaves, needles and branches. In addition, the contribution involves the interactions from both the soil and the canopy as multiple- or double-bounce scattering.

The condition of the ground layer is relevant for the detection of flooded vegetation. During standing water condition, the roughness of the ground decreases and the radiation is reflected

away from the sensor because of the specular smooth water surface. If this reflected radiation hits vertical structures such as stems or tree trunks, this can lead to multi- or double bounce scattering and thus to an increase in the backscattering values, which suggests the presence of water underneath the vegetation. The ability to detect flood under the vegetation depends on the transmittance (τ_c and τ_t) of microwave energy through the canopy layer and also on the canopy layer itself. In general, it should be noted that the factors leaf sizes, its shape and orientation, spatial variations in tree heights, density, basal area and species composition can cause significant spatial differences in the ability to detect inundation underneath the vegetation (Townsend 2002). In addition, the transmittance depends strongly on the sensor parameters, such as wavelength, polarization and incidence angle. The effects of sensor characteristics, environmental conditions, and their interactions on the SAR signal regarding flooded vegetation are described in detail in Section 4.1.
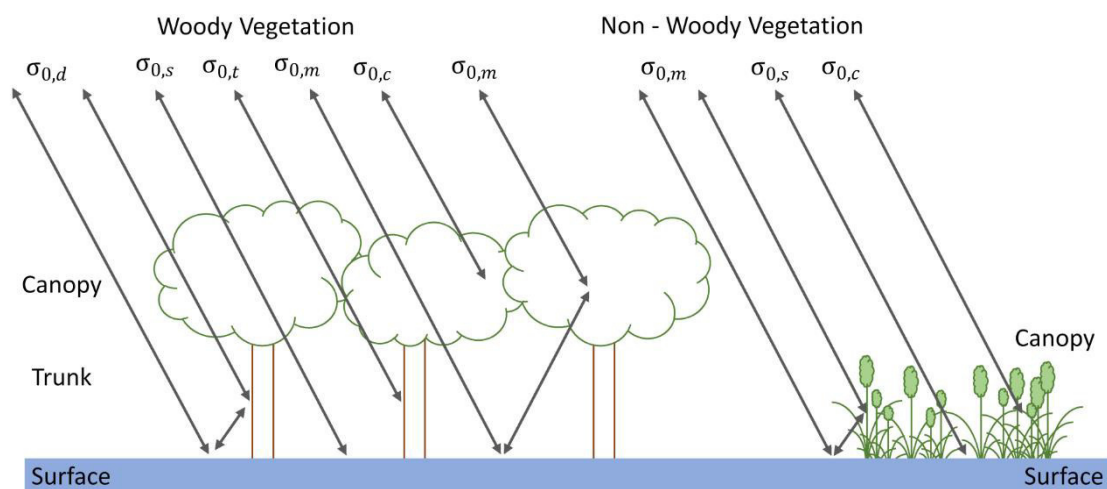
Figure 12: The elements of the two-layer and three-layer model with sources of scattering for non-woody vegetation and woody vegetation, respectively (modified after Kasischke and Bourgeau-Chavez (1997)).

4   Scientific publications

This work is a collection of research results obtained in recent years regarding the temporary flooded vegetation, which were published in several papers. The synthesis is carried out to answer the research questions described in the previous section. The work consists of three papers which have been published in relevant journals. Two of these papers were published in international peer-review journals, while a further paper was submitted to a peer-review journal and is currently under review. The first paper allows to situate the work within the research context, shows the potential and limitation of SAR time series data for flood detection with the focus on the derivation of TFV and points out the of future research needs. The second paper presents the new methodology for flood area detection with a focus on TFV based on dual-polarized S-1 C-band time series data and ancillary information. The method is applied to an example study area. The last paper examines the transferability of the developed approach to other study areas and different TFV types.

4.1   Paper I: SAR-based Detection of Flooded Vegetation – A Review of Characteristics and Approaches

Tsyganskaya, V., Martinis S., Marzahn P., and Ludwig. R. 2018. 'SAR-based detection of flooded vegetation – a review of characteristics and approaches'. In: International Journal of Remote Sensing. 39 (8). 2255–2293.

For a fundamental understanding of the influence of sensor- and object parameters on the backscatter coefficient regarding the flooded vegetation, a comprehensive review about the effects of sensor characteristics, environmental conditions, and their interactions on the SAR signal for the identification of flooded vegetation are described in Paper I. Furthermore, an overview of the state of the art in relation to the data sets and algorithms for the extraction of flooded vegetation is provided in the same publication showing their benefits, limitations and methodological trends. Above all, this paper gives the state of the art of the used SAR data sets and approaches regarding the detection of flooded vegetation and points out the potential research needs in this field.

Author's contributions: All authors contributed to the concept of the study, while all research, information collection, analysis and evaluation were performed by V. Tsyganskaya. The first version of the manuscript was written by V. Tsyganskaya, while all authors contributed with valuable input and expertise to the final document.
Status: published
Journal: International Journal of Remote Sensing (Taylor & Francis)
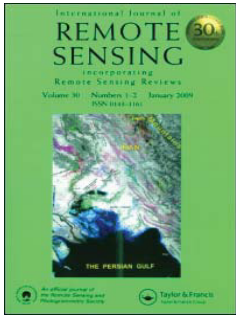
SAR-based detection of flooded vegetation – a review of characteristics and approaches

Viktoriya Tsyganskaya, Sandro Martinis, Philip Marzahn & Ralf Ludwig

Published online: 09 Jan 2018.

Submit your article to this journal 🗗

Article views: 15

View related articles 🗗

View Crossmark data 🗗

Taylor & Francis
Taylor & Francis Group

REVIEW ARTICLE

Check for updates

SAR-based detection of flooded vegetation – a review of characteristics and approaches

Viktoriya Tsyganskaya[a,b], Sandro Martinis [b], Philip Marzahn[a] and Ralf Ludwig[a]

[a]Department of Geography, Ludwig-Maximilians-Universität München, Munich, Germany; [b]German Remote Sensing Data Center (DFD), German Aerospace Center (DLR), Wessling, Germany

ABSTRACT

The ability of synthetic aperture radar (SAR) to detect flooded vegetation (FV) (the temporary or permanent occurrence of water-bodies underneath vegetated areas) offers a great benefit in the research fields of flood and wetland monitoring. The growing demand for near real-time information in flood monitoring and an increased awareness of the importance of wetland ecosystems are strong drivers for the ongoing research in these fields, where FV constitutes an essential part. This study reviewed 128 publications summarizing the knowledge about the relationships between the SAR parameters and the environmental conditions for the detection of FV. An advanced review of 83 studies was carried out to gain insights about applied classification techniques and SAR data for the extraction of FV. Although some trends emerged about which wavelengths, polarisations, or incidence angles to use, there is variation in the application of different classification techniques or using SAR-derived information depending on the data sets and the study area. Notable throughout the analysed articles is the growing demand for unsupervised and computationally efficient methods of higher accuracy for the extraction of FV. Based on the advances in SAR with regard to spatial and temporal resolution, the development of robust approaches for the extraction of FV from various and complex environments has to be further pursued.

1. Introduction

Detection and extraction of flooded vegetation (FV) is of particular importance for two application fields: wetland and flood monitoring. Wetlands comprise open water areas, as well as different types of FV (e.g. emerging woody, herbaceous vegetation) (White et al. 2015), which can be permanently or seasonally flooded. Wetlands are important ecosystems providing many essential services, such as flood control, sediment storage, wildlife habitat, filtering of contaminants, recreation, aesthetic value, and others (Millennium Ecosystem Assessment 2005). Despite these benefits, wetlands have been extensively converted to agriculture areas worldwide (Asselen et al. 2013) and

CONTACT Viktoriya Tsyganskaya ✉ viktoriya.tsyganskaya@iggf.geo.uni-muenchen.de 🖭 Ludwig-Maximilians-Universität München, Department of Geography, Luisenstr. 37, Munich 37, 80333, Germany

furthermore are endangered by climate change (Erwin 2009). Continuous monitoring of changes in wetlands contributes to their protection.

In comparison to wetland monitoring, detecting FV for flood monitoring is a relatively young field. Besides the detection of open waterbodies, the focus lies on the extraction of FV. The availability of detailed near real-time information about the extent of inundation areas at large scales is a significant data source for many institutions, such as humanitarian relief organizations, decision makers for crisis management or insurance companies. In contrast to open flood surfaces, there is little research on the detection of flooded areas underneath vegetation. However, the disregard of FV can lead to an underestimation of the extent of an inundation, which may lead to higher risk to human lives and damage of their properties. Furthermore, flood affects agricultural areas worldwide, entailing enormous economic losses (Trujillo 2015). These possible impacts show the importance to continue the investigations in the field of FV as a part of wetland detection and flood monitoring.

The terminology and definition of FV vary from survey to survey, depending on its scope and study area. Terms such as partially submerged vegetation (Martinis und Rieke 2015) or FV (e.g. Pierdicca et al. 2008; Pulvirenti et al. 2013; Pulvirenti et al. 2016; Martinez und Le Toan 2007; Martinis und Twele 2010) can be found in the corresponding literature. The designation FV is used to describe unspecified types of FV or as an umbrella term for different vegetation types (e.g. standing water underneath forested or in between agricultural areas) (Betbeder et al. 2014; Schlaffer et al. 2016). In the scope of this review, the term FV describes the temporary or permanent occurrence of a water surface beneath a vegetation canopy; however, it does not consider vegetation areas, which are completely covered by water. In agricultural or herbaceous areas, the leaves or stems of the plants visibly emerge above the water surface. In forests or tree stands, standing water can occur underneath the vegetation canopy during flood conditions. FV summarizes different terms related to the aforementioned definition used in the reviewed literature.

Synthetic aperture radar (SAR) is a well-known and well-established tool for the extraction of FV from space due to numerous advantages. In comparison to optical sensors, the SAR systems use longer wavelengths of the electromagnetic spectrum, allowing cloud penetration and therefore weather independent image acquisition. Furthermore, SAR systems are active sensors, transmitting and receiving their own electromagnetic impulses, which allows operations independent of daylight (Klemas 2013; Betbeder et al. 2014). A relatively high energy supply is required for SAR observations, which can be a restricting factor for the availability of SAR time series data and even for the acquisition of single images in some regions in the world. However, the recently launched C-band Sentinel-1 and L-band ALOS-2 satellite missions may now overcome this limitation and therefore provide a possibility for continuous monitoring of ground features and their changes over time with short revisit times (White et al. 2015). The main advantage of SAR technology, however, is the ability to detect FV due to its capability to penetrate the vegetation canopy to a certain extent depending on the wavelength and its sensitivity to water underneath the vegetation. SAR backscatter intensity (BI) values can significantly increase during the presence of water underneath vegetated areas due to the double- or multi-bounce interaction between the specularly reflecting water surface and vertical structures of the vegetation, such as trunks and stems (Moser et al. 2016; Pulvirenti et al. 2013; Pulvirenti et al. 2011a).

While there are clear advantages of SAR data regarding the detection of FV, there are a number of challenges regarding SAR image analysis and its interpretation, as well as limitations, particularly for FV mapping. Speckle, which is inherent to all SAR imagery, may lead to uncertainties in measurements and may consequently result in a decrease of the classification accuracy. This effect can be mitigated using spatial or temporal speckle filters (Lopes, Touzi, and Nezry 1990; Quegan und Yu 2001). Further limitations appear in hilly regions due to geometric and radiometric effects (e.g. foreshortening and layover) occurring in side-looking systems such as SAR (White et al. 2015). These effects increase with small look angles and steep slopes. A correction of these effects has to be applied to reduce their influence. Furthermore, the enhancement caused by double-bounce, as discussed before, is not always detectable depending on the environmental parameters (e.g. above-ground biomass) and sensor characteristics (e.g. wavelength). Finally, backscatter intensities of FV can be similar to the backscatter intensities of urban areas and bare soil areas with high-moisture content. This can result in confusion with FV and misclassification (Chapman et al. 2015; Pulvirenti et al. 2016). In summary, dealing with SAR data can be a challenging task; however, it also constitutes a great opportunity for the mapping of FV due to the aforementioned advantages, if the complexity of these data is well understood.

Overviews and reviews about the potential and capability of SAR systems for the detection of FV have been provided in the research fields of wetland and flood monitoring. These reports summarize the knowledge about the relationships between the sensor parameters (wavelength, polarisation, incidence angle) and environmental conditions (e.g. vegetation type, phenology of plants, soil moisture). Useful status reports have been provided by Hess, Melack, and Simonett (1990), Hall (1996), Schmullius and Evans (1997), Henderson and Lewis (2008), and Silva e al. (2008). Analysis and classification methods for the detection of FV have been summarized by Henderson and Lewis (2008). In addition, there have been more recent reviews briefly and fragmentarily discussing the detection of FV, as part of a more general overview (White et al. 2015) or in a context of a specific topic, such as object-based analysis in wetlands (Dronova 2015) or sensing of mangrove ecosystems (Kuenzer et al. 2011), emergent and submerged wetlands (Klemas 2013), and flood inundation with microwaves (Schumann und Moller 2015).

The technical progress of SAR systems and the advances in computer technology have led to an intensive effort to develop suitable algorithms for the extraction of FV from SAR imagery over the last decades. Furthermore, the growing demand for near real-time information in flood monitoring and an increased awareness of the importance of wetland ecosystems are strong drivers for ongoing research in these fields, where FV constitutes an essential part. This article aims to provide a comprehensive and current status of the possibilities regarding the detection and extraction of FV for both flood and wetland monitoring. The following objectives are addressed,

- to give an overview of sensor characteristics and environmental conditions and their effects on the SAR signal regarding the detection of FV,
- to review the current state of the art of the classification algorithms applied to various SAR data sets for the extraction of FV, and
- to demonstrate benefits and limitations of existing methods.

The article is composed of five sections. Section 2 describes the literature selection on which the analyses are based. Section 3 provides an overview of the knowledge about the relationship between SAR parameters (e.g. wavelength, polarisation, incidence angle) and environmental parameters (e.g. aboveground biomass, water level) related to FV. Section 4 addresses various SAR data sets, the specifications of the classification algorithms including their different tasks and their respective benefits and limitations. Section 5 summarizes and concludes the aforementioned findings and illustrates future trends as well as needs for improved extraction of FV.

2. Methodology

For identification of relevant publications, a combination of key terms linked to FV, their synonyms, and related terms (Table 1) were applied as structured queries for the period from 1 January 1985 to 26 July 2016 using Web of Science (http://apps.webofknowledge. com/) as a search engine. An initial gross selection of 547 results was determined after the search restriction to articles and reviews. Further selection was conducted based on the abstract of these articles. Studies were excluded where key terms were present, but that did not refer to any form of radar data application as data source alone or in combination with other information (e.g. optical data, elevation) for the analysis or/and detection of the temporal or permanent occurrence beneath vegetated areas. Studies that did not address any form of FV, e.g. studies on vegetation only or addressing open water alone, were also excluded. The resulting set of studies containing 128 articles (Appendix 1) was then used to give an overview about effects on the SAR signal by sensor characteristics (wavelength, polarisation, incidence angle), environmental parameters (e.g. aboveground biomass, soil moisture, water depth), and their interaction.

An advanced selection was performed for the identification of studies, which applied classification algorithms for the extraction of FV. Based on this search, 83 studies were determined, published in the period from 1994 to July 2016 (Table 2). This new set of articles provides an overview of the diversity of applied data sets and classification algorithms aiming at the extraction of FV. The data sets include various SAR-derived information (BI, polarimetric parameters [PPs], and interferometric coherence [IC]). Furthermore, the classification algorithms differ regarding the level of classification (pixel or segment based) and the temporal frequency of the applied SAR data, which is investigated by categorizing the studies into single date, change detection, order-independent multi-date, and time series approaches. The identified classification algorithms are categorized into various groups to demonstrate the diversity of applied methods, their number of occurrences in the studies, and their requirements for preliminary information, such as training samples (supervised or unsupervised approaches). Their benefits and limitations are

Table 1. Search key words applied to select studies for this review and the initial number of results for each combination of key words.

Key words (topics)	Number of results	Number of results (articles and reviews)
(radar OR microwave* OR SAR*) AND (flood* OR inundat*) AND ('flooded vegetation' OR forest* OR agricultur*) AND (classif* OR mapp* OR extract*)	265	186
(radar OR microwave* OR SAR*) AND wetland* AND (classif* OR mapp* OR extract*)	483	361

Table 2. Eighty-three selected SAR remote-sensing studies of FV.

Study ID	Reference	Sensor	Wavelength	Polarization	Incidence angle	PFV types	Location
1	Allen, Wang, and Gore (2013)	ALOS PALSAR	L	HH, HV	Unspecified	Wetland	Carolina, USA
2	Arnesen et al. (2013)	ALOS PALSAR	L	HH	28°–35°	Flooded forest	Brazil, South America
3	Augustejn and Warrender (1998)	Airborne Imaging Radar SAR	C, L, P	HH, HV, HV, VV	21°–34°	Forested wetlands	Maryland, Canada
4	Baghdadi et. al. (2001)	Airborne (SAR-580) ERS-2; RADARSAT-1	C	HH, HV, HV, VV	10°–60°	Wetland	Ontario, Canada
5	Betbeder et al. (2014)	TerraSAR-X	X	HH, VV	37°	Forested wetlands	France, Europe
6	Betbeder et al. (2015)	TerraSAR-X	X	HH,VV	37°	Wetland	France, Europe
7	Bian et al. (2016)	ALOS PALSAR	L	HH, HV	Unspecified	Flooded forest	Changchun, China
8	Bourgeau-Chavez et al. (2001)	Shuttle Imaging Radar-C, ERS-1, RADARSAT-1, JERS-1, ENVISAT ASAR, RADARSAT-2	L, C	HH, HV, HV, VV	25°	Forested wetlands	Virginia, USA
9	Bourgeau-Chavez et al. (2009)	JERS-1, RADARSAT-1, ERS-1, PALSAR	L, C	HH, VV, HV	35°, 23°, 47°	Wetland, flooded forest	Greate Lakes, Canada
10	Bourgeau-Chavez et al. (2016)	ALOS PALSAR, RADARSAT-2	L, C	HH	34°, 42°, 19°, 24°	Forested wetlands	Michigan, USA
11	Bouvet and Le Toan (2011)	ENVISAT	C	HH	17°–42°	Rice paddies	Vietnam, Asian
12	Brisco et al. (2011)	Airborne (SAR-580), Simulated RADARSAT-2	C	HH, HV, HV, VV	45°–60°	Wetland	Manitoba, Canada
13	Brisco et al. (2013b)	RADARSAT-2	C	HH, HV, HV, VV	26°, 36°, 41°	Rice, Wetland	China, Asian
14	Bwangoy et al. (2010)	JERS-1	L	HH	37°	Wetland	Congo, Africa
15	Cazals et al. (2016)	Sentinel-1	C	VV, VH	36°–42°	Flooded vegetation	French, Europe
16	Chapman et al. (2015)	ALOS PALSAR	L	HH	35°	Flooded vegetation	South America
17	Chen et al. (2014)	ALOS PALSAR	L	HH, HV, VH, VV	24°	Wetland	Yancheng, China
18	Corcoran et al. (2012)	RADARSAT-2	C	HH, HV, VH, VV	26°, 28°	Wetland	Minnesota, USA
19	Cordeiro and Rossetti (2015)	ALOS PALSAR	L	HH, VH	Unspecified	Wetland	Brazil, South America
20	Costa et al. (1997)	RADARSAT-1, JERS-1	C, L	HH	Unspecified	Flooded forest	Brazil, South America
21	Costa et al. (2002)	RADARSAT-1, JERS-1	C, L	HH	43°, 35°	Flooded forest	Brazilian, South America
22	Costa (2004)	RADARSAT-1, JERS-1	C, L	HH	43°, 35°	Flooded forest	Brazil, South America
23	Costa and Telmer (2006)	RADARSAT-1, JERS-1	C, L	HH	25°, 50°, 35°	Wetland	Brazilian, South America
24	Cremon, Rossetti, Dilce, and Zani (2014)	ALOS PALSAR	L	HH, HV	37°–41°	Flooded forest	Brazil, South America
25	De Grandi et al. (2000)	ERS-1	C	VV	Unspecified	Flooded forest	Central Africa

Table 2. (Continued).

Study ID	Reference	Sensor	Wavelength	Polarization	Incidence angle	PFV types	Location
26	Dwivedi, Rao, and Bhattacharya (1999)	ERS-1	C	VV	Unspecified	Wetland	Bangladesh, Asian
27	Evans et al. (2010)	RADARSAT-2, ALOS (PALSAR)	C, L	HH, HV	18°–43°, 20°–41°	Flooded forest	Brazil, South America
28	Evans and Costa (2013)	ALOS PALSAR, RADARSAT-2, ENVISAT ASAR	L, C	HH, HV	34°–39°	Wetland	Brazil, South America
29	Evans et al. (2014)	Radarsat-2, ALOS PALSAR	C, L	HH, HV	34°	Wetland	Brazil, South America
30	Ferreira-Ferreira et al. (2015)	ALOS PALSAR	L	HH, HV	39°	Flooded vegetation	Brazil, South America
31	Frappart et al. (2005)	JERS-1	L	HH	–	Flooded forest	Brazil, South America
32	Furtado, Silva, and Novo (2016)	RADARSAT-2	C	HH, HV, HV, VV	25°, 35°, 45°	Wetland	Brazil, South America
33	Gallant et al. (2014)	RADARSAT-2	C	HH, HV, HV, VV	20°–33°	Flooded vegetation	Minnesota, USA
34	Grenier et al. (2007)	RADARSAT-1	C	HH	20°–49°	Wetland	Quebec, Canada
35	Heine, Jagdhuber, and Itzerott (2016)	TerraSAR-X	X	HH, VV	38°–42°	Flooded vegetation	Germany, Europe
36	Hess (2003)	JERS-1	L	HH	34°–43°	Flooded forest, Wetland	Brazil, South America
37	Hess et al. (2015)	JERS-1	L	HH	Unspecified	Flooded forest	Brazil, South America
38	Hidayat et al. (2012)	ALOS PALSAR	L	HH	Unspecified	Flooded forest	Indonesian, Asian
39	Karszenbaum, et al. (2000)	RADARSAT-1, ERS-2	C	HH, VV	20°–46°	Wetland	Argentina, South America
40	Li and Chen (2005)	RADARSAT-1	C	HH	45°	Wetland	Ontario, Canada
41	Lee et al. (2015)	ALOS PALSAR	L	Unspecified	Unspecified	Wetland, flooded forest	Congo, Africa
42	Long, Fatoyinbo, and Policelli (2014)	ENVISAT ASAR, RADARSAT-2	C	HH	Unspecified	Flooded vegetation	Namibia, Africa
43	Maillard, Alencar-Silva, and Clausi (2008)	RADARSAT-1	C	HH	24°–31°, 41°–46°	Flooded forest	Brazil, South America
44	Martinez and Toan (2007)	JERS-1	L	HH	34°–43°	Flooded forest	Brazil, South America
45	Martinis and Twele (2010)	TerraSAR-X	X	HH	27°–36°	Flooded shrubs and grassland	Namibia, Africa
46	Marti-Cardona et al. (2013)	ENVISAT ASAR	C	HH, VV	19°–45°	Flooded vegetation	Spain, Europe
47	Mayaux et al. (2002)	ERS, JERS-1	L, C	VV, HH	19°–26°, 37°–42°	Flooded forest	Congo, Africa
48	Melack and Wang (1998)	JERS-1	L	HH	35°	Flooded forest	Brazil, South America
49	Miranda, Fonseca, and Carr (1998)	JERS-1	L	HH	Unspecified	Flooded forest	Brazil, South America

(Continued)

Table 2. (Continued).

Study ID	Reference	Sensor	Wavelength	Polarization	Incidence angle	PFV types	Location
50	Morandeira et al. (2016)	RADARSAT-2	C	HH, HV, HV, VV	42°–44°, 26°–28°	Wetland	Paraguay, South America
51	Moser et al. (2016)	TerraSAR-X	X	HH, VV	27°–28°	Wetland	Burkina Faso, Africa
52	Mwita et al. (2012)	ALOS PALSAR, ENVISAT ASAR	L, C	HH, HV, HV, VV; HH, HV	Unspecified	Wetland	Kenya, Africa
53	Na et al. (2013)	ENVISAT ASAR	C	HH, HV	19°–27°	Wetland	Heilongjiang, China
54	Na et al. (2015)	RADARSAT-2	C	HH, HV	26–31°	Forested wetlands	Heilongjiang, China
55	Pierdicca et al. (2008)	ERS-1	C	VV	Unspecified	Flooded woodland and grassland	Italy, Europe
56	Pistolesi, Ni-Meister, and McDonald (2015)	ALOS PALSAR	L	HH, HV	34°	Flooded forest	New York, USA
57	Podest and Saatchi (2002)	JERS-1	L	HH	Unspecified	Flooded vegetation	Brazil, South America
58	Pope, Rey-Benayas, and Paris (1994)	AIRSAR	C, L, P	HH, HV, HV, VV	35°–50°	Wetland	Belize, Central America
59	Pope, Rejmankova, and Paris (2001)	Endeavour (SIR-C)	C, L	HH, HV, HV, VV	26°	Wetland, flooded forest	Mexico, North America
60	Pulvirenti, Pierdicca, and Chini (2010)	COSMO-SkyMed	X	HH	Unspecified	Flooded forest	Myanmar, Asian
61	Pulvirenti et al. (2011a)	COSMO-SkyMed	X	HH	26°–51°	Flooded agriculture	Italy, Europe
62	Pulvirenti et al. (2011b)	COSMO-SkyMed	X	HH	35°, 22°	Flooded agriculture, flooded forest	Albania, Europa
63	Pulvirenti et al. (2013)	COSMO-SkyMed	X	HH	29°–47°	Flooded agriculture, flooded forest	Italy, Europe
64	Pulvirenti et al. (2016)	COSMO-SkyMed	X	HH	34°, 40°	Flooded agriculture	Italy, Europe
65	Rebelo, Senay, and McCartney (2012)	ALOS PALSAR	L	HH	Unspecified	Flooded vegetation	South Sudan, Africa
66	Robertson, King, and Davies (2015)	RADARSAT-2	C	HH, HV, HV, VV	18°–48°	Wetland	Ontario, Canada
67	Rodrigues and Souza-Filho (2011)	RADARSAT-2	C	HH	20°–31°	Flooded tropical forest	Brazil, South America
68	Schlaffer et al. (2016)	ENVISAT ASAR	C	HH	15°–45°	Wetland	Zambia, Africa
69	Simard, Saatchi, and De Grandi (2000)	JERS-1	L	HH	Unspecified	Flooded tropical forests	Gabun, Africa
70	Simard et al. (2002)	JERS-1, ERS-1	L, C	HH, VV	Unspecified	Flooded vegetation	Central Africa

(*Continued*)

Table 2. (Continued).

Study ID	Reference	Sensor	Wavelength	Polarization	Incidence angle	PFV types	Location
71	Souza-Filho et al. (2011)	SAR R99B sensor of the Amazon Surveillance System	L	HH, VV, VH	45°–53°	Flooded tropical forest	Brazil, South America
72	Townsend (2001)	RADARSAT-1	C	HH	23°–44°	Flooded forest	Carolina, USA
73	Townsend (2002)	RADARSAT-1, ERS-1	C	HH, VV	23°	Flooded forest	Carolina, USA
74	Töyrä, Pietroniro, and Martz (2001)	RADARSAT-1	C	HH	24°–47°	Flooded vegetation	Alberta, Canada
75	Töyrä et al. (2002)	RADARSAT-1	C	HH	24°–46°	Flooded vegetation	Alberta, Canada
76	Voormansik et al. (2014)	TerraSAR-X, ENVISAT ASAR	X, C	HH	42°, 24°	Flooded forest	Estonia, Europe
77	Wang et al. (1998)	ERS-1	C	VV	23°	Wetland	Ontario, Canada
78	Wang (2004)	JERS-1	L	HH	Unspecified	Wetland, flooded forest	Carolina, USA
79	Ward et al. (2014)	ALOS PALSAR	L	HH, HV	Unspecified	Flooded forest	Carolina, USA
80	Westra (2010)	ENVISAT ASAR	C	HH, HV, HV, VV	19°–36°	Wetland	Cameroon, Africa
81	Whitcomb et al. (2009)	JERS-1	L	HH	35°	Wetland	Alaska, USA
82	Zhao et al. (2014)	RADARSAT-2	C	HH, HV, HV, VV	37°–39°	Flooded forest	Northern Inner Mongolia, China
83	Zhang et al. (2015)	ALOS PALSAR, ENVISAT ASAR	L, C	HH, HV	34°	Wetland	Liaoning, China

summarized to promote the identification of methodological trends in the last decades and opportunities for further research on mapping FV.

3. Effects of sensor characteristics, environmental conditions, and their interactions on the SAR signal

The representation of FV in SAR images can vary and may be difficult to interpret because of complex interactions between SAR characteristics (wavelength, geometric resolution, polarisation, incidence angle) and environmental conditions (e.g. vegetation type, phenology of plants, soil moisture, water depth) (Hess, Melack, and Simonett 1990; Schumann and Moller 2015; Melack und Hess 2010). These different parameters can strongly influence the backscatter values and affect the ability to discriminate features on the ground surface, such as FV. Therefore, it is essential to identify sensor characteristics which can provide an appropriate basis for the development of methods aimed at the extraction of FV. This section is intended to show a further overview, supplemented by current findings about the relationship of sensor characteristics and environmental conditions having a positive effect on the detection of FV.

3.1. *Wavelength*

The backscatter values for FV vary as a function, amongst others, of radar wavelength depending on the vegetation density and structure, flood conditions, and soil moisture (Lang, Townsend, and Kasischke 2008).

Generally, the longer the wavelength, the higher the capability of the SAR signal to penetrate the vegetation canopy (Wang 2002; Hess 2003). Numerous studies concluded that L-band is suited to detect inundations beneath forested canopy and should be the preferred wavelength for this purpose (Hess, Melack, and Simonett 1990; Hess 2003; Betbeder et al. 2014). Le Toan et al. (1997), and Wang (2004) remarked, however, that the capability of L-band and also of other bands to penetrate some forested areas can be reduced or are even non-existent depending on the vegetation density, the gaps between or the height of the vegetation (see Section 3.4).

In comparison to L-band, the ability of shorter wavelengths, such as C-band, or X-band, to penetrate vegetation canopy is reduced (Costa et al. 2002; Hess 2003). Although the penetration of the C-band is limited, an increase in the backscatter values for FV was exhibited, during leaf-off as well as leaf-on conditions (Lang und Kasischke 2008; Townsend 2001), in dependency of the available polarisation (Townsend 2002). Zhang et al. (2016) showed that C-band is more useful at the initial growth stages if the density of the vegetation is low. Also, C-band data has the potential to detect paddy rice cultivation (Brisco et al. 2013b; Le Toan et al. 1997) and herbaceous wetlands (Grings et al. 2008).

X-band sensors (e.g. TerraSAR-X) produce detailed information due to their high resolution within the centimetre range (Airbus Defence and Space 2016). In general, the penetration of dense canopy by X-band is limited as a result of high interference with leaves, where backscatter is dominated by volume scattering (Voormansik et al. 2014). However, Martinis and Rieke (2015) and Voormansik et al. (2014) showed the potential of X-band to identify FV for sparse vegetation or during leaf-off conditions. In

this case, the transmissivity of the canopy is increased due to gaps in the canopy or no biomass at all and the contribution of double-bounce (interaction between water and tree trunks or branches) dominates the volume scattering. Some other studies demonstrated the ability of X-band to map FV in wetlands (Moser et al. 2016), in flooded marshland (Horritt 2003), and in olive groves (Pulvirenti et al. 2013).

Bourgeau-Chavez et al. (2001) underlined the importance of multi-frequency SAR data for consistent wetland mapping. In their study, the applied wavelengths complement their capability for the discrimination of flood underneath different vegetation types. While C-band was used to discriminate herbaceous vegetation from dry upland, the L-band was found best suitable to differentiate between flooded and non-flooded forest (Hess and Melack 2003; Zhang et al. 2016). Multi-frequency SAR data were also found useful to map flooding in wetland areas by Evans et al. (2010).

3.2. *Polarisation*

Polarisation describes the orientation of the electromagnetic field vector with respect to its direction of propagation of a SAR system, which can be horizontal (H) or vertical (V) for a single channel. The signal of a SAR system can be transmitted and received, co-polarised (HH or VV), and cross-polarised (HV or VH). Some advanced SAR systems are able to transmit and receive the signal in dual-polarised mode (HH and VV, HH and HV, VV and HV) and in all levels (HH, VV, HV, and VH). Dual- and fully polarimetric sensors are able to identify different scattering mechanisms, which are characteristic for different land-cover types (Lewis, Henderson, and Holcomb 1998; White et al. 2015).

Townsend (2002), Bourgeau-Chavez et al. (2001), Karszenbaum et al. (2000), Lang and Kasischke (2008), and Sang et al. (2014) suggested the use of HH polarisation in mapping flooded forests in comparison to VV polarisation relating to the orientation of the SAR signal for single-polarised data. This is due to the fact that the contribution of double-bounce scattering from the trunk-ground interaction is smaller at VV than at HH (Wang et al. 1995). In general, HH polarisation penetrates the vegetation canopy better than VV and, when striking the water surface, it is more strongly reflected in comparison to VV polarisation (Pierdicca et al. 2013). While the co-polarised backscatter is more sensitive to the double bounce, the cross-polarised one is more sensitive to volume scattering because of its depolarising characteristics (Marti-Cardona et al. 2010). Consequently, the backscatter increase due to FV is expected to be more detectable in co-polarised than in cross-polarised data (Hess, Melack, and Simonett 1990). Nevertheless, the combination of co- and cross-polarised data may improve the identification of FV as the double bounce allows a better discrimination between different FV types (Zhao et al. 2014).

Single-polarised SAR data are able to identify FV due to an increase in backscatter values in comparison to other land-cover types. These data are often used due to its greater coverage and higher spatial resolution in comparison to dual- or quad-polarised SAR data. The source of this increase in backscatter values is assumed to be the fact that vegetation under flood conditions can act as corner reflectors causing double-bounce effects (Moser et al. 2016; Pulvirenti et al. 2013). The individual backscatter mechanisms, such as double bounce, cannot be identified in single-polarised images. However, single-polarised data, which provide BI, may increase during flood conditions (Betbeder et al. 2014). Some objects (e.g. urban structures, ploughed bare soils) may cause similar

backscatter intensities as FV. The similarity of SAR backscatter only constitutes a critical issue when analysing single-polarised images (Schumann and Moller 2015; Martinis and Rieke 2015; Pulvirenti et al. 2016). The use of ancillary data (e.g. land-cover map, optical data) may reduce the confusion between the aforementioned objects by exclusion of non-vegetated features. In the past, studies increasingly used single-polarised data for the detection of different FV types, such as forested wetlands (Bourgeau-Chavez et al. 2001; Pistolesi, Ni-Meister, and McDonald 2015), marshland (Horritt 2003), as well as agricultural areas (Pulvirenti et al. 2011b; Kasischke et al. 2003).

Single-polarised SAR data only provide BI and, according to White et al. (2015) and Betbeder et al. (2014), are not quite efficient enough to detect FV due to the restricted information content about backscatter mechanism such as the double-bounce effect. SAR systems with multi-polarised SAR data (dual-polarised and fully polarised) have significant advantages in comparison to single-polarised SAR data, providing more information about the presence of water underneath the vegetation canopy (Souza-Filho et al. 2011).

Dual-polarised SAR data are generally used to produce ratios between two polarisation types. Brisco et al. (2011) mentioned that polarisation ratios using horizontal polarisation are appropriate for mapping FV for a generalized land-cover map. Furthermore, Mougin et al. (1999) and the aforementioned study indicate the suitability of the HH/HV ratio in separating FV from uplands. According to Le Toan et al. (1997) and Wang (2004), the ratio between HH and VV is higher for FV than that of most other land-cover classes, because the vertical polarised wave is more attenuated than the horizontally polarised one. Schmitt et al. (2012) designed an approach to identify FV by applying dual-polarised (HH-VV) data to distinguish between agricultural areas and swamp forest in wetlands. A recently developed approach that enables the extraction of FV by the decomposition of dual-polarised data was presented by Moser et al. (2016). The techniques for decomposition of dual-polarised SAR data are quite young; however, according to aforementioned studies, they produced promising results (see Section 4.1.2).

More known and common is the application of quad-polarised SAR data. The quad-polarised data have smaller area coverage in comparison to single- and dual-polarised SAR data. This can represent a drawback due to an inadequate coverage of the area of interest, depending on the study task. However, the quad-polarised data allow the application of polarimetric decomposition, which separates SAR signals into different scattering mechanisms: volume, single-bounce (on specular or rough surface), and dihedral scattering (double-bounce). The volume scattering mechanism represents multiple scatterings and can be found over forested and agricultural areas, where the SAR signal is diffusely backscattered by tree crowns or vegetation canopy. In case of single-bounce scattering on specular surfaces, the most of the SAR energy is reflected away from sensor. For example, these are flat open water surfaces, which often appear dark in a SAR image (Ulaby, Fung, and Moore 1986). Double- or multi-bounce scattering occurs between a specularly reflecting water surface and vertical structures of the vegetation, such as trunks and stems (Moser et al. 2016; Pulvirenti et al. 2013; Pulvirenti et al. 2011a). This scattering mechanism represents a key component for the detection of FV using SAR data.

The identification of scattering mechanisms enables the distinction of different cover types and environmental conditions, such as flood. The most frequent application of quad-polarised SAR data and decomposition techniques for detection of FV can be

found in the field of wetland monitoring due to the capability of this data to distinguish flooded and non-flooded conditions, as well as individual FV types, such as marshes and wooded wetlands or rushes (Robertson, King, and Davies 2015; Gallant et al. 2014; Schmitt und Brisco 2013; Morandeira et al. 2016; Betbeder et al. 2014). The individual decomposition techniques and their successes for the extraction of FV are described in Section 4.1.2.

3.3. *Incidence angle*

The utility of SAR data to detect FV is significantly influenced by the incident angle. It is defined as the angle between an imaginary line perpendicular to the Earth's surface and the radar signal. Depending on the satellite sensor, the incidence angles range between 10° and 65°. Thereby, the larger incidence angles are declared as shallow and the smaller angles are termed steep. Several studies, focused on the vegetation type forest, address an appropriate incidence angle for the differentiation between flooded and non-FV (Richards, Woodgate, and Skidmore 1987; Bourgeau-Chavez et al. 2001; Lang, Townsend, and Kasischke 2008). Previous investigations indicated that steeper incidence angles are preferential for the distinction of non-flooded and flooded forest (Kandus et al. 2001; Bourgeau-Chavez et al. 2001; Hess, Melack, and Simonett 1990; Richards, Woodgate, and Skidmore 1987; Costa et al. 2002). This circumstance can be explained by the SAR signal having a shorter path through the crown layer at steeper angles. As a result, the transmissivity of the vegetation canopy for SAR energy is increased. This leads to a potential increase in interaction between the surface water on the ground and the tree trunks. Shallow incidence angle signals are more influenced by the crown layer, resulting in increased volume scattering (Lang, Townsend, and Kasischke 2008; Hess 2003; Townsend 2001; Costa et al. 2002). According to the results of Lang, Townsend, and Kasischke (2008), the ability to detect waterbodies underneath forested areas did not decline as strongly as expected with increasing incidence angles, and less than expected at steeper incidence angles, in comparison to previous findings in the literature. Lang, Townsend, and Kasischke (2008) also mentioned that the angular signatures varied between different forest types and the capability to detect flooded forest is similar during the leaf-off and leaf-on conditions.

The backscatter signature of a target in two different images, acquired under similar environmental conditions, can vary in dependency of different incidence angles of these images. Depending on the task, the changes in backscatter due to different incidence angles have to be considered. For instance, Pulvirenti et al. (2011a) applied a simplified cosine model (Ulaby und Dobson 1989) assuming that the variation of backscatter can be approximated by cosine-squared function depending on the incidence angle itself. However, the use of multi-incident angle SAR images does not necessarily constitute a drawback. The results of Kandus et al. (2001) indicated that combinations of images with different incidence angles can improve the discrimination of different FV types in wetlands. In addition, Lang, Townsend, and Kasischke (2008) pointed out the benefits of multi-incident angle imagery for monitoring flood extent under forest canopies. Henderson and Lewis (2008) remarked that dense forest canopy can be appropriately detected by the combination of L-band, HH polarisation, and low-to-moderate incidence angle imagery. However, low incident angle in C-band and HH or VV polarised data is also suitable for a sparse canopy layer.

3.4. *Environmental conditions*

Besides sensor characteristics, the backscatter signature of FV is strongly affected by the environmental conditions and their characteristics, such as vegetative biomass over the ground/water (vegetation type, phenology of plants), soil moisture, and water depth. Several theoretical microwave scattering models can be found in the literature, which describe the interaction between the SAR transmitted microwave energy and vegetation or FV on the ground (Kasischke and Bourgeau-Chavez 1997; Wang et al. 1995). Low vegetation (low/moderate stage of growth) and high vegetation (e.g. deciduous forests, coniferous forests) are often considered separately in the literature (e.g. Pulvirenti et al. 2011b), because of the different effects that vegetation structure and density have on the signal intensity.

Vegetative aboveground biomass has been found to have a great influence on the scattering of FV (Pope et al. 1997). The biomass is described in various studies as canopy or crop density (e.g. Dwivedi, Rao, and Bhattacharya 1999; Grings et al. 2008) or as a combination between leafs and stems (Kasischke et al. 2003). Le Toan et al. (1997), Pope et al. (1997), Mougin et al. (1999), Sang et al. (2014), and Yu and Satschi (2016) found that SAR backscatter is increasing as a function of biomass and they determined saturation points at which water beneath the canopy cannot be detected any longer. The saturation point can shift depending on sensor characteristics (wavelengths, incidence angle, and polarisation) and environmental parameter (e.g. aboveground biomass) (Yu und Saatchi 2016; Sang et al. 2014). Before the saturation point (lower level of biomass), the transmissivity of the microwaves radiation through the vegetation canopy is possible due to the small size and density of scattering elements. If the saturation point is reached, the volume scattering from the canopy completely superimposes the contribution of double bounce from the interaction between the water surface and vertical vegetation structure (e.g. tree trunk, stems volume) (Costa et al. 2002; Kasischke et al. 2003; Aziz und White 2003). Consequently, the phenology of plants or leaf-on/leaf-off conditions highly affect the detection of FV depending on the sensor characteristics.

Beside the aboveground biomass, the contribution of the ground is another important environmental parameter influencing the backscatter signal of FV. Kasischke et al. (2003) showed an increase in backscatter through all biomass levels as soil moisture increases, provided that the transmissivity of the biomass still exists (the saturation point is not exceeded). In case of low soil moisture, as biomass increases, there is an increase due to volume scattering from the canopy; however, there is a little or no contribution from multi-interaction scattering. When the surface is flooded, there is no contribution of energy from the ground surface and the backscatter signal is dominated by the double-bounce scattering and the volume scattering from the vegetation canopy (Kwoun und Lu 2009).

Pulvirenti et al. (2011a) investigated that the water depth fluctuations significantly influence the backscatter intensities in FV areas due to the predominance of scattering mechanisms for agricultural and herbaceous vegetation. Depending on the height of the vegetation and the water depth, the double-bounce scattering can become a predominant effect and cause the increase in backscatter, while the volume scattering becomes subordinate (Bourgeau-Chavez et al. 2001; Bourgeau-Chavez, Kasischke, and Smith 1997; Grings et al. 2006; Kiage et al. 2005; Sang et al. 2014). If the emerging part of the plants

becomes too small, no considerable double-bounce scattering can be produced and the backscatter would not increase (Pulvirenti et al. 2011a). Consequently, the combination of sensor parameters and the knowledge concerning environmental properties and conditions is a crucial point for the extraction of FV.

4. Overview of methods and their data sets for the extraction of FV

Based on 83 selected studies, an overview of the diversity of applied data sets and classification algorithms aiming at the extraction of FV is given in this section. Furthermore, the classification algorithms are categorized and analysed based on the level of classification (pixel- or segment-based) and the temporal frequency of the applied SAR data. A list of the studies is provided in Table 2. Each of these studies includes a unique ID, which serves as a reference within this section.

4.1. SAR-derived information for image classification

For the extraction of FV various SAR-derived image, information were used in the studies comprising BI, PPs as well as IC. The number of occurrences of the SAR-derived information in the analysed studies is demonstrated in Figure 1.

4.1.1. Backscatter intensity
The BI for each pixel in a SAR image represents the basic SAR-derived information and the proportion of the SAR signal backscattered from the objects on the ground, depending on sensor characteristics (polarisation, frequency, incidence angle, and resolution) and environmental conditions of a target (e.g. size, shape, orientation, and moisture content). The BI values are often converted to a normalized radar cross section or backscattering coefficient, which is measured in decibel (dB) units (Henderson und Lewis 2008). Figure 1 shows that the majority of studies (69 of 83) used BI for the classifications of FV vegetation (ID 1–12, 14–16, 19–31, 34, 36–49, 52–63, 65, 67–81).
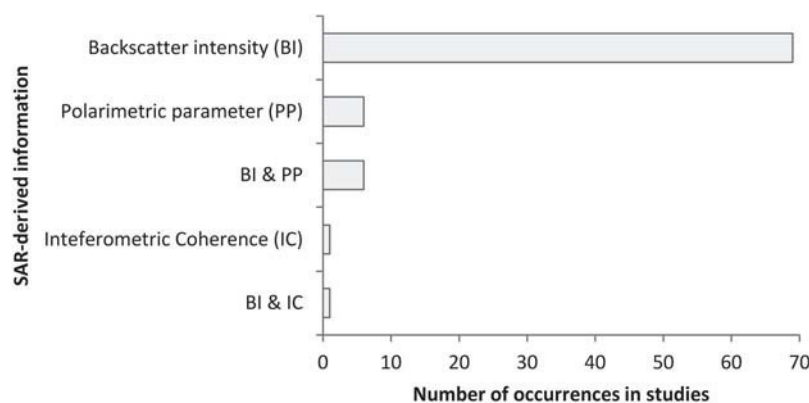

Figure 1. SAR-related information on which classifications were conducted and their number of occurrences for the extraction of FV in the selected studies.

4.1.2. *Polarimetric parameters*

The advancement of satellite systems in the recent years enables the acquisition of fully polarimetric data, transmitting and receiving the SAR signal in all four planes (HH, VV, HV, and VH). By preserving the phase information, the fully polarimetric data allow the decomposition of the SAR signal into the following three scattering mechanisms: single bounce (on specular or rough surface), volume and dihedral scattering (double-bounce) (see Section 3.2). The scattering mechanisms represent an example of PP, which are applied as extended SAR-derived information for the detection of FV. The identification of scattering mechanisms constitutes a great benefit for the extraction of FV in contrast to the single usage of BI. FV does not always have a clear BI signal that can be easily detected. For example high soil moisture conditions can cause similar backscatter values as FV. A significant challenge to differentiate both of these targets arises in the case of the application of BI on its own. The usage of PP can overcome this lack of information by providing different scattering mechanisms and consequently making it easier to separate FV types from upland areas (White et al. 2014; Heine, Jagdhuber, and Itzerott 2016) (Martinez and Le Toan 2007; Pulvirenti et al. 2011a; Pulvirenti et al. 2016; Wang und Davis 1997).

For the extraction of PP, various polarimetric decomposition methods have been developed. Usually, the polarimetric decompositions apply fully polarimetric SAR data (quad-pol data) for the extraction of FV. For the separation between FV and other areas, various decompositions (model-based and eigenvalue-based) were applied during the studies. Examples for model-based decompositions are the Freeman–Durden decomposition (ID 13, 18, 32, 33) and the Yamaguchi four-component decomposition (ID 17, 32, 82). These physically based models decompose the backscatter response from each pixel into three scattering mechanisms: volume scattering, double-bounce scattering (diplane scattering), and surface or single-bounce scattering using a Freeman–Durden decomposition (Brisco et al. 2011; Corcoran et al. 2012; Furtado, Silva, and Novo 2016; Gallant et al. 2014) and an additional fourth component (helical scattering) using the Yamaguchi four-component decomposition (Koch et al. 2012; Chen et al. 2014; Furtado, Silva, and Novo 2016; Zhao et al. 2014; Lee und Pottier 2009). One disadvantage of these models is the assumption of the objects symmetry, although most objects on the ground do not follow symmetrical orientation in consequence of their structure (Brisco et al. 2013b). However, these decompositions can be used to detect FV as two potentially perpendicular planes which act as a corner reflector in the presence of water (double-bounce scattering). The decomposition of the SAR signal into three- or four-channel images allows an easy comparison of the outputs.

An example for a decomposition based on eigenvectors is the Cloude–Pottier decomposition (Brisco et al. 2011; Chen et al. 2014; Corcoran et al. 2012; Zhao et al. 2014), which is used by further six studies (ID 13, 17, 18, 35, 50, 82). A further eigenvector-based decomposition for the derivation of PP is the Touzi incoherent decomposition (Touzi, Deschamps, and Rother 2007, 2009; Furtado, Silva, and Novo 2016; Patel, Srivastava, and Navalgund 2009), which is applied in three studies (ID 13, 17, 32). The eigenvalue-based decompositions use a coherency matrix to obtain eigenvectors and eigenvalues. Thereby, the physical scattering mechanisms are characterized by the eigenvectors and their strength (degree of randomness) is quantified by the eigenvalues (Cloude und Pottier 1997). PPs are important as they are often specific to one scattering type and

thus improve the classification of specific classes, such as FV (Heine, Jagdhuber, and Itzerott 2016).

The most common polarimetric decompositions can only be derived from fully polarised (quad-polarised) SAR data. However, the availability of quad-pol data is more limited (Moser et al. 2016; Schmitt et al. 2012). There are few decomposition approaches applicable for quad- and dual-polarised data. One of them is the method of normalized Kennaugh elements, which is adapted for any wavelength (Moser et al. 2016; Schmitt, Wendleder, and Hinz 2015) and also for all SAR sensors (ID 51). By retaining the phase information of dual-polarised data, the Kennaugh elements enable the interpretation of physical surface and double-bounce scattering mechanisms (Schmitt et al. 2012). In addition, the Shannon entropy (SE), which represents an eigenvector decomposition (Lee and Pottier 2009), can cope with dual-polarised data, too (ID 5, 6).

The compact polarimetric (CP) SAR system is configured to transmit only one polarisation, while two linear polarisations, horizontal and vertical, are received. This technique enables the creation of pseudo quad-pol data from a dual-polarised SAR system (Brisco et al. 2013b; Dabboor et al. 2015; Nord et al. 2009). An important requirement of CP is the maintenance of the relative phase between two received polarisations, which is necessary to construct CP images. The reason for the application of CP are the benefits of quad-pol data, such as improved classification through increased information content, while its drawbacks, such as reduced area coverage, are being avoided (Brisco et al. 2013b). Within this technique, m-delta decomposition is a suitable method to decompose the CP data. It is comparable to the Freeman–Durden decomposition. The simulated CP was investigated by Brisco et al. (2013b) using the m-delta decomposition for FV classification in wetland areas (ID 8).

Decompositions allow the extraction of physical information (backscatter mechanisms), but they do not represent a classification approach on their own. In the literature, the classification of decompositions for FV was mostly performed by machine-learning techniques (e.g. Support Vector Machine (ID 5, 6, 13), random forest classification (ID 18, 32, 35, 66, 82)), followed by distance-based classification methods (e.g. maximum likelihood classification (ID 13, 51), k-nearest-neighbour classification (KNNC) (ID 5, 17). However, also a few decision tree classifiers (ID 5, 17), two Wishard classifications (ID 17, 50), a single manual thresholding approach (MTA) (ID 33), and a single ISODATA clustering technique (ID 59) were performed based on decomposed SAR data.

Only, 12 studies performed a classification applying PP (ID 5, 6, 13, 17, 18, 32, 33, 35, 50, 51, 66, 82) (Figure 1). Several reasons for this uneven distribution can be assumed: (1) The application of PP requires dual- or quad-polarised data, in which the phase information is maintained. The advance in satellite systems during the last couple of years enables the extraction and application of the polarimetric information. (2) Based on different SAR sensors, the advanced polarisation modes might not always be available. In comparison to single-polarised data, reduced area coverage and resolution limit the usage of dual- or quad-polarised data. As a consequence, the application of polarimetric analysis for FV is restricted in comparison to the usage of BI values. (3) The preprocessing effort for BI is significantly lower in comparison to the derivation of PP (Betbeder et al. 2014; Morandeira et al. 2016; Robertson, King, and Davies 2015). (4) The interpretation of PP is likely to be more time consuming (e. g. interpretation of Pauli-Decomposition).

Figure 1 shows that exclusively PPs were applied in six different studies (ID 6, 13, 17, 18, 33, 50). Seven further studies used BI along with PP (ID 5, 32, 35, 51, 59, 66, 82). Thereby, the latter is used either as supplementary information to achieve higher accuracy for FV or as a comparison to BI-based results. Some of these studies performed comparisons of the accuracies for FV, which are described in the following. The application of BI only (HH, VV, HH/VV) resulted in poor kappa values (0.48, 0.33, 0.13) as reported by Betbeder et al. (2014). An improvement was reached using SE (kappa: 0.85) showing an accuracy of 90% PA (producer's accuracy) and 75% UA (user's accuracy) for FV. Furtado, Silva, and Novo (2016) reported that flooded forest had a 30–40% increase in PA and UA when polarimetric descriptors were used instead of only BI. The highest accuracy, therefore, is situated at 79% PA and 95% UA. Moser et al. (2016) demonstrated an increase in the PA (90%) and UA (90%) accuracy for FV extracted by PPs in comparison to the PA (79%) und UA (87%) based on BI. In addition, Robertson et al. (2016) applied BI and Cloude–Pottier decomposition for the extraction of FV showing that the UA (83%) and PA (67%) based on the BI are similar to the PA (80%) and UA (68%) based on Cloude–Pottier results. Overall, the application of PP constitutes an improvement of the accuracy for FV in comparison to results only achieved by using BI.

4.1.3. Interferometric coherence

A useful technique for the identification of FV constitutes the SAR interferometry through the usage of the IC, computable from two interferometric SAR images. The application of interferometric SAR technology is relatively new in the research field of the extraction of FV and limited based on several requirements of certain conditions, such as maintained phase information in the SAR data or a short temporal baseline between an interferometric pair (Pulvirenti et al. 2016). Recently published studies used IC information alone (ID 83) and in combination with the BI (ID 64) for the extraction of FV (Figure 1). The coherence might help differentiating between vegetation and bare soil areas, where the latter has considerably higher coherency values. Consequently, the coherence may replace the application of ancillary information, such as optical data or land-cover information, which is often used to separate between various objects with similar BI. The combination of both, BI values and associated phase coherence, enables the discrimination of non-flooded and FV (Alsdorf et al. 2000; Alsdorf, Smith, and Melack 2001; Kwoun and Zhong 2009; Oliver-Cabrera und Wdowinski 2016; Xie et al. 2013; Zhang et al. 2015).

4.2. Specification and comparison of applied classification techniques

Based on 83 studies, a comprehensive review of the classification techniques applied for the extraction of FV was conducted. The algorithms are placed in categories, due to their similarity towards each other and in regard to their application fields. Thereby, the number of the applied approaches can exceed the number of the analysed studies as a single study can implement more than one of these approaches (overall 101 classification algorithms in 83 studies).

These classification techniques can be categorized into supervised and unsupervised classification techniques (Figure 2). In general, supervised classification uses reference
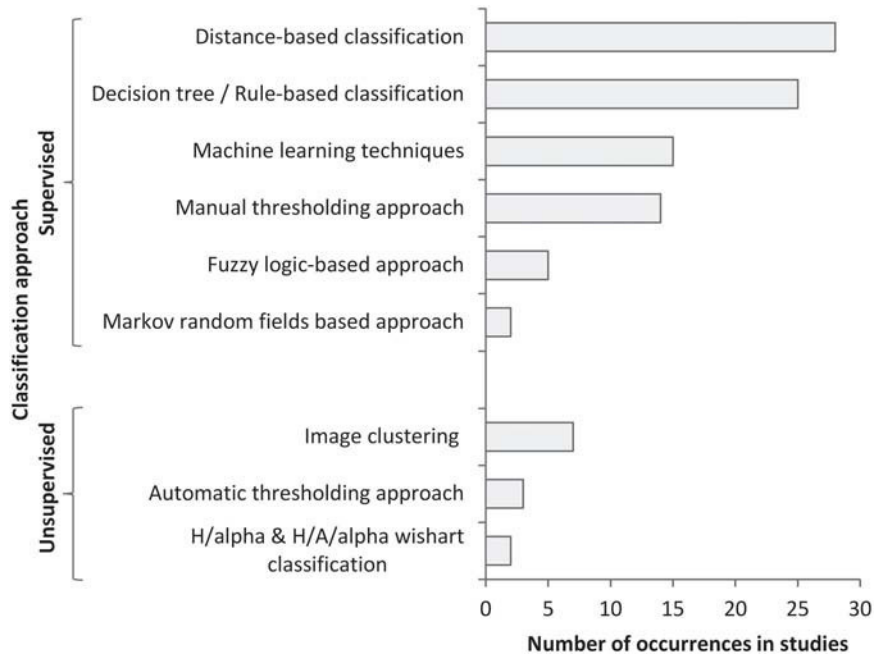
Figure 2. Supervised and unsupervised classification techniques and their number of occurrences for the extraction of FV in the selected studies.

classes obtained from training samples (reference data) to classify the image elements (Richards 2012). The majority of the performed classification algorithms in each study are supervised (89 studies). The number of occurrences of unsupervised techniques for the extraction of FV in the studies is comparatively low (12 studies). Furthermore, unsupervised classification algorithms are mostly applied as a part of a processing chain, which additionally includes a supervised classification algorithm or manual interaction steps.

The range of classification algorithms applied for the extraction of FV is diverse (Figure 2). The distance-based classification methods constitute the majority of the applied classification algorithms amongst the analysed studies (28 of 83). Whereby, algorithms are categorized as distance-based because they are using simple distance functions. Figure 3 shows the number of occurrences for distance-based classifications. Maximum likelihood classification (MLC) was identified as one of the most common classification techniques within the distance-based methods (15 of 29) applied for the extraction of FV (ID 8, 9, 12, 13, 23, 25, 49, 51, 53, 56, 57, 67, 71, 77, 80). The supervised KNNC was applied four times for the extraction of FV (ID 5, 17, 54, 80). A parallelepiped classification is one of the distance-based classification methods and was used in three studies (ID 26, 44, 49). Three of the distance-based classifications used the Mahalanobis distance (ID 43, 74, 75). Other two studies applied the Bhattacharyya distance (ID 20, 21, 22). Due to their simplicity, availability, and statistical transparency (no black box), these algorithms are popular tools not only for classification in general but also for detecting FV. Furthermore, they can be easily adapted to other study sites or data sets (Martinez and Le Toan 2007). Especially MLC and KNNC are often used as a reference for the performance of newly developed algorithms (Bourgeau-Chavez et al. 2001; Brisco et al.
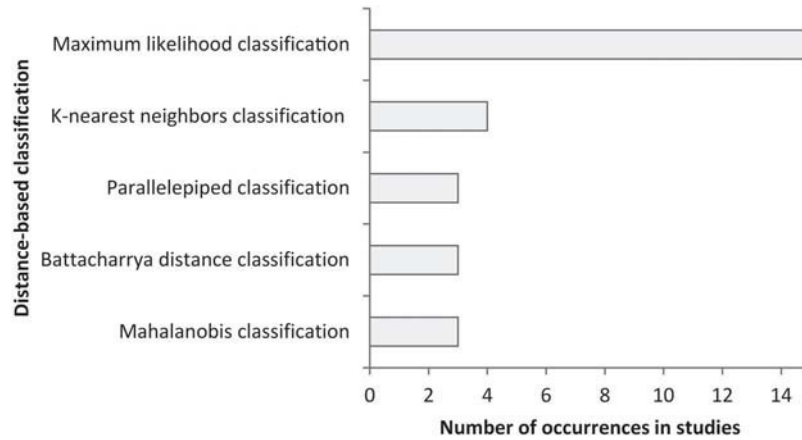
Figure 3. Categorization of distance-based classifications and their number of occurrences for the extraction of FV in the selected studies.

2013b). However, Na et al. (2015) remarked that MLC and KNNC are in general not suitable for the analysis of high dimensional data, which can constitute a drawback for the extraction of FV.

The second most common approach used in the reviewed studies (25 of 83) is the decision tree/rule-based classification (Figure 2), which includes decision tree classification (DTC) and hierarchical rule-based classification (HRBC).

Figure 4 shows the number of occurrences of both approaches, where the majority of studies (20) applied DTC for the extraction of FV (ID 2, 4, 5, 7, 9, 14, 17, 19, 40, 42, 44, 48, 52, 60, 69, 70, 72, 73, 78, 79). A decision tree classifier is well adapted for SAR image classification, because it does not assume a special probability density distribution of the given input data (Baghdadi et al. 2001; Hess et al. 1995). This algorithm is based on hierarchical rules representing thresholds used to iteratively split data in more homogeneous groups (Richards 2012), which can be easily refined after iterations (Martinez and Le Toan 2007). The automatic boundary definition constitutes an advantage because manually determining thresholds, especially for separation of FV to other classes, can be a complex process. A further advantage of decision trees is their flexibility and robustness regarding nonlinear and noisy relations among input features (Townsend 2002; Friedl und Brodley 1997; Na et al. 2015). This is a benefit for the detection of FV, because of the
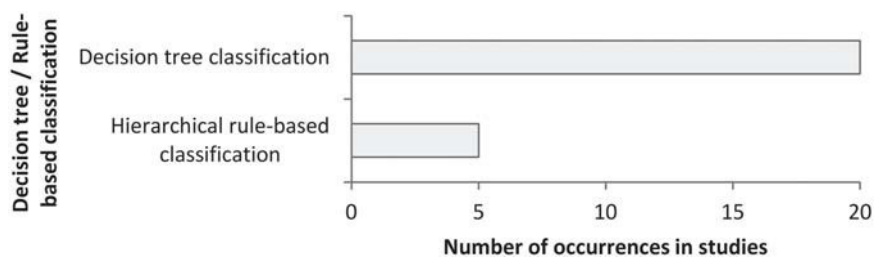

Figure 4. Decision tree and hierarchical rule-based classifications and their number of occurrences for the extraction of FV in the selected studies.

diversity of the applied input data for its extraction. Additionally, DTC requires less time for training in comparison to machine-learning algorithms (e.g. artificial neural networks [ANNs], Support Vector Machine) (Na et al. 2015).

Three studies used the HRBC for the extraction of FV (ID 27, 28, 29, 37, 47), in which the classification rules are designed by users based on their knowledge and expertise and can be iteratively changed depending on the results of the classification process. Therefore, specific characteristics of FV can be systematically integrated into the rule set. The transparency of this approach ensures that this knowledge can be used as basis for further studies and decisions. Furthermore, HRBC allows adding new rules or data sets without altering the predefined rules, while distance-based methods, such as MLC, may change all classes' rules due to additionally added information (Evans et al. 2010).

Several studies (15 of 83) used machine-learning techniques for the extraction of FV (Figure 2). Figure 5 shows various machine-learning techniques which were applied in the reviewed studies and their number of occurrences.

The majority of these techniques (11 of 15) is represented by the Random forest classification (RFC) (ID 10, 18, 24, 32, 35, 46, 53, 54, 66, 81, 82). RFC is an ensemble classifier containing multiple decision trees and consequently, the aforementioned advantages of DTC also shared by RFC. By averaging multiple decision trees, the usual overfitting of each decision tree can be reduced (Richards 2012). This algorithm efficiently determines the contribution of diverse information to a classification. However, the application of different information types without the understanding of the true relations within this information can also constitute a disadvantage. For instance, SAR data can be rated less important due to a better correlation of optical data with other features for the extraction of FV. In this particular case, RDF may ignore the context and set the priority to the highest correlated data. Furthermore, a large set of reference data is needed to mitigate misclassification caused by natural variability within FV (Robertson, King, and Davies 2015).

Support Vector Machine (SVM) classification, which is used in three studies (ID 5, 6, 13), aims to separate two different classes by determining the maximum-margin hyperplanes for a given training set. SVMs are intended for the determination of the best linear separation between two categories within a new feature space. Moreover, the SVM classification is suitable for high-dimensional data even though limited training data are available (Richards 2012), which is often the case when working with FV.
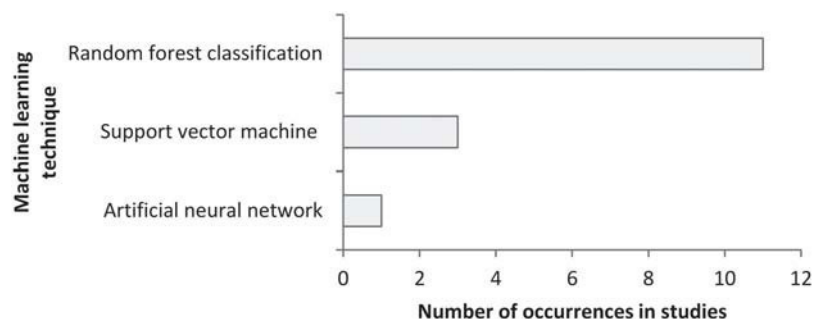

Figure 5. Machine-learning techniques and their number of occurrences for the extraction of FV in the selected studies.

A single study (ID 3) applied ANNs. This machine-learning algorithm is inspired by the neural structure of the human brain (Richards 2012). A huge disadvantage of this method is the fact that a large sample set is required to provide an effective training of the model. This in return could result in a high computation time. Nevertheless, ANN has demonstrated several advantages for image classification. Various heterogeneous data sources (e.g. temperature, SAR intensities, soil moisture level) can be combined as input. In addition, the algorithm works without any assumption about the distribution of the data (Augusteijn und Warrender 1998). As discussed above, both advantages are beneficial for the extraction of FV.

A fuzzy logic-based approach was applied in five studies (ID 34, 45, 55, 62, 63) to deal with the ambiguities of the SAR signature and to integrate different sources of information, such as SAR BI, elevation distance to open flood areas, and neighbourhood relationships between pixels. This constitutes an advantage regarding the extraction of FV. In classical set theory, an element may or may not belong to a set, as against in a fuzzy set, where all elements have different degrees of membership (Buckley und Eslami 2002). The selection of an appropriate membership function to build up a fuzzy set is subjective and it depends on the task and the available data. It can be challenging to locate FV in transition zones between open water and upland in SAR images due to their variations over the time (Wang 2004). Fuzzy logic has the ability to overcome these uncertainties by describing the increase of backscatter induced by FV using membership functions without crisp thresholds.

Another supervised method for the extraction of FV is the MTA used in 13 studies (ID 11, 15, 16, 30, 31, 33, 38, 39, 41, 64, 65, 76, 83). Defining the threshold value is a crucial point as environmental and sensor parameters show strong mutual dependencies. The threshold for FV has to be individually determined for each study area and is therefore non-transferable towards other regions. However, this method provides the ability to separate between FV and other classes quickly and without much effort, for example using histogram thresholding (ID 42, 76).

In contrast, Otsu's (Otsu 1979) and Kittler and Illingworth's (Kittler und Illingworth 1986) thresholding methods represent unsupervised classification techniques which automatically perform histogram shape-based thresholding (ID 45, 62, 63). A fast classification of clearly separable classes and therefore the creation of a quick overview of the existing classes are great benefits of automatic thresholding techniques. However, the separation between FV and non-FV is challenging due to the wide range of values within both categories that may lead to overlapping histograms. Therefore, the automatic thresholding technique is usually only applied as part of a processing chain for the extraction of FV.

Markov random fields (MRFs) are commonly used as part of an image classification processes and include various types of contextual information (e.g. spatial, hierarchical, and temporal). The knowledge about the dependencies between neighboured pixels reveals the connections within the data providing a more appropriate basis for image classification in contrast to the consideration of isolated pixels (Li 2001). This helps to overcome challenges regarding the heterogeneity and phenological changes within FV classes. Martinis and Twele (2010) and Maillard, Alencar-Silva, and Clausi (2008) adapted MRFs within a process chain for the classification of FV among other classes (ID 43, 45).

Amongst the vast number of classification approaches to extract FV from SAR data, image clustering was used in seven studies (ID 1, 36, 52, 58, 59, 61, 68). The number of occurrences of different image clustering techniques in the reviewed studies is demonstrated in Figure 6. Image clustering is used to identify relationships within the data without any previous information (trainings sets) by dividing image elements into groups containing same or similar properties (spatial and/or temporal). Image clustering leads to a reduction of the elements to be studied and therefore provides an appropriate basis for further analysis. Furthermore, grouping of elements constitutes an advantage for the extraction of FV by means of SAR data, because speckle noise can be compensated and variation within FV as well as phenological changes can be considered.

k-Means (ID 61), *k*-medoids (ID 68), and ISODATA (ID 1, 52, 58, 59) are iterative, non-hierarchical clustering techniques of similar design. While *k*-means uses centroids for the determination of cluster centres, *k*-medoids uses medoids, which makes this algorithm more stable towards outliers. Both algorithms calculate a predefined number of clusters, even though fewer clusters might describe the data more accurately (Park und Jun 2009; Richards 2012). This disadvantage is overcome by ISODATA, which automatically merges similar clusters and splits clusters with large standard deviation during the iteration process. An iterative clustering algorithm based on the Mahalanobis distance was performed by Hess (2003) for the extraction of flooded forest and wetland types (ID 36).

Wishart H/α and H/A/α unsupervised classifications were performed by two studies (ID 17, 50). These algorithms, especially designed for decomposed SAR data, require PP, which can be obtained by decomposition (see Section 4.1.2) of dual- or quad-polarised SAR data. Morandeira et al. (2016) applied these classifications to increase expertise on the backscatter response of herbaceous wetlands (ID 50).

A few studies provided a comparison of the accuracies of the results for different classification approaches, which were implemented based on the same constellation of data sets for each study. In order to give an idea of the range of performance statistics and to demonstrate the accuracies for various algorithms, the corresponding accuracies are summarized in the following. Chen et al. (2014) compared the accuracies of the results for wetland vegetation of three different classification approaches: Wishard
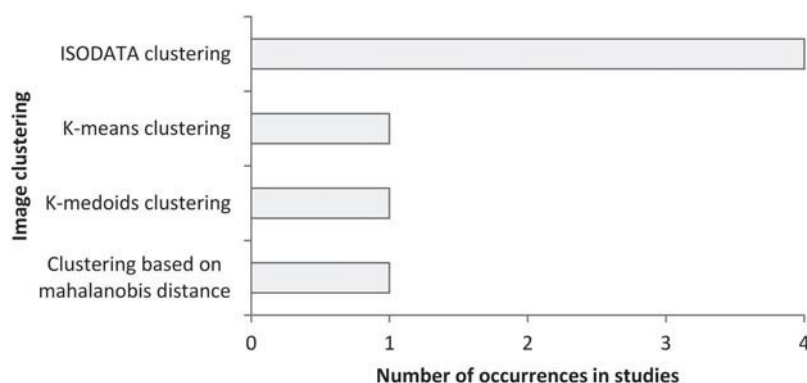

Figure 6. Image clustering techniques and their number of occurrences for the extraction of FV in the selected studies.

classification (PA: 95%, UA: 73%), KNNC (PA: 94%, UA: 78%), DTC (PA: 94%, UA: 80%). Whereby, DTC results in slightly better UA and similar or slightly worse PA compared to both others. Betbeder et al. (2014) used only the kappa index to indicate the accuracy for a study side including FV with different classification algorithm (KNNC: 0.74, DTC: 0.66, SVM using a Gaussian kernel: 0.85). The UA: 75%, PA: 90%, OA: 85% for FV were only demonstrated for SVM classifier. Na et al. (2015) showed that the results of forested and herbaceous wetlands extracted by RFC (UA: 81%, PA: 83%) outperform the results of KNNC (UA: 65%, PA: 35%).

4.3. *Pixel- and segment-based image classifications*

The classification techniques can be categorized in pixel- and segment based. In the traditional pixel-based method, each pixel of an image is classified separately, disregarding any neighbourhood relationships. By contrast, the segment-based image classification approach uses segmentation techniques to group the pixels according to their properties, such as spectral values, grey scales, texture features, or other characteristics (Mishra et al. 2016). Thereafter, the resulting segments can be classified into different land-cover features depending on the task.

Although the pixel-based approach is the most commonly used method for the extraction of FV, it may not be suitable to map heterogeneous features, such as FV, if the spatial resolution of the SAR data is finer than the objects on the ground. In this case, textural features can provide information corresponding more to FV objects and result in higher classification accuracy (Pulvirenti et al. 2011a). In contrast to pixel-based approaches, segments constitute an intuitive depiction of physical objects on the ground and allow the identification of semantic relationships. The identification of segments or regions of similar backscatter values enables these approaches to overcome the speckle noise (Hess 2003; Pulvirenti et al. 2011a). Segments are characterized by their spectral values or grey values, texture, shape, size, their neighbourhood relations, and other properties. For the extraction of FV, the texture is the most often used feature to perform a segmentation of image elements. The texture features enhance angular structures (e.g. edges) and provide information about the surfaces heterogeneity (Mishra et al. 2016). Different data sources can be combined by segments rather than by pixels due to their independence of spatial or spectral resolution (Evans et al. 2010).

In the literature, several segmentation techniques were applied to group the image elements for the extraction of FV. One of the well-known and commonly used segmentation techniques is the multiresolution segmentation. The pairwise comparison of pixel neighbours aims to minimize the heterogeneity of the resulting objects. The segmentation parameters of multiresolution segmentation have to be defined by the user, based on their knowledge and expertise, depending on the specific task. However, there is no consistent method to define the most appropriate segmentation parameter. Therefore, empirical investigations based on previous studies is necessary (Na et al. 2015; Robertson, King, and Davies 2015). Further techniques, such as Mallat's discrete wavelet transform (ID 69, 70) or Markov Random Fields (ID 43, 45), were used as a segmentation step. Commonly, the segmentation step is followed by the classification of the obtained segments applying a DTC (ID 2, 17, 19, 52, 69, 79) or a hierarchical rule-based approach (ID 27, 28, 29, 37).
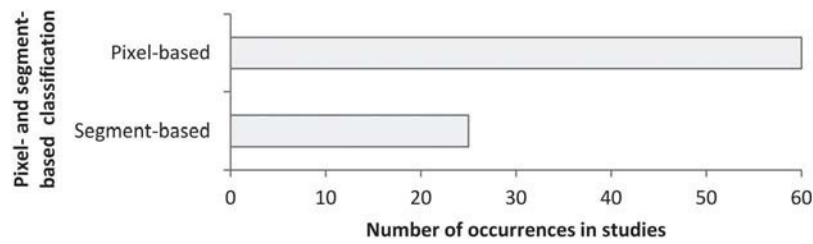
Figure 7. Pixel- and segment-based classification techniques and their number of occurrences for the extraction of FV in the selected studies.

Figure 7 shows the distribution of studies using either pixel- or segment-based classification. The majority of studies (58 of 83) applied the classification at the pixel-based scale (ID 1, 2–16, 18, 23–26, 31, 33, 35, 36, 38–42, 44, 47–51, 53–56, 58–60, 62, 64, 65, 67, 68, 70–83). The segment-based classification was performed in 23 studies (ID 2, 17, 19–22, 27–30, 32, 34, 37, 43, 45, 46, 52, 57, 61, 63, 66, 69, 79).

Three of these studies used both, pixel and segment level, to provide a comparison between the classification accuracy of the classification results (ID 17, 54, 80). A slight increase in the accuracy for FV in wetland areas was shown by Chen et al. (2014), by the application of an object-based approach (UA: 94%, PA: 81%) in comparison to a pixel-based approach (UA: 92%, PA: 77%). Na et al. (2015) demonstrated that the object-based classification (UA: 81%, PA: 83%) exceeds the pixel-based classification (UA: 67%, PA: 67%) for FV with the corresponding kappa index increasing from 0.7 to 0.8 (ID 54). Westra et al. (2010) presented the comparison between kappa values for pixel- (0.86) and for segment-based (0.83) approaches, which were carried out with different classification algorithms (MLC and KNNC). This may be the explanation for a decrease in kappa, which might not be affected by the application of pixel- and segment-based approaches. Therefore, these results are not comparable. Overall, the presumption can be made that the trend is towards segment-based approaches due to their higher accuracies.

4.4. Approaches depending on the number of applied images in combination with SAR-derived information

For the detection of FV, the aforementioned algorithms were applied on SAR data sets with a different number of images. Depending on the available number of SAR images, the selected studies can be categorized into four different approaches: single date, change detection, order-independent multi-date, and time-series approach (Figure 8), where more than one approach can occur in a single study. Furthermore, each category contains different SAR-derived information (BI, PP, and IC or their combination) (Section 4.3). There is a huge difference in the amount of the studies that performed a single date approach in comparison to those that performed multi-date approaches (change detection, order-independent multi-date, and time-series approach) using more than one image (52 vs 14, 52 vs 11, 52 vs six studies, respectively).

For the detection of FV, the single-date approach is a common method, in which the information of only one image for a current situation on the ground is considered. Despite these restrictions, the single-date approach is applied in 52 studies (ID 2–4, 12–14, 16, 17,
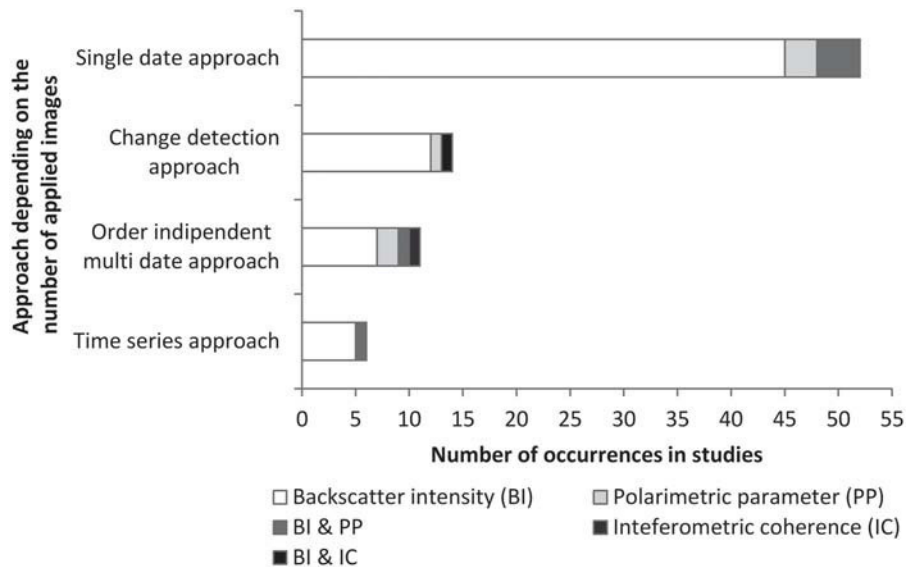
Figure 8. Summary of temporal frequency-related approaches combined with SAR-related information.

19–30, 32, 34, 35, 37, 40, 41, 43, 46, 48–50, 52–54, 56–58, 65–67, 70–76, 78–82). Land-cover maps, digital elevation models, or optical data are often used as auxiliary information to complement a single SAR date and to overcome the similarity within the BI as well as to improve the separability between FV and other classes (e.g. ID 27, 54, 72, 76). The more advanced SAR systems enable the acquisition of dual- or quad-polarised data providing extended information content in comparison to single-polarised data. In this case, ratios of the available polarisations or PP can be applied still considering only a single date. Despite this advantage, three of 52 single date approaches used PP to extract FV (ID 12, 13, 50) and four of 52 single-date approaches used both BI and PP (ID 32, 35, 66, 82). A single date only represents a snapshot of a current situations status and is therefore insufficient to detect potential changes over time.

The application of images acquired at multiple dates (two or more) may reveal the location and the extent of FV depending on the condition of their acquisition.

The reviewed studies using multiple dates can be categorized into change detection approach, order-independent multi-date approach, and time-series approach.

The change detection approach usually uses two images, acquired under dry and wet conditions, which enables to consider changes between two dates. Thereby, a change image is calculated based on the BI by the subtraction of each corresponding image element (pixel) in both images (Schumann, Di Baldassarre, and Bates 2009). The temporal change is often measured by the ratio of backscatter intensities between two dates rather than by the difference of intensities (Bouvet und Le Toan 2011). This difference between absolute backscatter intensities produces larger classification errors in regions with high backscatter than in regions with low backscatter. The ratio only depends on the relative change between two dates in SAR imagery and does not depend on the intensity level of the pixels (Rignot und van Zyl 1993). Fourteen studies demonstrated the applicability of the change detection approach for the extraction of

FV (ID 7, 10, 11, 31, 33, 39, 42, 45, 55, 60, 62, 64, 69, 77). Despite the advantage to detect changes between two images, the application of a change detection approach usually requires manual intervention for the selection of appropriate images. This selection of a scene acquired under dry conditions is critical because of the high variability in back-scatter for FV depending on the environmental conditions (see Section 3.4). In addition to BI, the change detection approach was conducted based on PP (ID 33) and on the combination of BI values with IC information (ID 64).

Several studies applied multi-temporal information without the direct consideration of changes between dates in advance (ID 8, 9, 18, 36, 44, 47, 59, 83), whereby two or more acquisition dates were taken into account. In this review, these methods are summarized as order-independent multi-date approach. This approach allows the integration of different acquisition dates without knowledge about their temporal sequence. Nevertheless, it is common to integrate data from various seasons (e.g. dry and wet). Especially in the field of wetland monitoring, this approach is very popular, because different types of FV can occur during different seasons. Typical classification algorithms used in this approach are decision tree, random forest, or Support Vector Machine. Because additional information can easily be integrated, the information of PP (ID 5, 6, 18) and of IC (ID 83) were increasingly applied compared to the other three approaches discussed in this section.

The time series approach may be an appropriate solution allowing a sequential extraction of changes over time for the investigation of FV, considering seasonal or annual fluctuations of the individual vegetation types. Similar to the order-independent multi-date approach, the time series approach enables the improvement of the relia-bility for mapping FV areas as a consequence of multiple observations of the same area. Furthermore, the flood evolution in FV areas within an inundation event can be ana-lysed. More details can be extracted by the shape of temporal profiles, which consider the effects of phenology and flooding and consequently enable a superior separation between FV and other classes (Betbeder et al. 2014). Overall, six studies performed the time series approach for extraction of FV. Thereby, five studies are based on BI values (ID 15, 38, 61, 63, 68); however, only one used PP as a foundation information (ID 51). Depending on the available number of SAR images, the information content can significantly increase. Martinez and Le Toan (2007) remarked that the improvement of FV accuracy depends not only on the higher number of scenes but also on the regularity of data acquisition. The complexity of analysis and processing of SAR data can consider-ably increase with the number of available images causing challenges in the extraction of the required information. The per-pixel analysis of backscatter time series can be CPU intensive and time consuming. In case of flood monitoring, where near real-time information is required, these characteristics may constitute a drawback. Nevertheless, several studies show benefits of the application of a time series approach. Pulvirenti et al. (2011a) demonstrated flood evolution mapping within FV by defining multi-temporal FV classes containing different stages of flood duration. Thereby, the definition of the classes was performed using multi-temporal profiles. For the extraction of the dynamics of FV, Moser et al. (2016) performed a multi-temporal classification on a stack of time-series data. Hidayat et al. (2012) calculated range, mean change, and standard deviation images using the temporal information from 20 SAR scenes. Schlaffer et al. (2016) recently introduced a harmonic model approach suitable for ENVISAT (Environmental Satellite) ASAR (advanced SAR) time-series data. This approach is

appropriate for modelling seasonal backscatter value patterns induced by different dynamics in wetlands, among others the flood evolution in vegetated areas. The harmonic model approach requires a time-series length of at least one seasonal cycle for clear classification of permanent or seasonal FV. This method represents an advanced time series approach contributing to a more automatic extraction of FV.

A comparison of the accuracy between the single image and multi-temporal approach is provided in a few of the reviewed studies and is described in the following. Wang et al. (1998) compared the accuracy of a single-date (51% correctly classified pixels) wetland classification with different combination of dates (72–85% correctly classified pixels) showing a clear improvement with higher temporal resolution. Furtado, Silva, and Novo (2016) demonstrated that the use of dual-season imagery in comparison to a single image brought the largest improvements in accuracies for flooded forest, among other classes. PA increased from 49% to 79% and UA increased from 64% to 95%, respectively. Despite the low accuracy performance reported by Heine, Jagdhuber, and Itzerott (2016), the best accuracy acquired from single-date classification (36% correctly classified proportion) was improved using multi-temporal data (45% correctly classified proportion). Zhao et al. (2014) showed that the accuracy classification of FV is improved by using multi date (PA: 97%, UA: 99%) in respect to single dates (PA: 80–92%, UA: 80–95%). Overall, an increase in accuracy using multi-date data instead of single images is reported, which can be explained by the increased information content including the seasonal stages of the plants. Thereby, the selection of specific dates constitutes the decisive factor and not necessarily their increased number Martinez and Le Toan (2007).

5. Conclusion

This review provides the current state of the art regarding the detection and extraction of FV based on 128 studies. An overview of the interaction between sensor characteristics and environmental conditions, and their effects on the SAR signal, is given. In addition, various SAR data sets and classification algorithms, as well as their benefits and limitations for the extraction of FV, are described.

As reported in earlier research reviews, longer wavelengths are still suggested for the detection of flooded forests. However, L-band and C-band can be used, both combined or individually, to separate between flooded forest, flooded herbaceous vegetation, and dry land classes. Current research also demonstrates the ability of X-band to detect FV in case of low biomass or leaf-off conditions. For the detection of FV, HH is preferred over VV and co-polarised in general over cross-polarised data. However, both are applied to discriminate between different FV types. Inhomogeneous statements were given about the application of polarisation ratios. Nevertheless, multi-polarised data were found to be valuable due to enhanced information content in comparison to single polarised data. Steeper incidence angles are still preferred over shallow ones. However, a few studies suggest that the detection of flood beneath forests with increasing incident angles is less limited than expected.

Besides sensor characteristics, the backscatter signature of FV is strongly affected by the environmental conditions and their characteristics. It was shown that the amount of the aboveground biomass is critical for the detection of FV. Therefore, saturation points of the SAR signal were determined, where the biomass increases and the water underneath the vegetation can no longer be detected. It was established that the location of the saturation

point is strongly influenced by sensor characteristics and depends on the vegetation type. Furthermore, advanced analysis of the relation between the water depth and the height of the plants has been conducted and their importance for the detection of flood in agricultural and herbaceous areas has been emphasized in several studies.

With technological advances, an increase in the variety of SAR data sets and classification algorithms has taken. BI using different polarisations is a proved basis for the extraction of FV. However, the application of PPs based on quad- or even dual-polarised SAR data leads to promising results. This is because of their increased information content and their ability to describe physical objects. Depending on the SAR data, various decomposition techniques were introduced for the extraction of PPs. In particular, the decomposition of dual-polarised data, which constitutes a compromise between information content, calculation complexity, and general availability, will provide a valuable foundation for future studies (Moser et al. 2016; Schmitt et al. 2012). IC is comparatively novel SAR-derived information which, although limited by its demanding requirements, can be beneficial as complementary information for BI (Pulvirenti et al. 2016) and reduce the need for external data (Chini et al. 2016).

The reviewed studies show some inconsistency in the application of classification algorithms used for the extraction of FV. This can be explained by the wide variety of the underlying data, which is often depending on the specific task but is mostly restricted by its availability. Thereby, the comparability of the results can be inhibited. A wide range of different classification techniques were applied in the studies, spanning from basic thresholding approaches to more complex algorithms like machine learning. A selection of a suitable algorithm for a certain task can be crucial for a successful classification and strongly depends on the applied data. With the increasing availability of data, due to a more continuous acquisition by SAR systems, such as Sentinel-1, current and prospective algorithms need to be examined in regards to their usability to extract FV. Although an increased utilization of the random forest algorithm can be noticed for wetland observations, no general trend was identified for the extraction of FV from SAR data. Even though unsupervised algorithms are applied within multiple process chains, still no completely unsupervised method exists that focuses on the extraction of FV.

The use of segmentation leads to more reliable results than pixel-based approaches, because it is less prone to speckle noise. Furthermore, segment-based approaches appear to be valuable alternatives, providing a depiction of real objects on the ground, mitigating the increasing heterogeneity of classes in high-resolution satellite imagery. Because of its potential, the segment-based approach should be more utilized for the detection of FV.

Single-image approaches are still preferred and are mostly used in combination with ancillary data, such as optical or elevation information, to describe land-cover types containing FV. The usage of multi-date SAR data sets seems to be attractive for wetland monitoring because it includes seasonal information. The comparisons between single and multi-date approaches within studies show an improvement in classification results. Short revisit times and systematic data acquisitions by satellite missions, such as Sentinel-1 (Aulard-Macler 2011) and Tandem-L (German Aerospace Center 2017), pave the way for the application of time series approaches which are already implemented, especially for flood monitoring (Schlaffer et al. 2016). Continuing efforts in the analysis of long-term profiles would expand the understanding about the seasonal and annual variability and enable the development of fully automated and potentially transferable processes for the extraction of FV.

Disclosure statement

No potential conflict of interest was reported by the authors.

ORCID

Sandro Martinis http://orcid.org/0000-0002-6400-361X

References

Airbus Defence and Space. 2016. "TerraSAR-X Documentation." Online verfügbar unter. Accessed 25 October 2017. http://www.intelligence-airbusds.com/en/228-terrasar-x-technical-documents.

Allen, T., Y. Wang, and B. Gore. 2013. "Coastal Wetland Mapping Combining Multi-Date SAR and LiDAR." *Geocarto International* 28 (7): 616–631. doi:10.1080/10106049.2013.768297.

Alsdorf, D. E., J. M. Melack, T. Dunne, L. A. K. Mertes, L. L. Hess, and L. C. Smith. 2000. "Interferometric Radar Measurements of Water Level Changes on the Amazon Flood Plain." *Nature* 404 (6774): 174–177. doi:10.1038/35004560.

Alsdorf, D. E., L. C. Smith, and J. M. Melack. 2001. "Amazon Floodplain Water Level Changes Measured with Interferometric SIR-C Radar." *IEEE Transactions Geoscience Remote Sensing* 39 (2): 423–431. doi:10.1109/36.905250.

Arnesen, A. S., T. S. F. Silva, L. L. Hess, E. M. L. M. Novo, C. M. Rudorff, B. D. Chapman, and K. C. McDonald. 2013. "Monitoring Flood Extent in the Lower Amazon River Floodplain Using ALOS/PALSAR ScanSAR Images." *Remote Sensing of Environment* 130: 51–61. doi:10.1016/j.rse.2012.10.035.

Asselen, S., P. H. Verburg, J. E. Vermaat, and J. H. Janse. 2013. "Drivers of Wetland Conversion: A Global Meta-Analysis." *PloS One* 8 (11): 1–13. doi:10.1371/journal.pone.0081292.

Augusteijn, M. F., and C. E. Warrender. 1998. "Wetland Classification Using Optical and Radar Data and Neural Network Classification." *International Journal of Remote Sensing* 19 (8): 1545–1560. doi:10.1080/014311698215342.

Aulard-Macler, M. 2011. *Sentinel-1 Product Definition, MDA Technical Note Ref. S1-RS-MDA-52–7440. MacDonald*. Richmond, Canada: Dettwiler and Associates (MDA).

Aziz, H. K., and K. White. 2003. "Using Mimics to Model L-Band SAR Mackscatter from a Peat Swamp Forest." *Journal of Tropical Forest Science* 15 (4): 546–556.

Baghdadi, N., M. Bernier, R. Gauthier, and I. Neeson. 2001. "Evaluation of C-Band SAR Data for Wetlands Mapping." *International Journal of Remote Sensing* 22 (1): 71–88. doi:10.1080/014311601750038857.

Betbeder, J., S. Rapinel, S. Corgne, E. Pottier, and L. Hubert-Moy. 2015. "TerraSAR-X Dual-Pol Time-Series for Mapping of Wetland Vegetation." *ISPRS Journal of Photogrammetry and Remote Sensing* 107: 90–98. doi:10.1016/j.isprsjprs.2015.05.001.

Betbeder, J., S. Rapinel, T. Corpetti, E. Pottier, S. Corgne, and L. Hubert-Moy. 2014. "Multitemporal Classification of TerraSAR-X Data for Wetland Vegetation Mapping." *Journal Applications Remote Sens* 8 (1): 83648. doi:10.1117/1.JRS.8.083648.

Bian, H., T. Yan, Z. Zhang, C. He, and L. Sheng. 2016. "Mapping Deciduous Broad-Leaved Forested Swamps Using ALOS/Palsar Data." *Chinese Geographic Sciences* 26 (3): 352–365. doi:10.1007/s11769-016-0805-2.

Bourgeau-Chavez, L., Y. Lee, M. Battaglia, S. Endres, Z. Laubach, and K. Scarbrough. 2016. "Identification of Woodland Vernal Pools with Seasonal Change PALSAR Data for Habitat Conservation." *Remote Sensing* 8 (6): 490. doi:10.3390/rs8060490.

Bourgeau-Chavez, L. L., E. S. Kasischke, and K. Smith. 1997. "Using Satellite Radar Imagery to Monitor Flood Conditions in Wetland Ecosystems of Southern Florida." In *Proc. SPIE 2959, Remote Sensing of Vegetation and Sea*, edited by G. Cecchi, G. D'Urso, E. T. Engman, and P. Gudmandsen, Taormina, Italy, 139–148.

Bourgeau-Chavez, L. L., E. S. Kasischke, S. M. Brunzell, J. P. Mudd, K. B. Smith, and A. L. Frick. 2001. "Analysis of Space-Borne SAR Data for Wetland Mapping in Virginia Riparian Ecosystems." *International Journal of Remote Sensing* 22 (18): 3665–3687. doi:10.1080/01431160010029174.

Bourgeau-Chavez, L. L., K. Riordan, B. Richard, N. Miller, and M. Nowels. 2009. "Improving Wetland Characterization with Multi-Sensor, Multi-Temporal SAR and Optical/Infrared Data Fusion." In *Advances in Geoscience and Remote Sensing*, edited by G. Jedlovec. Vukovar: Croatia: In-Teh.

Bouvet, A., and T. Le Toan. 2011. "Use of ENVISAT/ASAR Wide-Swath Data for Timely Rice Fields Mapping in the Mekong River Delta." *Remote Sensing of Environment* 115 (4): 1090–1101. doi:10.1016/j.rse.2010.12.014.

Brisco, B., A. Schmitt, K. Murnaghan, S. Kaya, and A. Roth. 2013a. "SAR Polarimetric Change Detection for Flooded Vegetation." *International Journal of Digital Earth* 6 (2): 103–114. doi:10.1080/17538947.2011.608813.

Brisco, B., L. Kun, B. Tedford, F. Charbonneau, S. Yun, and K. Murnaghan. 2013b. "Compact Polarimetry Assessment for Rice and Wetland Mapping." *International Journal of Remote Sensing* 34 (6): 1949–1964. doi:10.1080/01431161.2012.730156.

Brisco, B., M. Kapfer, T. Hirose, B. Tedford, and J. Liu. 2011. "Evaluation of C-Band Polarization Diversity and Polarimetry for Wetland Mapping." *Canadian Journal of Remote Sensing* 37 (1): 82–92. doi:10.5589/m11-017.

Brisco, B., R. Touzi, J. J. van der Sanden, F. Charbonneau, T. J. Pultz, and M. D'Iorio. 2008. "Water Resource Applications with RADARSAT-2? A Preview." *International Journal of Digital Earth* 1 (1): 130–147. doi:10.1080/17538940701782577.

Brown, I., S. Mwansasu, and L.-O. Westerberg. 2016. "L-Band Polarimetric Target Decomposition of Mangroves of the Rufiji Delta, Tanzania." *Remote Sensing* 8 (2): 140. doi:10.3390/rs8020140.

Buckley, J. J., and E. Eslami. 2002. *An Introduction to Fuzzy Logic and Fuzzy Sets*. Heidelberg: Physica-Verlag (Advances in soft computing).

Bwangoy, J.-R. B., M. C. Hansen, D. P. Roy, G. de Grandi, and C. O. Justice. 2010. "Wetland Mapping in the Congo Basin Using Optical and Radar Remotely Sensed Data and Derived Topographical Indices." *Remote Sensing of Environment* 114 (1): 73–86. doi:10.1016/j.rse.2009.08.004.

Cazals, C., S. Rapinel, P.-L. Frison, A. Bonis, G. Mercier, C. Mallet, S. Corgne, and J.-P. Rudant. 2016. "Mapping and Characterization of Hydrological Dynamics in a Coastal Marsh Using High Temporal Resolution Sentinel-1A Images." *Remote Sensing* 8 (7): 570. doi:10.3390/rs8070570.

Chapman, B., K. McDonald, M. Shimada, A. Rosenqvist, R. Schroeder, and L. Hess. 2015. "Mapping Regional Inundation with Spaceborne L-Band SAR." *Remote Sensing* 7 (5): 5440–5470. doi:10.3390/rs70505440.

Chen, Y., H. Xiufeng, J. Wang, and R. Xiao. 2014. "The Influence of Polarimetric Parameters and an Object-Based Approach on Land Cover Classification in Coastal Wetlands." *Remote Sensing* 6 (12): 12575–12592. doi:10.3390/rs61212575.

Chini, M., A. Papastergios, L. Pulvirenti, N. Pierdicca, P. Matgen, and I. Parcharidis. 2016. "SAR Coherence and Polarimetric Information for Improving Flood Mapping. In: 2016 IEEE International Geoscience & Remote Sensing Symposium." In *Proceedings IGARSS 2016-2016 IEEE International Geoscience and Remote Sensing Symposium. Beijing, China*, July 10-15, 2016, 7577–7580. Piscataway, NJ: IEEE.

Cloude, S. R., and E. Pottier. 1997. "An Entropy Based Classification Scheme for Land Applications of Polarimetric SAR." *IEEE Transactions Geoscience Remote Sensing* 35 (1): 68–78. doi:10.1109/36.551935.

Corcoran, J., J. Knight, B. Brisco, S. Kaya, A. Cull, and K. Murnaghan. 2012. "The Integration of Optical, Topographic, and Radar Data for Wetland Mapping in Northern Minnesota." *Canadian Journal of Remote Sensing* 37 (5): 564–582. doi:10.5589/m11-067.

Cordeiro, C. L. D. O., and D. D. F. Rossetti. 2015. "Mapping Vegetation in a Late Quaternary Landform of the Amazonian Wetlands Using Object-Based Image Analysis and Decision Tree Classification." *International Journal of Remote Sensing* 36 (13): 3397–3422. doi:10.1080/01431161.2015.1060644.

Costa, F., M. Novo, E. Mantovani, V. Ballester, and F. Ahern. 1997. "Classification of Floodplain Habitats (Lago Grande, Brazilian Amazon) with RADARSAT and JERS-1 Data." Presented ai GER'97 Conference, Ottawa, Canada, May 1997.

Costa, M. P. F. 2004. "Use of SAR Satellites for Mapping Zonation of Vegetation Communities in the Amazon Floodplain." *International Journal of Remote Sensing* 25 (10): 1817–1835. doi:10.1080/0143116031000116985.

Costa, M. P. F., and K. H. Telmer. 2006. "Utilizing SAR Imagery and Aquatic Vegetation to Map Fresh and Brackish Lakes in the Brazilian Pantanal Wetland." *Remote Sensing of Environment* 105 (3): 204–213. doi:10.1016/j.rse.2006.06.014.

Costa, M. P. F., O. Niemann, E. Novo, and F. Ahern. 2002. "Biophysical Properties and Mapping of Aquatic Vegetation during the Hydrological Cycle of the Amazon Floodplain Using JERS-1 and Radarsat." *International Journal of Remote Sensing* 23 (7): 1401–1426. doi:10.1080/01431160110092957.

Cremon, É., D. F. Rossetti, Dilce, and H. Zani. 2014. "Classification of Vegetation over a Residual Megafan Landform in the Amazonian Lowland Based on Optical and SAR Imagery." *Remote Sensing* 6 (11): 10931–10946. doi:10.3390/rs61110931.

Dabboor, M., L. White, B. Brisco, and F. Charbonneau. 2015. "Change Detection with Compact Polarimetric SAR for Monitoring Wetlands." *Canadian Journal of Remote Sensing* 41 (5): 408–417. doi:10.1080/07038992.2015.1104634.

de Grandi, G. F., P. Mayaux, J. P. Malingreau, A. Rosenqvist, S. Saatchi, and M. Simard. 2000. "New Perspectives on Global Ecosystems from Wide-Area Radar Mosaics: Flooded Forest Mapping in the Tropics." *International Journal of Remote Sensing* 21 (6–7): 1235–1249. doi:10.1080/014311600210155.

Dronova, I. 2015. "Object-Based Image Analysis in Wetland Research: A Review." *Remote Sensing* 7 (5): 6380–6413. doi:10.3390/rs70506380.

Dwivedi, R. S., B. R. M. Rao, and S. Bhattacharya. 1999. "Mapping Wetlands of the Sundaban Delta and It's Environs Using ERS-1 SAR Data." *International Journal of Remote Sensing* 20 (11): 2235–2247. doi:10.1080/014311699212227.

Erwin, K. L. 2009. "Wetlands and Global Climate Change. The Role of Wetland Restoration in a Changing World." *Wetlands Ecology Manage* 17 (1): 71–84. doi:10.1007/s11273-008-9119-1.

Evans, T. L., and M. Costa. 2013. "Landcover Classification of the Lower Nhecolândia Subregion of the Brazilian Pantanal Wetlands Using ALOS/PALSAR, RADARSAT-2 and ENVISAT/ASAR Imagery." *Remote Sensing of Environment* 128: 118–137. doi:10.1016/j.rse.2012.09.022.

Evans, T. L., M. Costa, K. Telmer, and T. S. F. Silva. 2010. "Using ALOS/PALSAR and RADARSAT-2 to Map Land Cover and Seasonal Inundation in the Brazilian Pantanal." *IEEE Journal Sel Topics Applications Earth Observations Remote Sensing* 3 (4): 560–575. doi:10.1109/JSTARS.2010.2089042.

Evans, T. L., M. Costa, W. M. Tomas, and A. R. Camilo. 2014. "Large-Scale Habitat Mapping of the Brazilian Pantanal Wetland. A Synthetic Aperture Radar Approach." *Remote Sensing of Environment* 155: 89–108. doi:10.1016/j.rse.2013.08.051.

Ferreira-Ferreira, J., T. S. F. Silva, A. S. Streher, A. G. Affonso, A. Furtado, F. de Luiz, B. R. Forsberg, et al. 2015. "Combining ALOS/PALSAR Derived Vegetation Structure and Inundation Patterns to Characterize Major Vegetation Types in the Mamirau? Sustainable Development Reserve, Central Amazon Floodplain, Brazil." *Wetlands Ecology Manage* 23 (1): 41–59. doi:10.1007/s11273-014-9359-1.

Frappart, F., F. Seyler, J.-M. Martinez, J. G. León, and A. Cazenave. 2005. "Floodplain Water Storage in the Negro River Basin Estimated from Microwave Remote Sensing of Inundation Area and Water Levels." *Remote Sensing of Environment* 99 (4): 387–399. doi:10.1016/j.rse.2005.08.016.

Friedl, M. A., and C. E. Brodley. 1997. "Decision Tree Classification of Land Cover from Remotely Sensed Data." *Remote Sensing of Environment* 61 (3): 399–409. doi:10.1016/S0034-4257(97)00049-7.

Furtado, L. F. D. A., T. S. F. Silva, and E. M. L. D. M. Novo. 2016. "Dual-Season and Full-Polarimetric C Band SAR Assessment for Vegetation Mapping in the Amazon várzea Wetlands." *Remote Sensing of Environment* 174: 212–222. doi:10.1016/j.rse.2015.12.013.

Gallant, A., S. Kaya, L. White, B. Brisco, M. Roth, W. Sadinski, and J. Rover. 2014. "Detecting Emergence, Growth, and Senescence of Wetland Vegetation with Polarimetric Synthetic Aperture Radar (SAR) Data." *Water* 6 (3): 694–722. doi:10.3390/w6030694.

German Aerospace Center. 2017. "Tandem-L. Satellite Mission Proposal for Monitoring Dynamic Processes on the Earth's Surface. Cologne. Online Verfügbar Unter." Accessed 27 August 2017. www.dlr.de/hr/en/Portaldata/32/Resources/dokumente/tdml/Tandem-L_Brochure_2017-05.pdf.

Grenier, M., A.-M. Demers, S. Labrecque, M. Benoit, R. A. Fournier, and B. Drolet. 2007. "An Object-Based Method to Map Wetland Using RADARSAT-1 and Landsat ETM Images. Test Case on Two

Sites in Quebec, Canada." *Canadian Journal of Remote Sensing* 33 (sup1): S28–S45. doi:10.5589/m07-048.

Grings, F. M., P. Ferrazzoli, H. Karszenbaum, M. Salvia, P. Kandus, J. C. Jacobo-Berlles, and P. Perna. 2008. "Model Investigation about the Potential of C Band SAR in Herbaceous Wetlands Flood Monitoring." *International Journal of Remote Sensing* 29 (17–18): 5361–5372. doi:10.1080/01431160802036409.

Grings, F. M., P. Ferrazzoli, J. C. Jacobo-Berlles, H. Karszenbaum, J. Tiffenberg, P. Pratolongo, and P. Kandus. 2006. "Monitoring Flood Condition in Marshes Using EM Models and Envisat ASAR Observations." *IEEE Transactions Geoscience Remote Sensing* 44 (4): 936–942. doi:10.1109/TGRS.2005.863482.

Hall, D. K. 1996. "Remote Sensing Applications to Hydrology; Imaging Radar." *Hydrological Sciences Journal* 41 (4): 609–624. doi:10.1080/02626669609491528.

Heine, I., T. Jagdhuber, and S. Itzerott. 2016. "Classification and Monitoring of Reed Belts Using Dual-Polarimetric TerraSAR-X Time Series." *Remote Sensing* 8 (7): 552. doi:10.3390/rs8070552.

Henderson, F. M., and A. J. Lewis. 2008. "Radar Detection of Wetland Ecosystems: A Review." *International Journal of Remote Sensing* 29 (20): 5809–5835. doi:10.1080/01431160801958405.

Hess, L. L. 2003. "Dual-Season Mapping of Wetland Inundation and Vegetation for the Central Amazon Basin." *Remote Sensing of Environment* 87 (4): 404–428. doi:10.1016/j.rse.2003.04.001.

Hess, L. L., J. M. Melack, A. G. Affonso, C. Barbosa, M. Gastil-Buhl, and E. M. L. M. Novo. 2015. "Wetlands of the Lowland Amazon Basin. Extent, Vegetative Cover, and Dual-Season Inundated Area as Mapped with JERS-1 Synthetic Aperture Radar." *Wetlands* 35 (4): 745–756. doi:10.1007/s13157-015-0666-y.

Hess, L. L., J. M. Melack, and D. S. Simonett. 1990. "Radar Detection of Flooding beneath the Forest Canopy. A Review." *International Journal of Remote Sensing* 11 (7): 1313–1325. doi:10.1080/01431169008955095.

Hess, L. L., and J. M. Melack. 2003. "Remote Sensing of Vegetation and Flooding on Magela Creek Floodplain (Northern Territory, Australia) with the SIR-C Synthetic Aperture Radar." In *Aquatic Biodiversity*, edited by K. Martens, 65–82. Dordrecht: Springer Netherlands.

Hess, L. L., J. M. Melack, S. Filoso, and Y. Wang. 1995. "Delineation of Inundated Area and Vegetation along the Amazon Floodplain with the SIR-C Synthetic Aperture Radar." *IEEE Transactions Geoscience Remote Sensing* 33 (4): 896–904. doi:10.1109/36.406675.

Hidayat, H., D. H. Hoekman, M. A. M. Vissers, and A. J. F. Hoitink. 2012. "Flood Occurrence Mapping of the Middle Mahakam Lowland Area Using Satellite Radar." *Hydrology Earth Systems Sciences* 16 (7): 1805–1816. doi:10.5194/hess-16-1805-2012.

Horritt, M. 2003. "Waterline Mapping in Flooded Vegetation from Airborne SAR Imagery." *Remote Sensing of Environment* 85 (3): 271–281. doi:10.1016/S0034-4257(03)00006-3.

Imhoff, M., M. Story, C. Vermillion, F. Khan, and F. Polcyn. 1986. "Forest Canopy Characterization and Vegetation Penetration Assessment with Space-Borne Radar." *IEEE Transactions Geoscience Remote Sensing* GE-24 (4): 535–542. doi:10.1109/TGRS.1986.289668.

Kandus, P., H. Karszenbaum, T. Pultz, G. Parmuchi, and J. Bava. 2001. "Influence of Flood Conditions and Vegetation Status on the Radar Backscatter of Wetland Ecosystems." *Canadian Journal of Remote Sensing* 27 (6): 651–662. doi:10.1080/07038992.2001.10854907.

Karszenbaum, H., P. Kandus, J. M. Martinez, T. Le Toan, J. Tiffenberg, and G. Parmuchi. 2000. *ERS-2, Radarsat SAR Backscattering Characteristics of the Parana River Delta Wetland, Argentina*. Argentina: Special Publication SP-461.

Kasischke, E. S., K. B. Smith, L. L. Bourgeau-Chavez, E. A. Romanowicz, S. Brunzell, and C. J. Richardson. 2003. "Effects of Seasonal Hydrologic Patterns in South Florida Wetlands on Radar Backscatter Measured from ERS-2 SAR Imagery." *Remote Sensing of Environment* 88 (4): 423–441. doi:10.1016/j.rse.2003.08.016.

Kasischke, E. S., and L. L. Bourgeau-Chavez. 1997. "Monitoring South Florida Wetlands Using ERS-1 SAR Imagery." *Photogrammetric Engineering & Remote Sensing* 63 (3): 281–291.

Kiage, L. M., N. D. Walker, S. Balasubramanian, A. Babin, and J. Barras. 2005. "Applications of Radarsat? 1 Synthetic Aperture Radar Imagery to Assess Hurricane?Related Flooding of Coastal

Louisiana." *International Journal of Remote Sensing* 26 (24): 5359–5380. doi:10.1080/01431160500442438.

Kittler, J., and J. Illingworth. 1986. "Minimum Error Thresholding." *Pattern Recognition* 19 (1): 41–47. doi:10.1016/0031-3203(86)90030-0.

Klemas, V. 2013. "Remote Sensing of Emergent and Submerged Wetlands: An Overview." *International Journal of Remote Sensing* 34 (18): 6286–6320. doi:10.1080/01431161.2013.800656.

Koch, M., T. Schmid, M. Reyes, and J. Gumuzzio. 2012. "Evaluating Full Polarimetric C- and L-Band Data for Mapping Wetland Conditions in a Semi-Arid Environment in Central Spain." *IEEE Journal Sel Topics Applications Earth Observations Remote Sensing* 5 (3): 1033–1044. doi:10.1109/JSTARS.2012.2202091.

Kuenzer, C., A. Bluemel, S. Gebhardt, T. V. Quoc, and S. Dech. 2011. "Remote Sensing of Mangrove Ecosystems. A Review." *Remote Sensing* 3 (12): 878–928. doi:10.3390/rs3050878.

Kwoun, O.-I., and L. Zhong. 2009. "Multi-Temporal RADARSAT-1 and ERS Backscattering Signatures of Coastal Wetlands in Southeastern Louisiana." *Photogramm Eng Remote Sensing* 75 (5): 607–617. doi:10.14358/PERS.75.5.607.

Lang, M. W., and E. S. Kasischke. 2008. "Using C-Band Synthetic Aperture Radar Data to Monitor Forested Wetland Hydrology in Maryland's Coastal Plain, USA." *IEEE Transactions Geoscience Remote Sensing* 46 (2): 535–546. doi:10.1109/TGRS.2007.909950.

Lang, M. W., E. S. Kasischke, S. D. Prince, and K. W. Pittman. 2008. "Assessment of C-Band Synthetic Aperture Radar Data for Mapping and Monitoring Coastal Plain Forested Wetlands in the Mid-Atlantic Region, U.S.A." *Remote Sensing of Environment* 112 (11): 4120–4130. doi:10.1016/j.rse.2007.08.026.

Lang, M. W., P. A. Townsend, and E. S. Kasischke. 2008. "Influence of Incidence Angle on Detecting Flooded Forests Using C-HH Synthetic Aperture Radar Data." *Remote Sensing of Environment* 112 (10): 3898–3907. doi:10.1016/j.rse.2008.06.013.

Le Toan, T., F. Ribbes, L.-F. Wang, N. Floury, K.-H. Ding, J. A. Kong, M. Fujita, and T. Kurosu. 1997. "Rice Crop Mapping and Monitoring Using ERS-1 Data Based on Experiment and Modeling Results." *IEEE Transactions Geoscience Remote Sensing* 35 (1): 41–56. doi:10.1109/36.551933.

Lee, H., T. Yuan, H. C. Jung, and E. Beighley. 2015. "Mapping Wetland Water Depths over the Central Congo Basin Using PALSAR ScanSAR, Envisat Altimetry, and MODIS VCF Data." *Remote Sensing of Environment* 159: 70–79. doi:10.1016/j.rse.2014.11.030.

Lee, J.-S., and E. Pottier. 2009. *Polarimetric Radar Imaging. From Basics to Applications*. Boca Raton: CRC Press (Optical science and engineering, 142).

Lewis, A. J., F. M. Henderson, and D. Holcomb. 1998. "Radar Fundamentals: The Geoscience Perspective." In *Principles and Applications of Imaging Radar*, 3rd ed. Vol. 2 edited by F. M. Henderson and A. J. Lewis, 131–181. New York: J. Wiley. (Manual of remote sensing).

Li, J., and W. Chen. 2005. "A Rule-Based Method for Mapping Canada's Wetlands Using Optical, Radar and DEM Data." *International Journal of Remote Sensing* 26 (22): 5051–5069. doi:10.1080/01431160500166516.

Li, S. Z. 2001. *Markov Random Field Modeling in Image Analysis*. Tokyo: Springer Japan (Computer Science Workbench).

Long, S., T. E. Fatoyinbo, and F. Policelli. 2014. "Flood Extent Mapping for Namibia Using Change Detection and Thresholding with SAR." *Environment Researcher Letters* 9 (3): 1–9. doi:10.1088/1748-9326/9/3/035002.

Lopes, A., R. Touzi, and E. Nezry. 1990. "Adaptive Speckle Filters and Scene Heterogeneity." *IEEE Transactions Geoscience Remote Sensing* 28 (6): 992–1000. doi:10.1109/36.62623.

Lu, Z., and O.-I. Kwoun. 2008. "Radarsat-1 and ERS InSAR Analysis over Southeastern Coastal Louisiana. Implications for Mapping Water-Level Changes beneath Swamp Forests." *IEEE Transactions Geoscience Remote Sensing* 46 (8): 2167–2184. doi:10.1109/TGRS.2008.917271.

Maillard, P., T. Alencar-Silva, and D. A. Clausi. 2008. "An Evaluation of Radarsat-1 and ASTER Data for Mapping Veredas (Palm Swamps)." *Sensors (Basel, Switzerland)* 8 (9): 6055–6076. doi:10.3390/s8096055.

Marti-Cardona, B., C. Lopez-Martinez, J. Dolz-Ripolles, and E. Bladè-Castellet. 2010. "ASAR Polarimetric, Multi-Incidence Angle and Multitemporal Characterization of Doñana Wetlands for Flood Extent Monitoring." *Remote Sensing of Environment* 114 (11): 2802–2815. doi:10.1016/j.rse.2010.06.015.

Marti-Cardona, B., J. Dolz-Ripolles, and C. Lopez-Martinez. 2013. "Wetland Inundation Monitoring by the Synergistic Use of ENVISAT/ASAR Imagery and Ancilliary Spatial Data." *Remote Sensing of Environment* 139: 171–184. doi:10.1016/j.rse.2013.07.028.

Martinez, J., and T. Le Toan. 2007. "Mapping of Flood Dynamics and Spatial Distribution of Vegetation in the Amazon Floodplain Using Multitemporal SAR Data." *Remote Sensing of Environment* 108 (3): 209–223. doi:10.1016/j.rse.2006.11.012.

Martinis, S., and A. Twele. 2010. "A Hierarchical Spatio-Temporal Markov Model for Improved Flood Mapping Using Multi-Temporal X-Band SAR Data." *Remote Sensing* 2 (9): 2240–2258. doi:10.3390/rs2092240.

Martinis, S., and C. Rieke. 2015. "Backscatter Analysis Using Multi-Temporal and Multi-Frequency SAR Data in the Context of Flood Mapping at River Saale, Germany." *Remote Sensing* 7 (6): 7732–7752. doi:10.3390/rs70607732.

Mayaux, P., G. F. de Grandi, Y. Rauste, M. Simard, and S. Saatchi. 2002. "Large-Scale Vegetation Maps Derived from the Combined L-Band GRFM and C-Band CAMP Wide Area Radar Mosaics of Central Africa." *International Journal of Remote Sensing* 23 (7): 1261–1282. doi:10.1080/01431160110092894.

Melack, J. M., and L. L. Hess. 2010. "Remote Sensing of the Distributions and Extent of Wetlands in the Amazon Basin." In *Amazonian Flodplain Forests: Ecophysiology, Ecology, Biodiversity and Sustainable Management: Ecological Studies*, edited by W. J. Junk, M. Piedade, F. Wittmann, P. Parolin, and J. Schöngart, 43–59, Netherlands: Springer.

Melack, J. M., and Y. Wang. 1998. "Delineation of Flooded Area and Flooded Vegetation in Balbina Reservoir (Amazonas, Brazil) with Synthetic Aperture Radar." *Erhandlungen - Internationale Vereinigung Fur Theoretische Und Angewandte Limnologie* 26: 2374–2377.

Millennium Ecosystem Assessment. 2005. *Ecosystems and Human Well-Being: Synthesis*. Washington, DC: Island Press.

Miranda, F. P., L. E. N. Fonseca, and J. R. Carr. 1998. "Semivariogram Textural Classification of JERS-1 (Fuyo-1) SAR Data Obtained over a Flooded Area of the Amazon Rainforest." *International Journal of Remote Sensing* 19 (3): 549–556. doi:10.1080/014311698216170.

Mishra, D. R., S. Ghosh, C. Hladik, J. L. O'Connell, and H. J. Cho. 2016. "Wetland Mapping Methods and Techniques Using Multisensor, Multiresolution Remote Sensing: Successes and Challenges." In *Remote Sensing of Water Resources, Disasters, and Urban Studies*, edited by P. S. Thenkabail, 191–220. Boca Raton: CRC Press (Remote sensing handbook).

Morandeira, N., F. Grings, C. Facchinetti, and P. Kandus. 2016. "Mapping Plant Functional Types in Floodplain Wetlands. An Analysis of C-Band Polarimetric SAR Data from RADARSAT-2." *Remote Sensing* 8 (3): 174. doi:10.3390/rs8030174.

Moser, L., A. Schmitt, A. Wendleder, and A. Roth. 2016. "Monitoring of the Lac Bam Wetland Extent Using Dual-Polarized X-Band SAR Data." *Remote Sensing* 8 (4): 302. doi:10.3390/rs8040302.

Mougin, E., C. Proisy, G. Marty, F. Fromard, H. Puig, J. L. Betoulle, and J. P. Rudant. 1999. "Multifrequency and Multipolarization Radar Backscattering from Mangrove Forests." *IEEE Transactions Geoscience Remote Sensing* 37 (1): 94–102. doi:10.1109/36.739128.

Mwita, E., G. Menz, S. Misana, and P. Nienkemper. 2012. "Detection of Small Wetlands with Multi Sensor Data in East Africa." *ARS* 01 (03): 64–73. doi:10.4236/ars.2012.13007.

Na, X., S. Zang, L. Liu, and M. Li. 2013. "Wetland Mapping in the Zhalong National Natural Reserve, China, Using Optical and Radar Imagery and Topographical Data." *Journal Applications Remote Sens* 7 (1): 73554. doi:10.1117/1.JRS.7.073554.

Na, X. D., S. Y. Zang, C. S. Wu, and W. L. Li. 2015. "Mapping Forested Wetlands in the Great Zhan River Basin through Integrating Optical, Radar, and Topographical Data Classification Techniques." *Environmental Monitoring and Assessment* 187 (11): 696. doi:10.1007/s10661-015-4914-7.

Nord, M. E., T. L. Ainsworth, J.-S. Lee, and N. J. S. Stacy. 2009. "Comparison of Compact Polarimetric Synthetic Aperture Radar Modes." *IEEE Transactions Geoscience Remote Sensing* 47 (1): 174–188. doi:10.1109/TGRS.2008.2000925.

Oliver-Cabrera, T., and S. Wdowinski. 2016. "InSAR-Based Mapping of Tidal Inundation Extent and Amplitude in Louisiana Coastal Wetlands." *Remote Sensing* 8 (5): 393. doi:10.3390/rs8050393.

Otsu, N. 1979. "A Threshold Selection Method from Gray-Level Histograms." *IEEE Transactions on Systems, Man, and Cybernetics* 9: 62–66. doi:10.1109/TSMC.1979.4310076.

Park, H.-S., and C.-H. Jun. 2009. "A Simple and Fast Algorithm for K-Medoids Clustering." *Expert Systems with Applications* 36 (2): 3336–3341. doi:10.1016/j.eswa.2008.01.039.

Patel, P., H. Srivastava, and R. Navalgund. 2009. "Use of Synthetic Aperture Radar Polarimetry to Characterize Wetland Targets of Keoladeo National Park, Bharatpur, India." *Current Science* 97 (4): 529–537.

Pierdicca, N., L. Pulvirenti, M. Chini, L. Guerriero, and L. Candela. 2013. "Observing Floods from Space: Experience Gained from COSMO-SkyMed Observations." *Acta Astronautica* 84: 122–133. doi:10.1016/j.actaastro.2012.10.034.

Pierdicca, N., M. Chini, L. Pulvirenti, and F. Macina. 2008. "Integrating Physical and Topographic Information into a Fuzzy Scheme to Map Flooded Area by SAR." *Sensors* 8 (7): 4151–4164. doi:10.3390/s8074151.

Pistolesi, L. I., W. Ni-Meister, and K. C. McDonald. 2015. "Mapping Wetlands in the Hudson Highlands Ecoregion with ALOS PALSAR. An Effort to Identify Potential Swamp Forest Habitat for Golden-Winged Warblers." *Wetlands Ecology Manage* 23 (1): 95–112. doi:10.1007/s11273-014-9381-3.

Podest, E., and S. Saatchi. 2002. "Application of Multiscale Texture in Classifying JERS-1 Radar Data over Tropical Vegetation." *International Journal of Remote Sensing* 23 (7): 1487–1506. doi:10.1080/01431160110093000.

Pope, K. O., E. Rejmankova, and J. F. Paris. 2001. "Spaceborne Imaging radar-C (SIR-C) Observations of Groundwater Discharge and Wetlands Associated with the Chicxulub Impact Crater, Northwestern Yucatan Peninsula, Mexico." *Geological Society of America Bulletin* 113 (3): 403–416. doi:10.1130/0016-7606(2001)113<0403:SIRCSC>2.0.CO;2.

Pope, K. O., E. Rejmankova, J. F. Paris, and R. Woodruff. 1997. "Detecting Seasonal Flooding Cycles in Marshes of the Yucatan Peninsula with SIR-C Polarimetric Radar Imagery." *Remote Sensing of Environment* 59 (2): 157–166. doi:10.1016/S0034-4257(96)00151-4.

Pope, K. O., J. M. Rey-Benayas, and J. F. Paris. 1994. "Radar Remote Sensing of Forest and Wetland Ecosystems in the Central American Tropics." *Remote Sensing of Environment* 48 (2): 205–219. doi: 10.1016/0034-4257(94)90142-2.

Pulvirenti, L., M. Chini, N. Pierdicca, and G. Boni. 2016. "Use of SAR Data for Detecting Floodwater in Urban and Agricultural Areas: The Role of the Interferometric Coherence." *IEEE Transactions Geoscience Remote Sensing* 54 (3): 1532–1544. doi:10.1109/TGRS.2015.2482001.

Pulvirenti, L., M. Chini, N. Pierdicca, L. Guerriero, and P. Ferrazzoli. 2011a. "Flood Monitoring Using Multi-Temporal COSMO-SkyMed Data. Image Segmentation and Signature Interpretation." *Remote Sensing of Environment* 115 (4): 990–1002. doi:10.1016/j.rse.2010.12.002.

Pulvirenti, L., N. Pierdicca, and M. Chini. 2010. "Analysis of Cosmo-SkyMed Observations of the 2008 Flood in Myanmar." *ItJRS* 79–90. doi:10.5721/ItJRS20104217.

Pulvirenti, L., N. Pierdicca, M. Chini, and L. Guerriero. 2011b. "An Algorithm for Operational Flood Mapping from Synthetic Aperture Radar (SAR) Data Using Fuzzy Logic." *Natural Hazards Earth Systems Sciences* 11 (2): 529–540. doi:10.5194/nhess-11-529-2011.

Pulvirenti, L., N. Pierdicca, M. Chini, and L. Guerriero. 2013. "Monitoring Flood Evolution in Vegetated Areas Using COSMO-SkyMed Data: The Tuscany 2009 Case Study." *IEEE Journal Sel Topics Applications Earth Observations Remote Sensing* 6 (4): 1807–1816. doi:10.1109/JSTARS.2012.2219509.

Quegan, S., and J. Yu. 2001. "Filtering of Multichannel SAR Images." *IEEE Transactions Geoscience Remote Sensing* 39 (11): 2373–2379. doi:10.1109/36.964973.

Rebelo, L.-M., G. B. Senay, and M. P. McCartney. 2012. "Flood Pulsing in the Sudd Wetland: Analysis of Seasonal Variations in Inundation and Evaporation in South Sudan." *Earth Interact* 16 (1): 1–19. doi:10.1175/2011EI382.1.

Richards, J. A. 2012. *Remote Sensing Digital Image Analysis. An Introduction*. 5th ed. Berlin, New York: Springer.

Richards, J. A., P. W. Woodgate, and A. K. Skidmore. 1987. "An Explanation of Enhanced Radar Backscattering from Flooded Forests." *International Journal of Remote Sensing* 8 (7): 1093–1100. doi:10.1080/01431168708954756.

Rignot, E. J. M., and J. J. van Zyl. 1993. "Change Detection Techniques for ERS-1 SAR Data." *IEEE Transactions Geoscience Remote Sensing* 31 (4): 896–906. doi:10.1109/36.239913.

Robertson, L. D., D. J. King, and C. Davies. 2015. "Object-Based Image Analysis of Optical and Radar Variables for Wetland Evaluation." *International Journal of Remote Sensing* 36 (23): 5811–5841. doi:10.1080/01431161.2015.1109727.

Rodrigues, S. W. P., and P. W. M. Souza-Filho. 2011. "Use of Multi-Sensor Data to Identify and Map Tropical Coastal Wetlands in the Amazon of Northern Brazil." *Wetlands* 31 (1): 11–23. doi:10.1007/s13157-010-0135-6.

Rosenqvist, A., C. M. Finlayson, J. Lowry, and D. Taylor. 2007. "The Potential of Long-Wavelength Satellite-Borne Radar to Support Implementation of the Ramsar Wetlands Convention." *Aquatic Conservatin: Marine. Freshwater Ecosystem* 17 (3): 229–244. doi:10.1002/aqc.835.

Sang, H., J. Zhang, H. Lin, and L. Zhai. 2014. "Multi-Polarization ASAR Backscattering from Herbaceous Wetlands in Poyang Lake Region, China." *Remote Sensing* 6 (5): 4621–4646. doi:10.3390/rs6054621.

Schlaffer, S., M. Chini, D. Dettmering, and W. Wagner. 2016. "Mapping Wetlands in Zambia Using Seasonal Backscatter Signatures Derived from ENVISAT ASAR Time Series." *Remote Sensing* 8: 5. doi:10.3390/rs8050402.

Schmitt, A., A. Wendleder, and S. Hinz. 2015. "The Kennaugh Element Framework for Multi-Scale, Multi-Polarized, Multi-Temporal and Multi-Frequency SAR Image Preparation." *ISPRS Journal of Photogrammetry and Remote Sensing* 102: 122–139. doi:10.1016/j.isprsjprs.2015.01.007.

Schmitt, A., and B. Brisco. 2013. "Wetland Monitoring Using the Curvelet-Based Change Detection Method on Polarimetric SAR Imagery." *Water* 5 (3): 1036–1051. doi:10.3390/w5031036.

Schmitt, A., B. Wessel, and A. Roth. 2010. "Curvelet-Based Change Detection on SAR Images for Natural Disaster Mapping." *Photogrammetrie-Fernerkundung-Geoinformation* 2010 (6): 463–474. doi:10.1127/1432-8364/2010/0068.

Schmitt, A., T. Leichtle, M. Huber, and A. Roth. 2012. "On the Use of Dual-Co-Polarized TerraSAR-X Data for Wetland Monitoring." *International Archives Photogramm Remote Sens Spatial Information Sciences* XXXIX-B7: 341–344. doi:10.5194/isprsarchives-XXXIX-B7-341-2012.

Schmullius, C. C., and D. L. Evans. 1997. "Review Article Synthetic Aperture Radar (SAR) Frequency and Polarization Requirements for Applications in Ecology, Geology, Hydrology, and Oceanography: A Tabular Status Quo after SIR-C/X-SAR." *International Journal of Remote Sensing* 18 (13): 2713–2722. doi:10.1080/014311697217297.

Schumann, G., G. Di Baldassarre, and P. D. Bates. 2009. "The Utility of Spaceborne Radar to Render Flood Inundation Maps Based on Multialgorithm Ensembles." *IEEE Transactions Geoscience Remote Sensing* 47 (8): 2801–2807. doi:10.1109/TGRS.2009.2017937.

Schumann, G. J.-P., and D. K. Moller. 2015. "Microwave Remote Sensing of Flood Inundation." *Physics and Chemistry of the Earth, Parts A/B/C* 83-84: 84–95. doi:10.1016/j.pce.2015.05.002.

Silva, T. S., F. Costa, P. F. Maycira, J. M. Melack, and E. M. L. M. Novo. 2008. "Remote Sensing of Aquatic Vegetation: Theory and Applications." *Environmental Monitoring and Assessment* 140 (1–3): 131–145. doi:10.1007/s10661-007-9855-3.

Simard, M., G. de Grandi, S. Saatchi, and P. Mayaux. 2002. "Mapping Tropical Coastal Vegetation Using JERS-1 and ERS-1 Radar Data with a Decision Tree Classifier." *International Journal of Remote Sensing* 23 (7): 1461–1474. doi:10.1080/01431160110092984.

Simard, M., S. S. Saatchi, and G. de Grandi. 2000. "The Use of Decision Tree and Multiscale Texture for Classification of JERS-1 SAR Data over Tropical Forest." *IEEE Transactions Geoscience Remote Sensing* 38 (5): 2310–2321. doi:10.1109/36.868888.

Souza-Filho, P. W. M., W. R. Paradella, S. W. P. Rodrigues, F. R. Costa, J. C. Mura, and F. D. Gonçalves. 2011. "Discrimination of Coastal Wetland Environments in the Amazon Region Based on Multi-Polarized L-Band Airborne Synthetic Aperture Radar Imagery." *Estuarine, Coastal and Shelf Science* 95 (1): 88–98. doi:10.1016/j.ecss.2011.08.011.

Touzi, R., A. Deschamps, and G. Rother. 2007. "Wetland Characterization Using Polarimetric RADARSAT-2 Capability." *Canadian Journal of Remote Sensing* 33: S56–S67. doi:10.5589/m07-047.

Touzi, R., A. Deschamps, and G. Rother. 2009. "Phase of Target Scattering for Wetland Characterization Using Polarimetric C-Band SAR." *IEEE Transactions Geoscience Remote Sensing* 47 (9): 3241–3261. doi:10.1109/TGRS.2009.2018626.

Townsend, P. A. 2001. "Mapping Seasonal Flooding in Forested Wetlands Using Multi-Temporal Radarsat SAR." *Photogrammetric Engineering & Remmote Sensing* 67 (7): 857–864.

Townsend, P. A. 2002. "Relationships between Forest Structure and the Detection of Flood Inundation in Forested Wetlands Using C-Band SAR." *International Journal of Remote Sensing* 23 (3): 443–460. doi:10.1080/01431160010014738.

Töyrä, J., A. Pietroniro, and L. W. Martz. 2001. "Multisensor Hydrologic Assessment of a Freshwater Wetland." *Remote Sensing of Environment* 75 (2): 162–173. doi:10.1016/S0034-4257(00)00164-4.

Töyrä, J., A. Pietroniro, L. W. Martz, and T. D. Prowse. 2002. "A Multi-Sensor Approach to Wetland Flood Monitoring." *Hydrology Processing* 16 (8): 1569–1581. doi:10.1002/hyp.1021.

Trujillo, M. 2015. "The impact of disasters on agriculture and food security." Rome, Italy: Food and Agriculture Organization of the United Nations

Ulaby, F. T., A. K. Fung, and R. K. Moore. 1986. *Microwave Remote Sensing: Active and Passiv. Volume II: Radar Remote Sensing and Surface Scattering and Emission Theory*. Norwood, MA: Artech House (Remote sensing).

Ulaby, F. T., and M. C. Dobson. 1989. *Handbook of Radar Scattering Statistics for Terrain*. Norwood, MA: Artech House (The Artech House remote sensing library).

Voormansik, K., J. Praks, O. Antropov, J. Jagomagi, and K. Zalite. 2014. "Flood Mapping with TerraSAR-X in Forested Regions in Estonia." *IEEE Journal Sel Topics Applications Earth Observations Remote Sensing* 7 (2): 562–577. doi:10.1109/JSTARS.2013.2283340.

Wang, J., J. Shang, B. Brisco, and R. J. Brown. 1998. "Evaluation of Multidate ERS-1 and Multispectral Landsat Imagery for Wetland Detection in Southern Ontario." *Canadian Journal of Remote Sensing* 24 (1): 60–68. doi:10.1080/07038992.1998.10874692.

Wang, Y. 2002. "Mapping Extent of Floods. What We Have Learned and How We Can Do Better." *Natural Hazards Reviews* 3 (2): 68–73. doi:10.1061/(ASCE)1527-6988(2002)3:2(68).

Wang, Y. 2004. "Seasonal Change in the Extent of Inundation on Floodplains Detected by JERS-1 Synthetic Aperture Radar Data." *International Journal of Remote Sensing* 25 (13): 2497–2508. doi:10.1080/01431160310001619562.

Wang, Y., and F. W. Davis. 1997. "Decomposition of Polarimetric Synthetic Aperture Radar Backscatter from Upland and Flooded Forests." *International Journal of Remote Sensing* 18 (6): 1319–1332. doi:10.1080/014311697218449.

Wang, Y., L. L. Hess, S. Filoso, and J. M. Melack. 1995. "Understanding the Radar Backscattering from Flooded and Nonflooded Amazonian Forests. Results from Canopy Backscatter Modeling." *Remote Sensing of Environment* 54 (3): 324–332. doi:10.1016/0034-4257(95)00140-9.

Ward, D. P., A. Petty, S. A. Setterfield, M. M. Douglas, K. Ferdinands, S. K. Hamilton, and S. Phinn. 2014. "Floodplain Inundation and Vegetation Dynamics in the Alligator Rivers Region (Kakadu) of Northern Australia Assessed Using Optical and Radar Remote Sensing." *Remote Sensing of Environment* 147: 43–55. doi:10.1016/j.rse.2014.02.009.

Wdowinski, S., W. Kim, F. Amelung, and T. Dixon. 2006. *Wetland InSAR: A New Space-Based Hydrological Monitoring Tool of Wetlands Surface Water Level Changes*, SP–634. Frescati, Italy: European Space Agency, (Special Publication) ESA SP.

Westra, T. 2010. "Optimal Envisat Advanced Synthetic Aperture Radar Image Parameters for Mapping and Monitoring Sahelian Floodplains." *Journal Applications Remote Sens* 4 (1): 43511. doi:10.1117/1.3368722.

Whitcomb, J., M. Moghaddam, K. McDonald, J. Kellndorfer, and E. Podest. 2009. "Mapping Vegetated Wetlands of Alaska Using L-Band Radar Satellite Imagery." *Canadian Journal of Remote Sensing* 35 (1): 54–72. doi:10.5589/m08-080.

White, L., B. Brisco, M. Dabboor, A. Schmitt, and A. Pratt. 2015. "A Collection of SAR Methodologies for Monitoring Wetlands." *Remote Sensing* 7 (6): 7615–7645. doi:10.3390/rs70607615.

White, L., B. Brisco, M. Pregitzer, B. Tedford, and L. Boychuk. 2014. "RADARSAT-2 Beam Mode Selection for Surface Water and Flooded Vegetation Mapping." *Canadian Journal of Remote Sensing* 40: 135–151.

Xie, C., Y. Shao, X. Ji, Z. Wan, and L. Fang. 2013. "Analysis of ALOS PALSAR InSAR Data for Mapping Water Level Changes in Yellow River Delta Wetlands." *International Journal of Remote Sensing* 34 (6): 2047–2056. doi:10.1080/01431161.2012.731541.

Yu, Y., and S. Saatchi. 2016. "Sensitivity of L-Band SAR Backscatter to Aboveground Biomass of Global Forests." *Remote Sensing* 8 (6): 522. doi:10.3390/rs8060522.

Zhang, M., L. Zhen, B. Tian, J. Zhou, and P. Tang. 2016. "The Backscattering Characteristics of Wetland Vegetation and Water-Level Changes Detection Using Multi-Mode SAR. A Case Study." *International Journal of Applied Earth Observation and Geoinformation* 45: 1–13. doi:10.1016/j.jag.2015.10.001.

Zhang, M., Z. Li, B. Tian, J. Zhou, and J. Zeng. 2015. "A Method for Monitoring Hydrological Conditions beneath Herbaceous Wetlands Using Multi-Temporal ALOS PALSAR Coherence Data." *International Archives Photogramm Remote Sensing Spatial Information Sciences* XL-7/W4: 221–226. doi:10.5194/isprsarchives-XL-7-W4-221-2015.

Zhao, L., J. Yang, L. Pingxiang, and L. Zhang. 2014. "Seasonal Inundation Monitoring and Vegetation Pattern Mapping of the Erguna Floodplain by Means of a RADARSAT-2 Fully Polarimetric Time Series." *Remote Sensing of Environment* 152: 426–440. doi:10.1016/j.rse.2014.06.026.

Appendix 1.

1	Allen, Wang, and Gore (2013)	31	Cremon, Rossetti, Dilce, and Zani (2014)
2	Alsdorf et al. (2000)	32	Dabboor et al. (2015)
3	Alsdorf, Smith, and Melack (2001)	33	De Grandi et al. (2000)
4	Arnesen et al. (2013)	34	Dwivedi, Rao, and Bhattacharya (1999)
5	Augusteijn and Warrender (1998)	35	Evans et al. (2010)
6	Aziz and White (2003)	36	Evans and Costa (2013)
7	Baghdadi et al. (2001)	37	Evans et al. (2014)
8	Betbeder et al. (2014)	38	Ferreira-Ferreira et al. (2015)
9	Betbeder et al. (2015)	39	Frappart et al. (2005)
10	Bian et al. (2016)	40	Furtado, Silva, and Novo (2016)
11	Bourgeau-Chavez, Kasischke, and Smith (1997)	41	Gallant et al. (2014)
12	Bourgeau-Chavez et al. (2001)	42	Grenier et al. (2007)
13	Bourgeau-Chavez et al. (2009)	43	Grings et al. (2006)
14	Bourgeau-Chavez et al. (2016)	44	Grings et al. (2008)
15	(Bouvet and Le Toan 2011)	45	Heine, Jagdhuber, and Itzerott (2016)
16	Brisco et al. (2008)	46	Hess et al. (1995)
17	Brisco et al. (2011)	47	Hess and Melack (2003)
18	Brisco et al. (2013a)	48	Hess et al. (2003)
19	Brisco et al. (2013b)	49	Hess et al. (2015)
20	Brown, Mwansasu, and Westerberg (2016)	50	Hidayat et al. (2012)
21	Bwangoy et al. (2010)	51	Horritt (2003)
22	Cazals et al. (2016)	52	Imhoff et al. (1986)
23	Chapman et al. (2015)	53	Kandus et al. (2001)
24	Chen et al. (2014)	54	Karszenbaum et al. (2000)
25	Corcoran et al. (2012)	55	Kasischke and Bourgeau-Chavez (1997)
26	Cordeiro and Rossetti (2015)	56	Kasischke et al. (2003)
27	Costa et al. (1997)	57	Kiage et al. (2005)
28	Costa et al. (2002)	58	Kwoun and Lu (2009)
29	Costa (2004)	59	Lang and Kasischke (2008)
30	Costa and Telmer (2006)	60	Lang et al. (2008)

61	Lee et al. (2015)
62	Le Toan et al. (1997)
63	Li and Chen (2005)
64	Long, Fatoyinbo, and Policelli (2014)
65	Lu and Kwoun (2008)
66	Maillard, Alencar-Silva, and Clausi (2008)
67	Marti-Cardona et al. (2010)
68	Marti-CardoMarti-Cardona, Dolz-Ripolles, and Lopez-Martinez (2013)
69	Martinez and Le Toan (2007)
70	Martinis and Twele (2010)
71	Martinis and Rieke (2015)
72	Mayaux et al. (2002)
73	Melack and Wang (1998)
74	Miranda, Fonseca, and Carr (1998)
75	Morandeira et al. (2016)
76	Moser et al. (2016)
77	Mougin et al. (1999)
78	Mwita et al. (2012)
79	Na et al. (2013)
80	Na et al. (2015)
81	Oliver-Cabrera and Wdowinski (2016)
82	Patel, Srivastava, and Navalgund (2009)
83	Pierdicca et al. (2008)
84	Pierdicca et al. (2013)
85	Pistolesi, Ni-Meister, and McDonald (2015)
86	Podest and Saatchi (2002)
87	Pope, Rey-Benayas, and Paris (1994)
88	Pope et al. (1997)
89	Pope, Rejmankova, and Paris (2001)
90	Pulvirenti, Pierdicca, and Chini (2010)

(*Continued*)

(Continued).

91	Pulvirenti et al. (2011a)	110	Townsend (2002)
92	Pulvirenti et al. (2011b)	111	Töyra et al. (2001)
93	Pulvirenti et al. (2013)	112	Töyra et al. (2002)
94	Pulvirenti et al. (2016)	113	Voormansik et al. (2014)
95	Rebelo, Senay, and McCartney (2012)	114	Wang et al. (1995)
96	Richards et al. (1987)	115	Wang and Davis (1997)
97	Robertson, King, and Davies (2015)	116	Wang et al. (1998)
98	Rodrigues and Souza-Filho (2011)	117	Wang (2002)
99	Rosenqvist et al. (2007)	118	Wang (2004)
100	Sang et al. (2014)	119	Ward et al. (2014)
101	Schlaffer et al. (2016)	120	Wdowinski et al. (2006)
102	Schmitt, Wessel, and Roth (2010)	121	Westra (2010)
103	Schmitt and Brisco (2013)	122	Whitcomb et al. (2009)
104	Simard, Saatchi, and De Grandi (2000)	123	White et al. (2014)
105	Simard et al. (2002)	124	Xie et al. (2013)
106	Souza-Filho et al. (2011)	125	Yu and Saatchi (2016)
107	Touzi, Deschamps, and Rother (2007)	126	Zhang et al. (2015)
108	Touzi, Deschamps, and Rother (2009)	127	Zhang et al. (2016)
109	Townsend (2001)	128	Zhao et al. (2014)

List of studies (128 articles) analysed in this review.
The IDs in Appendix 1 do not correspond to the study IDs in Table 2.

4.2 Paper II: Detection of Temporary Flooded Vegetation using Sentinel-1 Time Series Data

Tsyganskaya, V., Martinis S., Marzahn P., and Ludwig. R. 2018. 'Detection of Temporary Flooded Vegetation Using Sentinel-1 Time Series Data. Remote Sens'. Volume 8, pp. 1286

As a consequence of the high variability and low availability of the data sets and the resulting large range of different approaches for the derivation of TFV in Paper I, a novel method using globally and frequently available data sets of S-1 was developed. Paper II presents SAR time series approach based on S-1 C-band data, which integrates dual-polarized time series data and an ancillary information for the enhanced detection of the entire flood extent with the focus on TFV. The analysis of C-band time series data showed that certain multitemporal characteristics and patterns (increase and decrease during the flood period) are indicative for flood related classes, such as open water and TFV. Based on these findings, time series features were determined using VV, VH and their combinations. To ensure the comparability of the backscatter values of the vegetation for each image element and thus the independency of the different phenological development, a normalisation of backscatter values by Z-transform over the time series was implemented. The developed approach was used to map a flood event that occurred in spring 2017 in Namibia containing flooded high grass land as a temporary flooded vegetation area. Results indicate reliable classification and demonstrate that the inclusion of TFV enhance the extraction of flood extent.

Author's contributions: All authors contributed to the concept of the study, while all programming work, calculations, analysis, results generation, validation and interpretation of the results were performed by V. Tsyganskaya. In addition, V. Tsyganskaya prepared the first version of the manuscript. S. Martinis, P. Marzahn, and R. Ludwig commented on last version of the manuscript.
Status: published
Journal: Remote Sensing (MDPI)

Detection of Temporary Flooded Vegetation Using Sentinel-1 Time Series Data

Viktoriya Tsyganskaya [1,2,*], Sandro Martinis [2], Philip Marzahn [1] and Ralf Ludwig [1]

[1] Department of Geography, Ludwig Maximilian University of Munich, Luisenstr. 37, Munich 80333, Germany; p.marzahn@iggf.geo.uni-muenchen.de (P.M.); r.ludwig@lmu.de (R.L.)

[2] German Aerospace Center (DLR), German Remote Sensing Data Center (DFD), Oberpfaffenhofen, 82234 Wessling, Germany; Sandro.Martinis@dlr.de

[*] Correspondence: tsyganskaya.viktoriya@gmx.de; Tel.: +49-176-2221-3000

Abstract: The C-band Sentinel-1 satellite constellation enables the continuous monitoring of the Earth's surface within short revisit times. Thus, it provides Synthetic Aperture Radar (SAR) time series data that can be used to detect changes over time regardless of daylight or weather conditions. Within this study, a time series classification approach is developed for the extraction of the flood extent with a focus on temporary flooded vegetation (TFV). This method is based on Sentinel-1 data, as well as auxiliary land cover information, and combines a pixel-based and an object-oriented approach. Multi-temporal characteristics and patterns are applied to generate novel times series features, which represent a basis for the developed approach. The method is tested on a study area in Namibia characterized by a large flood event in April 2017. Sentinel-1 times series were used for the period between September 2016 and July 2017. It is shown that the supplement of TFV areas to the temporary open water areas prevents the underestimation of the flood area, allowing the derivation of the entire flood extent. Furthermore, a quantitative evaluation of the generated flood mask was carried out using optical Sentinel-2 images, whereby it was shown that overall accuracy increased by 27% after the inclusion of the TFV.

Keywords: temporary flooded vegetation (TFV); SAR; Sentinel-1; time series data; classification; flood mapping

1. Introduction

Flooding affects societies, economies, and ecosystems worldwide and can have a devastating impacts. For the development of flood risk mitigation plans or disaster relief services, information about the flood extent in affected regions is an important information source for many institutions involved in crisis management, such as relief organizations, governmental authorities, and insurance companies [1,2].

Numerous current studies focus on flood mapping using various algorithms that enable the detection of temporary open water [3–5]. Besides these areas, the extraction of temporary flooded vegetation (TFV) areas is essential for mapping the entire flood extent. TFV can be described as areas where water bodies occur temporarily underneath vegetation [6]. The disregard of these areas can lead to an underestimation of the whole flood extent. Ground-based observations or aerial vehicles are not always sufficient for the mapping of large-scale floods due to weather conditions, technical limitations, or high risks. Satellite remote sensing data, especially Synthetic Aperture Radar (SAR), allows one to overcome these challenges and covers an extensive area of the Earth's surface for a near-real time detection of large-scale flood events independent of daylight and weather conditions [7,8] and is suitable for the detection of water underneath the vegetation areas.

Smooth open water surfaces act as specular reflectors and are therefore characterized by low SAR backscatter values. These areas can be well differentiated from non-water regions showing higher backscatter values. In comparison, TFV shows highly complex backscatter behaviour, due to double- or multi-bounce interactions between the smooth open water surfaces and the vertical structures of the vegetation, such as trunks or stems. During the presence of water underneath vegetated areas, the SAR backscatter intensity values can significantly increase [9–11].

SAR-based techniques for the detection of TFV include simple approaches like manual thresholding [12,13] or automatic thresholding [11,14,15], distance-based classification methods [16,17], clustering algorithms [18,19], decision tree [7,20], or rule-based classification [21,22]. Furthermore, more advanced approaches based on machine learning [23–25], fuzzy logic [11,26], Markov Random Field modelling [14], or wishart classifications [27–29] are applied in dependency on the task, the availability of polarization modes, and phase information, as well as spatial or temporal resolution [6].

For the extraction of TFV, most of the approaches focus on a single-image, which represents only a snapshot of a current flood situation [12,30,31]. Other classification approaches use change detection techniques for the extraction of TFV, which allow one to detect potential changes in backscatter intensities [25,26,32–35]. Thereby, the selection of the scenes acquired under dry and flood conditions highly influences the classification results. Furthermore, the increase of backscatter intensities, which is induced by TFV, may not clearly be separable from backscatter intensities from dry vegetation depending on its phenological stage [36]. Time series approaches can be more appropriate for the extraction of flood related classes by allowing the inclusion of seasonal or annual fluctuations of the backscatter. Furthermore, as a consequence of multiple observations of the same area, multi-temporal data can enable an improvement of the reliability for mapping TFV areas. The shape of multi-temporal radar backscatter profiles can be used to derive multi-temporal features enabling a more detailed extraction of flood-related classes [6,7]. Only few studies address the detection of TFV based on multi-temporal satellite imagery, which either depends on the chronological order and regularity of satellite images [19,37] or the use of a limited amount of SAR time steps [11,34]. Furthermore, the application of multi-temporal approaches is limited due to the low availability of respective SAR data in the past. SAR systematic and long-term data acquisition within short revisit times by satellite missions such as Sentinel-1 finally enables the usage of multi-temporal data.

Although the pixel-based approach is the most commonly used method for the extraction of TFV [6], object-based approaches are emerging as an effective method for complex image classification [18,30,38,39]. On the one hand side, the objects are suitable to map heterogeneous classes, such as TFV, if the spatial resolution of the SAR data is higher than the objects on the ground [6]. On the other hand, the grouping of pixels to objects with similar backscatter values in SAR images allows one to reduce speckle noise [10,40]. Furthermore, objects enable the consideration of semantic or spatial contextual relationships, which helps to cope with heterogeneous feature such as TFV [6,11]. Several segmentation techniques, which group pixels into meaningful or perceptual regions (objects) for the extraction of TFV, can be found in the literature, including multiresolution segmentation [24,41], Mallat's discrete wavelet transform [42], Markov Random Fields [14,43], and clustering approaches [10,11]. The combination of segmentation techniques with SAR time-series data can be used to discover multi-temporal characteristics and patterns, allowing for the extraction of useful information from enormous and complex data sets [44] and empowering the derivation of time series features with the advantages of an object-based approach.

In contrast to methods for the extraction of open water surfaces for flood detection [4,45,46], there is little research for the detection of the entire flood extent comprising TFV besides open water areas [11,25,29]. An example for automatic flood detection of open water in near-real time (NRT) by Sentinel-1 data is given by Twele et al. [47]. In the framework of the Center for Satellite Based Crisis Information (ZKI) located at the German Aerospace Center (DLR), this method is designed to provide a fully automatic web-based Sentinel-1 Flood Service (S-1FS) for rapid provision of open flood extent information for humanitarian relief activities and civil security issues worldwide [48,49]. This S-1FS is

aimed to be extended and improved by the addition of TFV areas, which are derived by the developed time series approach within this paper.

This article introduces a time series approach for the derivation of an entire flood extent with a focus on the extraction of temporary open water (TOW) and temporary flooded vegetation (TFV) using multi-temporal S-1 imagery. The objectives of this work are:

1. To investigate the characteristics and patterns of SAR time series data and to show their potential regarding the detection of TOW and TFV;
2. To derive time series features, which are used as a basis for a time series approach focusing on the detection of TOW and TFV;
3. To classify the entire flood extent, including TOW and TFV in the analysed study area;
4. To improve the results of external approach DLR's S-1FS [47] by supplementing temporary open water by TFV areas.

2. Materials

2.1. Study Area

The study area is located in the Caprivi Strip in the north-eastern part of Namibia, bordered by the countries Zambia, Zimbabwe, and Botswana (Figure 1). The focus is on the Chobe-Sambesi flood plain, which is formed by the Zambezi and Chobe river and is influenced by seasonal floods in March and April [33,50]. Large areas of high grasslands dominate the landscape [51]. During flooding, the area is therefore characterized not only by TOW areas but also by extensive TFV areas. The extent of the study area is indicated by the red rectangle in Figure 1.
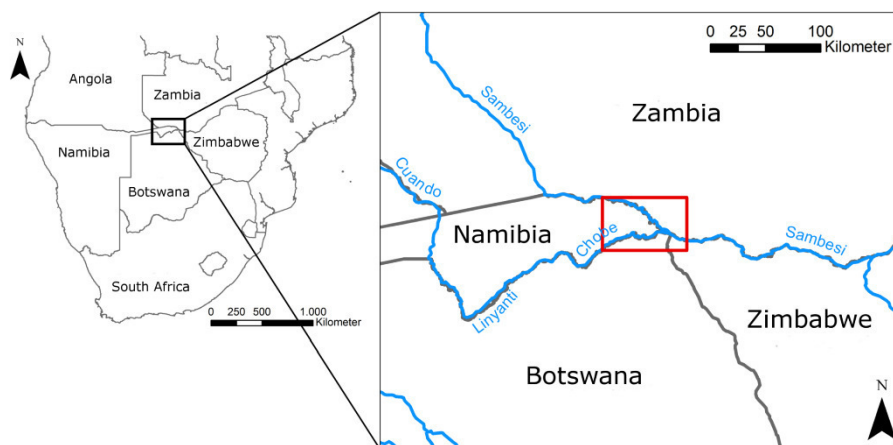

Figure 1. Location map of the study area (red rectangle) in Namibia.

2.2. Data Sets

A time series of 25 Sentinel-1 (S-1) B images with identical orbit configuration (same image geometry) was used to derive the flood-related classes. The Sentinel-1 mission consists of two satellites (Sentinel-1A/B) equipped by C-band (wavelengths [λ] = 5.6 cm) sensors that allow one to monitor the Earth's surface at a repeat frequency of six days. The characteristics of the used images and the acquisition dates are listed in Table 1. Only images with an interval of 12 days could be used for the study area in the analysed period, since only one sensor (Sentinel-1 B) provided both polarizations VV and VH of the Interferometric Wide Swath (IW) mode and was already processed by ESA as Ground Range Detected High Resolution (GRDH) products. The flood event was covered by three S-1 images, whereby the scene acquired on 6th of April 2017 was used as a flood image for further analysis and classification. This flood scene is chosen due to the temporal proximity of the reference

data. The validation of the developed approach was carried out on the basis of a 27 km^2 large extent in the study area. Figure 2b shows the validation extent of the preprocessed S-1 image at the flooding event (6 April 2017) for VV polarization. The generation of the reference data was carried out by visual interpretation and manual digitalisation of a high-resolution optical Sentinel-2 (S-2) image, which was recorded on 8 April 2017. When the backscatter image and optical data were compered, no changes in the flood extent could be observed within the span of two days. The digitised reference mask is shown in Figure 2b.

Table 1. Characteristics and acquisition dates of the used S-1 satellite data. S-1 scenes are acquired under the same orbit conditions. The scene acquired on 6 April 2017 was used within this study as flood event image.

Characteristics of the used Sentinel-1 Data		No.	Date	No.	Date
Wavelength	5.6 cm	1	2 September 2016	14	17 February 2017
Mode	Interferometric Wide Swath (IW)	2	26 September 2016	15	1 March 2017
Polarization	VV, VH	3	08 October 2016	16	13 March 2017
Frequency	C-Band (GHz)	4	20 October 2016	17	25 March 2017
Resolution	20 × 22 m (ground range and azimuth)	5	1 November 2016	18	6 April 2017
		6	13 November 2016	19	18 April 2017
Pixel spacing	10 × 10 m	7	25 November 2016	20	30 April 2017
Inc. angle	30.4°–46.2°	8	7 December 2016	21	12 May 2017
Pass direction	Ascending	9	19 December 2016	22	24 May 2017
Relative orbit	116	10	31 December 2016	23	5 June 2017
Product level	Level-1 (Ground Range Detected High Resolution (GRDH))	11	12 January 2017	24	29 June 2017
		12	24 January 2017	25	23 July 2017
		13	5 February 2017		

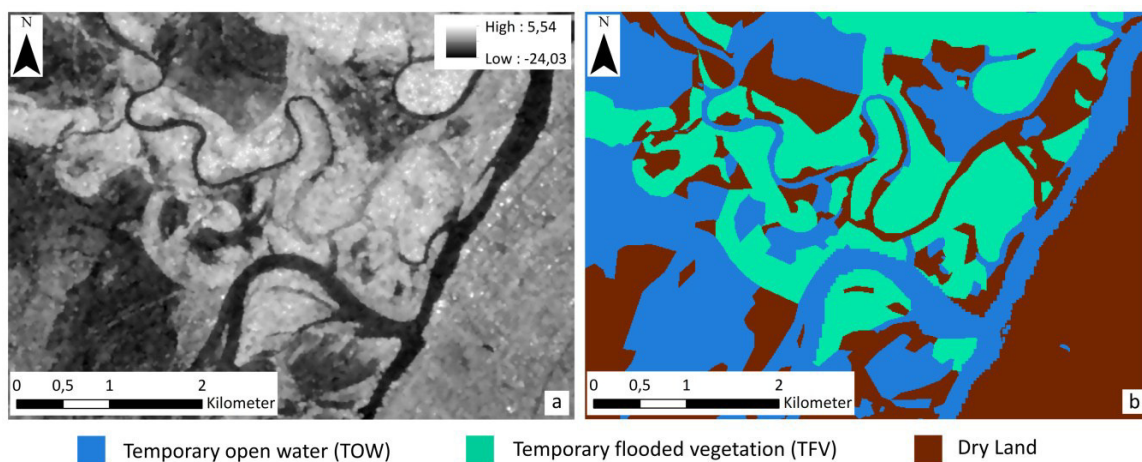Temporary open water (TOW) Temporary flooded vegetation (TFV) Dry Land

Figure 2. Validation extent of the preprocessed S-1 image at the flood event (6 April 2017) for VV polarization (**a**). Digitized validation mask based on S-2 data (8 April 2017) (**b**).

Urban areas and TFV are both characterized by strong double-bounce and multiple scattering effects. This makes their separation considerably more difficult. For the identification of urban areas, the Global Urban Footprint (GUF) was therefore used as additional information, which was derived on the basis of TerraSAR-X and TanDEM-X SAR data [52]. The spatial resolution of the GUF is 0.4 arcseconds (~12 m). Figure 3a shows the GUF for the study area. In the developed approach, the GUF layer is used as the exclusion layer. Since the focus of the study is on the derivation of TFV areas, urban areas are excluded from the analysis regarding flood and are not considered in the methodology.

All regions that lie below an elevation of 20 m above the nearest water network were defined as flood-prone in order to prevent misclassifications in elevated areas. For this purpose, the 'Height above

nearest drainage' (HAND) index [53] has been integrated as binary mask to exclude areas above the mentioned threshold of 20 m before classification [47]. The HAND index with about 90 m resolution is based on the height and flow direction information provided by the product "Hydrosheds" [54]. Figure 3b shows the HAND mask for the study area in Namibia.

The separation between permanent open water surfaces and TOW areas was done by the use of SRTM Water Body Data (SWBD), which was applied as a permanent water mask. This product was created by the National Geospatial Intelligence Agency (NGA) [55] on the basis of data from the Shuttle Radar Topography Mission (SRTM30), which took place in February 2000, and it is freely available as a vector data set. SWBD was chosen for its resolution and global availability of SRTM data. Figure 3c shows the SWBD mask for the study area.
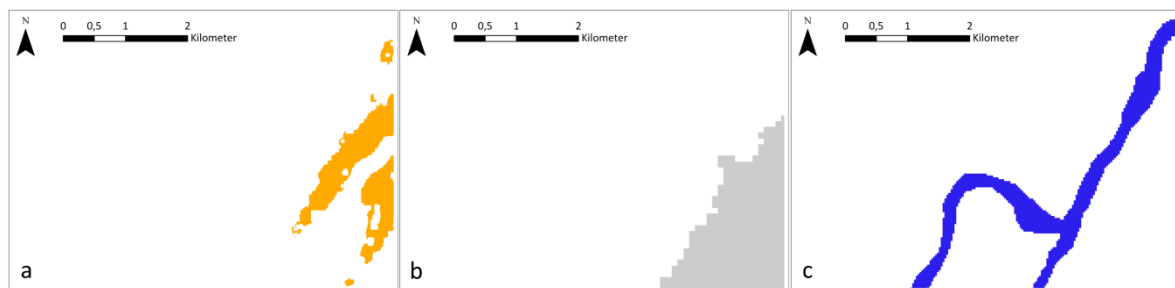
Figure 3. Additional information in the study area Namibia. Global Urban Footprint (GUF) (**a**), exclusion mask (threshold 20 m) of the height above nearest drainage (HAND) index (**b**), SRTM Water Body Data (SWBD) (**c**).

3. Methods

The process chain (Figure 4) of the time series approach for the derivation of the flood related classes consists of pixel- (deep orange arrow) and segment-based (bright orange arrows) parts. The pixel-based steps include the generation of time series features and their normalisation based on VV- and VH-polarisation layer stacks (see Section 3.2). Simultaneously, the object generation takes place using a clustering approach based on the combination of the VV and VH time series layer stacks (see Section 3.3). In the next step, normalised time series features are combined with the generated cluster image to produce cluster-based time series features. The features are the basis for a thresholding approach (see Section 3.4) that enables the derivation of TOW and TFV. It can be performed using pixel-based or object-based time series features, while the latter also requires the generation of pixel-based normalized time series features. The exclusion layers, including the GUF and the HAND index, allow one to mask out urban areas and to consider topographical information before the extraction of times series features and the generation of objects is performed. The preprocessing is not shown in Figure 4; however, it is essential for the creation of time series stacks. The implemented preprocessing steps are described in Section 3.1.
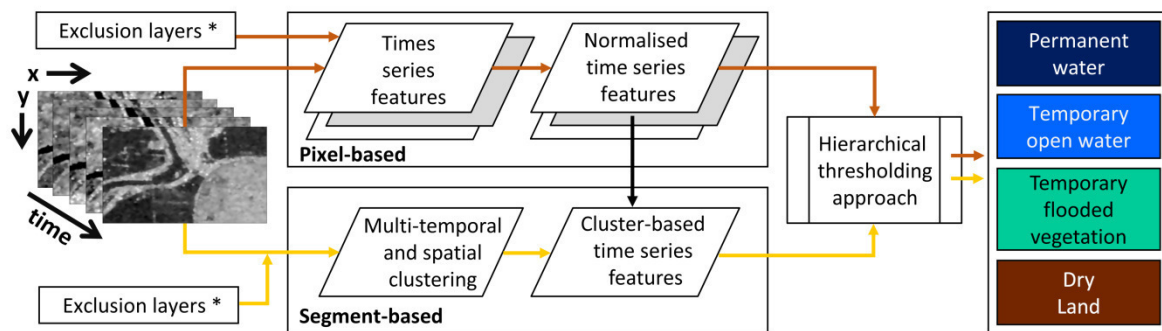
Figure 4. Classification process chain for the extraction of temporary open water and temporary flooded vegetation based on SAR time series data. The deep orange arrows represent the pixel-based process part, while bright orange arrows show the object-based part of the process chain. * Global Urban Footprint (GUF), Height above Nearest Drainage (HAND) index, and SRTM Water Body Data (SWBD) as exclusion layers.

3.1. Image Preprocessing

An automated preprocessing for all used S-1 images is performed in a Python script using SNAP Toolbox (version 4.0.0) [56] components. It includes the radiometric calibration to sigma naught, a range Doppler terrain correction by using the SRTM digital terrain model [57], the co-registration of the individual data, and speckle filtering. The coregistration of the images is necessary to perform an analysis based on time series data. It is essential that the images match in their position with pixel accuracy, otherwise the backscatter values over time could lead to a distorted picture of the desired classes. The spatial refined Lee filter with a window size of 7 × 7 were used to reduce the noise in the SAR data [58,59]. This filter allows the preservation of the structure in the image by filtering homogeneous surfaces and preserving edges, as well as flood-related temporal characteristics and patterns. These preprocessing steps were carried out for both polarizations VV and VH, resulting in two independent time series. The result is a multi-temporal layer stack for each polarization.

3.2. Derivation of Time Series Features

On the basis of the preprocessed SAR time series data, an analysis of the multi-temporal profiles was carried out to determine the characteristics and patterns of the flood-related classes (TOW and TFV) (see Section 4.1). Accordingly, the decrease and/or increase of the backscatter values in the SAR time series data at the analysed date of the flood event for each polarization and polarization ratio is essential information, which can be used to derive TOW and TFV. The extraction of flood-relevant time series characteristics is based on these multi-temporal characteristics and patterns.

The backscatter values are influenced by different environmental conditions, whereby the intensity of the backscatter decrease or increase can vary within the desired classes. Influencing conditions such as varying land-cover classes, wind, water depth, or heterogeneity of the different vegetation types and their phenological stages can cause these variations [18,60,61]. Therefore, it is not always possible to compare the increase or decrease of the absolute backscatter values over time. In order to ensure the comparability, absolute backscatter values at the analysed date of the flood event were normalized over the time series for each pixel. This is achieved by the Z-transform of backscatter values and has been implemented by the following formula:

$$Z = (x - \mu)/\sigma \tag{1}$$

Hereby, x corresponds to backscatter values for the analysed date at the flood event, μ represents the mean and σ the standard deviation of the backscatter values of a pixel over the time series. The transformed backscatter values allow spatial comparability of the data and are referred to

hereinafter as Z-Score images. Because of the normalized description of the decrease or increase of the backscatter values, and the Z-Score in connection with the respective polarizations, their ratio (VV/VH) and their combinations (VV + VH, VV-VH) represent the essential time series features for the derivation of TOW and TFV. Mean value, median, and the standard deviation over the time series are considered as auxiliary information for the calculation of the Z-Score or as additional information in the later classification.

A quantitative analysis of the time series features was carried out using the Random Forest (RF) method to investigate the potential of those to derive the TOW and TFV. Therefore, training data for two flood-related classes and a third class representing Dry Land areas were defined based on the reference data and analysed by RF. RF is an ensemble learning method based on the construction of a large number of decision trees using training data. The RF classifier is relatively robust against outliers and noise, which is important for spatially variable SAR data [62]. Besides performing a supervised classification, the application of RF algorithm allows one to derive the importance of different features. By determining their importance, one can identify which time series feature has the highest contribution to the classification results or is most reliable for the derivation of TOW and/or TFV. In addition, RF was used to analyse whether a single time series characteristic or combination of time series characteristics, and which one, allows for high classification accuracy for the two searched classes. As a result, redundant information is sorted out, and the information essential for classification is identified.

3.3. Clustering Approach for Segment Generation

The derivation of the TOW and TFV was done based on both pixels and segments. Among other advantages, such as a reduction of speckle, the usage of segments allows for the reduction of intra-class variability, which can be caused by the high spatial level of detail of the S-1 data. Clustering represents a common method to perform image segmentation under consideration of multi-spectral and multi-temporal data [63]. Cluster algorithms have already been used as segmentation methods for the derivation of TFV [64–66]. The grouping of pixels into segments was implemented for the study area using a k-means cluster algorithm. k-means is an iterative, unsupervised method that assigns each pixel to a cluster using the minimum distance. This technique is widely used due to its simple implementation. In addition, k-means produces relatively high-quality clusters with low computational effort [67–69].

Segmentation by k-means was carried out in several steps. First, multi-temporal clustering was performed. Therefore, a SAR time series data stack, containing the VV and VH polarizations, is used. This allows one to integrate the temporal component and both polarizations for the generation of clusters. Second, a spatial component was integrated by means of spatial clustering based on the multi-polarised SAR image at the analysed date of the flood event. In order to combine the multi-temporal and spatial information, both cluster images, multi-temporal and spatial, were intersected with each other.

In contrast to other segmentation methods such as multiresolution segmentation [24,41], k-means clustering requires the definition of only a single parameter: the number of clusters. In order to determine this parameter for both the multi-temporal cluster and spatial cluster image, a range for the number of clusters between 5 and 100 has been defined. Thereafter, all possible combinations of the number of clusters for multi-temporal and spatial clustering were performed. Although all possible combinations for the defined areas were tested, it turned out that the combination of 10 multi-temporal clusters and 5 spatial clusters was the best cluster number combination in terms of classification accuracy and computation efficiency. Finally, the combined clusters were examined for their spatial independence and split into their spatially connected segments. The resulting segmented image was used beside the pixel image as a basis for the classification of TOW and TFV.

3.4. Hierarchical Thresholding Approach

The last step in the classification process chain (Figure 4) is the hierarchical thresholding approach, which is divided into three consecutive steps. First of all, the permanent open water surfaces are identified using the SWBD mask (see Section 2) and excluded from further analysis. In addition, GUF and HAND masks (see Section 2) were used as exclusion layers before the next step. The other two steps are based on the remaining unclassified image elements using the derived time series features (see Section 3.2). The threshold values for the corresponding time series features are automatically generated by a decision tree classifier [62] using reference-based training data (see Section 3.2). The automatic threshold definition represents a great advantage, since manually determining thresholds, especially for separation of TFV to other classes, can be a complex process [6]. With the aid of the aforementioned time series features and corresponding threshold values, the class TOW was derived firstly. Equivalent to TOW, the remaining unclassified image elements were separated into TFV and Dry Land in the last step.

4. Results

4.1. Multi-Temporal Characteristics and Patterns of Backscatter Intensities

The analysis of multi-temporal characteristics and patterns was performed based on preprocessed SAR time series data (see Section 3.1). For this purpose, pixels of the time series layer stacks were combined into objects using clustering methods (see Section 3.3). Objects are less susceptible to noise than pixels, and they can be used to create spatial contextual time series profiles, which allow one to derive object-related characteristics and patterns. Examples of object-based time series profiles for TOW and TFV, which were identified from the training data set acquired on 8 April 2017, are shown in Figures 5 and 6. These objects contain 1148 pixels for TOW and 1054 pixels for TFV, respectively. The box plots represent a range of the backscatter values within the segment for each date. The time series are shown for the two single polarizations VV (Figures 5a and 6a), VH (Figures 5b and 6b), and their ratio VV/VH (Figures 5c and 6c) for the same segment. In addition, the multi-temporal behaviour of the NDVI and NDWI values for the same time-period is displayed in Figures 5d and 6d and in Figures 5e and 6e, which serve as a comparison to the SAR time series data. These ratios are not integrated in the methodology as a data set. The analysed flood event image (6 April 2017) is indicated by a blue bar.

Figure 5 shows the multi-temporal characteristics and patterns of the backscatter values for TOW. Compared to all other dates in the time series, a significant decrease of the backscatter values can be observed at the analysed date during the flood event (blue bar) (Figure 5a,b). The ratio of the two polarizations (Figure 5c) shows no change at the analysed date of the flood event. This indicates a similar or equal change in both polarizations. As a comparison to the SAR time series data, NDVI values were used, which were derived from the S-2 data sets. Despite the cloud-related data gap between November 2016 and March 2017, there is a comparable reduction in the NDVI values for the analysed date at the flood event. In combination with the decrease of the backscatter values, this confirms the occurrence of water at the analysed date. In addition, the NDWI shows an increase in the values at the date of flooding, which indicates the occurrence of water.
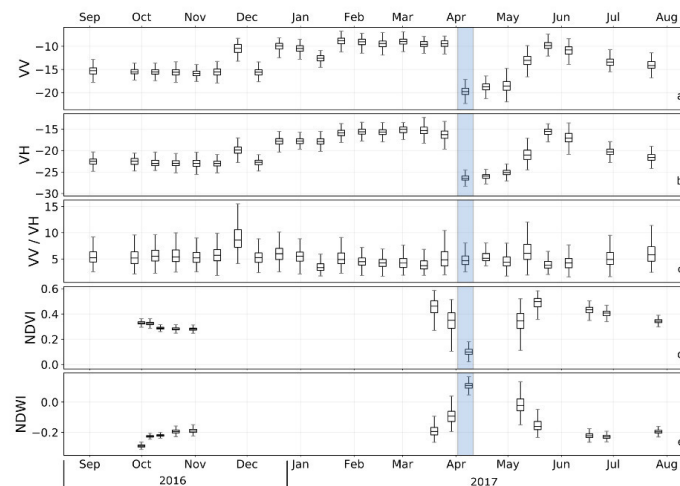
Figure 5. Multi-temporal behaviour of the backscatter intensity for TOW areas for VV (**a**), VH (**b**), the ratio VV/VH (**c**), NDVI values (**d**), and NDWI values (**e**). The blue bars mark the analysed date at the flood event.

Figure 6 shows an example of multi-temporal characteristics and patterns for TFV areas. Compared to TOW, TFV is characterized by an increase in the backscatter values at the analysed date in VV polarization. In contrast to the increase of the backscatter values in VV polarisation, a decrease of the backscatter values occurs in VH polarisation during the flood event (Figure 6b). The ratio between these two polarizations shows an increase for TFV at the analysed date (Figure 6c). As a comparison to the SAR time series data, NDVI values for TFV were derived from the S-2 data and are displayed for the same period (Figure 6d). At the analysed date, there is only a very slight change in the NDVI values. In addition, NDWI shows a slight increase in values, which indicates the occurrence of water in the vegetated areas. Nevertheless, the NDWI values remain in the negative range, and it seems that there are no open water areas but a mixture of standing water and vegetation. Accordingly, it can be confirmed that the increase in backscatter values in VV polarization is caused by flooding and not by any phenological changes. Overall, the increase in backscatter values for TFV in VV polarization is significantly lower compared to the decrease in the backscatter values for TOW areas.
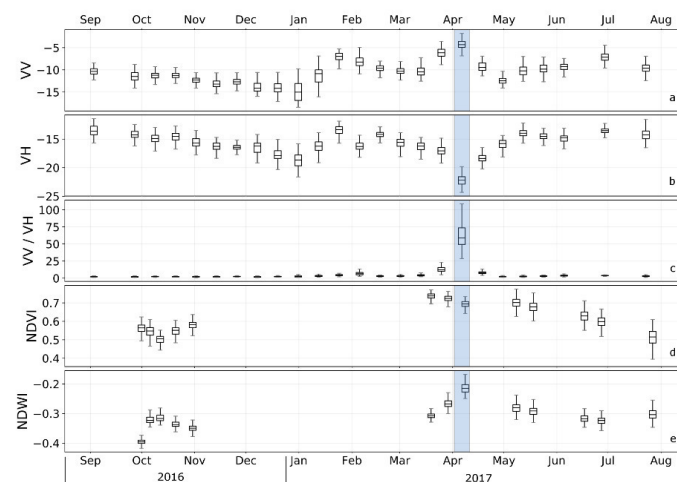

Figure 6. Multi-temporal behaviour of the backscatter intensity for TFV areas for VV (**a**), VH (**b**), the ratio VV/VH (**c**), NDVI values (**d**), and NDWI values (**e**). The blue bars mark the analysed date at the flood event.

4.2. Relevant Time Series Features

Relevant time series features were determined for the derivation of the flood-related classes based on trainings data, which were taken from the reference data. The total number of training pixels for each of the three classes is 15,559 (TOW), 15,563 (TFV), and 11,550 (Dry Land). The importance of time series features for each class was implemented by RF (see Section 3.2). The analysed time series features include Z-Score for the VV and VH polarizations, Z-Score for the ratio between VV and VH, and two Z-Score combinations VV + VH and VV-VH.

The training data were used to visualize the distribution and separability of the classes with respect to the derived time series features in a histogram. Figure 7 shows histogram distributions of the training data for each aforementioned class and time series feature. The separability between the TOW and other classes is clearly recognizable for Z-Score VV and Z-Score VV + VH. The overlap between the histograms of the classes TOW and Dry Land is strongly pronounced for Z-Score VV + VH and Z-Score VV/VH. In addition, there is an overlap to TFV by using Z-Score VH. The separability of TFV from other classes can be observed for Z-Score VV, Z-Score VV-VH, and Z-Score VV/VH. In particular, Z-Score VV/VH appears as a suitable time series feature to distinguish the TFV from other classes.
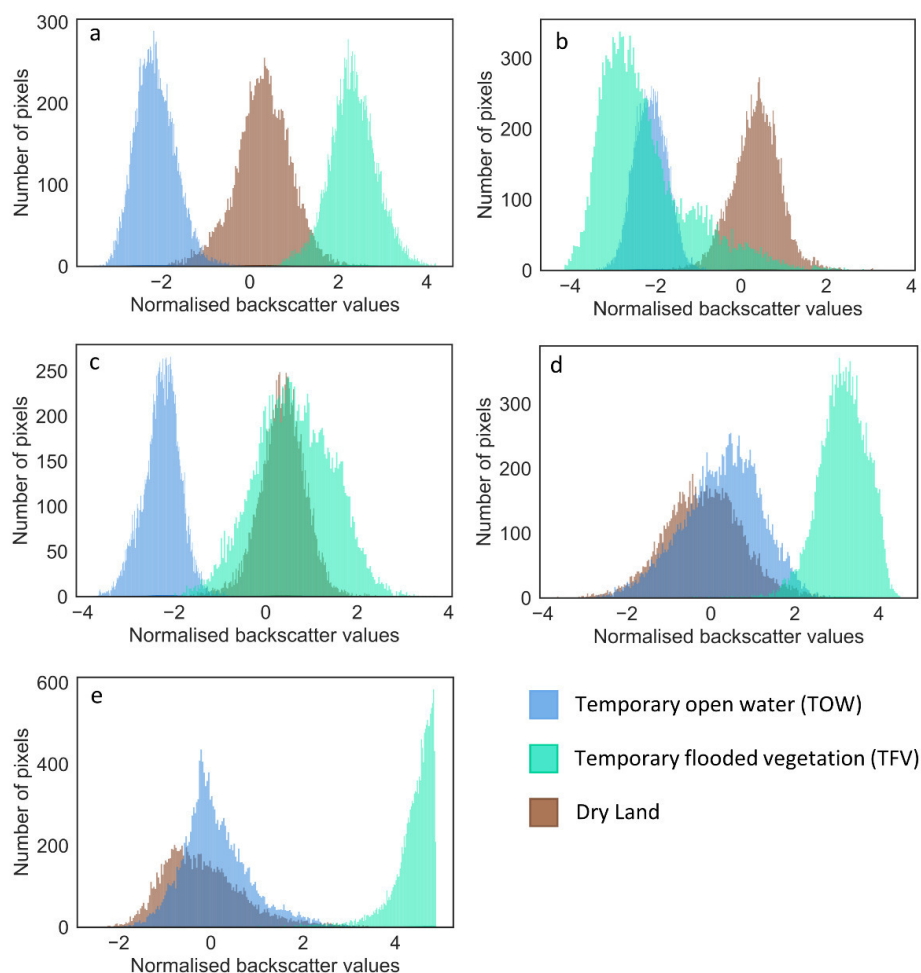

Figure 7. Histogram distributions of training data for the classes TOW, TFV, and Dry Land for individual time series features. Z-score VV (**a**), Z-score VH (**b**), Z-Score VV + VH (**c**), Z-Score VV-VH (**d**), and Z-Score VV/VH (**e**).

The RF algorithm was used to quantify the importance of time series features for the TOW and TFV classes (see Section 3.2). Thereby, the contribution of each time series feature was determined for

the derivation ... 000 estimators
and a maximu... ...rameters were
used to exclu... ...series features
for the classes TOW and TFV. It can be observed that for TOW, Z-Score VV, and Z-Score VV + VH, there are time series features with the highest contributions of 34.9% and 34.4%, respectively. The time series feature with the highest contribution (43.1%) for the TFV class is Z-Score VV/VH.
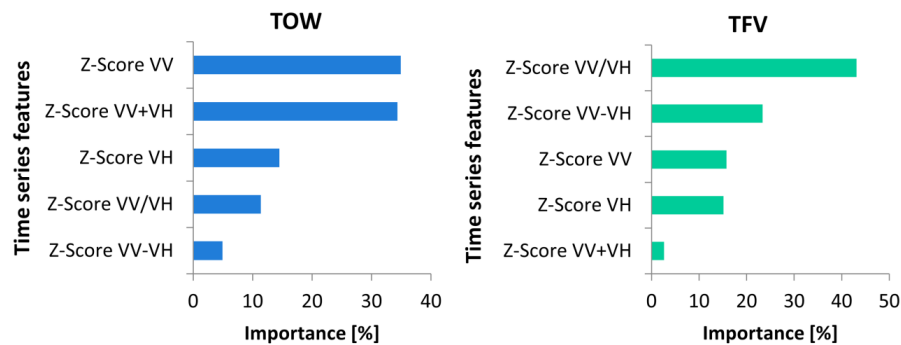
Figure 8. Importance of the time series features, which were determined by the Random Forest algorithm for TOW (blue bars) and TFV (green bars). The features are sorted by their highest to lowest importance.

The time series feature with the highest contribution does not necessarily represent the highest possible classification accuracy. Therefore, it is analysed whether a single feature or a combination of multiple features would result in the highest possible classification accuracy for the respective desired class. For this purpose, a Random Forest classification was performed based on aforementioned training data. The use of the time series features with the highest contribution and the two highest contributions for the classification resulted in an overall accuracy (OA) of approximately 98.0% for the TOW class. In comparison, the combination of all time series features resulted in only 93.1%. Equivalent for the TFV class, the time series feature with the highest contribution achieved an OA of 98.2%, whereby the combination of two or all of the time series features resulted in lower accuracy (97.5% and 96.2%).

RF algorithm's importance shows that Z-Score VV represents the most reliable time series feature and the feature with the highest contribution for the extraction of the TOW. For the extraction of the TFV, Z-Score VV/VH represents the most reliable time series feature and the feature with the highest contribution. The analysis of the OA with the RF algorithm also showed that the combination of all time series features is less accurate than the classification accuracy based on the time series feature with the highest contribution for the classes TOW and TFV. Based on these findings, the time series features Z-Score VV and Z-Score VV/VH were used to derive classes TOW and TFV by means of the time series approach.

4.3. Classification Results

The classification of the S-1 image (6 April 2017) at the date of the flood event was performed based on a S-1 time series layer stack for the period between 2 September 2016 and 23 July 2017. Validation of the classification was performed using the S-2-based reference flood mask.

Figure 9a shows the pixel-based classification result of the time series approach for the investigated area in Namibia, which includes the classes permanent open water, TOW, TFV, and Dry Land, while Figure 9b represents the object-based classification result. For visual comparison, the validation mask is shown in Figure 2b. A visual comparison of the two classification images with the validation mask reveals the clear similarity of the area extent for each class. As expected, the pixel-based classification appears to be slightly noisier in comparison to the object-based classification.

Figure 10 shows the intersection between the validation data and the results based on pixel-based (a) and object-based (b) classification, respectively. Areas of correspondence, as well as misclassified areas, can be shown by this intersection. The orange areas, which are marked as TFV in the classification, however, representing Dry Land in the validation data, can be visually identified as largest misclassification areas. Another significant misclassification can be identified by yellow areas. These areas represent the Dry Land class in the classification image and the TFV class in the validation data, and are slightly larger in the pixel-based classification compared to the object-based classification. Recognisable are also bright blue areas, which can be found at the transect zone between Dry Land and TOW. While these areas represent Dry Land in the reference data, they are classified as TOW. The visual comparison between pixel and object-based classification shows that the extent of bright blue areas in both classifications is similar; this is also the case for all other remaining small misclassified areas. A further difference between pixel- and object-based classification can be observed in the red areas, which represent Dry Land in the classification and TOW in the validation data. Overall, the comparison between pixel- and object-based classification shows that fewer misclassified areas occur in the object-based classification.
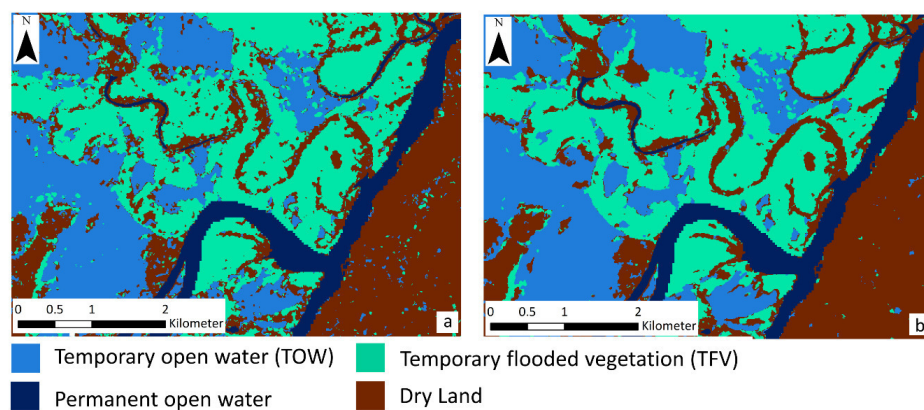

Figure 9. Pixel-based classification result (**a**) and object-based classification result (**b**) for the study area in Namibia.
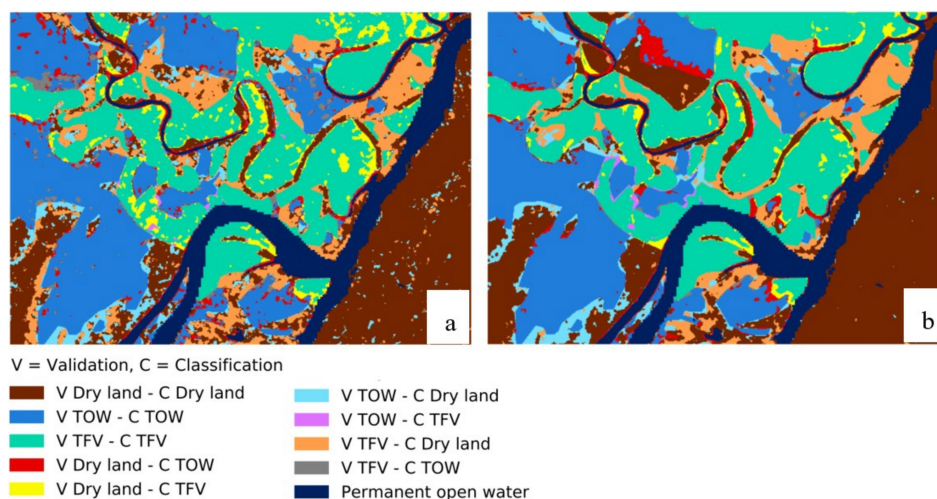

Figure 10. Areas of correspondence and misclassifications for the classes TOW, TFV, and Dry Land using pixel-based (**a**) and object-based (**b**) classification, which are generated by the intersection of the classifications and the validation data.

The quantification of the classification accuracy of TOW, TFV, and Dry Land was performed using OA, producer accuracy (PA), user accuracy (UA), and Kappa index (K). The accuracies for pixel-based and object-based classification are shown in Figure 11. The accuracy values (UA and PA) for the TOW class are 85.1% and 82.6% for pixel-based classification, and 85.8% (UA) and 85.5% (PA) for object-based classification, respectively. In comparison, the accuracy of the class TFV is lower, with 67.9% (UA) and 86.32% (PA) for pixel-based classification, and 76.1% (UA) and 91.2% (PA) for object-based classification. For the class Dry Land, the UA and PA are 74.8% and 59.0% for the pixel-based classification. For the object-based classification, these are 80.8% (UA) and 67.0% (PA), respectively. The improvement was mainly achieved in the UA area for TFV by 8.1% and PA for Dry Land by 8.0%. Overall, the OA of object-based classification is about 5.0% higher compared to pixel-based classification. The Kappa index is also 0.08 higher for the object-based classification. In addition, a confidence interval was calculated for each of the accuracy values [70]. For the pixel-based classification, the largest confidence interval lies at 0.38% for dry land producer accuracy. For object-based classification, the largest confidence interval is 0.37% for the same class and accuracy.
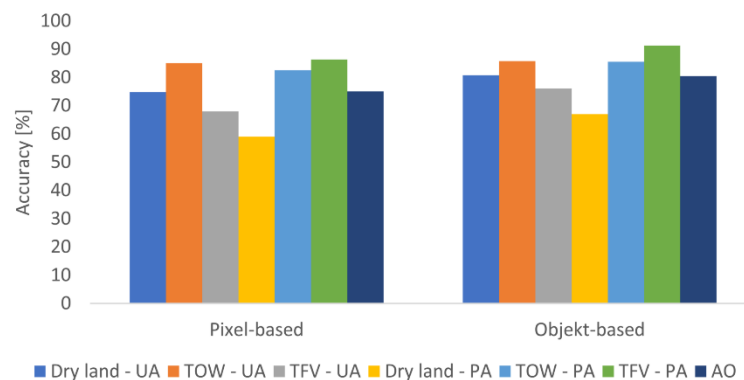

Figure 11. Accuracy assessment results for pixel- and object-based classification, which are generated by means of the time series approach.

In addition to the classification of the validation extent, the classification for the entire study area was generated based on the same time series characteristics and the corresponding threshold values for the classes TOW and TFV. Figure 12a shows the pixel-based classification and Figure 12b the object-based classification. A difference between both classifications can be observed. In particular, the Dry Land areas of the pixel-based classification appear to be noisier in comparison to the Dry Land areas of the object-based classification and show slightly higher overestimation for all areas, especially for Dry Land. Both figures show that the disregard of the TFV areas would result in an enormous underestimation of the flood extent.
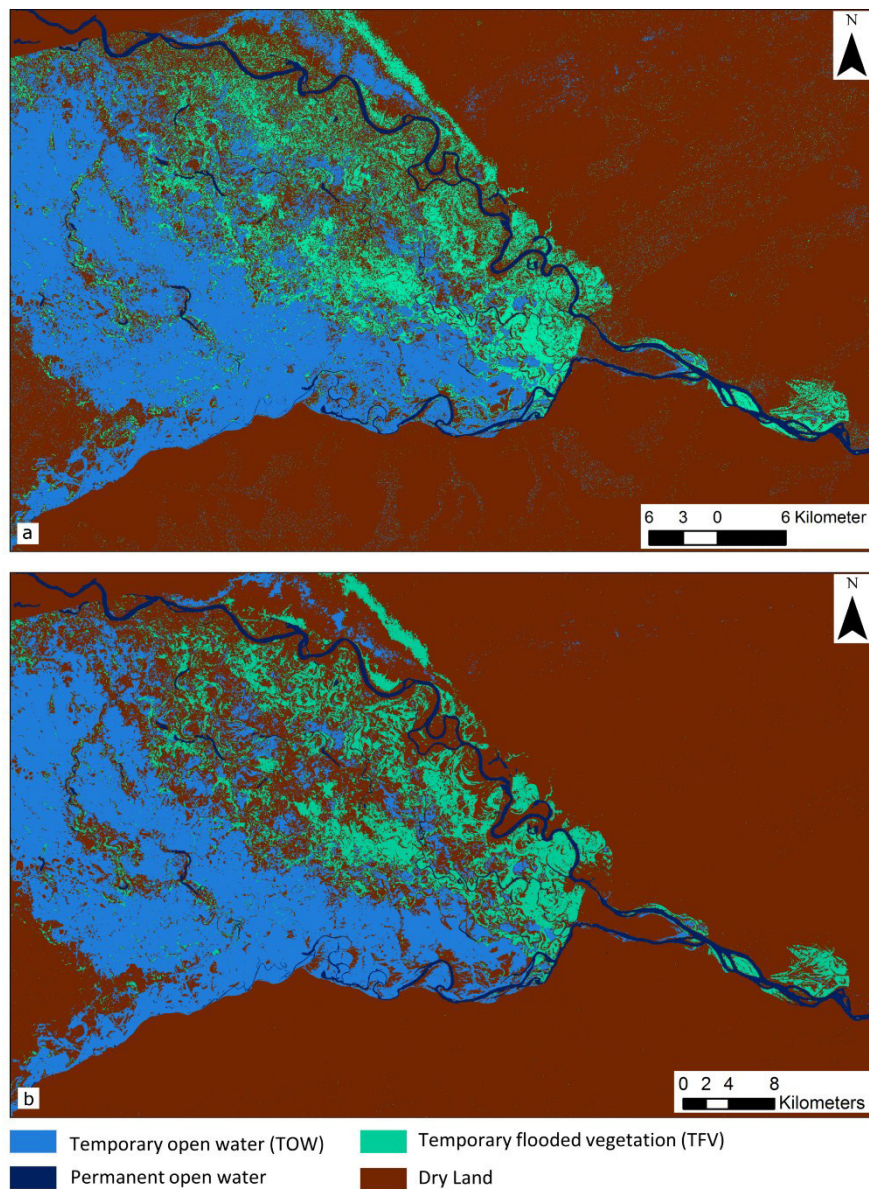
Figure 12. Pixel-based classification result for the entire study area in Namibia (**a**). Object-based classification result for the entire study area in Namibia (**b**).

4.4. Improvement of the Sentinel-1 Flood Service

Figure 13a shows the classification result of the S-1FS (see Section 1) for the validation area in Namibia, which initially only contains the open flood water areas [47]. For the extension and improvement of the S-1FS, the open flood areas were supplemented by TOW and TFV of the time series approach, in order to detect the entire flood extent. The object-based classification result was used as a supplement, since higher accuracy could be achieved compared to pixel-based classification results.

An accuracy assessment was carried out for both the classification results of the S-1FS and the supplemented classification results of the S-1FS. The classes TFV and TOW, both in the validation data and in the supplemented classification of the S-1FS, were combined into a single class: flood. This represents the entire flood extent. The modified reference data is shown in Figure 13d. The merging of the classes of TOW and TFV provides a more comprehensive coverage of the flood extent in the reference data compared to the results of the S-1FS (Figure 13a). Figure 13b shows the classification result of the S-1FS, which are supplemented by TOW, and Figure 13c represents the S-1FS classification

result simultaneously supplemented by TOW and TFV of the time series approach. The validation of the S-1FS and the two supplemented S-1FS classification results were performed using OA, PA, UA, and Kappa Index (Figure 14). A significant improvement in classification accuracy is observed for PA Flood and UA Dry Land, which are 57.1% and 31.0%, respectively. This improvement is mainly achieved by supplementing the S-1FS classification results with the TFV surfaces. Thereby, the OA increases by 27.0% and the Kappa coefficient increases from 0.24 to 0.69.

4.5. Number of Images

Besides the sensor characteristics and environmental conditions, the number of images used for the developed time series approach is another important element that can influence the accuracy of the classification result. 25 S-1 images were used to derive flood-related classes for the study area in Namibia. The time series was used to obtain the statistical multi-temporal distribution of the backscatter values for the flood-related classes (see Section 3.2). For this purpose, it was analysed whether a lower number of images in the time series has an effect on the classification results. In each time series, fewer images were used starting with the original classification of 24 images decreasing in increments of 1, whereby the analysed flood date image was included in each classification run. Figure 15 shows the OAs and Kappa coefficients for 24 classification results, each based on time series with a different number of applied images. In addition, a confidence interval was calculated for each AO. The use of a single image, together with the image taken at the time of the flood results in the lowest accuracy. The same classification resulted in the largest confidence interval 0.19%. Overall, it can be observed that the fewer images are used in the time series, the lower is the OA and Kappa coefficient.
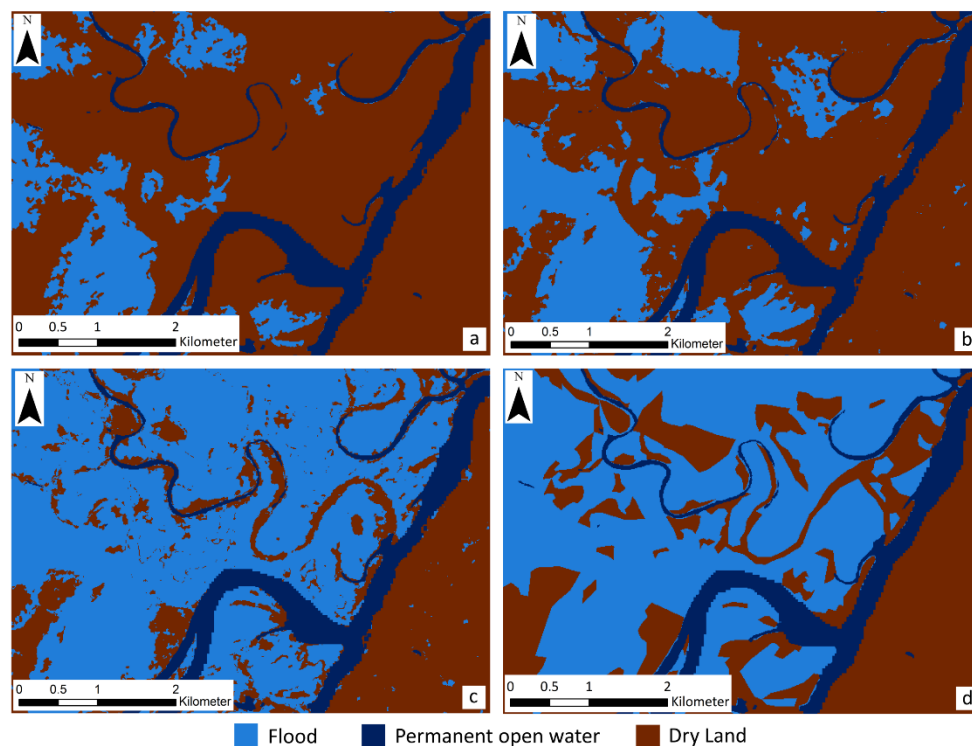

Figure 13. Classification result of the S-1FS (**a**), classification results of the S-1FS supplemented by TOW areas of the time series approach (**b**), classification results of the S-1FS supplemented by TOW and TFV areas of the time series approach (**c**), and validation image with merged flood areas (TOW + TFV) (**d**).
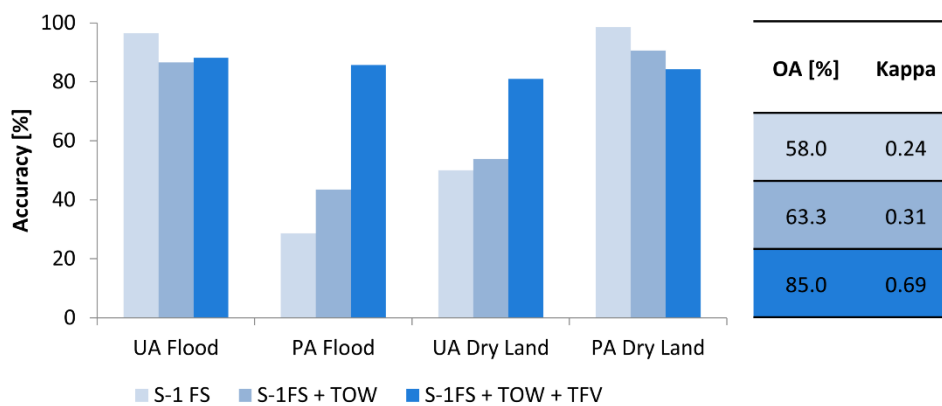
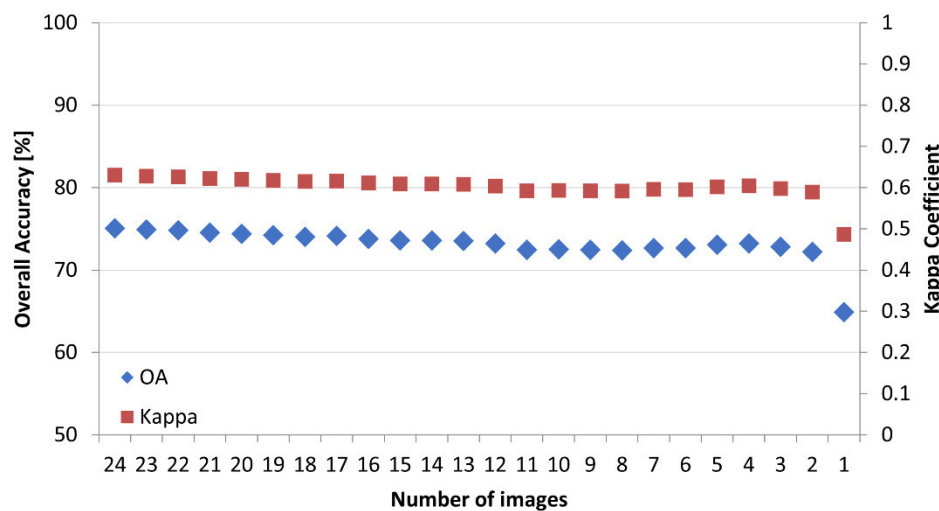**Figure 14.** Accuracy assessment results based on the S-1FS and its improvement (S-1FS + TOW and S-1FS + TOW + TFV).

Figure 15. Overall Accuracy (AO) and Kappa Coefficient for each classification run based on a decreasing number of images.

5. Discussion

5.1. Multi-Temporal Characteristics and Time Series Features

The analysed characteristics and patters of SAR time series data clearly show a decrease in backscatter values for TOW and an increase in backscatter values for TFV at the analysed date of the flood event (Figures 5 and 6). Thereby, the decrease indicates the occurrence of open water surfaces, which are characterized by low backscatter values, in which the emitted sensor energy is reflected away by the specular water surface [71]. The increase can be explained by the double- or multi-bounce interactions between the specular water surface and the vertical structures of the vegetation [9–11]. In many previous studies, similar behaviour of the backscatter values for the classes TOW and TFV is described [11,20,25]. These characteristics and patters in backscatter values are a prerequisite for the detection of the flood-related classes. The length of the decrease or increase of the backscatter values depends on the duration of the flood, the spatial extent, and the revisit time of the satellite.

It should also be noted that backscatter values can be strongly influenced by the environmental conditions (see Section 4.2). For example, wind or heavy rainfall can roughen the water surface and reduce or even erase the typical decrease in backscatter values during the flood event [4,9]. The increase in backscatter at the date of the flood can also be strongly influenced by the interaction between sensor

characteristics (wavelength, angle of incidence, and polarisation) [6] and environmental conditions, such as aboveground biomass [72–74] or the relation between water level and plant height [10]. Such external environmental conditions can have a limiting impact on the methodology presented here.

In previous studies, absolute backscatter values are applied for the extraction of flood-related classes [10,37]. This can lead to underestimation or overestimation of the TFV areas and limits the use of the method. These disadvantages can be compensated by the normalisation of backscatter values over the time series, which ensure the comparability of the increase or decrease in backscatter values for each image element independent of the different types of phenological development of the vegetation. Moreover, the developed method enables simple management of SAR time series data without the use of extensive methods to describe the seasonality or the typical vegetation conditions. In comparison to other studies [19,37], which are based on the dependency of the sequential dates order of the multi-temporal SAR data, the technique presented in this paper can deal with non-sequential or irregular times series data. Sentinel-1 scenes acquired within a period of two years, which are containing the flood event, the flood event made it possible to distinguish the natural range of variation for the analysed vegetation from the changes induced by a flood event.

The decrease and the increase of the backscatter values in SAR time series data were used for the extraction of time series features. Therefore, not only the polarizations VV and VH were applied, but also their combination. By combining polarizations, the effects, such as different sensitivities of the polarisations to objects, can also be intensified, e.g., by mathematically induced stretching of the data [75–77]. The intensity of the amplification was quantified using the RF method (Figure 8). For the extraction of TOW, Z-Score VV was determined by a RF classifier as the most reliable time series feature, having the highest contribution in comparison to the VH based time series features. While this finding matches the results of other studies [4,47], some studies [25,37] prefer VH as a basis for the classification. This ambivalence can probably be explained by different sensor characteristics and environmental conditions in the studies.

The time series feature Z-Score VV/VH proved to be most suitable for the derivation of TFV. This can be explained by the different sensitivity of VV and VH for backscattering mechanisms [78], which causes the backscatter values to increase for VV and decrease for VH. In case of TFV, the increase of the backscatter values can usually be detected by VV polarization due to the double-bounce effect. The double-bounce effect cannot be detected due to the depolarizing property of VH polarization, and the increase of the backscatter values is not expected in VH. Because of the difference or ratio between these two polarisations, the increase in VV is intensified, allowing a more effective derivation of TFV compared to a simple use of VV polarisation.

In the example of Namibia, VV seems to be influenced by the double-bounce-effect indicating the occurrence of TFV [60,79], whereby VH is not influenced by the interaction between water surface and vegetation. Instead, VH is dominated by the specular reflection because of flooded soil in between the vegetation, which consequently results in a decrease in backscatter values. According to the difference in the backscatter between VV and VH for the analysed flood date, the time series feature Z-Score VV/VH was successfully used for the extraction of the TFV.

5.2. Classification Results

The comparison of the time series approach results with the reference mask provides good correspondence of 75.0% (OA, pixel-based) and 80.5% (OA, object-based) for the whole flood extent, comprising both classes TOW and TFV. Cazals et al. [37] achieved a similar OA (82.0%) using backscatter intensities of S-1 time series data for the detection of flooded areas, comprising TOW and TFV. However, a sequential time series is necessary for this method. Furthermore, the comparability of the validation results is limited by the differences between the study areas, including the vegetation types, the sizes of the individual classes, and the ratio in size between these classes and environmental conditions.

In the following, the classification results are discussed in comparison to the validation image (Figure 10). It can be observed that the areas of the correctly classified classes (TOW = blue, TFV = green, Dry Land = brown) predominate; however, misclassifications are present. The misclassifications occur mostly for TFV in the classification image, which is marked as Dry Land in the validation image. Indeed, in these areas the VV and VH polarisations of the time series features Z-Score VV/VH have a significant difference during the flood event and are therefore classified as TFV. Nevertheless, these areas are marked as Dry Land in the validation image. This contradiction can be explained by the fact that the interpretation of optical data in relation to TFV is challenging, and water under the vegetation cover cannot always be clearly identified in the validation image. In addition, the temporal shift between the flood image (6 April 2017) and the validation image (8 April 2017) might also be a reason for the aforementioned misclassifications. Even so, no change in the flood extend could be observed; a receding flood extent (Figure 5) until the date of the S-2 acquisition could be possible. Thus, misclassified areas can indeed represent Dry Land; however, they can also constitute TFV areas in the S-1 flood image. Another significant misclassification is represented by yellow areas. For these areas, the interaction between water surfaces and vegetation may not be strong enough to cause an increase in the backscatter values in VV polarisation [10,80,81]. Accordingly, there is no increase in the Z-Score VV/VH time series feature, so these areas were classified as Dry Land. The light blue areas represent confusion between TOW in the classification results and Dry Land in the validation image. These misclassifications may be caused by an insufficient decrease of the backscatter values in the VV polarisation at the analysed date of the flood event, which could not be detected by the generated threshold value. The transitional zones between TOW and dry areas have always been challenging to detect [82], because of the rapidly changing conditions during the flood event. Despite the misclassifications, the results show that for TOW 85.8% (UA) and 85.5% (PA) and for TFV 76.1% (UA) and 91.2% (PA) could be achieved.

In addition, it was shown that the object-based classification compared to pixel-based classification can help to detect more precisely the areas affected by flood. This can be explained by the fact that the heterogeneity of the TFV in S-1 imagery is reduced by grouping pixels into objects providing a depiction of real objects on the ground. In the TOW area, misclassifications to Dry Land could also be partially reduced. They may have been caused by environmental conditions such as wind, which only affected a few pixels in an object. It also seems that speckle in the SAR data could also be reduced by using objects for classification (Figure 10). However, it should be noted that an additional step to calculate objects must be performed. The results of previous studies also confirm that object-based classification reaches higher accuracies in comparison to pixel-based classifications [27,41].

The validation of the S-1FS results, which were supplemented with the results of the developed SAR time series approach, show that this addition led to an improvement in the classification results of the S-1FS. Although the results of the fully automatic near-real time S-1FS have been significantly improved, it should be noted that the developed SAR time series approach requires training data for the initialization, and that several images (time series) are used to derive the TFV. Thereby, preprocessing is more time-consuming compared to the S-1FS and depends on the number of images used in the time series, the classification basis applied (pixel- or object-based), and the duration for the extraction of training data by an expert. Apart from the above-mentioned steps, the actual classification process only takes a few seconds. A minimum number of data sets in the time series depends on the duration of the flood and the number of S-1 images that have been acquired during the flood. The less non-flooded dates used in the time series, the lower the classification accuracy. If available, it is recommended to include at least one vegetation cycle in order to consider the entire seasonality or phenology. Thus, the statistical distribution of the backscatter values over the entire vegetation cycle is considered [19]. Considering the above-mentioned prerequisite for the SAR time series approach, it was possible to achieve a significant improvement in classification accuracy of S-1FS for PA Flood and UA Dry Land. This was accomplished by supplementing the TOW of S-1FV with the TFV areas (Figure 13).

6. Conclusions

While most methods are aimed at the detection of temporary open water (TOW) areas, the developed method especially focuses on the detection of temporarily flooded vegetation (TFV), which allows the detection of flood areas without underestimating the flood extent. The developed method is based on Sentinel-1 C-band time series data and on additional information taking into account backscatter intensity, permanent water, and topographical and urban information, and uses a hierarchical thresholding approach to combine this information. This approach was used to map a flood event that occurred in spring 2017 in the Chobe-Sambesi flood plain in Namibia.

Normalized time series features were derived based on VV and VH polarisation and their combinations. The time series feature using VV polarisation performed better for the derivation of TOW than the composite of the derived time series features together. The time series feature using the ratio between VV and VH performed best for the derivation of TFV. This demonstrated that both polarizations, and especially their combination, are relevant for the detection of TFV. The classification results showed that the developed SAR time series approach is well suited to map flood in vegetated areas. By supplementing the TOW with the TFV areas, the accuracy of the classification results was significantly improved, and the entire flood extent could be detected. This highlights the importance of the extraction of TFV areas besides TOW for floodplain monitoring.

In the developed approach, the urban areas were not included; however, those will be integrated in the future as a refinement of the methodology. The developed method can be used to monitor future long-term flooding and flood dynamics. Furthermore, the classification results can serve as supplement information in the evaluation of ground observations or as inputs to hydrological models. In combination with the method developed here, the growing Sentinel-1 archive will be used in the future to analyse different TFV types aiming at the continued improvement of the derivation of the entire inundation area during flood events.

Conflicts of Interest: The authors declare no conflict of interest.

References

1. Smith, D.I. Flood Damage Estimation—A Review of Urban Stage Damage Curves and Loss Functions. *Water SA* **1994**, *20*, 231–238.
2. Moel, H.D.; van Alphen, J.; Aerts, J.C.J.H. Flood maps in Europe–methods, availability and use. *Nat. Hazards Earth Syst. Sci.* **2009**, *9*, 289–301. [CrossRef]
3. Li, Y.; Martinis, S.; Plank, S.; Ludwig, R. An automatic change detection approach for rapid flood mapping in Sentinel-1 SAR data. *Int. J. Appl. Earth Obs. Geoinf.* **2018**, *73*, 123–135. [CrossRef]
4. Clement, M.A.; Kilsby, C.G.; Moore, P. Multi-temporal synthetic aperture radar flood mapping using change detection. *J. Flood Risk Manag.* **2017**, *39*, 130. [CrossRef]
5. Dasgupta, A.; Grimaldi, S.; Ramsankaran, R.A.A.J.; Pauwels, V.R.N.; Walker, J.P. Towards operational SAR-based flood mapping using neuro-fuzzy texture-based approaches. *Remote Sens. Environ.* **2018**, *215*, 313–329. [CrossRef]
6. Tsyganskaya, V.; Martinis, S.; Marzahn, P.; Ludwig, R. SAR-based detection of flooded vegetation—A review of characteristics and approaches. *Int. J. Remote Sens.* **2018**, *39*, 2255–2293. [CrossRef]
7. Betbeder, J.; Rapinel, S.; Corpetti, T.; Pottier, E.; Corgne, S.; Hubert-Moy, L. Multitemporal Classification of TerraSAR-X Data for Wetland Vegetation Mapping. *J. Appl. Remote Sens.* **2014**, *8*, 83648. [CrossRef]

8. Klemas, V. Remote Sensing of Emergent and Submerged Wetlands: An Overview. *Int. J. Remote Sens.* **2013**, *34*, 6286–6320. [CrossRef]

9. Moser, L.; Schmitt, A.; Wendleder, A.; Roth, A. Monitoring of the Lac Bam Wetland Extent Using Dual-Polarized X-Band SAR Data. *Remote Sens.* **2016**, *8*, 302. [CrossRef]

10. Pulvirenti, L.; Chini, M.; Pierdicca, N.; Guerriero, L.; Ferrazzoli, P. Flood Monitoring using Multi-Temporal COSMO-SkyMed Data: Image segmentation and signature interpretation. *Remote Sens. Environ.* **2011**, *115*, 990–1002. [CrossRef]

11. Pulvirenti, L.; Pierdicca, N.; Chini, M.; Guerriero, L. Monitoring Flood Evolution in Vegetated Areas Using COSMO-SkyMed Data: The Tuscany 2009 Case Study. *IEEE J. Sel. Top. Appl. Earth Obs. Remote Sens.* **2012**, *6*, 1807–1816. [CrossRef]

12. Chapman, B.; McDonald, K.; Shimada, M.; Rosenqvist, A.; Schroeder, R.; Hess, L. Mapping Regional Inundation with Spaceborne L-Band SAR. *Remote Sens.* **2015**, *7*, 5440–5470. [CrossRef]

13. Voormansik, K.; Praks, J.; Antropov, O.; Jagomagi, J.; Zalite, K. Flood Mapping with TerraSAR-X in Forested Regions in Estonia. *IEEE J. Sel. Top. Appl. Earth Obs. Remote Sens.* **2014**, *7*, 562–577. [CrossRef]

14. Martinis, S.; Twele, A. A Hierarchical Spatio-Temporal Markov Model for Improved Flood Mapping Using Multi-Temporal X-Band SAR Data. *Remote Sens.* **2010**, *2*, 2240–2258. [CrossRef]

15. Pulvirenti, L.; Pierdicca, N.; Chini, M.; Guerriero, L. An Algorithm for Operational Flood Mapping from Synthetic Aperture Radar (SAR) Data using Fuzzy Logic. *Nat. Hazards Earth Syst. Sci.* **2011**, *11*, 529–540. [CrossRef]

16. Brisco, B.; Schmitt, A.; Murnaghan, K.; Kaya, S.; Roth, A. SAR Polarimetric Change Detection for Flooded Vegetation. *Int. J. Digit. Earth* **2011**, *6*, 103–114. [CrossRef]

17. Li, J.; Chen, W. A rule-based method for mapping Canada's wetlands using optical, radar and DEM data. *Int. J. Remote Sens.* **2005**, *26*, 5051–5069. [CrossRef]

18. Hess, L.L.; Melack, J.M. Remote Sensing of Vegetation and Flooding on Magela Creek Floodplain (Northern Territory, Australia) with the SIR-C Synthetic Aperture Radar. *Hydrobiologia* **2003**, *500*, 65–82. [CrossRef]

19. Schlaffer, S.; Chini, M.; Dettmering, D.; Wagner, W. Mapping Wetlands in Zambia Using Seasonal Backscatter Signatures Derived from ENVISAT ASAR Time Series. *Remote Sens.* **2016**, *8*, 402. [CrossRef]

20. Martinez, J.; Le Toan, T. Mapping of Flood Dynamics and Spatial Distribution of Vegetation in the Amazon Floodplain using Multitemporal SAR Data. *Remote Sens. Environ.* **2007**, *108*, 209–223. [CrossRef]

21. Evans, T.L.; Costa, M.; Tomas, W.M.; Camilo, A.R. Large-Scale Habitat Mapping of the Brazilian Pantanal Wetland: A synthetic aperture radar approach. *Remote Sens. Environ.* **2014**, *155*, 89–108. [CrossRef]

22. Hess, L.L.; Melack, J.M.; Affonso, A.G.; Barbosa, C.; Gastil-Buhl, M.; Novo, E.M.L.M. Wetlands of the Lowland Amazon Basin: Extent, Vegetative Cover, and Dual-season Inundated Area as Mapped with JERS-1 Synthetic Aperture Radar. *Off. Sch. J. Soc. Wetland Sci.* **2015**, *35*, 745–756. [CrossRef]

23. Bourgeau-Chavez, L.; Lee, Y.; Battaglia, M.; Endres, S.; Laubach, Z.; Scarbrough, K. Identification of Woodland Vernal Pools with Seasonal Change PALSAR Data for Habitat Conservation. *Remote Sens.* **2016**, *8*, 490. [CrossRef]

24. Robertson, L.D.; King, D.J.; Davies, C. Object-Based Image Analysis of Optical and Radar Variables for Wetland Evaluation. *Int. J. Remote Sens.* **2015**, *36*, 5811–5841. [CrossRef]

25. Zhao, L.; Yang, J.; Li, P.; Zhang, L. Seasonal inundation monitoring and vegetation pattern mapping of the Erguna floodplain by means of a RADARSAT-2 fully polarimetric time series. *Remote Sens. Environ.* **2014**, *152*, 426–440. [CrossRef]

26. Pierdicca, N.; Chini, M.; Pulvirenti, L.; Macina, F. Integrating Physical and Topographic Information Into a Fuzzy Scheme to Map Flooded Area by SAR. *Sensors* **2008**, *8*, 4151–4164. [CrossRef]

27. Chen, Y.; He, X.; Wang, J.; Xiao, R. The Influence of Polarimetric Parameters and an Object-Based Approach on Land Cover Classification in Coastal Wetlands. *Remote Sens.* **2014**, *6*, 12575–12592. [CrossRef]

28. Morandeira, N.; Grings, F.; Facchinetti, C.; Kandus, P. Mapping Plant Functional Types in Floodplain Wetlands: An Analysis of C-Band Polarimetric SAR Data from RADARSAT-2. *Remote Sens.* **2016**, *8*, 174. [CrossRef]

29. Plank, S.; Jüssi, M.; Martinis, S.; Twele, A. Mapping of flooded vegetation by means of polarimetric Sentinel-1 and ALOS-2/PALSAR-2 imagery. *Int. J. Remote Sens.* **2017**, *38*, 3831–3850. [CrossRef]

30. Arnesen, A.S.; Silva, T.S.F.; Hess, L.L.; Novo, E.M.L.M.; Rudorff, C.M.; Chapman, B.D.; McDonald, K.C. Monitoring flood extent in the lower Amazon River floodplain using ALOS/PALSAR ScanSAR images. *Remote Sens. Environ.* **2013**, *130*, 51–61. [CrossRef]

31. Melack, J.M.; Wang, Y. Delineation of flooded area and flooded vegetation in Balbina Reservoir (Amazonas, Brazil) with synthetic aperture radar. *J. SIL Proc.* **1998**, *26*, 2374–2377. [CrossRef]

32. Frappart, F.; Seyler, F.; Martinez, J.-M.; León, J.G.; Cazenave, A. Floodplain water storage in the Negro River basin estimated from microwave remote sensing of inundation area and water levels. *Remote Sens. Environ.* **2005**, *99*, 387–399. [CrossRef]

33. Long, S.; Fatoyinbo, T.E.; Policelli, F. Flood Extent Mapping for Namibia using Change Detection and Thresholding with SAR. *Environ. Res. Lett.* **2014**, *3*, 1–9. [CrossRef]

34. Pulvirenti, L.; Pierdicca, N.; Chini, M. Analysis of Cosmo-Sky Med observations of the 2008 flood in Myanmar. *Ital. J. Remote Sens.* **2010**, *42*, 79–90. [CrossRef]

35. Pulvirenti, L.; Chini, M.; Pierdicca, N.; Boni, G. Use of SAR Data for Detecting Floodwater in Urban and Agricultural Areas: The Role of the Interferometric Coherence. *IEEE Trans. Geosci. Remote Sens.* **2016**, *54*, 1532–1544. [CrossRef]

36. Martinis, S.; Rieke, C. Backscatter Analysis Using Multi-Temporal and Multi-Frequency SAR Data in the Context of Flood Mapping at River Saale, Germany. *Remote Sens.* **2015**, *7*, 7732–7752. [CrossRef]

37. Cazals, C.; Rapinel, S.; Frison, P.-L.; Bonis, A.; Mercier, G.; Mallet, C.; Corgne, S.; Rudant, J.-P. Mapping and Characterization of Hydrological Dynamics in a Coastal Marsh Using High Temporal Resolution Sentinel-1A Images. *Remote Sens.* **2016**, *8*, 570. [CrossRef]

38. Costa, M.P.F. Use of SAR Satellites for Mapping Zonation of Vegetation Communities in the Amazon Floodplain. *Int. J. Remote Sens.* **2004**, *25*, 1817–1835. [CrossRef]

39. Evans, T.L.; Costa, M.; Telmer, K.; Silva, T.S.F. Using ALOS/PALSAR and RADARSAT-2 to Map Land Cover and Seasonal Inundation in the Brazilian Pantanal. *IEEE J. Sel. Top. Appl. Earth Obs. Remote Sens.* **2010**, *3*, 560–575. [CrossRef]

40. Hess, L. Dual-Season Mapping of Wetland Inundation and Vegetation for the Central Amazon Basin. *Remote Sens. Environ.* **2003**, *87*, 404–428. [CrossRef]

41. Na, X.D.; Zang, S.Y.; Wu, C.S.; Li, W.L. Mapping Forested Wetlands in the Great Zhan River Basin through Integrating Optical, Radar, and Topographical Data Classification Techniques. *Environ. Monit. Assess.* **2015**, *187*, 187–696. [CrossRef] [PubMed]

42. Maillard, P.; Alencar-Silva, T.; Clausi, D.A. An Evaluation of Radarsat-1 and ASTER Data for Mapping Veredas (Palm Swamps). *Sensors (Basel)* **2008**, *8*, 6055–6076. [CrossRef] [PubMed]

43. Cremon, É.H.; Rossetti, D.D.F.; Zani, H. Classification of Vegetation over a Residual Megafan Landform in the Amazonian Lowland Based on Optical and SAR Imagery. *Remote Sens.* **2014**, *6*, 10931–10946. [CrossRef]

44. Aghabozorgi, S.; Seyed, S.A.; Ying Wah, T. Time-series clustering—A decade review. *Inf. Syst.* **2015**, *53*, 16–38. [CrossRef]

45. Schlaffer, S.; Matgen, P.; Hollaus, M.; Wagner, W. Flood Detection from Multi-Temporal SAR data using Harmonic Analysis and Change Detection. *Int. J. Appl. Earth Obs. Geoinf.* **2015**, *38*, 15–24. [CrossRef]

46. Martinis, S.; Kersten, J.; Twele, A. A fully automated TerraSAR-X based flood service. *ISPRS J. Photogramm. Remote Sens.* **2015**, *104*, 203–212. [CrossRef]

47. Twele, A.; Cao, W.; Plank, S.; Martinis, S. Sentinel-1-based flood mapping: A fully automated processing chain. *Int. J. Remote Sens.* **2016**, *45*, 2990–3004. [CrossRef]

48. Voigt, S.; Kemper, T.; Riedlinger, T.; Kiefl, R.; Scholte, K.; Mehl, H. Satellite Image Analysis for Disaster and Crisis-Management Support. *IEEE Trans. Geosci. Remote Sens.* **2007**, *45*, 1520–1528. [CrossRef]

49. Martinis, S.; Twele, A.; Plank, S.; Zwenzner, H.; Danzeglocke, J.; Strunz, G.; Lüttenberg, H.-P.; Dech, S. The International Charter 'Space and Major Disasters': DLR's Contributions to Emergency Response Worldwide. *PFG–J. Photogramm. Remote Sens. Geoinf. Sci.* **2017**, *85*, 317–325. [CrossRef]

50. Burke, J.; Pricope, N.; Blum, J. Thermal Imagery-Derived Surface Inundation Modeling to Assess Flood Risk in a Flood-Pulsed Savannah Watershed in Botswana and Namibia. *Remote Sens.* **2016**, *8*, 676. [CrossRef]

51. Namibia Nature Foundation. Wetland Habitats in the Chobe-Zambezi River System. Available online: http://www.nnf.org.na/RARESPECIES/InfoSys/IMAGES/WetlandGrazers/fig10habitatsChobeZam.gif (accessed on 5 January 2018).

52. Esch, T.; Taubenböck, H.; Roth, A.; Heldens, W.; Felbier, A.; Thiel, M.; Schmidt, M.; Müller, A.; Dech, S. TanDEM-X mission—New perspectives for the inventory and monitoring of global settlement patterns. *J. Appl. Remote Sens.* **2012**, *6*, 061702. [CrossRef]

53. Rennó, C.D.; Nobre, A.D.; Cuartas, L.A.; Soares, J.V.; Hodnett, M.G.; Tomasella, J.; Waterloo, M.J. HAND, a new terrain descriptor using SRTM-DEM: Mapping terra-firme rainforest environments in Amazonia. *Remote Sens. Environ.* **2008**, *112*, 3469–3481. [CrossRef]

54. Lehner, B.; Verdin, K.; Jarvis, A. New Global Hydrography Derived from Spaceborne Elevation Data. *Eos Trans. AGU* **2008**, *89*, 93. [CrossRef]

55. Farr, T.G.; Rosen, P.A.; Caro, E.; Crippen, R.; Duren, R.; Hensley, S.; Kobrick, M.; Paller, M.; Rodriguez, E.; Roth, L.; et al. The Shuttle Radar Topography Mission. *Rev. Geophys.* **2007**, *45*, 1485. [CrossRef]

56. ESA. Sentinel-1 Toolbox (S1TBX): Version 4.0.0. Available online: https://sentinel.esa.int/web/sentinel/toolboxes/sentinel-1 (accessed on 27 February 2018).

57. Jarvis, A.; Reuter, H.I.; Nelson, A.; Guevara, E. Hole-filled SRTM for the globe Version 4. Available online: http://srtm.csi.cgiar.org (accessed on 27 February 2018).

58. Lee, J.-S. Refined filtering of image noise using local statistics. *Comput. Graph. Image Process.* **1981**, *15*, 380–389. [CrossRef]

59. Lee, J.-S.; Pottier, E. Polarimetric Radar Imaging: From basics to applications. In *Optical Science and Engineering*; CRC Press: Boca Raton, FL, USA, 2009; Volume 142.

60. Hess, L.L.; Melack, J.M.; Simonett, D.S. Radar Detection of Flooding Beneath the Forest Canopy: A review. *Int. J. Remote Sens.* **1990**, *11*, 1313–1325. [CrossRef]

61. Schumann, G.J.-P.; Moller, D.K. Microwave Remote Sensing of Flood Inundation. *Phys. Chem. Earth* **2015**, *83–84*, 84–95. [CrossRef]

62. Breiman, L. Random Forests. *Mach. Learn.* **2001**, *45*, 5–32. [CrossRef]

63. Fu, K.S.; Mui, J.K. A survey on image segmentation. *Pattern Recognit.* **1981**, *13*, 3–16. [CrossRef]

64. Allen, T.; Wang, Y.; Gore, B. Coastal wetland mapping combining multi-date SAR and LiDAR. *J. Geocarto Int.* **2013**, *28*, 616–631. [CrossRef]

65. Mwita, E.; Menz, G.; Misana, S.; Nienkemper, P. Detection of Small Wetlands with Multi Sensor Data in East Africa. *ARS* **2012**, *1*, 64–73. [CrossRef]

66. Pope, K.O.; Rey-Benayas, J.M.; Paris, J.F. Radar remote sensing of forest and wetland ecosystems in the Central American tropics. *Remote Sens. Environ.* **1994**, *48*, 205–219. [CrossRef]

67. Napoleon, D.; Ramaraj, E. An Efficient Segmentation of Remote Sensing Images for the Classification of Satellite Data Using K-Means Clustering Algorithm. *IJIRST–Int. J. Innov. Res. Sci. Technol.* **2014**, *1*, 314–319.

68. Xu, E.; Jia, Z.; Wang, L.; Hu, Y.; Yang, J. Remote Sensing Image Segmentation Model Based on the Otsu Rule and K-means Clustering Algorithm. *Inf. Technol. J.* **2014**, *13*, 690–696. [CrossRef]

69. Rekik, A.; Zribi, M.; Benjelloun, M.; Hamida, A.B. A k-Means Clustering Algorithm Initialization for Unsupervised Statistical Satellite Image Segmentation. In Proceedings of the 2006 1ST IEEE International Conference on E-Learning in Industrial Electronics, Hammamet, Tunisia, 18–20 December 2007; pp. 11–16.

70. Richards, J.A. *Remote Sensing Digital Image Analysis: An Introduction*, 5th ed.; Springer: Berlin, Germany, 2012.

71. Ulaby, F.T.; Fung, A.K.; Moore, R.K. *Microwave Remote Sensing: Active and Passive. Volume II: Radar Remote Sensing and Surface Scattering and Emission Theory*; Remote Sensing Artech House: Norwood, MA, USA, 1986.

72. Kasischke, E.S.; Smith, K.B.; Bourgeau-Chavez, L.L.; Romanowicz, E.A.; Brunzell, S.; Richardson, C.J. Effects of Seasonal Hydrologic Patterns in South Florida Wetlands on Radar Backscatter Measured from ERS-2 SAR Imagery. *Remote Sens. Environ.* **2003**, *88*, 423–441. [CrossRef]

73. Costa, M.P.F.; Niemann, O.; Novo, E.; Ahern, F. Biophysical properties and mapping of aquatic vegetation during the hydrological cycle of the Amazon floodplain using JERS-1 and Radarsat. *Int. J. Remote Sens.* **2002**, *23*, 1401–1426. [CrossRef]

74. Yu, Y.; Saatchi, S. Sensitivity of L-Band SAR Backscatter to Aboveground Biomass of Global Forests. *Remote Sens.* **2016**, *8*, 522. [CrossRef]

75. Ulaby, F.T.; Long, D.G. *Microwave Radar and Radiometric Remote Sensing*; Artech House: Norwood, MA, USA, 2015.

76. Schmitt, A.; Wendleder, A.; Hinz, S. The Kennaugh Element Framework for Multi-Scale, Multi-Polarized, Multi-Temporal and Multi-Frequency SAR Image Preparation. *ISPRS J. Photogramm. Remote Sens.* **2015**, *102*, 122–139. [CrossRef]

77. Moser, L.; Schmitt, A.; Wendleder, A. Automated Wetland Delineation from Multi-Frequency and Multi-Polarized SAR Images in High Temporal and Spatial Resolution. *ISPRS Ann. Photogramm. Remote Sens. Spat. Inf. Sci.* **2016**, *III-8*, 57–64. [CrossRef]

78. Marti-Cardona, B.; Lopez-Martinez, C.; Dolz-Ripolles, J.; Bladè-Castellet, E. ASAR polarimetric, multi-incidence angle and multitemporal characterization of Doñana wetlands for flood extent monitoring. *Remote Sens. Environ.* **2010**, *114*, 2802–2815. [CrossRef]

79. Chini, M.; Papastergios, A.; Pulvirenti, L.; Pierdicca, N.; Matgen, P.; Parcharidis, I. SAR coherence and polarimetric information for improving flood mapping. In Proceedings of the IEEE International Geoscience & Remote Sensing Symposium, Beijing, China, 10–15 July 2016; pp. 7577–7580.

80. Bourgeau-Chavez, L.L.; Kasischke, E.S.; Brunzell, S.M.; Mudd, J.P.; Smith, K.B.; Frick, A.L. Analysis of Space-Borne SAR data for Wetland Mapping in Virginia Riparian Ecosystems. *Int. J. Remote Sens.* **2001**, *22*, 3665–3687. [CrossRef]

81. Sang, H.; Zhang, J.; Lin, H.; Zhai, L. Multi-Polarization ASAR Backscattering from Herbaceous Wetlands in Poyang Lake Region, China. *Remote Sens.* **2014**, *6*, 4621–4646. [CrossRef]

82. Malinowski, R.; Groom, G.; Schwanghart, W.; Heckrath, G. Detection and Delineation of Localized Flooding from WorldView-2 Multispectral Data. *Remote Sens.* **2015**, *7*, 14853–14875. [CrossRef]

4.3 Paper III: Flood Monitoring in Vegetated Areas Using Multitemporal Sentinel-1 data: Impact of Time Series Features

Tsyganskaya V., Martinis S., and Marzahn P. 2018. 'Flood monitoring in vegetated areas using multitemporal Sentinel-1 data: Impact of time series features'.

Paper III addresses the transferability of the developed approach in Paper II for further study areas and different vegetation types. Based on two independent study areas in Greece/Turkey and China containing different vegetation types, such as high grassland and forested areas, are analyzed. The results confirm the findings of Paper II regarding the used time series features in both studies. However, it was also shown that for the detection of different TFV types, such as high grassland and forests, different time series features are relevant. Besides vegetation types, other factors such as environmental conditions also have a strong influence on the radar signal. This study shows the limitations of the transferability for the developed method due to different vegetation types occurring in flood affected areas. Nevertheless, the visualization and quantification of the results demonstrates that TFV can be reliably extracted with the proposed approach in different study areas. This study laid a cornerstone for a global, automatic and improved flood detection including TFV areas based on S-1 time series data.

Author's contributions: The concept of this study was developed by V. Tsyganskaya, P. Marzahn, and Sandro Martinis, while V. Tsyganskaya was responsible for the implementation, which included the preparation of data, generation and validation of flood classification maps, and methodological comparison of relevant features and their discussion.
Status: published
Journal: Remote Sensing (MDPI)

Flood Monitoring in Vegetated Areas Using Multitemporal Sentinel-1 Data: Impact of Time Series Features

Viktoriya Tsyganskaya [1,*], **Sandro Martinis** [2] **and Philip Marzahn** [1]

[1] Department of Geography, Ludwig Maximilian University of Munich, Luisenstr. 37, Munich 80333, Germany
[2] German Aerospace Center (DLR), German Remote Sensing Data Center (DFD), Oberpfaffenhofen, 82234 Wessling, Germany
[*] Correspondence: tsyganskaya.viktoriya@gmx.de

Abstract: Synthetic Aperture Radar (SAR) is particularly suitable for large-scale mapping of inundations, as this tool allows data acquisition regardless of illumination and weather conditions. Precise information about the flood extent is an essential foundation for local relief workers, decision-makers from crisis management authorities or insurance companies. In order to capture the full extent of the flood, open water and especially temporary flooded vegetation (TFV) areas have to be considered. The Sentinel-1 (S-1) satellite constellation enables the continuous monitoring of the earths surface with a short revisit time. In particular, the ability of S-1 data to penetrate the vegetation provides information about water areas underneath the vegetation. Different TFV types, such as high grassland/reed and forested areas, from independent study areas were analyzed to show both the potential and limitations of a developed SAR time series classification approach using S-1 data. In particular, the time series feature that would be most suitable for the extraction of the TFV for all study areas was investigated in order to demonstrate the potential of the time series approaches for transferability and thus for operational use. It is shown that the result is strongly influenced by the TFV type and by other environmental conditions. A quantitative evaluation of the generated inundation maps for the individual study areas is carried out by optical imagery. It shows that analyzed study areas have obtained Producer's/User's accuracy values for TFV between 28% and 90%/77% and 97% for pixel-based classification and between 6% and 91%/74% and 92% for object-based classification depending on the time series feature used. The analysis of the transferability for the time series approach showed that the time series feature based on VV (vertical/vertical) polarization is particularly suitable for deriving TFV types for different study areas and based on pixel elements is recommended for operational use.

Keywords: flood mapping; temporary flooded vegetation (TFV); Sentinel-1; time series data; Synthetic Aperture Radar (SAR)

1. Introduction

Flood events are the most frequent and widespread natural hazards worldwide and can have devastating economic, social, and environmental impacts [1,2]. Precise and timely information on the extent of flooding is therefore essential for various institutions such as relief organizations, decision-makers of crisis management authorities or insurance companies [3].

Satellite Synthetic Aperture Radar (SAR) is particularly suitable for flood mapping, as this tool supports the large-scale, cross-border detection of the affected area independent of illumination and weather conditions [4–6]. The decisive advantage, however, is that in addition to open water surfaces,

temporary flooded vegetation (TFV) can also be detected in dependency of system and environmental parameters [7]. TFV are areas where water bodies temporarily occur underneath the vegetation [8]. To avoid underestimations of the flooding, the derivation of both classes is essential to cover the entire flood extent.

Smooth open water is characterized by low SAR backscatter values due to its specular surface. In comparison, TFV shows a significant increase in backscatter, especially in the VV (vertical/vertical) polarization, which is caused by the complex double- or multi-bounce interaction between smooth open water surfaces and the structure of vegetation (e.g., tree trunks, stems) [8–10].

Most approaches are based on the backscatter intensity allowing the detection of TFV by the identification of increased backscatter values compared to other objects (e.g., [4,11–15]). Others utilize polarimetric decomposition and/or interferometric SAR (InSAR) coherence [7,16–19] to reduce confusion with urban areas or to minimize the misclassification of shadowed regions as non-flooded vegetation. Polarimetric decompositions, such as Freeman–Durden, Yamaguchi four-component, Cloude–Pottier, or m-chi decompositions, have all been demonstrated to be suitable for the extraction of TFV [7,20–28]. However, the availability of full polarimetric data is often limited regarding the extent and temporal coverage.

In the literature, various methods for deriving the flood extent based on SAR data can be found depending on the task, polarization modes, phase information, as well as spatial or temporal resolution of the satellite sensor [29]. Some of them include, for example, visual interpretation [30], histogram thresholding approaches [31,32], image texture-based methods [33], Markov Random Field modeling [34], or Wishart classifications [17,35,36], which are mostly applied on single images. Change detection techniques in combination with algorithms, such as manual or automatic thresholding [21,37] and fuzzy logic [38,39], allow the extraction of potential changes between two images acquired under dry and flood conditions. Change detection methods are often carried out by using absolute backscatter values [40], which do not consider the chance intensity of backscatter values within vegetation. This can lead to classification errors in regions with high vegetation growth variability or with different vegetation types.

A few advanced techniques, among other machine learning techniques [11], decision tree [41], or rule-based classification [13,42] use satellite time series [4,40,43–47] or multi-dates [11,38,48–52], which allow the inclusion of multi-temporal, -polarized or/and ancillary information for the extraction of temporary open water (TOW) and TFV classes. Thereby, seasonal or annual fluctuations of backscatter and multiple observations of the same area can be used to improve the reliability of mapping the flood extent or even the flood dynamics [43]. Moreover, the use of multitemporal approaches has been in the past limited due to the low availability of corresponding SAR data. However, since October 2014, the Sentinel-1 (S-1) satellite constellation has continuously and systematically captured the earths surface with C-band SAR data at short repetition time, enabling the use of SAR multi-temporal data for systematic and operational flood monitoring. Using this data source, Tsyganskaya et al., [8] recently showed a time series approach for the detection of TFV.

This study aims to show the potential of the SAR time series approach proposed in Tsyganskaya et al., [8] regarding the extraction of the entire flood extent with the focus on TFV for two independent study areas in Greece/Turkey and China. The main focus of the study is to demonstrate the impact of the time series features on the classification results and to show their potential for operational use. The objectives in detail are as follows:

- to investigate the relevance of polarization and time series features for the derivation of TFV with respect to vegetation types in both study areas;
- to examine if the relevant time series features for the analyzed study areas correspond to the relevant time series features of the previous study area (Namibia) in [8], despite the occurrence of different vegetation types and

- to identify a single time series feature that is relevant for the extraction of different TFV types and for all study areas in order to demonstrate the potential for the transferability and operational use of this time series approach.

2. Materials and Methods

2.1. Study Areas and Available Data Sets: Greece/Turkey and China

Besides the study area in Namibia described in [8], two further study areas with different vegetation types were used for the impact analysis of time series features for the extraction of TFV. Compared to [8] and to each other, both study areas have different vegetation types, which are described in this section. One of the study areas is part of the Evros catchment, located at the border between Greece and Turkey (Figure 1a) is one of the study areas.
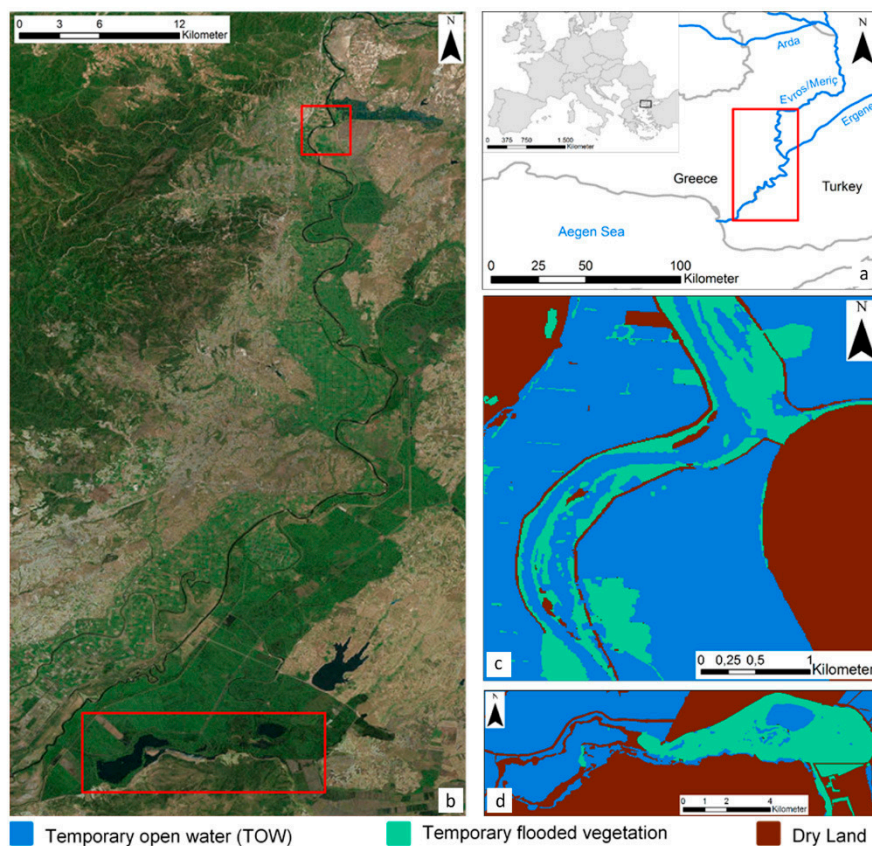

Figure 1. Overview map with the location of the study area (red rectangle) in Greece/Turkey (**a**). Study area in Greece/Turkey (Satellite data: Esri, DigitalGlobe, GeoEye, Earthstar Geographics, CNES/Airbus DS, USDA, USGS, AeroGRID, IGN, and the GIS Use Community) (**b**). The red rectangles represent the reference mask extents for northern (**c**), and southern (**d**) areas. The reference masks based on World-View 2 data (March 11, 2015) (**c**) and RapidEye (April 4, 2015) data (**d**).

With a length of 515 km and a basin of about 52,900 km^2, the Evros river represents the second largest river in Eastern Europe. The period of highest discharge usually occurs between December and April. Several severe, large-scale floods frequently hit the catchment area, particularly in the southern part. The focus of the study lies on a flood event in spring 2015. The flood-affected areas consisted of farmland and forested areas where the water remained for over several weeks. For the analysis and classification, a time series of 60 dual-polarized S-1 scenes was used, which were acquired under the same orbital conditions between October 2014 and December 2016 (Table 1). Five S-1 images covered the flood event. Figure 1b shows the extent of the northern and southern areas of interest, where two

scenes, acquired on March 12, 2015 and April 5, 2015 were considered for classification as flood event images due to their temporal proximity to reference data for the two different areas. The northern area is dominated by TFV consisting of deciduous forest, whereby the majority of agricultural fields are entirely inundated during the flood event. In the southern part of the study area, TFV occurs mostly in high grassland areas.

Table 1. Acquisition dates of the Sentinel (S-1) satellite data used for Greece/Turkey. The scenes acquired on March 12, 2015 and April 5, 2015 (highlighted with blue background) were used as flood event images for two different parts (northern and southern) of the Greece/Turkey study area.

No	Date	No	Date	No	Date	No	Date
1	October 19, 2014	16	June 16, 2015	31	January 6, 2016	46	July 16, 2016
2	October 31, 2014	17	June 28, 2015	32	January 18, 2016	47	July 28,2016
3	November 24, 2014	18	July 10, 2015	33	January 30, 2016	48	August 9, 2016
4	December 6, 2014	19	July 22, 2015	34	February 11, 2016	49	August 21, 2016
5	December 18, 2014	20	August 15, 2015	35	February 23, 2016	50	September 2, 2016
6	December 30, 2014	21	August 27, 2015	36	March 6, 2016	51	September 14, 2016
7	January 11, 2015	22	September 8, 2015	37	March 18, 2016	52	September 26, 2016
8	February 4, 2015	23	September 20, 2015	38	March 30, 2016	53	October 2, 2016
9	February 16, 2015	24	October 2, 2015	39	April 11, 2016	54	October 14, 2016
10	March 12, 2015	25	October 14, 2015	40	April 23, 2016	55	October 26, 2016
11	March 24, 2015	26	October 26, 2015	41	May 5, 2016	56	November 7, 2016
12	April 5, 2015	27	November 19, 2015	42	May 17, 2016	57	November 19, 2016
13	April 17, 2015	28	December 1, 2015	43	May 29, 2016	58	December 1, 2016
14	May 11, 2015	29	December 13, 2015	44	June 10,2016	59	December 13, 2016
15	June 4, 2015	30	December 25, 2015	45	July 4, 2016	60	December 25, 2016

Validation of the classification was performed based on two reference masks (Figure 1c,d). The generation of the reference data was carried out by visual interpretation and manual digitalization of high-resolution optical WorldView-2 (Figure 2) and RapidEye (Figure 3) images, acquired on March 11, 2015 and April 4, 2015, respectively. Although the radar data and the optical image have a temporal shift of one and two days respectively, no changes in the flood extent could be observed.
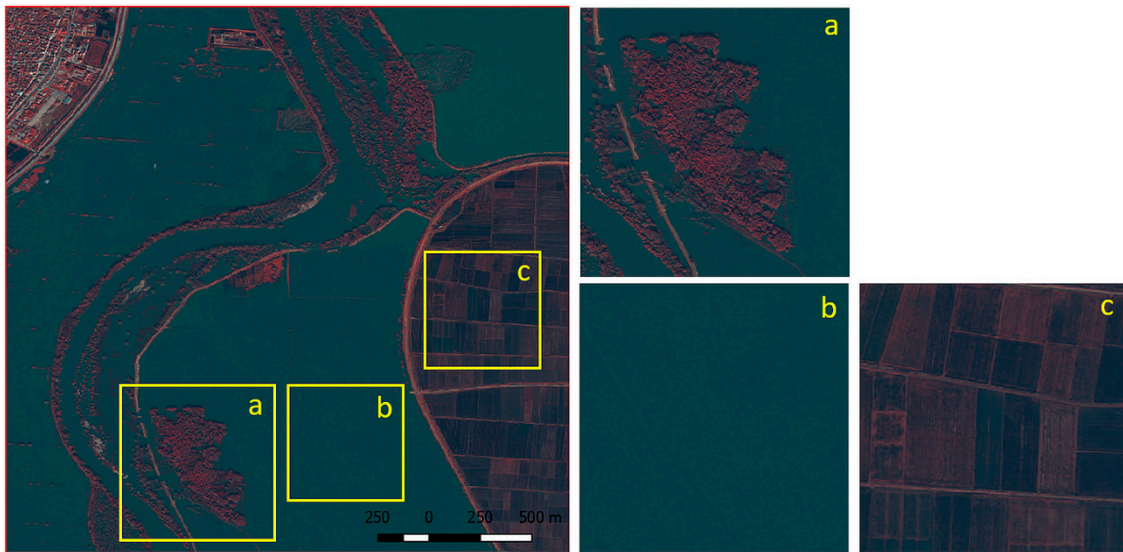
Figure 2. High-resolution false-color (NIR (near infrared), green, blue) WorldView2 image (March 11, 2015) (© European Space Imaging/DigitalGlobe) for northern Greece/Turkey containing temporary flooded vegetation (TFV) (**a**), temporary open water (TOW) (**b**), and dry land (DL) (**c**).
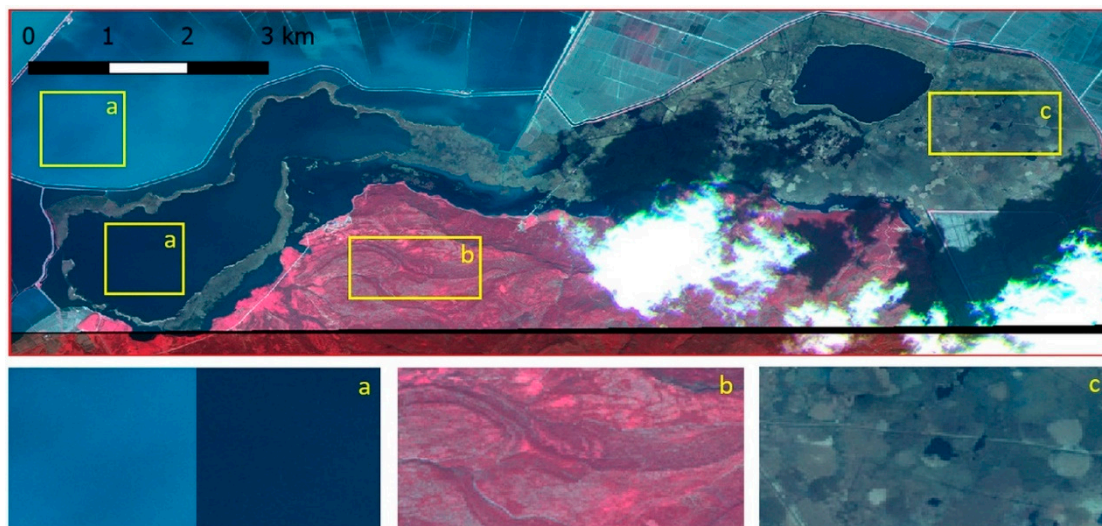

Figure 3. High-resolution false-color (NIR, green, blue) RapidEye image (April 04, 2015). (© Planet Labs Inc.) for southern Greece/Turkey containing TOW (**a**), DL (**b**), and TFV (**c**).

The second test case is the Dong Ting Lake, which is the second largest lake in China, located in the Hunan Province (Figure 4a). It is a flood-basin of the Yangtze River and thus varies seasonally in size. During the annual floods, it can expand to 2691 km² three times its size compared to the dry season. A flood event in summer 2017 (Figure 4b) was chosen. For this study, 38 dual-polarized S-1 scenes were used, which were acquired between October 2016 and February 2018 (Table 2). The scene acquired on June 28, 2017 is characterized by the largest flood extent. In addition, the selection of the analyzed flood image is carried out due to the temporal proximity to the reference data. Comparable to the study area in Greece/Turkey, the generation of the reference flood mask was carried out using a high-resolution optical Sentinel-2 (S-2) image (Figure 5), which was acquired on June 27, 2017 (Table 2). For the derivation of the reference mask, all bands with a resolution of 10 m and their combinations of the S-2 scene were used. The reference extent and the digitalized reference mask is shown in Figure 4c. No changes in flood extent were observed between the analyzed flood image and the optical scene.
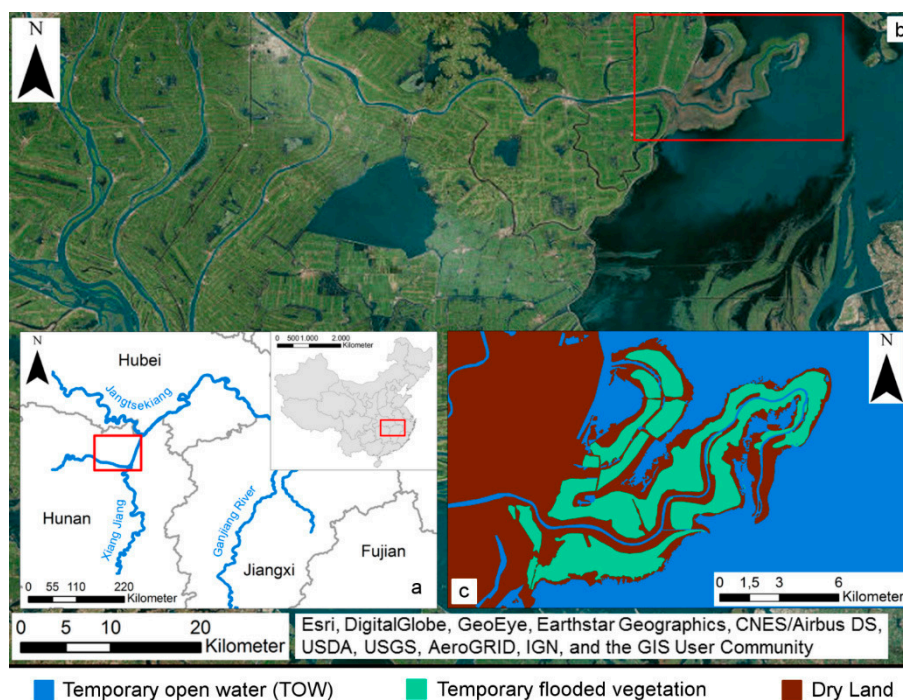
Temporary open water (TOW) Temporary flooded vegetation Dry Land

Figure 4. Overview map with the location of the study area (red rectangle) in China (**a**), study area in China (**b**). The red rectangle represents the reference mask extent (**c**), which was derived from S-2 data (June 27, 2017).

Table 2. Acquisitions dates of the S-1 satellite data used for China. The scene acquired on June 28, 2017 (highlighted with blue background) was used within this study as a flood event image.

No	Date	No	Date	No	Date	No	Date
1	October 19, 2016	11	February 16, 2017	21	July 10, 2017	31	November 19, 2017
2	October 31, 2016	12	February 28, 2017	22	July 22, 2017	32	December 1, 2017
3	November 12, 2016	13	March 12, 2017	23	August 3, 2017	33	December 13, 2017
4	November 24, 2016	14	March 24, 2017	24	August 15, 2017	34	December 25, 2017
5	December 6, 2016	15	April 5, 2017	25	August 27, 2017	35	January 6, 2018
6	December 18, 2016	16	April 17, 2017	26	September 8, 2017	36	January 30, 2018
7	December 30, 2016	17	April 29, 2017	27	October 2, 2017	37	February 11, 2018
8	January 11, 2017	18	June 11, 2017	28	October 14, 2017	38	February 23, 2018
9	January 23, 2017	19	June 4, 2017	29	October 26, 2017		
10	February 4, 2017	20	June 28, 2017	30	November 7, 2017		

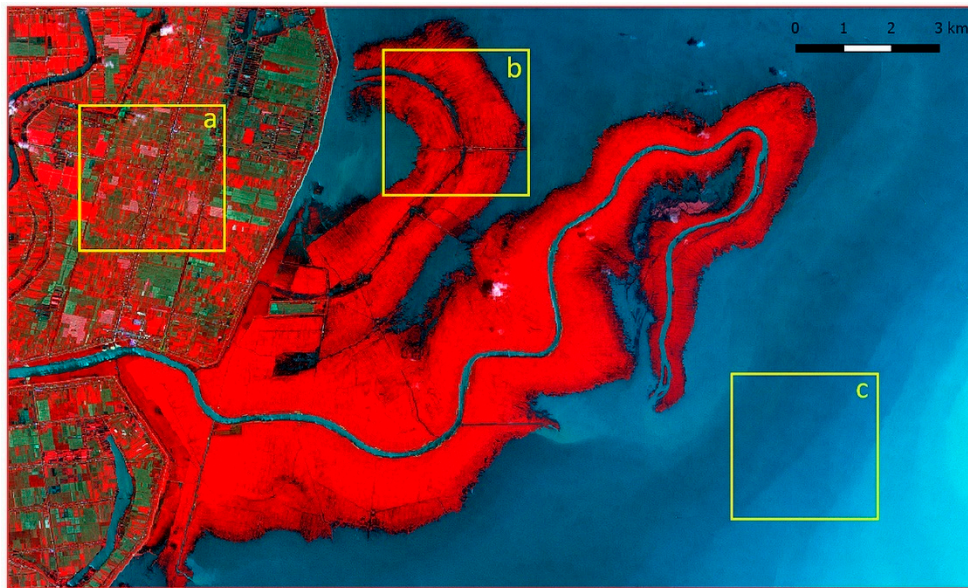| Temporary open water (TOW) | Temporary flooded vegetation | Dry Land |

Figure 5. High-resolution false-color (NIR, green, blue) Sentinel-2 image (June 27, 2017) for southern Greece/Turkey containing DL (**a**), TFV (**b**) and TOW (**c**).

According to the ESA (European Space Agency) acquisition plan for S-1 constellation, dual-polarized images of the S-1A with an interval of 12 days were available for the study areas and the analyzed acquisition period. These data sets are processed and provided by ESA as Ground Range Detected High Resolution (GRDH) products. According to [8], an automated preprocessing of the time series data for both areas and both polarizations VV and VH (vertical/horizontal) was carried out in several steps. The characteristics of all used S-1 data are listed in Table 3.

Table 3. Characteristics of the S-1 data used.

Sensor Properties	Values
Wavelength Mode	Interferometric Wide Swath (IW)
Polarization	VV – VH
Frequency	C-band (GHz)
Resolution	20×22 m (az. × gr. range)
Pixel spacing	10×10 m (az. × gr. range)
Inc. angle	30.5°–46.3°
Orbit	Ascending
Product-level	Level-1 (Ground Range Detected High Resolution (GRDH))

In addition to the satellite data, ancillary information was used to avoid misclassification of the desired flood-related classes [8] in both study areas. Initially, permanent open water (POW) surfaces were identified by the 30 m SRTM Water Body Data (SWBD) [53]. Besides POW, information regarding urban areas and topography was integrated by using the Global Urban Footprint (GUF) and Height Above Nearest Drainage (HAND) index. Urban areas, as well as TFV, are characterized by strong double- and multiple-bounce backscattering effects. Therefore, the GUF [54] mask is used to identify and exclude urban areas. In order to prevent misclassifications in elevated areas, the HAND index [55] was used to identify and exclude areas with an elevation of greater than 20 m above the nearest water network [56].

2.2. Methodology

The foundation for the analysis of the impact of time series features on the flood extent derivation is the SAR time series approach [8]. This method provides the opportunity to generate flood maps including the classes TOW, TFV and Dry Land (DL) based on different time series features. The main steps of the classification process for the generation of the flood maps are summarized below.

The S-1 time series data presented in Section 2.1 provide a foundation for the generation of two independent multi-temporal layer stacks for each polarization and for each study area via an image preprocessing step. In addition, three further multitemporal stacks are generated, including the combinations of polarization (VV + VH, VV − VH, VV/VH). The ratio between VV and VH was calculated by using linear units, whereby for the elimination of outliers (e.g., due to speckle) only the values within the 5th and 95th percentiles were considered.

Based on findings about characteristics and patterns for TOW and TFV [8], the time series features were determined using the z-transform of the backscatter values for each pixel over the time series and for the available multi-temporal layer stack. The z-transform allows the normalization of the backscatter values over the time series and ensures that the image elements of the analyzed flood scene are comparable with each other when considering the individual seasonal fluctuation of vegetation. The normalized time series features are termed as Z-Score. In relation to the polarizations, the time series features are Z-Score VV, Z-Score VH, the combination of polarization, Z-Score VV + VH, Z-Score VV − VH and the ratio Z-Score VV/VH, which represent the foundation for the derivation of TOW and TFV [8]. Based on training data, two time series features with the highest contribution for the derivation of the desired classes (TOW and TFV) were identified for each study area by using Random Forest Algorithm. These features were used in the last step of the classification approach.

The classification of the flood-related classes was carried out based on pixels and objects. The K-means clustering algorithm [57] was applied for the generation of clusters using SAR time series data and the analyzed flood image. The resulting multitemporal and spatial cluster images were intersected with each other to combine multi-temporal and spatial information. The time series features, which are based on pixels, were merged with the segmented image by averaging the corresponding values within each object.

The hierarchical thresholding approach is the last step in the classification process chain, which allows a successive derivation of the desired classes based on the image elements (pixels or segments). First of all, the permanent water surfaces are identified by the SWBD mask (see Section 2.1). On the remaining image elements, the TOW, TFV and Dry Land (DL) are then derived consecutively using the relevant time series features. The corresponding thresholds were determined automatically using the decision tree classifier and the above-mentioned training data. For further details and an in-depth explanation see [8]. The implementation of the entire approach was done in Python. The quantification of the classification accuracy of TOW, TFV, and DL was carried out using overall accuracy (OA), producer accuracy (PA), user accuracy (UA), and kappa index (K).

In order to investigate the impact of time series features for the derivation of TFV and to show the potential of time series features for the transferability to different study areas and thus for the operational use, a statistical comparison of the classification accuracies based on different study areas and TFV types was performed. Thereby, a single time series feature was searched for, which allows the extraction of different types of TFV with high accuracy for all study areas. Besides the study areas described in Section 2.1, the study area in Namibia, which was analyzed in Tsyganskaya et al., [8], was also used for the investigation.

In order to identify a single time series feature, which can then be used for all study areas, the mean value and the coefficient of variation (CV) were determined based on user accuracy (UA) and producer accuracy (PA) for each time series feature. The mean value represents the total accuracy for the TFV classification of all study areas and for each time series feature. The higher the mean value, the more relevant is the time series feature for all study areas. In addition, the CV was used to quantify the variance of the data relative to the mean. The variance of the values is particularly

relevant with regard to the outliers in UA and PA. The lower the CV, the lower the distance/scatter between the classification accuracies of the study areas for a time series feature and the more relevant is a time series feature for all study areas and thus for their transferability. Thus, the two statistical quantities allow the comparison between the classification results and the time series features for all study areas simultaneously.

3. Results and Discussion

3.1. Level of Contribution of the Time Series Features

Based on the knowledge about the characteristics and patterns of the time series data for the two polarizations and their combinations, time series features were derived [8]. Using training data for each of the study areas, those features were examined for their relevance to the extraction of the desired classes, TOW and TFV. For this purpose, similarly large training data sets were derived from optical images for the three classes TOW, TFV, and DL and for each of the study areas. Using Random Forest Algorithm, it was identified which time series features provide the highest contribution to the classification results and are, therefore, most relevant for the derivation of flood-related classes. Furthermore, it was examined whether a single time series feature or a combination of time series features enables the highest classification accuracy for the two desired classes. As a result, redundant information can be sorted out and the information required for classification identified.

Tables 4 and 5 show the level of contribution of the analyzed time series features for the derivation of the above-mentioned classes and the three study areas. Z-Score VV + VH represents the time series feature with the highest contribution for TOW for all study areas (Table 5). This can be explained by the fact that for both VV and VH polarizations the backscatter values decrease at the analyzed date of the flood [8]. An example of the backscatter value decrease in VV and VH is shown in Figure 6, which was created for a TOW segment from the validation data. Z-Score VV + VH combines both sources of information, whereby the decrease of the backscatter values is intensified. Figure 2b shows the enlarged view of the high-resolution WorldView2 image, demonstrating the presence of the corresponding TOW at the analyzed flood date. Further examples of TOW and the analyzed extent of study areas in southern Greece/Turkey and China are demonstrated in Figures 3a and 5c. In addition to both polarizations, the multi-temporal behavior of the Normalized Difference Vegetation Index (NDVI) values for the same time-period is displayed in Figure 6 serving as a comparison to the SAR time series data. NDVI values were derived from the LANSAT 8 data sets. Despite the cloud-related data gap for 2014, the beginning of 2015 and the beginning of 2016, a strong decrease in the NDVI values for the analyzed date of the flood event can be observed. In combination with the decrease of the backscatter values, this confirms the occurrence of water at the analyzed date. For the classification of TFV, different time series features with the highest contribution or relevance can be identified for the individual study areas. The differences can be attributed to the different types of vegetation and the different environmental conditions in the study areas.

Table 4. Random forest importance analysis of the time series features for TOW and individual study areas. The rows highlighted in blue represent the time series features with the highest contribution (importance).

	Southern Greece/Turkey (%)	Northern Greece/Turkey (%)	China (%)
Z-Score VV	35.64	29.26	31.35
Z-Score VH	15.51	23.07	24.61
Z-Score VV + VH	39.44	35.3	33.37
Z-Score VV – VH	5.91	7.33	3.87
Z-Score VV/VH	3.51	5.08	6.81

Table 5. Random forest importance analysis of the time series features for TFV and individual study areas. The rows highlighted in green represent the time series features with the highest contribution (importance).

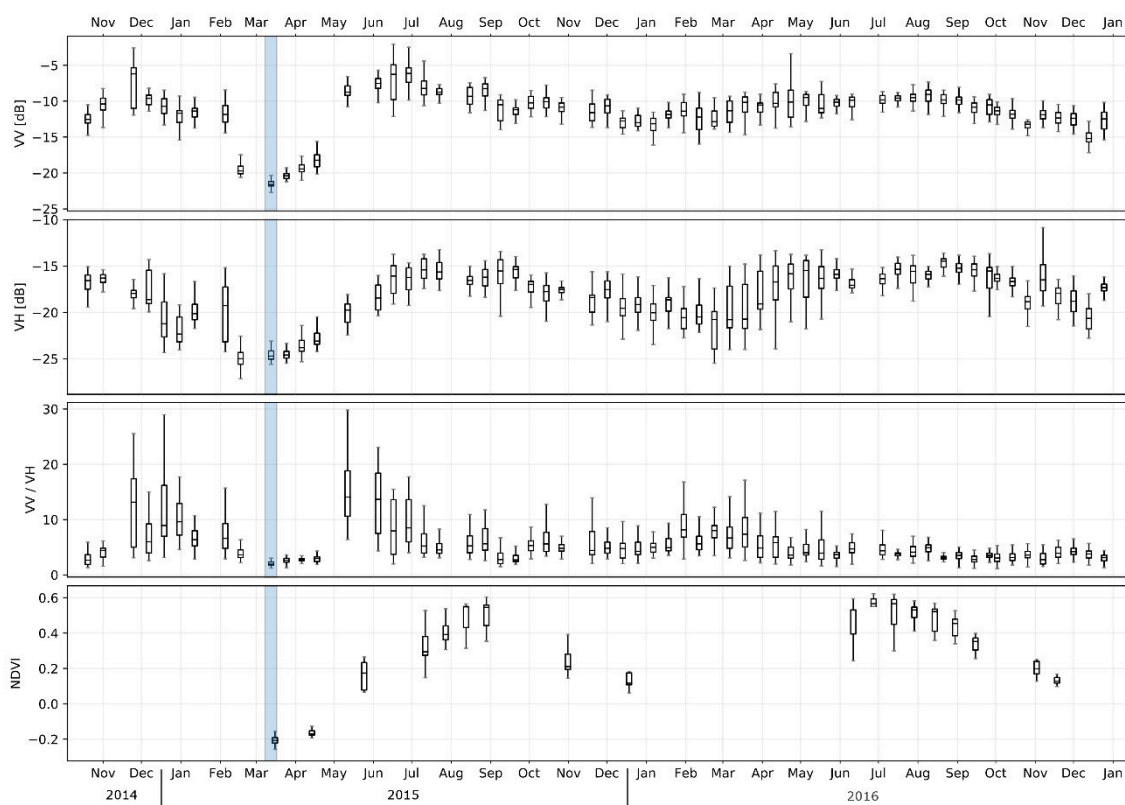|	Southern Greece/Turkey (%)	Northern Greece/Turkey (%)	China (%)
Z-Score VV	32.61	28.39	33.21
Z-Score VH	2.79	11.30	17.32
Z-Score VV + VH	18.66	21.53	33.84
Z-Score VV – VH	41.57	16.37	8.56
Z-Score VV/VH	4.38	22.41	7.10

Figure 6. Multitemporal behavior of the backscatter intensity for TOW areas for VV (decibel (dB)), VH (dB), VV/VH (linear scale), and Normalized Difference Vegetation Index (NDVI) values in northern Greece/Turkey. The blue bars mark the analyzed date at the flood event.

For the study area in southern Greece/Turkey, the Z-Score VV − VH is the most relevant time series feature for the derivation of TFV (Table 5). This can be explained by the strong difference between the polarizations VV and VH (Figure 7). Thereby, VV polarization shows a strong increase at the flood date compared to the rest of the time series and VH polarization shows low or almost no increase at the flood date.
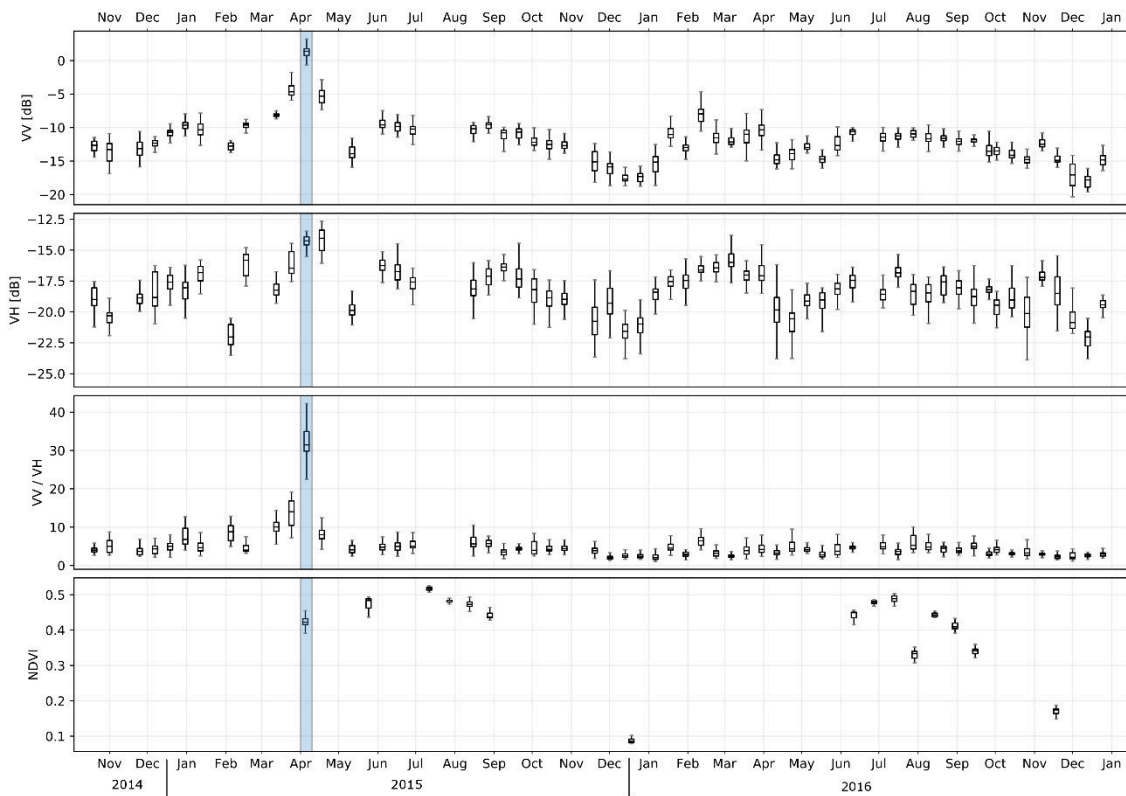
Figure 7. Multitemporal behavior of the backscatter intensity for TFV areas for VV (dB), VH (dB), VV/VH (linear scale), and NDVI values in southern Greece/Turkey. The blue bars mark the analyzed date at the flood event.

The different behavior of both polarizations can be explained by the different sensitivity of VV and VH to specific backscattering mechanisms, which caused an increased difference in the backscatter values between the two polarizations at the analyzed date of the flood. In comparison, the difference between the polarizations for the dry dates shows a smaller variability. The different sensitivity is on the one hand due to the fact that the double-bounce effect occurs more strongly in the VV polarization and leads to the backscatter. On the other hand, backscatter is in general lower for cross-polarization (HV or VH), as no ideal corner reflectors can be produced due to their depolarizing properties [5,58,59]. As a result, it is reported that the increase of the backscatter values by TFV can be more reliably detectable by co-polarized data than by cross-polarized data [60]. However, the combination of co- and cross-polarized data can improve the identification of TFV [26]. The NDVI values in Figure 7 confirm that the increase in VV polarization was not caused by seasonal or other changes in vegetation, but is flood-related, as no sudden increase in NDVI values could be identified at the flood date.

For the study area in northern Greece/Turkey, Z-Score VV is the most relevant feature (Table 5). As previously mentioned in Section 2.1, this study area is dominated by deciduous forest (Figure 2a), which was under leaf-on conditions at the date of the flood. It should be noted that the penetration of the forest canopy may be restricted by C-band and environmental parameters (e.g., aboveground biomass) [61,62]. Yu and Satschi [63] reported that the SAR backscatter values increase depending on the biomass and that the soil signal can no longer be detected if a certain degree of saturation has been reached. Thereby, the volume scattering from the canopy completely superimposes the contribution of the double bounce effects from the interaction between the water surface and vertical vegetation structure and TFV can no longer be identified. Therefore, there is hardly any signal difference between VV and VH at the flood date (Figure 8), which is confirmed by the low importance of Z-Score VV − VH. Compared to that the small increase in importance of the VV/VH can be explained by a small proportion of TFV in the forested areas due to limited penetration into the forest crown, as described

above. In the case of northern Greece/Turkey the importance increases, because the outliers were eliminated by using the Z-Score VV/VH feature. For southern Greece/Turkey on the contrary, using the Z-Score VV/VH the outlier reduction caused also an elimination of extreme values caused by TFV. This led to a drop of the importance in VV/VH in comparison to the Z-Score VV − VH. Regarding the most relevant time series feature Z-Score VV for the northern Greece/Turkey study area, it is assumed that the backscatter in VV polarization is dominated by the contribution of the forest canopy and moreover the volume scattering represents the main scattering mechanism. Due to the sensitivity of the VV polarization for the double bounce effect, however, a slight increase in the backscattering values at the flood date was detected, which can indicate TFV (Figure 8). The NDVI values were derived from the LANDSAT 8 data and show that the slight increase of the backscatter values in both polarizations at the date of flood can be attributed to the flood event and not to any change in vegetation.
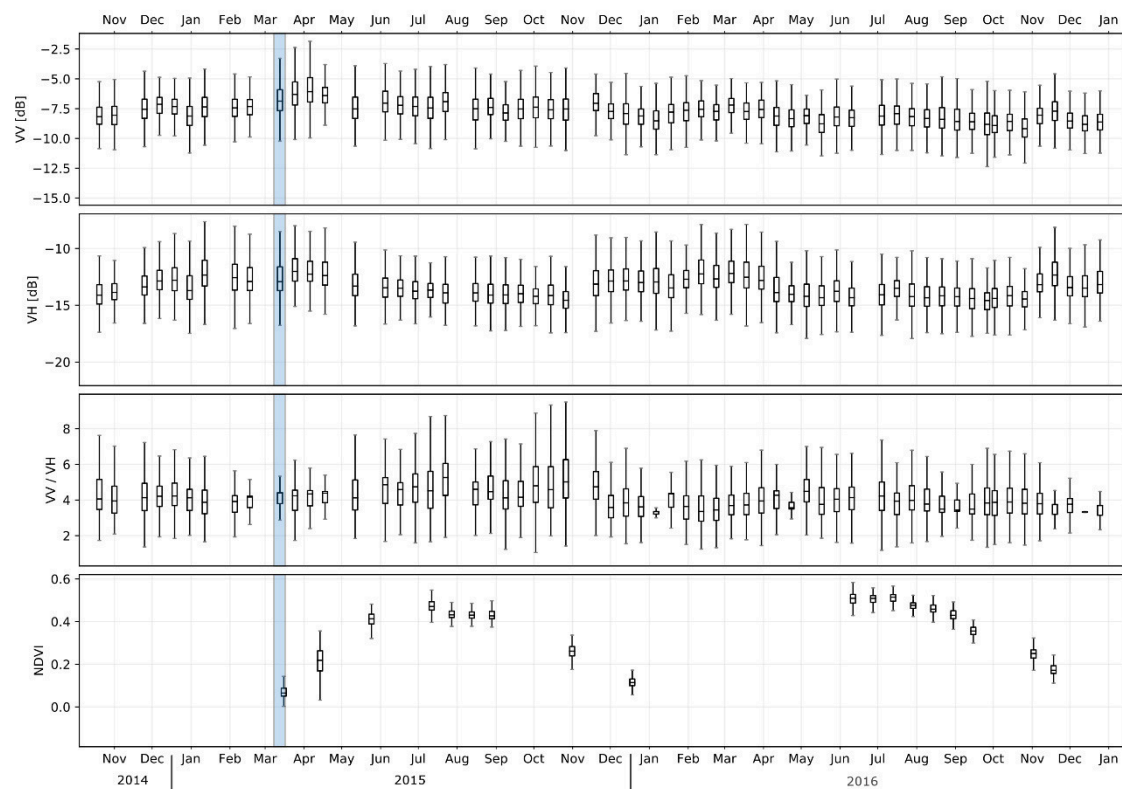

Figure 8. Multitemporal behavior of the backscatter intensity for TFV areas for VV (dB), VH (dB), VV/VH (linear scale), and NDVI values in northern Greece/Turkey. The blue bars mark the analyzed date at the flood event.

For the study area in China, Z-Score VV + VH represents the most relevant time series feature for the derivation of the TFV (Table 5). The time series feature indicates that in both polarizations an increase of the backscatter values has occurred at the analyzed date of the flood. This can be confirmed in Figure 9. Both polarizations increase at the analyzed flood date, whereas the stronger increase can be observed in VV polarization. The sum of the two polarizations intensifies the increase of the backscatter values at the same date. Although only a few cloud-free optical Sentinel-2 images are available that cover the study area in China for the analyzed time period, it can be observed that there is no increase in the NDVI values at the analyzed flood date (Figure 9). This leads to the deduction that the increase in SAR time series data is not related to phenological changes. Figure 5b shows a high-resolution Sentinel-2 image demonstrating the presence of the corresponding TFV area at the analyzed flood date.
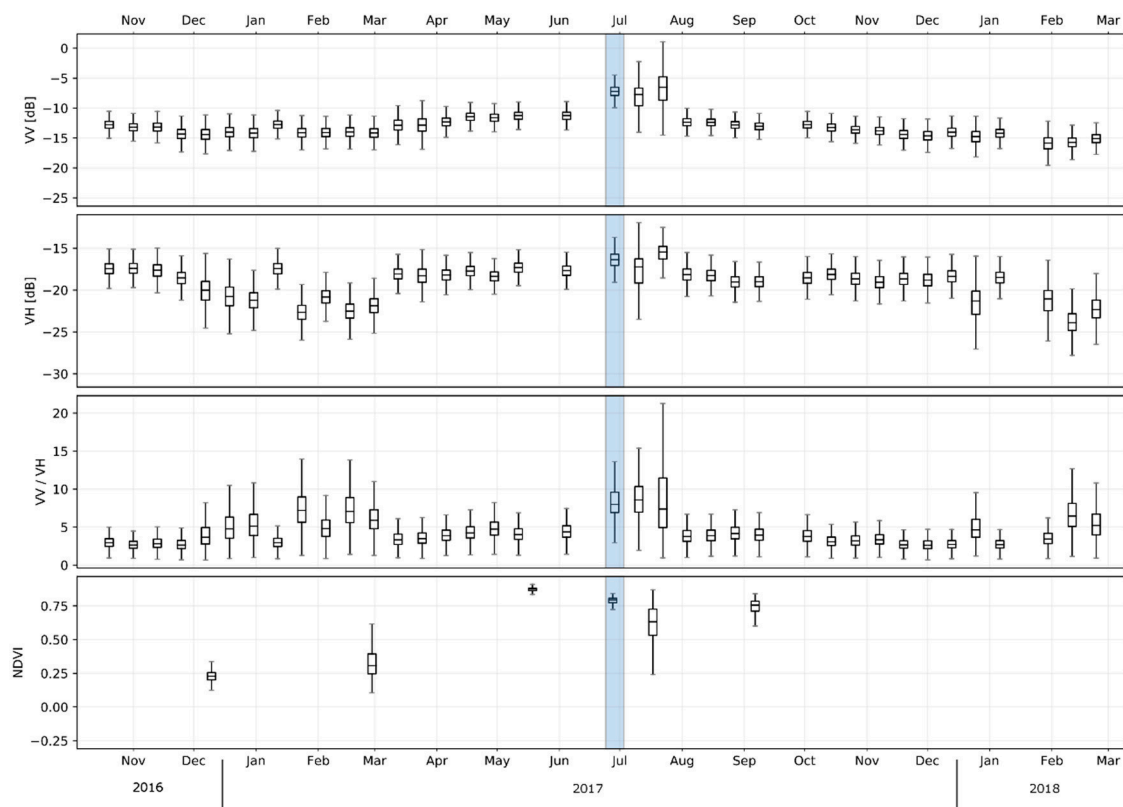
Figure 9. Multitemporal behavior of the backscatter intensity for TFV areas for VV (dB), VH (dB), VV/VH (linear scale), and NDVI values in China. The blue bars mark the analyzed date at the flood event.

Since the TFV type is high grassland and reed (Figure 5b) [64], which is similar to the structure of some crops (rice, wheat), it is assumed that the vegetation can be penetrated by the C-band data [10,65]. Therefore, it is expected that the increase in backscatter values will occur at the time of the flood in the VV polarization due to their sensitivity to the double impact effect. However, the increase in VH polarization cannot be confirmed by the depolarizing property mentioned above. Instead, the latter increase is a result of the combination of environmental parameters. The contribution of the soil under the vegetation plays a decisive role in this process. Due to of possible unevenness of the soil (microtopography) and the low water level, it is possible that a part of the soil surface beneath the vegetation was only partially flooded. In the flood-free areas underneath the vegetation, the soil moisture may have increased at the date of the flood compared to non-flooded conditions. Simultaneously, water could have accumulated in the sinks, which could also lead to standing water beneath vegetation in the same region. Due to different sensitivities of VV and VH to the respective conditions, the latter can dominate the respective polarization. The analyses from the literature confirm that an increase in soil moisture in both VV and VH causes an increase in the backscatter values and can be detected by the sensor depending on the biomass amount [66,67]. The TFV, which is represented by the double-bounce effect, can only be detected by VV polarization, as the depolarizing property of VH polarization does not allow sensitivity to double-bounce [68]. The mixture of these two cases by micro topographical differences explains the increase not only of backscatter values for VV, but also for VH and, thus, the relevance of Z-Score VV + VH for the derivation of TFV in the study area of China.

A comparison of the relevant time series features with the results of the study of Tsyganskaya et al., [8] shows that for the class TOW, Z-Score VV + VH is also one of the time series features with the highest contribution. For TFV, the most relevant time series characteristic (Z-Score VV − VH) is confirmed only for the study area in the southern area of interest of Greece/Turkey. In the other

two example areas, the algorithm determined different relevant time series features due to different environmental conditions (e.g., vegetation type, topography, soil moisture) and their interaction.

Based on a previous analysis in Tsyganskaya et al., [8], the time series feature with the highest contribution can achieve a higher classification accuracy compared to the combination of all time series features. Therefore, a single time series feature with the highest contribution was used for the classification for deriving the desired classes. This identification step is performed automatically by the algorithm using training data. Moreover, these examples show that the use of both polarizations is relevant for the derivation of flooded areas.

3.2. Classification Results

The classification of the study area in southern Greece/Turkey was carried out based on the S-1 time series stack (October 19, 2014–December 25, 2016) containing the flood image (April 4, 2015). This classification was validated using the S-2-based reference mask (April 5, 2015). Figure 10a shows the pixel-based classification result of the time series approach, which comprises the classes POW, TOW, TFV, and DL, while Figure 10b shows the object-based classification result. For visual comparison, the validation mask is shown in Figure 1d. It is noticeable that the areas of the classes TOW, TFV, and DL contain more small structures of the other classes in the pixel-based classification compared to the object-based classification. The usage of objects reduces this noise; however, it also can lead to the loss of details and thus information. In general, the use of pixel- or object-based classification depends strongly on the kind of the landscape under investigation. In the case of flooding in vegetated areas, a single, isolated pixel could contain water ponds and so differ from its neighboring pixels. Due to limited visibility in optical data, these areas could not be identified during the generation of the validation mask.
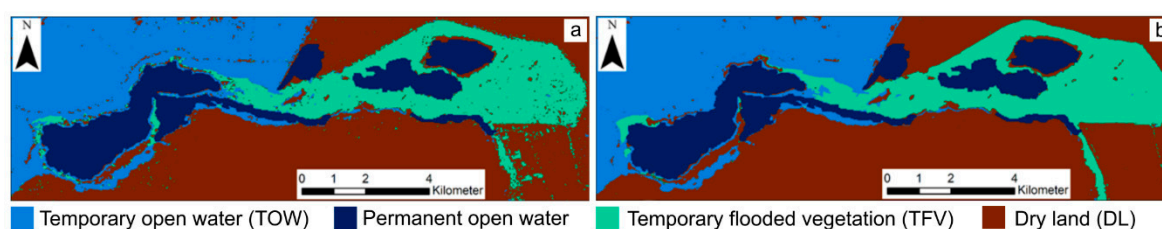

Temporary open water (TOW)　Permanent open water　Temporary flooded vegetation (TFV)　Dry land (DL)

Figure 10. Pixel-based classification result (**a**), object-based classification result (**b**) for the study area in southern Greece/Turkey.

For the study area in northern Greece/Turkey, the classification is based on the S-1 time series stack (October 19, 2014–December 25, 2016), with the flood image being acquired on March 12, 2015. Validation of this classification was performed using the S-2-based reference mask (March 15, 2015). Figure 11a shows the pixel-based classification result for the study area of northern Greece/Turkey, which comprises the classes POW, TOW, TFV, and DL, while Figure 11b shows the object-based classification result. Compared to the validation mask (Figure 1c), both pixel- and object-based classification show only a low representativity of the class TFV. This can be explained by the low penetration of the vegetation (deciduous forest (Figure 2a)) by the C-band data, which is reduced in this case [8]. In addition, occasional TFV areas in the classification can be identified in DL of the validation mask, especially in the pixel-based classification. These could be small areas of water (ponds or temporary water accumulations). In combination with vertical structures of the agricultural areas or grassland, the double bounce effect can also be produced resulting in an increase in the backscatter values at the date of the flood. These areas were also classified as TFV, though they could not, however, be identified during the generation of the validation mask due to limited visibility in optical data.
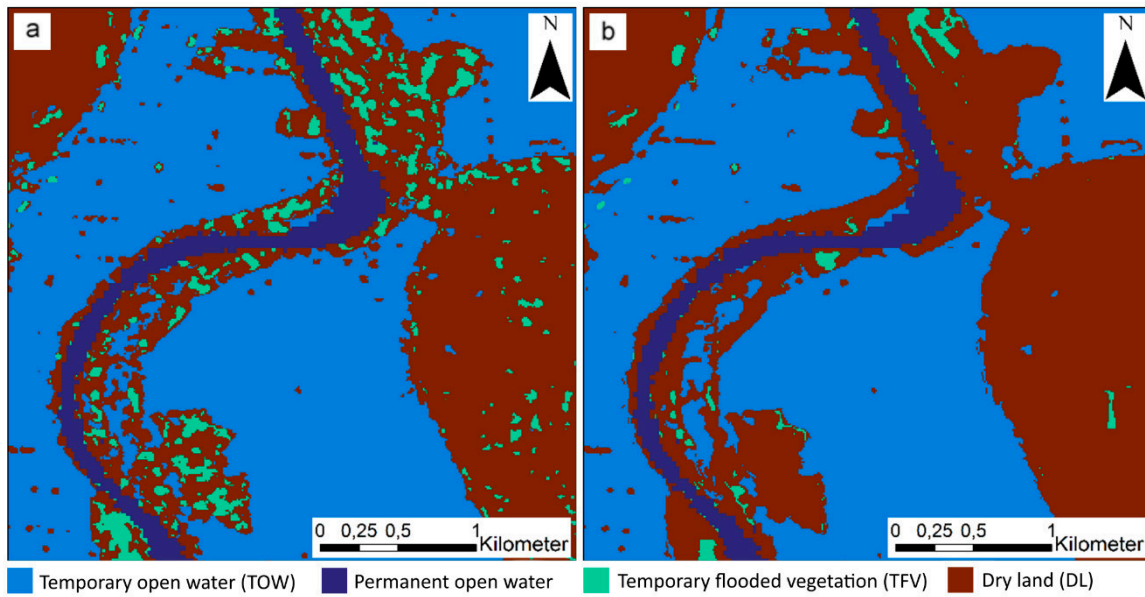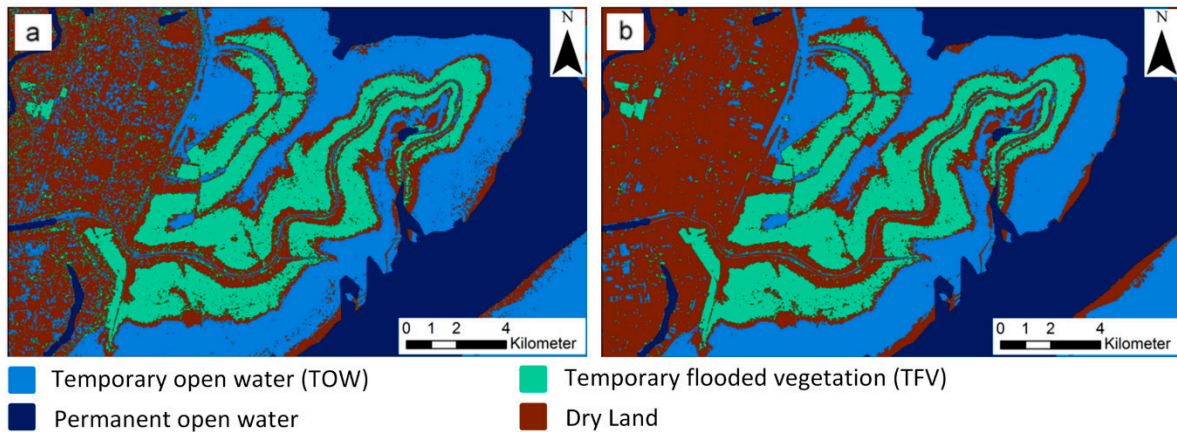
Figure 12. Pixel-based classification result (**a**), object-based classification result (**b**) and validation mask (c) for the study area in China.

The comparison between the classification results and the validation mask reveals the occurrence of TOW in DL. DL also occurs between the permanent water surfaces and the TOW areas. On the one hand, the confusion between these two classes can arise due to small areas of water occurring in the agricultural areas. On the other hand, the duration of a flood event can lead to an accumulation of S-1 images, containing the inundation and a decrease of images without flooding. This can cause a higher fluctuation range and a lower mean value when generating the time series features, which in particular can lead to confusion with DL, as the areas between permanent water and TOW demonstrate. The combination of these two conditions makes the above-mentioned confusions between the classes possible. Therefore, the use of a time series with at least one vegetation cycle is recommended, as

the statistical range of the backscatter values of the vegetation stages is detected and thus sufficiently represented [8].

The accuracy values for the pixel-based and object-based classifications for the respective study areas are shown in Table 6. The OA for all study areas ranges between 80% and 87%. In comparison, in [8] the authors achieved a similar or even slightly lower OA for the pixel-based (75%) and object-based (82%) classification. The accuracy assessment for the study area in northern Greece/Turkey shows high values for the TOW class but strong misclassifications for TFV (PA: 28% for pixel-based and 6% for object-based) and DL (UA: 57% for pixel-based and 53% for object-based). This indicates a significant confusion between these two classes and can be explained by different environmental conditions (see Section 3.1). The accuracy values show no significant difference between pixel-based and object-based classification, except for the PA values of TFV. When applying object-based classification, it should be noted that the small-scale flood areas could be generalized by merging the pixels to objects. However, object-based classification can help to exclude pixels which can be confused with a flood-related increase in values due to dominant environmental conditions, such as soil moisture, topography, or surface roughness, which can cause a small-scale increase or decrease in the backscatter. In addition, objects are less susceptible to speckle noise than pixels [29].

Table 6. Accuracy assessment for the pixel- and object-based classification for the individual study areas. Overall accuracy (OA) in %, Producer accuracy (PA) in %, User accuracy (UA) in %, and Kappa index (K).

	Southern Greece/Turkey (%)		Northern Greece/Turkey (%)		China (%)	
	Pixel-based	Object-based	Pixel-based	Object-based	Pixel-based	Object-based
DL—UA	76.64	77.62	56.65	53.25	85.26	87.66
TOW—UA	86.53	86.87	97.58	98.23	79.73	85.65
TFV—UA	90.37	92.17	76.83	73.86	78.28	83.01
DL—PA	77.86	79.61	91.67	96.60	69.89	78.95
TOW—PA	85.94	86.38	91.02	91.67	90.47	91.14
TFV—PA	89.52	90.09	28.18	6.32	90.09	91.23
OA	84.26	85.17	81.47	79.59	81.37	85.84
Kappa	0.76	0.78	0.66	0.63	0.71	0.78

3.3. Time Series Features—Transferability Analysis

For the transferability analysis of the classification approach, several pixel-based and object-based classification runs were carried out for each study area and its subareas using the individual time series features. For each run, the most relevant time series feature (Z-Score VV + VH) was used for the derivation of TOW (Section 3.1). Simultaneously, each time series feature was used in each study area to derive the TFV, so that 20 pixel-based and 20 object-based classification products could be generated. For each result, an accuracy assessment was performed. Since the analysis of the different time series features refers to the TFV, the PA and UA of TFV were selected as indicators to represent the classification accuracy of the TFV. The accuracy values PA and UA for the individual study areas and the five analyzed time series features for pixel-based classification are shown in Table 7 and for object-based classification in Table 8. The relevant time series features that were identified by the Random Forest Algorithm (Section 3.1) are highlighted in dark green for the respective study areas for the PA and UA values. These tables show that different time series features are relevant for the individual study areas. The low PA values seen for northern Greece in both tables can be explained by the specific TFV type that dominates this study area, namely flooded forest areas. In this case, the penetration of the forest crown is limited by C-band data, whereby the water under the vegetation can only be partially detected.

Table 7. The accuracy values PA and UA of the pixel-based classification for the individual study areas as a function of the five analyzed time series features. The relevant time series features for the individual study areas, which were identified by the Random Forest Algorithm (Section 3.1) and corresponding PA and UA values are highlighted in dark green. Optimum of statistical variables (mean value of UA / PA and coefficient of variables) for time series features is highlighted in light green.

	Z-Score VV		Z-Score VH		Z-Score VV + VH		Z-Score VV − VH		Z-Score VV/VH	
	UA	PA	UA	PA	UA	PA	UA	PA	UA	PA
Namibia	88.72	78.43	47.11	90.52	85.64	82.38	92.62	69.96	67.90	86.32
China	82.26	92.65	51.26	99.30	78.28	90.09	52.37	99.24	44.46	99.50
North Greece	76.83	28.18	50.34	0.81	65.85	3.26	37.10	4.71	68.58	56.72
South Greece	96.10	77.17	35.25	42.22	94.89	53.17	90.37	89.52	60.85	93.48
Mean values of UA and PA	77.54		52.10		69.18		65.74		72.23	
Coefficient of variance	0.22		0.41		0.36		0.47		0.18	

Table 8. The accuracy values PA and UA of the object-based classification for the individual study areas as a function of the five analyzed time series features. The relevant time series features for the individual study areas, which were identified by the Random Forest Algorithm (Section 3.1) and corresponding PA and UA values are highlighted in dark green. Optimum of statistical variables (mean value of UA / PA and coefficient of variables) for time series features is highlighted in light green.

	Z-Score VV		Z-Score VH		Z-Score VV + VH		Z-Score VV − VH		Z-Score VV/VH	
	UA	PA	UA	PA	UA	PA	UA	PA	UA	PA
Namibia	84.05	80.71	49.26	17.47	84.37	5.99	54.93	89.29	76.1	91.2
China	82.38	92.65	62.51	92.46	83.01	91.23	66.68	97.06	42.86	97.86
North Greece	73.86	6.32	50.35	0.82	65.99	3.29	48.61	2.92	68.75	57.22
South Greece	97.05	87.81	26.90	31.64	98.52	75.19	92.17	90.09	65.20	92.74
Mean values of UA and PA	75.57		41.43		63.44		67.72		73.99	
Coefficient of variance	0.31		0.62		0.52		0.40		0.19	

As described in the methodology, two quantities, mean value and CV, were derived based on the UA and PA values to provide a foundation for the identification of a single robust time series feature for the derivation of TFV types and for all study areas. If a time series feature reaches a high mean value compared to other time series features and shows at the same time the smallest CV, it is relevant for all study areas. Considering Tables 7 and 8, it is not apparent which time series feature would be suitable since the two statistical variables achieve the optimum at different time series features (highlighted in light green). The Z-Score VV shows the highest mean value (77.54%) for pixel-based classification and (75.57%) for object-based classification compared to other time series features, but Z-Score VV/VH shows the lowest CV value (0.18) for pixel-based and (0.19) for object-based.

For a distinct identification of the most relevant time series feature, the two statistical variables have to be considered simultaneously. In Figure 13, the two quantities are plotted on two different axes. The larger the mean value and the smaller the CV, the more suitable is a time series feature for the extraction of TFV for all study areas. The lower right corner of the diagram is thus the point that represents the optimum between both statistical quantities. The closer a time series feature lies to this optimum, the more relevant is the time series feature for all study areas.
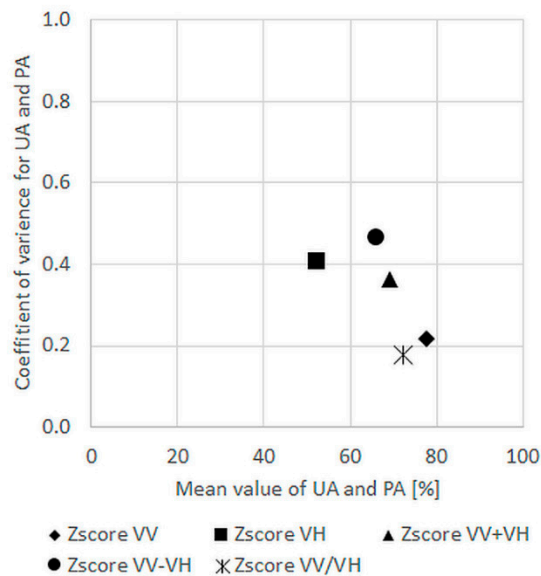
Figure 13. Comparison of pixel-based time series features as a function of mean value and coefficient of variation. The statistical values (mean value and coefficient of variance) were calculated on the basis of the PA and UA accuracy values.

Compared to other time series features, Z-Score VV is the shortest regarding the distance between the optimum and the time series feature for pixel-based classification (Figure 13). Thus, this time series feature seems to be the most relevant for the operational derivation of the class TFV, when using pixels as a foundation. The relevance of Z-Score VV is due to the fact that VV polarization is more influenced by the double-bounce effect indicating the presence of TFV. In comparison, VH is more influenced by different environment conditions and may change for different TFV types and study areas (Section 3.1). The distances of the Z-Score VV/VH to the optimal point differ from the distance between the Z-Score VV and optimal point only slightly. This shows that VH polarization also has an influence on the classification results and can be important in combination with VV polarization provided that the environmental conditions in the analyzed study area are known and characterized.

This relevance is also shown in Figure 14, where the relevant feature based on objects is the Z-Score VV/VH, which contains both polarizations. Based on the findings in Section 3.1, which show that the increase in the VV time series at the date of the flood for TFV is more significant compared to the VH time series because the VH signal is influenced more by environmental conditions than by TFV, the Z-Score VV feature based on pixel elements is recommended for operational use. In addition, the mean value of UA and PA for the pixel-based classification for the Z-Score VV time series feature is highest (77.54%) compared to all other mean values of UA and PA. The combination of Z-Score VV + VH and Z-Score VV/VH based on pixel elements is recommended for operative use for extraction of the TOW and TFV, respectively. When no feature importance has to be calculated during the classification and the pre-processing of the S-1 data [8] has already taken place, the classification process takes between 1 and 5 minutes, depending on the available computing performance and the extent of the study area. The maximum extent that was analyzed is one-third of S-1 GRD images. By specifying the time series features the user, interaction is omitted and apart from the initialization of the algorithm the classification can be performed automatically. For the optimization and extension of the approach regarding different TFV types, further research in other study areas will be beneficial.
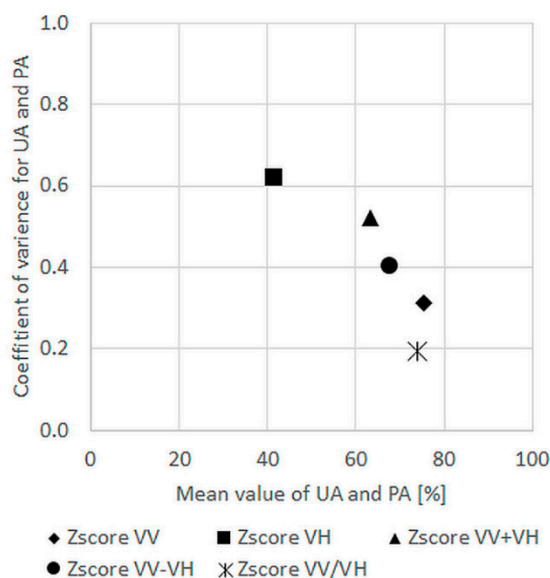
Figure 14. Comparison of object-based time series features as a function of mean value and coefficient of variation. The statistical values (mean value and coefficient of variance) were calculated on the basis of the PA and UA accuracy values.

4. Conclusions

The results of the study areas in northern and southern Greece/Turkey and in China show the potential of the method presented in Tsyganskaya et al., [8] using S-1 time series data to extract the total flood extent considering both temporary open water (TOW) and temporary flooded vegetation (TFV). In particular, different types of TFV were analyzed. The individual flood extent was determined by time series features, which represent the characteristics of both classes.

This study confirms the results of the study of Tsyganskaya et al., [8], showing that the Z-Score VV+VH, which was derived based on the characteristics mentioned above, is the most relevant time series feature for the extraction of the TOW areas in all study areas. For the derivation of TFV, three different time series features were determined by the algorithm for individual study areas. This can be explained by the complex structure of the vegetation, the various analyzed vegetation types, and the dependency of the TFV on environmental conditions (e.g., vegetation type, soil moisture, topography), which differ in all study areas. Nevertheless, in the results for all study areas OA values reached between 80% and 87%, which were slightly higher even compared to the results in [8]. For the study area in northern Greece, the TFV areas could only partially be derived based on the C-band data due to the presence of forested vegetation, which reduces the penetration of the SAR signal. In both other study areas, TFV in high grassland/reed was successfully classified.

The potential of the time series approach for transferability as a prerequisite for operational use was analyzed by comparing time series features with respect to their suitability for the derivation of TFV for all study areas simultaneously. For the comparison, statistical quantities were derived from the classification accuracies PA and UA of the TFV. For TFV, Z-Score VV, or Z-Score VV/VH appear to be the most relevant time series feature for pixel-based and object-based classification, respectively. Nevertheless, Z-Score VV is recommended for operational use based on pixel elements for the extraction of TFV as this allows improved differentiation to non-flood dates due to the more significant increase in the VV time series for TFV at the date of the flood compared to the VH time series. The Z-Score VV + VH is recommended for the extraction of TOW surfaces, because of the unanimity regarding the feature importance calculation for all study areas (Section 3.1). Since the time series features have been defined and no feature importance needs to be calculated, the user interaction is reduced to the initialization of the classification process and the computation time decreases.

Overall, the approach can be used for irregularly occurring flood events, as well as for irregularly acquired S-1 images. It is flexible for individual applications depending on the vegetation and takes account of the seasonal changes by the use of multitemporal data. The presented SAR time series approach lays the cornerstone for automatic flood detection on a global scale, allowing the detection of the entire flood extent by supplementing the TOW with TFV areas.

References

1. The International Disaster-Emergency Events Database (EMDAT). *OFDA/CRED International Disaster Database*; Université catholique de Louvain: Brussels, Belgium, 2019; Available online: https://www.emdat.be (accessed on 1 August 2019).

2. Centre for Research on the Epidemiology of Disasters (CRED); The United Nations Office for Disaster Risk Reduction (UNISDR). 2018 Review of Disaster Events. 2019. Available online: https://www.emdat.be/publications (accessed on 31 August 2019).

3. Klemas, V. Remote Sensing of Floods and Flood-Prone Areas: An Overview. *J. Coast. Res.* **2014**, *31*, 1005–1013. [CrossRef]

4. Cazals, C.; Rapinel, S.; Frison, P.-L.; Bonis, A.; Mercier, G.; Mallet, C.; Corgne, S.; Rudant, J.-P. Mapping and Characterization of Hydrological Dynamics in a Coastal Marsh Using High Temporal Resolution Sentinel-1A Images. *Remote Sens.* **2016**, *8*, 570. [CrossRef]

5. Martinis, S.; Rieke, C. Backscatter Analysis Using Multi-Temporal and Multi-Frequency SAR Data in the Context of Flood Mapping at River Saale, Germany. *Remote Sens.* **2015**, *7*, 7732–7752. [CrossRef]

6. Pulvirenti, L.; Pierdicca, N.; Chini, M. Analysis of Cosmo-SkyMed observations of the 2008 flood in Myanmar. *Ital. J. Remote Sens.* **2010**, *42*, 79–90. [CrossRef]

7. Brisco, B.; Shelat, Y.; Murnaghan, K.; Montgomery, J.; Fuss, C.; Olthof, I.; Hopkinson, C.; Deschamps, A.; Poncos, V. Evaluation of C-Band SAR for Identification of Flooded Vegetation in Emergency Response Products. *Can. J. Remote Sens.* **2019**. [CrossRef]

8. Tsyganskaya, V.; Martinis, S.; Marzahn, P.; Ludwig, R. Detection of Temporary Flooded Vegetation Using Sentinel-1 Time Series Data. *Remote Sens.* **2018**, *10*, 1286. [CrossRef]

9. Moser, L.; Schmitt, A.; Wendleder, A. Automated Wetland Delineation from Multi-Frequency and Multi-Polarized SAR Images in High Temporal and Spatial Resolution. *ISPRS Ann. Photogramm. Remote Sens. Spat. Inf. Sci.* **2016**, *3*, 57–64. [CrossRef]

10. Pulvirenti, L.; Pierdicca, N.; Chini, M.; Guerriero, L. Monitoring Flood Evolution in Vegetated Areas Using COSMO-SkyMed Data: The Tuscany 2009 Case Study. *IEEE J. Sel. Top. Appl. Earth Obs. Remote Sens.* **2012**, *6*, 1807–1816. [CrossRef]

11. Betbeder, J.; Rapinel, S.; Corpetti, T.; Pottier, E.; Corgne, S.; Hubert-Moy, L. Multitemporal Classification of TerraSAR-X Data for Wetland Vegetation Mapping. *J. Appl. Remote Sens.* **2014**, *8*, 83648. [CrossRef]

12. Chapman, B.; McDonald, K.; Shimada, M.; Rosenqvist, A.; Schroeder, R.; Hess, L. Mapping Regional Inundation with Spaceborne L-Band SAR. *Remote Sens.* **2015**, *7*, 5440–5470. [CrossRef]

13. Evans, T.L.; Costa, M.; Tomas, W.M.; Camilo, A.R. Large-Scale Habitat Mapping of the Brazilian Pantanal Wetland. A synthetic aperture radar approach. *Remote Sens. Environ.* **2014**, *155*, 89–108. [CrossRef]

14. Hess, L. Dual-Season Mapping of Wetland Inundation and Vegetation for the Central Amazon Basin. *Remote Sens. Environ.* **2003**, *87*, 404–428. [CrossRef]

15. Lang, M.W.; Kasischke, E.S.; Prince, S.D.; Pittman, K.W. Assessment of C-band synthetic aperture radar data for mapping and monitoring Coastal Plain forested wetlands in the Mid-Atlantic Region, USA. *Remote Sens. Environ.* **2008**, *112*, 4120–4130. [CrossRef]

16. Chini, M.; Papastergios, A.; Pulvirenti, L.; Pierdicca, N.; Matgen, P.; Parcharidis, I. SAR coherence and polarimetric information for improving flood mapping. In Proceedings of the 2016 IEEE International Geoscience & Remote Sensing Symposium, Beijing, China, 10–15 July 2016; pp. 7577–7580.

17. Morandeira, N.; Grings, F.; Facchinetti, C.; Kandus, P. Mapping Plant Functional Types in Floodplain Wetlands. An Analysis of C-Band Polarimetric SAR Data from RADARSAT-2. *Remote Sens.* **2016**, *8*, 174. [CrossRef]

18. Touzi, R.; Deschamps, A.; Rother, G. Wetland Characterization using Polarimetric RADARSAT-2 Capability. *Can. J. Remote Sens.* **2007**, *33*, S56–S67. [CrossRef]

19. Pulvirenti, L.; Chini, M.; Pierdicca, N.; Boni, G. Use of SAR Data for Detecting Floodwater in Urban and Agricultural Areas: The Role of the Interferometric Coherence. *IEEE Trans. Geosci. Remote Sens.* **2016**, *54*, 1532–1544. [CrossRef]

20. Baghdadi, N.; Bernier, M.; Gauthier, R.; Neeson, I. Evaluation of C-band SAR Data for Wetlands Mapping. *Int. J. Remote Sens.* **2001**, *22*, 71–88. [CrossRef]

21. Gallant, A.; Kaya, S.; White, L.; Brisco, B.; Roth, M.; Sadinski, W.; Rover, J. Detecting Emergence, Growth, and Senescence of Wetland Vegetation with Polarimetric Synthetic Aperture Radar (SAR) Data. *Water* **2014**, *6*, 694–722. [CrossRef]

22. White, L.; Brisco, B.; Pregitzer, M.; Tedford, B.; Boychuk, L. RADARSAT-2 Beam Mode Selection for Surface Water and Flooded Vegetation Mapping. *Can. J. Remote Sens.* **2014**, *40*, 135–151.

23. Brisco, B.; Schmitt, A.; Murnaghan, K.; Kaya, S.; Roth, A. SAR Polarimetric Change Detection for Flooded Vegetation. *Int. J. Digit. Earth* **2011**, *6*, 103–114. [CrossRef]

24. De Grandi, G.F.; Mayaux, P.; Malingreau, J.P.; Rosenqvist, A.; Saatchi, S.; Simard, M. New Perspectives on Global Ecosystems from Wide-Area Radar Mosaics. Flooded forest mapping in the tropics. *Int. J. Remote Sens.* **2010**, *21*, 1235–1249. [CrossRef]

25. Dabboor, M.; White, L.; Brisco, B.; Charbonneau, F. Change Detection with Compact Polarimetric SAR for Monitoring Wetlands. *Can. J. Remote Sens.* **2015**, *41*, 408–417. [CrossRef]

26. Zhao, L.; Yang, J.; Li, P.; Zhang, L. Seasonal Inundation Monitoring and Vegetation Pattern Mapping of the Erguna Floodplain by Means of a RADARSAT-2 Fully Polarimetric Time Series. *Remote Sens. Environ.* **2014**, *152*, 426–440. [CrossRef]

27. Koch, M.; Schmid, T.; Reyes, M.; Gumuzzio, J. Evaluating Full Polarimetric C- and L-Band Data for Mapping Wetland Conditions in a Semi-Arid Environment in Central Spain. *IEEE J. Sel. Top. Appl. Earth Obs. Remote Sens.* **2012**, *5*, 1033–1044. [CrossRef]

28. Lee, J.-S.; Pottier, E. *Polarimetric Radar Imaging: From Basics to Applicationsvol*; CRC Press: Boca Raton, FL, USA, 2009; p. 142.

29. Tsyganskaya, V.; Martinis, S.; Marzahn, P.; Ludwig, R. SAR-based Detection of Flooded Vegetation–A Review of Characteristics and Approaches. *Int. J. Remote Sens.* **2018**, *39*, 2255–2293. [CrossRef]

30. Chini, M.; Pulvirenti, L.; Pierdicca, N. Analysis and Interpretation of the COSMO-SkyMed Observations of the 2011 Japan Tsunami. *IEEE Geosci. Remote Sens. Lett.* **2012**, *9*, 467–471. [CrossRef]

31. Long, S.; Fatoyinbo, T.E.; Policelli, F. Flood Extent Mapping for Namibia using Change Detection and Thresholding with SAR. *Environ. Res. Lett.* **2014**, *9*, 035002. [CrossRef]

32. Voormansik, K.; Praks, J.; Antropov, O.; Jagomagi, J.; Zalite, K. Flood Mapping with TerraSAR-X in Forested Regions in Estonia. *IEEE J. Sel. Top. Appl. Earth Obs. Remote Sens.* **2014**, *7*, 562–577. [CrossRef]

33. Horritt, M.S.; Mason, D.C.; Luckman, A.J. Flood Boundary Delineation from Synthetic Aperture Radar Imagery Using a Statistical Active Contour Model. *Int. J. Remote Sens.* **2001**, *22*, 2489–2507. [CrossRef]

34. Martinis, S.; Twele, A. A Hierarchical Spatio-Temporal Markov Model for Improved Flood Mapping Using Multi-Temporal X-Band SAR Data. *Remote Sens.* **2010**, *2*, 2240–2258. [CrossRef]

35. Chen, Y.; He, X.; Wang, J.; Xiao, R. The Influence of Polarimetric Parameters and an Object-Based Approach on Land Cover Classification in Coastal Wetlands. *Remote Sens.* **2014**, *6*, 12575–12592. [CrossRef]

36. Plank, S.; Jüssi, M.; Martinis, S.; Twele, A. Mapping of Flooded Vegetation by Means of Polarimetric Sentinel-1 and ALOS-2/PALSAR-2 imagery. *Int. J. Remote Sens.* **2017**, *38*, 3831–3850. [CrossRef]

37. Karszenbaum, H.; Kandus, P.; Martinez, J.M.; Le Toan, T.; Tiffenberg, J.; Parmuchi, G. *Radarsat SAR Backscattering Characteristics of the Parana River Delta Wetland, Argentina*; ESA Publication: Auckland, New Zealand, 2000.

38. Pierdicca, N.; Chini, M.; Pulvirenti, L.; Macina, F. Integrating Physical and Topographic Information into a Fuzzy Scheme to Map Flooded Area by SAR. *Sensors* **2008**, *8*, 4151–4164. [CrossRef] [PubMed]

39. Pulvirenti, L.; Pierdicca, N.; Chini, M.; Guerriero, L. An Algorithm for Operational Flood Mapping from Synthetic Aperture Radar (SAR) Data using Fuzzy Logic. *Nat. Hazards Earth Syst. Sci.* **2011**, *2*, 529–540. [CrossRef]

40. Bouvet, A.; Le Toan, T. Use of ENVISAT/ASAR wide-swath data for timely rice fields mapping in the Mekong River Delta. *Remote Sens. Environ.* **2011**, *115*, 1090–1101. [CrossRef]

41. Martinez, J.; Le Toan, T. Mapping of Flood Dynamics and Spatial Distribution of Vegetation in the Amazon Floodplain using Multitemporal SAR Data. *Remote Sens. Environ.* **2007**, *108*, 209–223. [CrossRef]

42. Hess, L.L.; Melack, J.M.; Affonso, A.G.; Barbosa, C.; Gastil-Buhl, M.; Novo, E.M.L.M. Wetlands of the Lowland Amazon Basin. Extent, Vegetative Cover, and Dual-season Inundated Area as Mapped with JERS-1 Synthetic Aperture Radar. *Wetlands* **2015**, *35*, 745–756. [CrossRef]

43. Schlaffer, S.; Chini, M.; Dettmering, D.; Wagner, W. Mapping Wetlands in Zambia Using Seasonal Backscatter Signatures Derived from ENVISAT ASAR Time Series. *Remote Sens.* **2016**, *8*, 402. [CrossRef]

44. Ferreira-Ferreira, J.; Silva, T.S.F.; Streher, A.S.; Affonso, A.G.; de Almeida Furtado, L.F.; Forsberg, B.R.; de Moraes Novo, E.M.L. Combining ALOS/PALSAR derived vegetation structure and inundation patterns to characterize major vegetation types in the Mamirau? Sustainable Development Reserve, Central Amazon floodplain, Brazil. *Wetlands Ecol. Manag.* **2015**, *23*, 41–59. [CrossRef]

45. Lee, H.; Yuan, T.; Jung, H.C.; Beighley, E. Mapping wetland water depths over the central Congo Basin using PALSAR ScanSAR, Envisat altimetry, and MODIS VCF data. *Remote Sens. Environ.* **2015**, *159*, 70–79. [CrossRef]

46. Li, J.; Chen, W. A rule-based method for mapping Canada's wetlands using optical, radar and DEM data. *Int. J. Remote Sens.* **2005**, *22*, 5051–5069. [CrossRef]

47. Marti-Cardona, B.; Dolz-Ripolles, J.; Lopez-Martinez, C. Wetland inundation monitoring by the synergistic use of ENVISAT/ASAR imagery and ancilliary spatial data. *Remote Sens. Environ.* **2013**, *139*, 171–184. [CrossRef]

48. Bourgeau-Chavez, L.; Lee, Y.; Battaglia, M.; Endres, S.; Laubach, Z.; Scarbrough, K. Identification of Woodland Vernal Pools with Seasonal Change PALSAR Data for Habitat Conservation. *Remote Sens.* **2016**, *8*, 490. [CrossRef]

49. Zhang, M.; Li, Z.; Tian, B.; Zhou, J.; Zeng, J. A Method for Monitoring Hydrological Conditions Beneath Herbaceous Wetlands Using Multi-temporal ALOS PALSAR Coherence Data. *Int. Arch. Photogramm. Remote Sens. Spat. Inf. Sci.* **2015**, *6*, 221–226. [CrossRef]

50. Evans, T.L.; Costa, M. Landcover classification of the Lower Nhecolândia subregion of the Brazilian Pantanal Wetlands using ALOS/PALSAR, RADARSAT-2 and ENVISAT/ASAR imagery. *Remote Sens. Environ.* **2013**, *128*, 118–137. [CrossRef]

51. Grings, F.M.; Ferrazzoli, P.; Karszenbaum, H.; Salvia, M.; Kandus, P.; Jacobo-Berlles, J.C.; Perna, P. Model investigation about the potential of C band SAR in herbaceous wetlands flood monitoring. *Int. J. Remote Sens.* **2008**, *29*, 5361–5372. [CrossRef]

52. Lang, M.W.; Kasischke, E.S. Using C-Band Synthetic Aperture Radar Data to Monitor Forested Wetland Hydrology in Maryland's Coastal Plain, USA. *IEEE Trans. Geosci. Remote Sens.* **2008**, *46*, 535–546. [CrossRef]

53. Farr, T.G.; Rosen, P.A.; Caro, E.; Crippen, R.; Duren, R.; Hensley, S.; Kobrick, M.; Paller, M.; Rodriguez, E.; Roth, L.; et al. The Shuttle Radar Topography Mission. *Rev. Geophys.* **2007**, *45*, 1485. [CrossRef]

54. Esch, T.; Taubenböck, H.; Roth, A.; Heldens, W.; Felbier, A.; Thiel, M.; Schmidt, M.; Müller, A.; Dech, S. TanDEM-X Mission—New Perspectives for the Inventory and Monitoring of Global Settlement Patterns. *J. Appl. Remote Sens.* **2012**, *6*, 061702. [CrossRef]

55. Rennó, C.D.; Nobre, A.D.; Cuartas, L.A.; Soares, J.V.; Hodnett, M.G.; Tomasella, J.; Waterloo, M.J. HAND, a New Terrain Descriptor Using SRTM-DEM: Mapping terra-firme rainforest environments in Amazonia. *Remote Sens. Environ.* **2008**, *112*, 3469–3481. [CrossRef]

56. Twele, A.; Cao, W.; Plank, S.; Martinis, S. Sentinel-1-based Flood Mapping: A fully Automated Processing Chain. *Int. J. Remote Sens.* **2016**, *37*, 2990–3004. [CrossRef]

57. Richards, J.A. *Remote Sensing Digital Image Analysis*; Springer: Berlin, Germany, 2013.

58. Lewis, F.M.; Henderson, A.J. *Principles and Applications of Imaging Radar: Manual of Remote Sensingvol*; Wiley: New York, NY, USA, 1998; Volume 2.

59. Marti-Cardona, B.; Lopez-Martinez, C.; Dolz-Ripolles, J.; Bladè-Castellet, E. ASAR Polarimetric, Multi-Incidence Angle and Multitemporal Characterization of Doñana Wetlands for Flood Extent Monitoring. *Remote Sens. Environ.* **2010**, *114*, 2802–2815. [CrossRef]

60. Hess, L.L.; Melack, J.M.; Simonett, D.S. Radar Detection of Flooding Beneath the Forest Canopy: A review. *Int. J. Remote Sens.* **1990**, *11*, 1313–1325. [CrossRef]

61. Sang, H.; Zhang, J.; Lin, H.; Zhai, L. Multi-Polarization ASAR Backscattering from Herbaceous Wetlands in Poyang Lake Region, China. *Remote Sens.* **2014**, *6*, 4621–4646. [CrossRef]

62. Woodhouse, I.H. *Introduction to Microwave Remote Sensing*; CRC Press Taylor & Francis: Boca Raton, FL, USA, 2006.

63. Yu, Y.; Saatchi, S. Sensitivity of L-Band SAR Backscatter to Aboveground Biomass of Global Forests. *Remote Sens.* **2016**, *8*, 522. [CrossRef]

64. Hu, J.-Y.; Xie, Y.-H.; Tang, Y.; Li, F.; Zou, Y.-A. Changes of Vegetation Distribution in the East Dongting Lake After the Operation of the Three Gorges Dam, China. *Front. Plant Sci.* **2018**, *9*, 582. [CrossRef] [PubMed]

65. Ulaby, F.T.; Long, D.G. *Microwave Radar and Radiometric Remote Sensing*; Artech House: Norwood, Switzerland, 2015.

66. Bousbih, S.; Zribi, M.; Lili-Chabaane, Z.; Baghdadi, N.; El Hajj, M.; Gao, Q.; Mougenot, B. Potential of Sentinel-1 Radar Data for the Assessment of Soil and Cereal Cover Parameters. *Sensors* **2017**, *17*, 2617. [CrossRef]

67. Kasischke, E.S.; Smith, K.B.; Bourgeau-Chavez, L.L.; Romanowicz, E.A.; Brunzell, S.; Richardson, C.J. Effects of Seasonal Hydrologic Patterns in South Florida Wetlands on Radar Backscatter Measured from ERS-2 SAR Imagery. *Remote Sens. Environ.* **2003**, *88*, 423–441. [CrossRef]

68. Kwoun, O.; Lu, Z. Multi-temporal RADARSAT-1 and ERS Backscattering Signatures of Coastal Wetlands in Southeastern Louisiana. *Photogramm. Eng. Remote Sens.* **2009**, *75*, 607–617. [CrossRef]

5 Conclusion and outlook

This thesis focuses on the extraction of TFV areas for improved flood detection. As a foundation the new generation of dual polarized C-Band satellites, such as the dual polarized S-1 constellation, with high revisit frequencies is applied. The increased availability of SAR imagery and the use of C-band data provide a foundation for frequent and accurate large-scale flood monitoring. Furthermore, the possibility of detecting and extracting flooded areas even under the vegetation is growing. The major goal of this thesis is to develop a SAR times series-based approach for the extraction of TFV and improved and transferable flood extent derivation using a new generation of temporally and spatially high-resolution C-band SAR satellite data. The publications present the steps performed, the challenges emerging from this as well as the final results and their critical discussion. The key findings of this work are summarized in the following conclusion along with the research questions presented in Section 1.3.

Research question 1: Does the comparison of the state of the art of the method provide an identification of the trends regarding the SAR-based classification algorithms for the extraction of TFV?

The comparison of the state-of-the-art method revealed some inconsistencies in the application of classification algorithms for the extraction of TFV. It can be explained by the wide variety of the applied data, which often depends on the individual task, but is mostly limited by its availability. A large variety of different classification techniques were applied in the investigated studies, ranging from simple threshold approaches to more complex algorithms such as machine learning. Single image approaches are still preferred and mostly applied in combination with additional data, such as optical or elevation information, to describe TFV and other ground cover types (Tsyganskaya et al. 2018b). Significantly fewer studies apply change detection techniques, which requires manual intervention for the selection of an image acquired under dry conditions. The selection of an image with dry conditions for a change detection approach is crucial because it has an impact on the differentiability to an image indicating flood conditions and thus whether the selected image provides a suitable foundation for flood detection.

Although the comparison of the state of the art of the methods in Tsyganskaya et al. (2018b) shows a low application of studies with multi-date or time series SAR data, the use of such data is promising, because these data include the information about the seasonal changes of the backscatter signal regarding the vegetation. SAR time series data provide the opportunity to distinguish seasonal fluctuations from flood-related outliers over the given timeframe. The use of multitemporal SAR data in combination with the increasing availability of data, short revisit times and systematic data acquisition by satellite missions, such as Sentinel-1, paves the way for the application of SAR time series approaches.

Overall, the overview of the state of the art in relation to the data sets and algorithms available in the future for the extraction of TFV showed a methodological trend towards a SAR time series approach. The comparably low use of SAR time series data and only few existing SAR time series approaches for the detection of TFV show the potential need for research in this area. Continuing efforts in the analysis of long-term profiles will increase understanding about the seasonal and annual variability and enable the development of potentially transferable and operationally

usable approaches for the extraction of TFV and for the improved flood detection (Section 4.2 and 4.3).

Research question 2: Are the multitemporal characteristics and patterns of the SAR time series data suitable for identifying flood-related classes (TOW and TFV)?

The analysis of dual-polarized C-band time series data revealed specific multitemporal characteristics and patterns (decrease and increase of backscatter values during the flood period), which are indicative of flood related classes, such as temporary open water (TOW) and temporary flooded vegetation (TFV). The multi-temporal behavior of the flood-related classes has been analyzed for the two single polarizations (VV, VH) and their ratio VV/VH. A significant decrease of the backscatter values for TOW could be identified for both polarizations on the analyzed time period during the flood event. The ratio of these two polarizations shows no change at the analyzed date of the flood event, which indicates a simultaneous and similar change in both polarizations during the flood event. On the contrary, TFV is characterized by an increase in the backscatter values on the analyzed flood date in VV polarization (Tsyganskaya et al. 2018a). This increase can be explained by the double- or multi-bounce interactions between the specular water surface and the vertical structures of the vegetation (Moser et al. 2016, Pulvirenti et al. 2011b, Pulvirenti et al. 2012). Compared to VV polarization, VH polarization shows a decrease of the backscatter value for TFV. Due to the depolarizing property of VH polarization, the double-bounce effect cannot be detected and the increase in backscattering values is not expected in VH (Henderson and Lewis 1998, Marti-Cardona et al. 2010, Martinis and Rieke 2015). The backscatter value of the polarization ratio increases at the time of flood, because of the aforementioned different behavior between VV and VH (Tsyganskaya et al. 2018a).

To ensure that the decrease or increase of the backscatter signal is not related to phenological or other influences, but rather corresponds to the flood-related changes, the multi-time behavior of the NDVI and NDWI ratios, derived from optical images, was included in the analysis. The use of characteristics and patterns allows for the integration of seasonal changes and thus the identification of the variation of the backscatter values for the non-flooded condition. The consideration of this information leads to improved differentiability between the backscatter values on the flood date and the backscatter values acquired under dry conditions.

Research question 3: Do the operational dual-polarized SAR systems have the potential to provide time series features for the derivation of flood related classes (TOW and TVF)?

Based on multitemporal characteristics and patterns, time series features were determined using VV, VH and their combinations. To ensure the comparability of the changes for each image element and thus the independency of the different phenological developments of the vegetation or other local environmental influences, the normalization of backscatter values over the time series for each image element was implemented. For this purpose, the time series features were developed using each of the polarizations (VV, VH) and their combinations (VV/VH, VV-VH, VV+VV) individually (Tsyganskaya et al. 2018a). Considering the backscatter values on the flood date and the mean value and standard deviation of the backscatter values from the non-flood dates, the generation of the time series features was performed by Z-transform for each image element. When calculating the time series features, this irregularity of

the data, such as gaps, is not necessary, assuming the decrease or increase during the flood time is present.

The time series features were generated for four independent study areas. In order to reduce the redundant information and thus the application complexity, time series features were identified for each individual study area regarding their informational relevance for the identification of flood-related classes. The identification was implemented by applying the Random Forest Algorithm based on the study area-related training data. With this method, relevant time series features for the extraction of flood-related classes (TOW and TFV) could be identified using dual-polarized SAR data.

For TOW, a single time series feature based on the polarization combination VV+VH was independently identified for each study area. However, different time series features for TFV were identified for different study areas containing the relevant information for differentiation in to other classes. The time series features based on the polarization ratio VV/VH, polarization combination VV-VH, polarization VV and polarization combination VV+VH were identified for the study areas Namibia, Southern Greece/Turkey, Northern Greece/Turkey and China, respectively. This can be attributed to the complexity of the TFV vegetation and the strong influence of the environmental conditions (vegetation types, water level, topography (Tsyganskaya et al. 2018b) in each of the analyzed study areas having a strong influence on the radar signal (Tsyganskaya et al. 2019).

Research question 4: Are dual-polarized Sentinel-1 time series data suitable for the development of a robust classification approach for TFV extraction and improved flood detection?

Utilizing the time series features with the highest contribution for TOW and TFV for each of the study areas, a supervised hierarchical threshold-based method was applied to the derivation of the flood extent. The approach developed here was used to map large-scale flood events that occurred in Namibia, at the border between Greece and Turkey and in China containing TFV areas. The results indicate a reliable classification with an overall accuracy between of 75.0% and 84.3% for a pixel-based and 80.5% and 87.3 % for an object-based approach and refer to the flood extent assessment for the individual study areas with individual time series features (Tsyganskaya et al. 2018a, Tsyganskaya et al. 2019). In addition, it was demonstrated that the inclusion of TFV enhances the extraction of an entire flood extent by 27.0%. In addition, the Kappa coefficient increased from 0.24 to 0.69. Overall, the classification results show that the dual-polarized Sentinel-1 time series approach allows for a reliable extraction of the TFV area and thus improved flood detection.

Since the approach developed here is based on the information about the increase and decrease of backscatter values observed in the time series during the flood period, it is essential that the number of images capturing flood conditions does not exceed the number images capturing non-flood conditions. Periodically occurring events within an investigated period can also reduce the intensity of the changes during the flood event. This may affect the differentiability, especially between classes TFV and dry land, as the increase in time series data for TFV is not as pronounced as the decrease for TOW. Furthermore, the use of a time series with at least one vegetation cycle is recommended, as the statistical range of the backscatter values of the vegetation stages is detected and thus sufficiently represented (Tsyganskaya et al. 2018a). Nevertheless, the application is particularly suitable for the derivation of flood extent in relation to extreme events, since the SAR time series approach is based on the indirect identification of outliers.

5   Conclusion and outlook

The robustness of the time series approach is achieved by integrating a variety of ancillary information, such as the distribution of permanent water and urban areas, as well as information about the topography. On the one hand, this information allows for the preventive avoidance of confusion between permanent water surfaces and TOW areas, while on the other hand the prevention of water-lookalikes, such as shadows in mountainous areas. In addition, the identification of urban areas helps to prevent lookalikes to TFV, since they are characterized by strong double-bounce and multiple scattering effects. Since the focus of the study is on the derivation of TFV areas and a high probability of confusion of backscatter values between flooded urban areas and TFV exists, and the derivation of floodplains in urban areas is a highly complex issue, these areas are excluded in the methodology. Nevertheless, flood mapping in urban areas is of great importance, as most fatalities and economic losses occur during floods in urban areas and should be addressed in an independent research project in the future.

Research question 5: Can the SAR time series approach be transferred to different study areas and vegetation types using a single time series feature for the extraction of TFV and thus be applied operationally?

In order to answer this research question, a comparison of the time series features based on statistical values was carried out for all study areas. This method is applied to the transferability analysis of the SAR times series approach, allowing for the identification of a single time series feature, which can be used for the derivation of the TFV types for all study areas simultaneously. Thereby, the potential of the SAR time series approach for operational use was demonstrated. The analysis is carried out based on accuracy values, obtained by multiple runs of the SAR time series approach with each of the time series features for the study areas in Namibia, in Greece/Turkey and in China containing different vegetation types, such as high grassland and forested areas. The visualization and quantification of the time series features comparison demonstrates that Z-Score VV + VH and Z-Score VV are recommended for the operational use for the derivation of the TOW and TFV for analyzed study areas, respectively. Because no feature importance has to be calculated during the classification process, the calculation time decreases significantly. In addition, the user interaction is reduced to the initialization of the classification process, since the time series features have already been defined.

With the upcoming new spaceborne SAR sensor operating at L-band, such as TanDEM-L (German Aerospace Center 2017), new opportunities for the synergetic use of C-band und L-band data will arise. In combination with the short revisit time of TanDEM-L, the proposed time series approach could be initially transferred and adapted to the L-band data. Since the SAR signal in the C- and L-band has different penetration depths into vegetation crowns, better results for the derivation of the TFV in forest areas, as already observed in previous studies based on other L-band SAR satellite data (Hess et al. 1990) using TanDEM-L data, can be expected.

The achievements of this thesis provide a pathway for the future flood monitoring with the focus on TFV providing an enhanced derivation of flood extent from S-1 time series C-band data worldwide. It has been shown that the flood extent can be extracted more precisely due to the new component the TFV.

Reference

Ansari, A. A.; and S. S. Gill. 2014. 'Eutrophication'. Causes, Consequences and Control Dordrecht: Springer Netherlands.

Arnhold, T. 2008. 'Vegetation hardly affected by extreme flood events'. First publication on the impacts on flora and fauna of the Elbe flood of 2002. Hg. v. Helmholtz Centre for Environmental Research (UFZ). Available online at: https://www.ufz.de/index.php?en=35643).

Bähr, H.-P., and T. Vögtle. (Hg.). 1998. 'Digitale Bildverarbeitung'. Anwendung in Photogrammetrie, Kartographie und Fernerkundung 3. Ed. Heidelberg: Wichmann.

Bamler, R., and B. Schättler. 1993. 'SAR data acquisition and image formation'. *In: SAR geocoding: data and systems*. 53–102.

Bayanudin, A. A., and R. H. Jatmiko. 2016. 'Orthorectification of Sentinel-1 SAR (Synthetic Aperture Radar) Data in Some Parts of South-eastern Sulawesi Using Sentinel-1 Toolbox'. *In: IOP Conference Series: Earth and Environmental Science*. 47.

Bayer, T., and R. Winter. 1990. 'Correction of relief effects in SAR-images of vegetated areas'. *In: 10th Annual International Symposium on Geoscience and Remote Sensing.* College Park, Maryland, USA: IEEE. 2215–2218.

Bhatta, B. 2011. 'Remote sensing and GIS'. 2. Ed. New Delhi, India: Oxford University Press.

Bourgeau-Chavez, L. L., E. S. Kasischke, and K. Smith. 1997. 'Using satellite radar imagery to monitor flood conditions in wetland ecoystems of southern Florida'. *In: Proc. SPIE 2959, Remote Sensing of Vegetation and Sea*. Taormina, Italy. 139–148.

Bronstert, A. 2003. 'Floods and Climate Change'. Interactions and Impacts *In: Risk Analysis*. 23 (3). 545–557.

Ciszewski, D., and T. M. Grygar. 2016. 'A Review of Flood-Related Storage and Remobilization of Heavy Metal Pollutants in River Systems'. *In: Water, air, and soil pollution*. 227 (7). 239.

Copernicus. 2018. 'What is Copernicus?'. Available online at: http://copernicus.eu/. (Accessed: 28.10.2018).

CRED, and UNISDR. 2019. '2018 Review of Disaster Events'. Available online at: https://www.emdat.be/publications).

Curlander, J. C., and R. N. MacDonough. 1991. 'Synthetic aperture radar'. Systems and signal processing New York, NY: Wiley (A Wiley Interscience publication).

Damm, C. 2013. 'Ecological restoration and dike relocation on the river Elbe, Germany'.

Dobson, C. M., F. T. Ulaby, and L. E. Pierce. 1995. 'Land-cover classification and estimation of terrain attributes using synthetic aperture radar'. *In: Remote Sensing of Environment*. 51 (1). 199–214.

EMDAT. 2019. 'OFDA/CRED International Disaster Database, Université catholique de Louvain – Brussels – Belgium'. Available online at: https://www.emdat.be/. (Accessed: 01.08.2019).

Reference

ESA. 2018a. 'Copernicus Open Access Hub'. Available online at:
https://scihub.copernicus.eu/dhus/#/home. (Accessed: 28.10.2018).

ESA. 2018b. 'Sentinel-1'. Available online at:
https://sentinel.esa.int/web/sentinel/missions/sentinel-1. (Accessed: 28.10.2018).

FAO. 2011. 'Global food losses and food waste – Extent, causes and prevention.'. Rome.

Frost, V. S., J. A. Stiles, K. S. Shanmugan, and J. C. Holtzman. 1982. 'A Model for Radar Images
and Its Application to Adaptive Digital Filtering of Multiplicative Noise'. *In: IEEE
Transactions on Pattern Analysis and Machine Intelligence*. PAMI-4 (2). 157–166.

Garssen, A. G., A. Baattrup-Pedersen, T. Riis, B. M. Raven, C. C. Hoffman, J. T. A. Verhoeven, and
M. B. Soons. 2017. 'Effects of increased flooding on riparian vegetation'. Field experiments
simulating climate change along five European lowland streams *In: Global change biology*.
23 (8). 3052–3063.

Gergel, S. E., M. D. Dixon, and M. G. Turner. 2002. 'Consequences of human-altered floods'.
Levees, floods, and floodplain forests along the wisconsin river *In: Ecological Applications*.
12 (6). 1755–1770.

German Aerospace Center. 2017. 'Tandem-L'. Satellite Mission Proposal for Monitoring
Dynamic Processes on the Earth's Surface Available online at:
www.dlr.de/hr/en/Portaldata/32/Resources/dokumente/tdml/Tandem-
L_Brochure_2017-05.pdf. (Accessed: 27.08.2017).

Hafeez, F., N. Zafar, R. Nazir, H. M. R. Javeed, M. Rizwan, S. A. A. Faridullah et al. 2019.
'Assessment of flood-induced changes in soil heavy metal and nutrient status in Rajanpur,
Pakistan'. *In: Environmental monitoring and assessment*. 191 (4). 234.

Hein, A. 2004. 'Processing of SAR Data'. Fundamentals, Signal Processing, Interferometry
Berlin, Heidelberg s.l.: Springer Berlin Heidelberg (Signals and Communication
Technology).

Henderson, F. M., and A. J. Lewis. (Hg.). 1998. 'Principles and Applications of Imaging Radar'.
New York: J. Wiley (2).

Hess, L. L., J. M. Melack, and D. S. Simonett. 1990. 'Radar Detection of Flooding Beneath the
Forest Canopy'. A review *In: International Journal of Remote Sensing*. 11 (7). 1313–1325.

IPPC. 2012. 'Managing the Risks of Extreme Events and Disasters to Advance Climate Change
Adaptation'. Unter Mitarbeit von Field, C.B., V. Barros, T.F. Stocker, D. Qin, D.J. Dokken, K.L.
Ebi, M.D. Mastrandrea, K.J. Mach, G.-K. Plattner, S.K. Allen, M. Tignor, and P.M. Midgley (ED.)
Cambridge: Cambridge University Press.

IPPC. 2013. 'The Physical Science Basis. Contribution of Working Group I to the Fifth
Assessment Report of the Intergovernmental Panel on Climate Change'. Unter Mitarbeit von
Stocker, T.F., D. Qin, G.-K. Plattner, M. Tignor, S.K. Allen, J. Boschung, A. Nauels, Y. Xia, V. Bex
and P.M. Midgley Cambridge New York: Cambridge University Press.

Junk, Wolfgang J. (Hg.). 1997. 'The Central Amazon Floodplain'. Ecology of a Pulsing System
Berlin, Heidelberg: Springer Berlin Heidelberg (Ecological Studies, Analysis and Synthesis,
126).

Reference

Kasischke, E. S., and L. L. Bourgeau-Chavez. 1997. 'Monitoring South Florida Wetlands Using ERS-1 SAR Imagery'. *In: Photogrammetric Engineering & Remote Sensing*. 63. 281–291.

Kiage, L. M., N. D. Walker, S. Balasubramanian, A. Babin, and J. Barras. 2005. 'Applications of Radarsat?'. Synthetic Aperture Radar Imagery to Assess Hurricane-Related Flooding of Coastal Louisiana *In: International Journal of Remote Sensing*. 26 (24). 5359–5380.

Klausing, H., and W. Holpp. 2010. 'Radar mit realer und synthetischer Apertur'. Konzeption und Realisierung München: Oldenbourg Wissenschaftsverlag (Naturwissenschaft und Technik II 6-2010).

Klimo, E., and H. Hager. (Hg.). 2001. 'The floodplain forests in Europe'. Current situation and perspectives Leiden: Brill (European Forest Institute research report, 10).

Kryspin-Watson, J., S. Dharmavaram, Z. Stanton-Geddes, and B. Chia. 2017. 'Land use planning for urban flood risk management'. : Global Facility for Disaster Reduction and Recovery.

Kundzewicz, Z. W., I. Pińskwar, and G. R. Brakenridge. 2018. 'Changes in river flood hazard in Europe'. A review *In: Hydrology Research*. 49 (2). 294–302.

Lee, J.-S. 1981. 'Refined filtering of image noise using local statistics'. *In: Computer Graphics and Image Processing*. 15 (4). 380–389.

Lee, J.-S., and E. Pottier. 2009. 'Polarimetric Radar Imaging'. From basics to applications Boca Raton: CRC Press (142).

Lewis, A. J., F. M. Henderson, and D. Holcomb. 1998. 'Radar Fundamentals: The Geoscience Perspective'. *In: F. M. Henderson und A. J. Lewis (Hg.)*: *Principles and Applications of Imaging Radar*. New York: J. Wiley (2). 131–181.

Lillesand, T. M.; Kiefer, R. W.; Chipman, J. W. 2008. 'Remote sensing and image interpretation'. 6. ed. Hoboken, NJ: Wiley.

Lillesand, T. M., R. W. Kiefer, and J. W. Chipman. 2015. 'Remote sensing and image interpretation'. Seventh edition Hoboken, NJ: Wiley.

Long, S., T. E. Fatoyinbo, and F. Policelli. 2014. 'Flood Extent Mapping for Namibia using Change Detection and Thresholding with SAR'. *In: Environmental Research Letters*. 9 (3). 1–9.

Machar, I., H. Hager, V. Pechanec, J. Kulhavy, and J. Mindas. 2019. 'Floodplain Forests—Key Forest Ecosystems for Maintaining and Sustainable Management of Water Resources in Alluvial Landscape.'. *In:* Zelenakova M., Fialová J., Negm A. (Hg.): *Assessment and Protection of Water Resources in the Czech Republic.* Cham: Springer Water. Springer.

Marti-Cardona, B., C. Lopez-Martinez, J. Dolz-Ripolles, and E. Bladè-Castellet. 2010. 'ASAR Polarimetric, Multi-Incidence Angle and Multitemporal Characterization of Doñana Wetlands for Flood Extent Monitoring'. *In: Remote Sensing of Environment*. 114 (11). 2802–2815.

Martinez, J., and T. Le Toan. 2007. 'Mapping of Flood Dynamics and Spatial Distribution of Vegetation in the Amazon Floodplain using Multitemporal SAR Data'. *In: Remote Sensing of Environment*. 108. 209–223.

Martinis, S., J. Kersten, and A. Twele. 2015. 'A fully automated TerraSAR-X based flood service'. *In: ISPRS Journal of Photogrammetry and Remote Sensing*. 104. 203–212.

Reference

Martinis, S., and C. Rieke. 2015. 'Backscatter Analysis Using Multi-Temporal and Multi-Frequency SAR Data in the Context of Flood Mapping at River Saale, Germany'. *In: Remote Sensing*. 7 (6). 7732–7752.

Moreira, A., P. Prats-Iraola, M. Younis, G. Krieger, I. Hajnsek, and K. P. Papathanassiou. 2013. 'A Tutorial on Synthetic Aperture Radar'. *In: IEEE Geoscience and Remote Sensing Magazine*. 1 (1). 6–43.

Moser, L., A. Schmitt, and A. Wendleder. 2016. 'Automated Wetland Delineation From Multi-Frequency and Multi-Polarized SAR Images in High Temporal and Spatial Resolution'. *In: ISPRS Annals of Photogrammetry, Remote Sensing and Spatial Information Sciences*. III-8. 57–64.

Mouginis, P. 2017. 'Introduction to Radar Remote Sensing.'. Available online at: http://satftp.soest.hawaii.edu/space/hawaii/vfts/kilauea/radar_ex/page2.html. (Accessed: 28.10.2018).

Natura 2000. 2019. 'Auenwald Plötzkau (SPA0017)'. Available online at: https://www.natura2000-lsa.de/natura_2000/front_content.php?idart=355&idcat=33&lang=1&pn_note=checked.

OECD. 2017. 'Diffuse Pollution, Degraded Waters: Emerging Policy Solutions'. OECD Studies on Water Paris: OECD Publishing.

Pierdicca, N., M. Chini, L. Pulvirenti, and F. Macina. 2008. 'Integrating Physical and Topographic Information Into a Fuzzy Scheme to Map Flooded Area by SAR'. *In: Sensors*. 8 (7). 4151–4164.

Pulvirenti, L., M. Chini, N. Pierdicca, and G. Boni. 2016. 'Use of SAR Data for Detecting Floodwater in Urban and Agricultural Areas: The Role of the Interferometric Coherence'. *In: IEEE Transactions on Geoscience and Remote Sensing*. 54 (3). 1532–1544.

Pulvirenti, L., M. Chini, N. Pierdicca, L. Guerriero, and P. Ferrazzoli. 2011a. 'Flood Monitoring using Multi-Temporal COSMO-SkyMed Data'. Image segmentation and signature interpretation *In: Remote Sensing of Environment*. 115 (4). 990–1002.

Pulvirenti, L., N. Pierdicca, and M. Chini. 2010. 'Analysis of Cosmo-SkyMed observations of the 2008 flood in Myanmar'. *In: Italian Journal of Remote Sensing*. 79–90.

Pulvirenti, L., N. Pierdicca, M. Chini, and L. Guerriero. 2011b. 'An Algorithm for Operational Flood Mapping from Synthetic Aperture Radar (SAR) Data using Fuzzy Logic'. *In: Natural Hazards and Earth System Science*. 11 (2). 529–540.

Pulvirenti, L., N. Pierdicca, M. Chini, and L. Guerriero. 2012. 'Monitoring Flood Evolution in Vegetated Areas Using COSMO-SkyMed Data'. The Tuscany 2009 Case Study *In: IEEE Journal of Selected Topics in Applied Earth Observations and Remote Sensing*. 6 (4). 1807–1816.

Raney, R. K. 1998. 'Radar Fundamentals: Technical Perspective.'. *In: F. M. Henderson und A. J. Lewis (Hg.)*: *Principles and Applications of Imaging Radar, Bd.* 2. New York: J. Wiley (2). 9–130.

Rao, K. K., S. K. Patwardhan, A. Kulkarni, K. Kamala, S. S. Sabade, and K. K. Kumar. 2014. 'Projected changes in mean and extreme precipitation indices over India using PRECIS'. *In: Global and Planetary Change*. 113. 77–90.

Reference

Richards, J. A. 2009. 'Remote Sensing with Imaging Radar'. Berlin, Heidelberg: Springer-Verlag Berlin Heidelberg (Signals and Communication Technology).

Ritchie, H., and M. Roser. 2019. 'Natural Disasters'. Available online at: OurWorldInData.org.

Schädler, G., P. Berg, D. Düthmann, H. Feldmann, J. Ihringer, H. Kunstmann et al. 2012. 'Flood Hazards in a Changing Climate'. Projekt report: Center for Disaster Management and Risk Reduction Technology (CEDIM).

Schlaffer, S., M. Chini, D. Dettmering, and W. Wagner. 2016. 'Mapping Wetlands in Zambia Using Seasonal Backscatter Signatures Derived from ENVISAT ASAR Time Series'. *In: Remote Sensing*. 8 (5).

Stefanidis, S., and D. Stathis. 2013. 'Assessment of flood hazard based on natural and anthropogenic factors using analytic hierarchy process (AHP)'. *In: Natural Hazards*. 68 (2). 569–585.

Thistlethwaite, J., A. Minano, J. A. Blake, D. Henstra, and D. Scott. 2018. 'Application of re/insurance models to estimate increases in flood risk due to climate change'. *In: Geoenvironmental Disasters*. 5 (1). 158.

Townsend, P. A. 2001. 'Mapping Seasonal Flooding in Forested Wetlands Using Multi-Temporal Radarsat SAR'. *In: Photogrammetric Engineering & Remmote Sensing*. 67. 857–864.

Townsend, P. A. 2002. 'Relationships between Forest Structure and the Detection of Flood Inundation in Forested Wetlands using C-band SAR'. *In: International Journal of Remote Sensing*. 23 (3). 443–460.

Tsyganskaya, V., S. Martinis, P. Marzahn, and R. Ludwig. 2018a. 'Detection of Temporary Flooded Vegetation Using Sentinel-1 Time Series Data'. *In: Remote Sensing*. 10 (8). 1286.

Tsyganskaya, V., S. Martinis, P. Marzahn, and R. Ludwig. 2018b. 'SAR-based Detection of Flooded Vegetation – A Review of Characteristics and Approaches'. *In: International Journal of Remote Sensing*. 39 (8). 2255–2293.

Tsyganskaya, V., Sandro Martinis, and Philip Marzahn. 2019. 'Flood Monitoring in Vegetated areas Using Multitemporal Sentinel-1 data: Impact of time series features'. *In: Water*. submitted

Tully, K., K. Gedan, R. Epanchin-Niell, A. Strong, E. S. Bernhardt, T. BenDor et al. 2019. 'The Invisible Flood'. The Chemistry, Ecology, and Social Implications of Coastal Saltwater Intrusion *In: BioScience*. 69 (5). 368–378.

Ulaby, F. T., and D. G. Long. 2015. 'Microwave Radar and Radiometric Remote Sensing'. Norwood: Artech House.

UNISDR. 2019. '2018 Review of Disaster Events'. Available online at: https://www.cred.be/2018-review-disaster-events.

Vormoor, K., D. Lawrence, M. Heistermann, and A. Bronstert. 2015. 'Climate change impacts on the seasonality and generation processes of floods – projections and uncertainties for catchments with mixed snowmelt/rainfall regimes'. *In: Hydrology and Earth System Sciences*. 19 (2). 913–931.

Reference

Wang, Y., L. L. Hess, S. Filoso, and J. M. Melack. 1995. 'Understanding the radar backscattering from flooded and nonflooded Amazonian forests'. Results from canopy backscatter modeling *In: Remote Sensing of Environment*. 54 (3). 324–332.

Woodhouse, I. H. 2006. 'Introduction to Microwave Remote Sensing'. Boca Raton, Fla.: CRC Press Taylor & Francis.

Zhao, L., J. Yang, P. Li, and L. Zhang. 2014. 'Seasonal Inundation Monitoring and Vegetation Pattern Mapping of the Erguna Floodplain by Means of a RADARSAT-2 Fully Polarimetric Time Series'. *In: Remote Sensing of Environment*. 152. 426–440.

Zischg, A. P., P. Hofer, M. Mosimann, V. Röthlisberger, J. A. Ramirez, M. Keiler, and R. Weingartner. 2018. 'Flood risk (d)evolution'. Disentangling key drivers of flood risk change with a retro-model experiment *In: The Science of the total environment*. 639. 195–207.